Author: Kumar, Manohar
Title: A study of electron scattering through noise spectroscopy
Issue Date: 2012-12-05

A STUDY OF ELECTRON SCATTERING THROUGH NOISE SPECTROSCOPY

A STUDY OF ELECTRON SCATTERING THROUGH NOISE SPECTROSCOPY

Proefschrift

ter verkrijging van
de graad van Doctor aan de Universiteit Leiden,
op gezag van Rector Magnificus prof. mr. P. F. van. der. Heijden,
volgens belsuit van het College voor Promoties,
te verdedigen op vrijdag 5 December 2012
klokke 11:15 uur

door

Manohar KUMAR

geboren te Barauni, Bihar, India.
in 1979

Promotiecommissie:

Promotor:

Prof. dr. J. M. van Ruitenbeek	Universiteit Leiden.

Overige leden:

Prof. dr. E. R. Eliel	Universiteit Leiden.
Prof. dr. A. Levy Yeyati	Universidad Autónoma de Madrid, Spain.
Dr. O. Tal	Weizmann Institute, Rehovot, Israel.
Dr. Y. M. Blanter	Technische Universiteit Delft.
Prof. dr. C. W. J. Beenakker	Universiteit Leiden.
Prof. dr. ir. T. H. Oosterkamp	Universiteit Leiden.

ISBN 978-90-8593-142-3

Casimir PhD Series, Leiden-Delft 2012-36

This work is part of the research program of the Foundation for Fundamental Research on Matter (FOM), which is part of the Netherlands Organization for Scientific Research (NWO)

Cover design: Manohar Kumar
An electronic version of this dissertation is available at

http://repository.leidenuniv.nl/

Science is a wonderful thing
if one does not have to earn one’s living at it.

Albert Einstein

CONTENTS

PREFACE

When the miniaturization of an electronic circuit reaches the scale of single molecules we arrive in a regime dominated by quantum effects. In laboratory experiments, such systems often are made up of a single organic molecule, or a group of metal atoms, bridging two metallic leads. Unlike bulk metals the flow of the electrons here is dominated by the local potential landscape of the molecules or the atoms through which the electron is flowing. Interaction of the conduction electrons with these low dimensional local species, *i.e.* atoms or molecules, reveals their inherent properties. Many properties have been predicted to play a role, such as local vibration modes, the Frank Condon effect, mechanical shuttling, and many body effects such as the Kondo effect. Many of these have been studied experimentally on atomic and molecular systems. Most previous studies have been limited to current - voltage spectroscopy, *i.e.* to the measurement of conductance. The conductance is a time averaged property of the system. It can be viewed as the first moment of the probability distribution of the effective charge being transmitted during the measurement time. The second moment, which measures the spread of this probability distribution from its mean value, provides information which is not present in the mean value. In electron transport physics this second moment is known as shot noise. Hence, the famous quote by Rolf Landauer is very appropriate: "*The noise is the signal*". Hence, noise spectroscopy has become one of the focus themes in nanoelectronics and nanophysics.

Two widely discussed concepts which have been a delight for physicists are electron - electron interactions and electron - vibron interactions. Both of these interactions have been much studied in various atomic and molecular systems. However, most of these studies have been limited to differential conductance spectroscopy. Electron transport in atomic and molecular systems is quite rich and lots of new phenomena have been predicted related to the two interactions mentioned. Our experimental studies here are concerned with new exciting features related to these interactions. Here we have combined both, conductance and noise spectroscopy, to study these effects.

An electron traversing the bridging atom or molecule in a contact has a finite probability of interacting with the local vibrons. This interaction is often observed in a measurement of the differential conductance as a step upward, or a step downward, depending on the transmission probability and other details of the conductance channels. Shot noise, being the second moment of the electron transmission distribution, is more sensitive to this interaction. Shot noise is expected to show deviations from the classical Lesovik-Levitov noise for bias voltages above the vibron energy. For simple systems with a single conductance channel this inelastic correction in the noise has been predicted to change sign at a transmission probability $\tau \simeq 0.15$ and at $\tau \simeq 0.85$. Our shot noise studies here are limited to the inelastic correction in noise around the higher transmission cross-over value $\tau \simeq 0.85$. Since most shot noise studies on atomic or molecular conductors are affected by $1/f$ noise we have developed a noise setup operating at high frequencies(300kHz – 10MHz), which permits the study of noise in simple molecular systems like Pt-D_2-Pt and Au-O-Au.

The force acting on the atoms or molecules by traversing electrons has been recently highlighted by theoretical work which demonstrated that this force is non-conservative. This has led to interesting developments in the fundamentals of electron transport. The non-conservative force acts specifically on nearly degenerate orthogonal vibration modes, which gives rise to "runway modes" at high currents. The force leads to high amplitude oscillations of the atom or molecule in the contact which eventually causes its break down. Until today these concepts have only been formulated theoretically and no quantitative experimental tests have been reported. Here, we have performed preliminary studies of anomalous noise properties in Au atomic contacts and discuss these in relation to the predicted effects due to non-conservative forces.

Magnetism plays a central role in much of condensed matter physics, be it itinerant magnetism or localized magnetic moments, and its interest is tightly connected to applications, such as data storage. The control and read-out of the magnetism of a single atom can be seen as the holy grail of data storage technology. It has been long predicted that some non-magnetic transition metals such as Pt, Pd and Ir, should undergo a transition to a ferromagnetic state upon reduction of the atomic co-ordination number, due to the resulting increase in the density of states at the Fermi energy. Specifically, long Pt atomic chains have been predicted to become magnetic upon stretching, but to date there have been no experimental observations that directly demonstrate itinerant magnetism in Pt atomic chains. Here, we have studied conductance and shot noise for this system in order to probe into the magnetic order of the itinerant electrons.

At the other extreme of magnetism we find localized magnetic moments. Recent studies by Calvo *et al.* on ferromagnetic atomic contacts have shown resonance features near zero voltage bias and these were attributed to the Kondo effect. This was quite unexpected because the Kondo effect is normally associated with inhomogeneous states, with one type of electron system providing the itinerant electrons and the other providing a localized magnetic moment. The Kondo effect in an atomic contact made up of all the same ferromagnetic metal atoms was quite a new concept. Our noise studies on $s-d$ and $s-p$ itinerant atomic and molecular systems form an extension of the work by Calvo *et al.*

This thesis forms a small step towards further understanding of electron transport in atomic and molecular conductors. Noise studies on these systems reveal minuscule perturbations in electron transport, and show the potential of noise spectroscopy in molecular electronics research.

Manohar Kumar
Leiden, December 2012

1

NOISE : BASIC THEORETICAL CONCEPTS

The flow of electrons in a conductor is a stochastic random process due to the discrete nature and randomness in its transfer. The flow of electrons fluctuates around a mean value i.e. the average current. The fluctuation away from the mean current is known as current noise. It has two components: a) The equilibrium noise i.e. thermal noise also known as Johnson-Nyquist noise. It originates from the random motion of electrons in the conductor within the $k_B T$ *width of the Fermi distribution function. b) The non-equilibrium noise i.e. shot noise. The origin of shot noise is due to the randomness in electron reflection at a scatterer. The first full expression for the shot noise in mesoscopic conductors was first derived by Lesovik and Levitov [1]. Since then much advancement has been made in theoretical understanding of the non equilibrium phenomena in mesoscopic devices. Scattering theory, Green function formalisms, Boltzmann-Langevin and counting field theory approaches have been developed to understand the noise in mesoscopic systems. The scattering approach, also known as Landauer-Büttiker approach is a simple quantum mechanical approach which relates the transport properties of the device to the scattering properties of quasiparticles. Here, I introduce scattering matrix formalism to relate the fluctuations in electron transport to the transport properties. Although this approach fails to take into account the effect of inelastic scattering and electron spin correlations in noise, which are central themes of this thesis, it explains beautifully the suppression of noise in atomic contacts. The extensions to inelastic scattering and spin correlations in noise will be developed in later chapter.*

1.1 STATISTICS: AN INTRODUCTION TO RANDOM PROCESSES AND MOMENTS OF A DISTRIBUTION

LET us first look into some basic concepts of statistics[2]. The probability $P(x,t)$ of outcome x at time t is defined as the ratio of outcome x to all possible outcomes for a series of events $x(t)$. It defines the average behavior of events $x(t)$ for determination of $x's$ rate of occurrence. The distribution function $W(x_1,t_1)$ defining the probability can be written in terms of the probability itself *i.e.* $W(x_1,t_1) = P\{x(t_1) \leq x_1\}$. It states the probability for x at t_1 to have a value smaller or equal to x_1. If the distribution function of the random process is differentiable then its probability density function can be written in terms of its distribution function:

$$w(x_1,\ t_1) = \frac{\partial W(x_1,t_1)}{\partial x_1} \tag{1.1}$$

One can use the probability density function, to calculate the mean of the random processes.

$$\langle x(t)\rangle\ = \int_{-\infty}^{\infty} x(t)\, dW(x) = \int_{-\infty}^{\infty} dx\ x\ w(x,t) \tag{1.2}$$

Similarly, higher order moments can be computed from the probability density function using $\langle \delta x(t)\rangle = \langle x(t) - \langle x\rangle\rangle$ which is the deviation of a random quantity $x(t)$ from its mean value $\langle x\rangle$.

$$\langle [\delta x(t)]^r\rangle = \int_{-\infty}^{\infty} dx\ [\delta(x)]^r\ w(x,t) \tag{1.3}$$

The second order central moment is the most important moment of the random process. It is known as the variance. It is also known as fluctuations or noise. Hence, noise measurement is nothing but measurement of the variance of the random processes. Now let's try to understand why the study of fluctuations and higher order moments are important. Figure (1.1) depicts three different hypothetical experiments, counting the rate of occurrence of certain events. The mean rate of occurrence of the events is 10 in all three experiments. Hence by just looking at the mean we will not be able to see the difference between these experiments. If we look at the histograms of these experiments then we can easily see that while (a) and (b) have similar shapes of the probability distribution functions, (c) has a different one. Regarding the variance of (a) and (b), one observes that (a) has a higher variance than (b).

Hence, the higher moments of the fluctuations reveal more information than contained in just the mean values. Figure (1.2) shows the physical significance of the first few central moments. It shows that one should examine also the higher

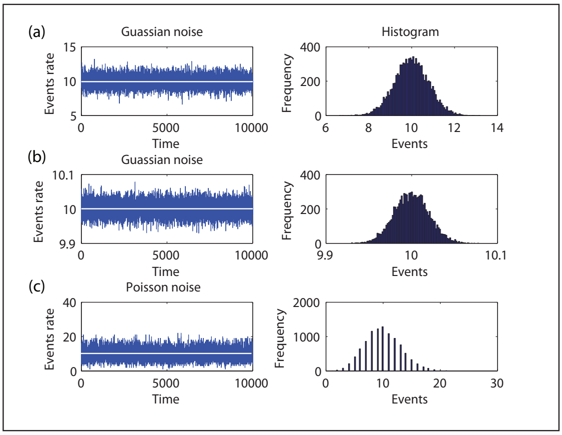

FIGURE 1.1: Fluctuations in measurement: Showing three different simulated measurements along with their frequency spectra. (a) Gaussian events with $\sigma = 0.8$. (b) Gaussian events with $\sigma = 0.02$. (c) Poissonian distribution with $\mu = 10$.

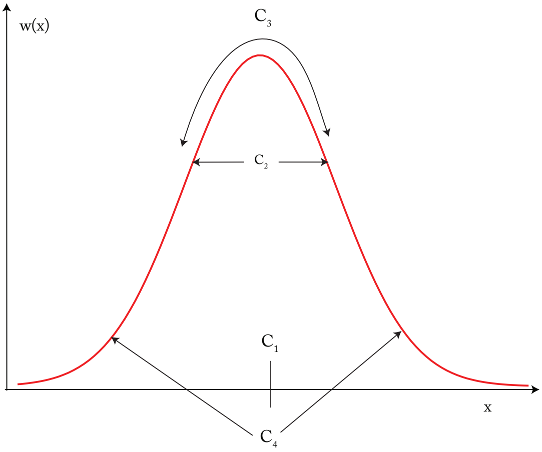

FIGURE 1.2: Probability density function showing the significance of the lowest order moments. C_1 is the mean, C_2 is the variance, C_3 is the skewness (asymmetry between left and right tails) and C_4 is the sharpness of the tails.

order of moments, not only the mean values to understand the underlying phenomena in random processes.

1.2 CORRELATION TECHNIQUES

In studies of random processes different correlation techniques are employed to look into any statistical regularity in the random processes. Coming back the noise, which is just the second order moment of the probability distribution function of the random process, it is usually measured in terms of the power in each frequency bin. The noise power can be calculated using the autocorrelation function. The autocorrelation function gives the correlation of a random signal $x(t)$ with the function itself but delayed by a time interval of τ. The autocorrelation function for a stationary stochastic random process is defined as:

$$\phi_x(\tau) = \lim_{T\to\infty} \frac{1}{T}\int_{-T/2}^{T/2} x(t)x(t+\tau)\,dt. \tag{1.4}$$

It measures the correlation of the random process *w.r.t.* time. The spectral density of noise can be calculated using the Fourier transformation of the autocorrelation

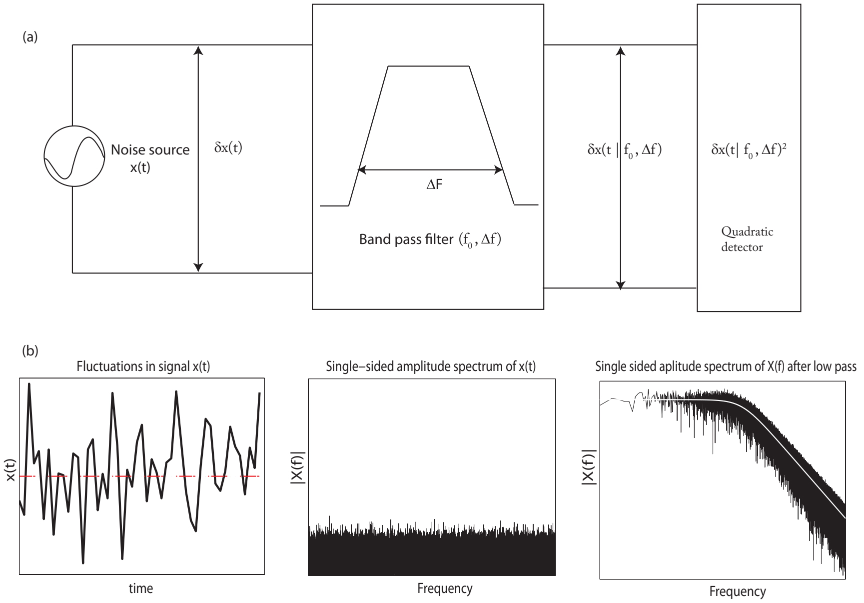

FIGURE 1.3: Fluctuations in the measurement and its bandwidth limited measurement using the quadratic detector: (a) A conceptual demonstration of the noise measurement (b) Noise and its spectral density. The roll off in the spectral density is due to effective low pass behavior of the measurement system.

function [Wiener - Khintchine formula] [3, 4].

$$S_x(\omega) = \int_{-\infty}^{\infty} \phi_x(\tau) e^{-j\omega\tau}\, dt. \tag{1.5}$$

For a bandwidth limited measurement, which is more realistic to the experimental world, the power spectral density is measured per unit frequency. A simple schematic representation of noise measurement is shown in figure (1.3). Here the fluctuation power spectral density is measured using a quadratic detector. Power spectral density is plotted on a logarithmic scale. The signal is measured around a central frequency f_0 with effective bandwidth of δf.

1.3 QUANTUM TRANSPORT: A SCATTERING APPROACH

QUANTUM transport refers to the transport of electrons within their phase coherence length. A typical quantum conductor is shown in figure (1.4). The constriction in the narrow neck regime is provides the quantum confinement *i.e.* the width of the neck should be smaller than the scattering length. Due to the quantum confinement in the narrow neck regime, electrons in that regime can be treated as particles in a box. Here, the electrons are confined along the x and y axis but they are free to move along the z axis. The Schrödinger equation for the electrons in the confining potential can be written as:

$$\frac{\hbar^2}{2m^*}\nabla^2\psi(x,y,z) + V(x,y,z)\psi = E\psi(x,y,z) \tag{1.6}$$

where $V(x,y,z)$ is the confining potential and $\psi(x,y,z)$ is an eigen state of electrons confined in the box. Solving the above equation for the case of particles in a long box,

$$E = E_x + E_y + \frac{\hbar^2 k_z}{2m^*}, \tag{1.7}$$

where $E_x = \frac{\hbar^2}{2m^*}\left(\frac{n_x\pi}{w_x}\right)^2$ and $E_y = \frac{\hbar^2}{2m^*}\left(\frac{n_y\pi}{w_y}\right)^2$, and w_x and w_y are the width of the constriction in x and y directions, respectively. These eigen states are called transmission channels and the corresponding eigen vectors are called modes. A pictorial representation is shown in figure (1.4). Equation (1.7) states that for a given Fermi energy and constriction width, only certain transverse states are allowed. Such a phenomenon was first observed in a 2-dimensional electron gas by van Wees *et al.* and Wharam *et al.* [5, 6] in 1988, where they changed the constriction by means of a gate potential and observed a variation in the current in discrete steps. These discrete steps are integral multiples of the universal conductance quantity $2e^2/h$, that we will refer to as the quantum conductance G_0.

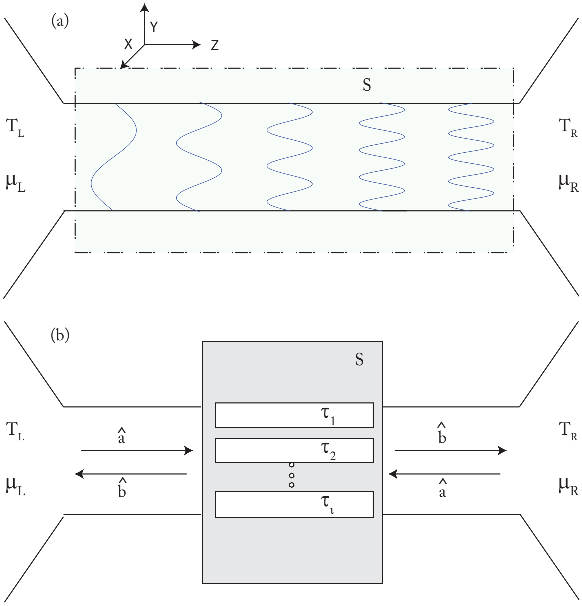

FIGURE 1.4: A schematic of a ballistic conductor attached to perfect leads: (a) The dotted-dashed line shows the quantum conductor. The electrons are emitted from the left and right leads into the quantum conductor, with an electron chemical energy μ_L and μ_R, respectively. (b) The grey shaded region shows the scattering region connected to bulk reservoirs through perfect leads having incoming and outgoing states.

The simple particle-in-a-box model helps to understand the quantized conductance of a narrow channel, but it fails to explain the fluctuations in the current. The simplest approach to a better understanding of quantum conductance is to use the scattering approach, also known as the Landauer-Büttiker formula. In this approach, a quantum conductor is modeled as a scattering regime connected to electron reservoirs through perfectly transmitting leads. There are four main assumptions in this formalism:

- The quantum conductor is modeled as a scattering regime connected to a reservoirs through perfectly transmitting leads.
- The reservoirs act as a perfect sources and sinks for the transmitted and reflected electrons irrespective of their initial energy states.
- The energy and phase of the electron states is preserved in the scasttering region and in the leads.

- * The quantum conductor can be either in equilibrium or in a non-equilibrium state. This is included in the formalism through the Fermi Dirac distribution function of the reservoirs connected to the leads.

Now let us implement this approach for a two-terminal quantum conductor. Electrons propagate through the leads as plane waves with longitudinal momentum $k_\parallel$ and quantized transverse momentum $k_\perp$. If there are N independent scattering states in the quantum conductor then there will be 2N states in the leads (each scattering state will be accompanied by a partially reflected and a transmitted state) as shown in figure (1.4). Let us introduce four operators which can create and annihilates the electrons in the states defined by the quantum conductor: $\hat{b}_{\alpha i}$ and $\hat{b}^\dagger_{\alpha i}$ are the annihilation and creation operators in i^{th} outgoing eigen state of the lead $\alpha (= L, R)$. They annihilate and create the electrons in states moving away from the scattering center. $\hat{a}_{\alpha i}$ and $\hat{a}^\dagger_{\alpha i}$ are annihilation and creation operators for the i^{th} incoming eigen states in lead $\alpha (= L, R)$. The incoming and outgoing states can be related to each other using a scattering matrix s.

$$\begin{pmatrix} \hat{b}_{L1} \\ \hat{b}_{L2} \\ \vdots \\ \hat{b}_{Ln} \\ \hat{b}_{R1} \\ \hat{b}_{R2} \\ \vdots \\ \hat{b}_{Rn} \end{pmatrix} = s \begin{pmatrix} \hat{a}_{L1} \\ \hat{a}_{L2} \\ \vdots \\ \hat{a}_{Ln} \\ \hat{a}_{R1} \\ \hat{a}_{R2} \\ \vdots \\ \hat{a}_{Rn} \end{pmatrix} \tag{1.8}$$

Here s is a scattering matrix of dimension $2N \times 2N^1$. The block structure of s matrix is given as:

$$s = \begin{pmatrix} r & t' \\ t & r' \end{pmatrix} \tag{1.9}$$

where $r_{N\times N}$ and $r'_{N\times N}$ are square sub matrices describing the reflected electron wave for the left and right leads respectively. The off-diagonal matrices $t_{N\times N}$ and $t'_{N\times N}$ describe the effective transfer of electrons through the scattering regime. Since the number of electrons is fixed, s is unitary. In absence of a magnetic field *i.e.* under time reversal symmetry, s is symmetric. The fact that s is unitary and

---

[1] Here the size of the scattering matrix depends on the number of modes in the left and the right leads. In general, the sizes of the left and right lead can differ, in which case the dimension would be $(M + N) \times (M + N)$

symmetric permits us to diagonalize the matrices into scattering matrices of independent channels. This allows us to determine the current in each eigen state or channel [2] and sum over all independent quantum channels to obtain the total current. The net current in a quantum channel is the difference between the incoming and the outgoing state occupation numbers of the electrons. The current in lead α and quantum channel n is given as:

$$\hat{I}_{\alpha n}(t) = \frac{2e}{2\pi\hbar}\int dEdE' e^{i(E-E')t/\hbar}\left(\hat{a}^{\dagger}_{\alpha n}(E)\hat{a}_{\alpha n}(E') - \hat{b}^{\dagger}_{\alpha n}(E)\hat{b}_{\alpha n}(E')\right). \tag{1.10}$$

Here α, β represent the L,R reservoirs connecting to the scattering regime. For simplicity we take the current in the left lead only, from here onwards. Using the scattering matrix relation 1.8 the current in lead $\alpha = L$ and for the single-channel case can be written in terms of $\hat{a_\alpha}$ and $\hat{a_\alpha}^{\dagger}$,

$$\hat{I}_L(t) = \frac{2e}{2\pi\hbar}\sum_{\alpha\beta}\int dEdE' e^{i(E-E')t/\hbar}(\hat{a}^{\dagger}_{\alpha}A_{\alpha\beta}(L;E,E')\hat{a}_{\beta}(E')) \tag{1.11}$$

and $A_{\alpha\beta}(L;E,E')$ represents the matrix defined from scattering matrix s *i.e.* $A_{\alpha\beta}(L;E,E') = \delta_{\alpha L}\delta_{\beta L} - s^{\dagger}_{L\alpha}(E)s_{L\beta}(E')$. The average current $\langle I_L(t)\rangle$ can be given as:

$$\langle\hat{I}_L(t)\rangle = \frac{2e}{2\pi\hbar}\int dEdE' e^{i(E-E')t/\hbar}\langle\hat{a}^{\dagger}_{\alpha}A_{\alpha\beta}(L;E,E')\hat{a}_{\beta}(E')\rangle \tag{1.12}$$

Using $\langle\hat{a}^{\dagger}_{\alpha}(E)\hat{a}_{\beta}(E')\rangle = \delta_{\alpha\beta}\delta(E-E')f_{\alpha}(E)$, where $f_\alpha(E)$ describes the Fermi Dirac distribution in reservoir α, and taking into account the unitary property of matrix s, the average current can be given as,

$$\langle\hat{I}(t)\rangle = \frac{2e}{2\pi\hbar}\int dE\left(f_L(E) - f_R(E)\right)t^*(E)t(E). \tag{1.13}$$

Neglecting the energy dependence of $t(E)$ on the scale of $k_B T$ and eV, one obtains the conductance for the single channel case as,

$$G = \frac{2e^2}{h}\tau, \tag{1.14}$$

with $\tau = t^*(E)t(E)$. Generalizing the Landauer-Büttiker formalism for multiple channels gives simply a superposition of all transmission eigen channels. Since $t^{\dagger}t$ has been diagonalized the conductance G can be given as,

$$G = \frac{2e^2}{h}\sum_{i=1}^{N}\tau_i. \tag{1.15}$$

---

[2] The concepts of eigen channel and eigen states are interchangeable

Hence the Landauer-Büttiker formalism states that the effective conductance is the linear addition of the transmission probabilities of all eigen channels. It is quite intuitive to state that the effective numbers of channels is limited by the narrowest region in the quantum conductor[3].

Equation (1.15), does not yet explain the fluctuations in the current. The fluctuations in the current due to the random flow of discrete electrons has two components: equilibrium noise *i.e.* thermal noise and non-equilibrium noise *i.e.* shot noise. Noise is characterized by its spectral density as stated in equation (1.4). The power spectral density is the Fourier transform of the current - current correlation function.

$$S(\omega) = 2\int_0^{\infty} dt e^{i\omega t}\langle \delta I(t+t_0)\delta I(t_0)\rangle \tag{1.16}$$

For the simplest case of a single-channel two-terminal device the noise spectrum can be written as

$$S(\omega) = \frac{1}{2}\int_0^{\infty} dt e^{i\omega t}\langle \delta\hat{I}_\alpha(t)\delta\hat{I}_\beta(0) + \delta\hat{I}_\beta(0)\delta\hat{I}_\alpha(t)\rangle, \tag{1.17}$$

where $\delta\hat{I}(t) = \hat{I} - \langle\hat{I}\rangle$. From equation(1.10) and (1.11) $\delta\hat{I}(t)$ can be written as:

$$\delta\hat{I}(t) = \frac{2e}{2\pi\hbar}\int dE dE' \sum_{\alpha\beta} A_{\alpha\beta}[\hat{a}^\dagger_\alpha(E)\hat{a}_\beta(E') - \langle\hat{a}^\dagger_\alpha(E)\hat{a}_\beta(E')\rangle]e^{i(E-E')t/\hbar} \tag{1.18}$$

Using the above equations, the noise power can be further simplified to

$$S_I(\omega) = \frac{2e^2}{2\pi\hbar}\sum_{\alpha\beta}\int dE A^2_{\alpha\beta}\left[f_\alpha(E)(1-f_\beta(E+\hbar\omega)) + f_\alpha(E+\hbar\omega)(1-f_\beta(E))\right] \tag{1.19}$$

In the zero frequency limit, $\omega \to 0$ the noise power density can be written as:

$$S_I = \frac{2e^2}{2\pi\hbar}\sum_{\alpha\beta}\int dE A^2_{\alpha\beta}\left[f_\alpha(E)(1-f_\beta(E) + f_\alpha(E)(1-f_\beta(E)\right] \tag{1.20}$$

For the case of a single quantum channel $A_{\alpha\beta}(L) = \delta_{\alpha L}\delta_{\beta L} - s^\dagger_{L\alpha}s_{L\beta}$, hence the noise power spectral density is:

$$S_I = \frac{2e^2}{h}\int dE\,\tau(E)\left[(f_\alpha(1-f_\alpha) + f_\beta(1-f_\beta)) + \tau(E)(1-\tau(E))(f_\alpha - f_\beta)^2\right]. \tag{1.21}$$

---

[3] In 2 DEG quantum point contacts the steps of quantum conductance are seen in the conductance due to the constriction that is controlled by the applied gate potential. Similar kinds of quantized steps are seen in atomic conductors, but here the conductance channels are attributed to the hybridized valence orbitals of atoms or molecules bridging the bulk leads. The interpretation is based on calculations, for example, using a tight a binding approach by Cuevas *et al.*[7], and was experimentally verified by Scheer *et al.*[8] and Brom *et al.*[9].

Since $\tau(E)$ changes insignificantly on the experimental energy scale we can neglect its energy dependence, so that we obtain

$$S_I = \frac{2e^2}{h}\left[eV\coth(\frac{eV}{2k_BT})\tau(1-\tau)+2k_BT\tau^2\right]. \tag{1.22}$$

The above equation (1.22) can be generalized to the multi-channel case, known as the Lesovik-Levitov expression,

$$S_I = \frac{2e^2}{h}\left[eV\coth(\frac{eV}{2k_BT})\sum_{n=1}^{N}\tau_n(1-\tau_n)+2k_BT\sum_{i=1}^{N}\tau_n^2\right]. \tag{1.23}$$

In the limit of $V \to 0$ the noise power spectral density reduces to

$$S_I(0) = 4k_BTG, \tag{1.24}$$

which is the equilibrium noise as the both leads are in equilibrium within the k_BT width of their Fermi Dirac distribution. This is also known as thermal noise or Johnson-Nyquist noise. The first term in equation(1.22) is voltage dependent and hence contributes to the non-equilibrium noise which is also known as shot noise. The cross over from the shot noise to thermal noise is quite smooth. For $eV \ll k_BT$, thermal noise dominates over shot noise and the non-linear dependence on V is gradually smoothed to a linear dependence of the noise on V at lower temperatures. This cross over phenomenon was first observed by H. Birk *et al.*[10]. Thermal noise does not give much information about the conductor apart from the impedance or electron temperature of the sample. Thermal noise is often used as a calibration measurement for the shot noise measurement. I will discuss this procedure in the section on Shot noise analysis in more detail below. For $T \to 0$ shot noise in the conductor is given as:

$$S_I(0) = \frac{e^3V}{\pi\hbar}\sum_{n=1}^{N}\tau_n(1-\tau_n). \tag{1.25}$$

Hence, shot noise is not determined just by the conductance, like thermal noise, but it is dependent on the effective transmission and reflection coefficients of the quantum channels. In the case of completely closed and open channels, the shot noise vanishes completely. The maximum shot noise level is seen for a half-open quantum channel. Taking $\tau_n \to 0$, for all n, the shot noise takes the Poisson value as stated by Schotkky in 1926.

$$S_I(0) = \frac{e^3V}{\pi\hbar}\sum_{n=1}^{N}\tau_n \tag{1.26}$$

This is known as full shot noise. Comparing equation (1.25) with (1.26) shot noise in a quantum conductor always deviates from the full shot noise as $S_I(0) = 2eIF$. The factor measuring the deviation is known as the Fano factor F, which can be written as,

$$F = \frac{\sum_{n=1}^{N} \tau_n (1-\tau_n)}{\sum_{n=1}^{N} \tau_n}, \tag{1.27}$$

with $0 \leq \tau_n \leq 1$. The Lesovik-Levitov expression, equation(1.23) is a function of the Fano factor F, temperature T and the bias voltage V. Expression (1.23) can be written as the difference between noise at non-equilibrium $S_I(0)$ and the thermal noise $S_{th}(0)$,

$$S_I(0) - S_{th}(0) = \frac{2e^2}{h}\left[2k_BT\sum_{n=1}^{N}\tau_n^2 + eV\coth\left(\frac{eV}{k_BT}\right)\sum_{n=1}^{N}\tau_n(1-\tau_n)\right] - 4k_BT\frac{2e^2}{h}\sum_{n=1}^{N}\tau_n. \tag{1.28}$$

Let us define the excess noise as $S_{ex} = S_I(0) - S_{th}(0)$, then the expression for the normalized excess noise can be simplified to,

$$\frac{S_{ex}}{S_{th}(0)} = F\left[\frac{eV}{2k_BT}\coth\left(\frac{eV}{2k_BT}\right) - 1\right] \tag{1.29}$$

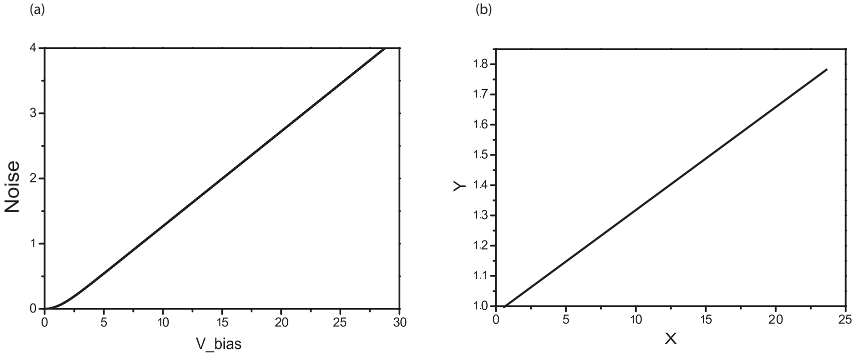

FIGURE 1.5: Shot noise *w.r.t.* bias voltage: (a) Noise is a non linear function of V_{bias} for $eV \leq k_BT$ and approaches a linear function for $eV > k_BT$ (b)The normalized excess noise, *i.e.* $\frac{S_{exc}}{S_{th}(0)}$ plot *w.r.t.* the reduced bias $X = \frac{eV}{2k_BT}\coth\left(\frac{eV}{2k_BT}\right)$ is a simple linear function for which the slope gives the Fano factor.

Hence, expression (1.29) shows that slope of the normalized excess noise *w.r.t.* reduced bias $X = \frac{eV}{2k_BT}\coth\left(\frac{eV}{2k_BT}\right)$ gives the Fano factor, as can be seen from figure (1.5).

A note on shot noise

From the Lesovik-Levitov expression (1.23), it follows that for $\tau_n = 1$ or $\tau_n = 0$, for all channels n noise is absent in the quantum conductor. But for a channel with $0 < \tau_n < 1$, the electron wave packet splits into a reflected and a transmitted wave packet and this occurs randomly. The electron is detected as transmitted or reflected and this occurs randomly. This randomness gives the shot noise in the quantum conductor. Hence shot noise is due to both the wave and the particle nature of the electron. This is shown in figure (1.6) as an example. The different kinds of interaction of the traversing electron in the conductor leads to deviations of noise from the Lesovik-Levitov value. These deviations can be lumped into the factor called the Fano factor. Hence, the study of the Fano factor gives information about the kinetics of the electron transport in the quantum conductor. In mesoscopic physics, shot noise is currently extensively used to determine the different kinds of underlying kinetics of the electron during its transport.

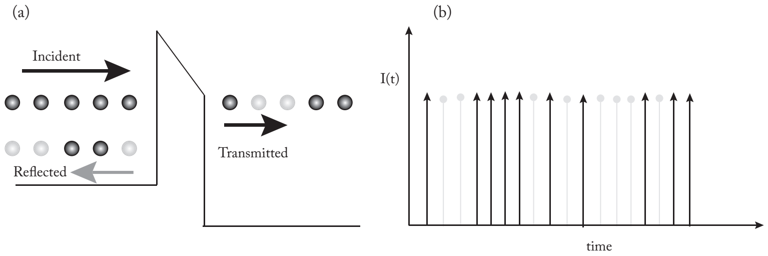

FIGURE 1.6: Shot noise in a tunnel junction due to random motion of the electron: Electrons approach the contact at regular intervals but get reflected randomly and hence the pulses of transmitted electrons are random, giving noise in measurement. Each transmitted electron pulse gives a tick in the current meter. These series of ticks over the large measurement time ensemble gives a measure of the average noise.

I give a short overview of experimental studies of shot noise on different systems: The first observations of suppression of shot noise by high-transmission conductance channels in point contacts were made in two dimensional electron gas systems by Renikov *et al.* [11] and Kumar *et al.* [12]. They measured the noise for a point contact. The shot noise evolves from the full shot noise with $F \sim 1$ at the nearly pinched-off regime to $F \sim 0$ on the first plateau of the quantum conductance, as expected from the theory. In another series of experiments, by de-

Picciotto *et al.* [13] and Saminadayar *et al.* [14], the fractional charge in the fractional quantum hall regime was measured. This experiment was a direct manifestation of Laughlin's concept of the quasiparticles having fractional charge and taking part in the charge transport in the fractional quantum Hall regime.

In a completely different system, a superconductor-normal metal diffusive contact, the shot noise measurement revealed the 2e charge of elementary processes taking part in the conduction [15]. This shot noise measurement revealed the effective charge of the quasiparticles taking part in the conduction. In similar 2DEG point contacts as mentioned above, non-integer conductance steps are seen at 0.7G_0, widely known as the 0.7 anomaly. This 0.7 anomaly has been reported to be related to the intrinsic electron spin. This spin interaction effect was first revealed in shot noise measurements by Roche *et al.* [16]. The shot noise measurement shows the spin polarized channel taking part in the conductance. Parallel to above developments, shot noise measurements in atomic contacts have been used to identify the number of eigen channels participating in the conductance. First such measurement were reported by van den Brom *et al.* [9] on Au and Al atomic contacts, revealing 1 and 3 channels taking part in the conduction, respectively. In a similar system, Dj/"ukic *et al.* [17] have shown the presence of a single dominant channel in the single-molecule junction Pt-D_2-Pt. Shot noise measurements were used as a tool by Tal *et al.* [18] to show the cross over between point contact spectroscopy and inelastic tunneling spectroscopy at $\tau = 0.5$. In this thesis we report on the use of noise to show the effect of electron-electron and electron-vibron interaction in quantum electron transport in atomic and molecular junctions.

1.4 RANDOM TELEGRAPH NOISE

RANDOM telegragh noise is associated to Markovian processes where a random process x(t) is a continuous time function randomly jumping between two well defined states. A process is called Markovian if the probability of the transition between the states depends upon the present state and does not depend upon its previous history. Hence Markovian processes are memoryless.

Such processes are common in systems like atomic contacts, molecular junctions, single electron transistors, tunnel junctions *etc.*, where the resistance of the system fluctuates between a higher resistance R_u and a lower resistance R_l due to the movement of atoms between two metastable states or due to charge fluctuations in a double-well potential. A schematic of such process is shown in figure (1.7). The probability of making a single transition from state R_i to state R_j in a small interval time δt is inversely proportional to the mean life time τ_i of state R_i. Hence the decay rate for occupational probability of states R_l and R_u can be defined as $\delta t/\tau_l$ and $\delta t/\tau_u$. The probability to find the system in state R_i can be

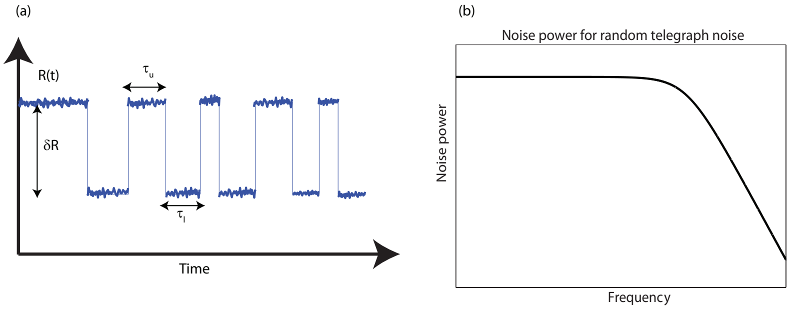

FIGURE 1.7: Illustration of two-level fluctuations. (a) A quantum system is jumping between two metastable states with finite mean life time and the electrons participating in the quantum transport sense the two states. Hence the effective transmission probability of the electron fluctuates between two values. Here, such phenomenon is translated in a change in the resistance of the system δR with finite life time τ_u for the higher resistive state and τ_l for the lower resistive state. (b) The power spectral density of the corresponding two level fluctuations with a Lorentzian line shape with cut-off frequency given by the mean life time *i.e.* $f_0 = \frac{1}{\tau_u+\tau_l}$ of the two states.

given as,

$$P_i = \frac{\tau_i}{\sum\limits_{i=u,l} \tau_i}. \tag{1.30}$$

Since a random telegraph signal is memoryless, the switching between two states with known average rates can be described by a Poisson distribution and its characteristic function. The autocorrelation function for this Poisson process is given as:

$$\begin{aligned}\phi(\tau) &= P_1 P_2 (R_l - R_u)^2 e^{-(\nu_1+\nu_2)\tau} \\ &= P_1 P_2 (\delta R)^2 e^{-\nu\tau}\end{aligned} \tag{1.31}$$

where $\nu = (\nu_1 + \nu_2)$ and $\nu_i = 1/\tau_i$. The Fourier transform of $\phi(\tau)$, using the Wiener-Khintchine theorem, gives its power spectral density.

$$S_R(\omega) = 4\delta R^2 P_1 P_2 \left[\frac{\tau}{1+\omega^2\tau^2}\right] \tag{1.32}$$

The power spectrum of a random telegraph signal (RTS) is Lorentzian in shape with a cutoff frequency given by the mean life time of the two states, and one such spectrum is shown in figure (1.7).

1.5 1/*f* NOISE

$\frac{1}{f}$ NOISE or flicker noise as it was termed by Schottky, often hampers low frequency noise measurements. It has universal presence in all kinds of conductors and semiconductors. Its power spectral density increases with the decrease of frequency as suggested by its onomatopoetic name $1/f$. There is a famous paradox related to $1/f$ noise, "If $1/f$ noise behavior holds down to zero frequency then its noise power would be infinite"[19]. Until today no experimental evidence has shown this behavior. All the experiments have finite frequency bandwidths. The lower bound of frequency(f_l) is limited by the measurement time(t) *i.e.* $f_l \propto \frac{1}{t}$ and hence to observe such an infinite power, one needs to measure for infinite duration of time. However, until now none of the experiments has shown any plateau appearing for f approaching zero. At higher frequency, the power spectral density of $1/f$ noise diminishes until it reaches the noise floor of amplifier and hence it becomes immeasurable at higher frequency. The corner frequency of $1/f$ noise is defined as the frequency point at which its noise spectral density sinks into the noise floor of the amplifier. Depending upon the nature of the system, its corner frequency ranges from 10^2 to 10^6Hz. Figure (1.8b) shows the typical $1/f$ noise in an atomic or molecular junction.

Although its presence is universal in all kinds of conductors, there is no central cause for its origin. Its origin is often more complex and widely unknown in condensed matter physics. The most accepted view for its origin in metals is that

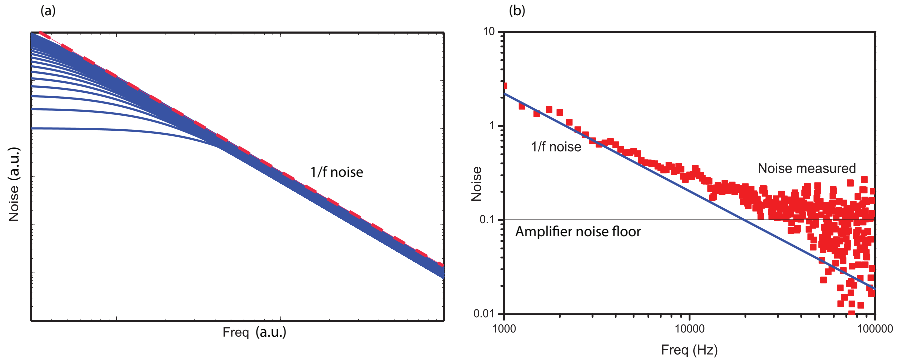

FIGURE 1.8: (a) Conceptual model for the origin of $1/f$ noise as a superposition of different two-level fluctuations with different effective mean life times, adding up to $1/f$ noise behavior. The envelope of the cumulative Lorentzian shapes is shown as the dashed, resembling $1/f$ behavior. (b) Power spectral density of $\frac{1}{f}$ noise in a Au – O_2 – Au junction. The typical corner frequency for such systems is around 30KHz.

it can be interpreted as a superposition of many two-level fluctuations with different amplitudes δR_i and a range of decay rates ν_i. Its power spectrum can be calculated as the sum over all individual RTS. If the time constant of the ensemble is within the limit $\tau \in \{\tau_1, \tau_2\}$ and the probability distribution of the system to stay in state R_i at time t is given as P_i with its power spectral density$S_{RTS}(\omega, \tau_i)$ given by equation(1.32), then total power spectrum would be given by,

$$S(\omega) = \int_{\tau_1}^{\tau_2} S_{RTS}(\omega, \tau_i) P_i d\tau_i \propto \frac{1}{f} \tag{1.33}$$

for the frequency range $\frac{1}{\tau_2} < f < \frac{1}{\tau_1}$. A conceptual demonstration is shown in figure (1.8a), where different Lorentzians with different time constants are integrated to obtain a $1/f$-like spectral density behavior.

Detailed studies on the properties of $1/f$ noise have been done on metallic and semiconductor systems by Hooge [20]. He has proposed a phenomenological expression for metallic systems,

$$S_v(f) = \gamma \frac{V^{2+\beta}}{N_c f^{\alpha}} \tag{1.34}$$

This formula is known as Hooge's formula. Here α, β and γ are constants. N_c is the number of charge carriers in the sample. The typical values for metallic systems are: $0.9 \leq \alpha \leq 1.4$, $\gamma \simeq 2 \times 10^{-3}$, $\beta \simeq 0$.

REFERENCES

[1] L.S.Levitov and G.B.Lesovik, *Charge distribuition in quantum shot noise*, Pis'ma Zh. Eksp. Teor. Fiz. **58**, 225 (1993).

[2] S. H. Kogan, *Electronic noise and fluctuations in solids* (Cambridge University press, 1996).

[3] N. Wiener, *Generalized harmonic analysis*, Acta Mathematica **55**, 117 (1930).

[4] A. Khintchine, *Korrelationstheorie der statistischen Prozese*, Math. Annalen **109**, 604 (1934).

[5] B. J. van Wees, L. P. Kouwenhoven, H. van Houten, C. W. J. Beenakker, J. E. Mooij, C. T. Foxon, and J. J. Harris, *Quantized conductance of magnetoelectric subbands in ballistic point contacts*, Physical Review Letters **38**, 3625 (1988).

[6] D. A. Wharam, T. J. Thornton, R. Newbury, M. Pepper, H. Ahmed, J. E. F. Frost, D. G. Hasko, D. C. Peacock, D. A. Ritchie, and G. A. C. Jones, *One-dimensional transport and the quantisation of the ballistic resistance*, Journal of Physics C: Solid State Physics **21**, L209 (1988).

[7] J C Cuevas and A Levy Yeyati and A Martä and G Rubio Bollinger and C Untiedt and N Agrät , *Evolution of Conducting Channels in Metallic Atomic Contacts under Elastic Deformation*, Physical Review Letters **81**, 2990 (1998).

[8] Elke Scheer and N Agräit and J C Cuevas and A Levy Yeyati and B Ludoph and Martin-Rodero Alvaro and G R Bollinger and J van Ruitenbeek and U Cristian, *The signature of chemical valence in the electrical conduction through a single-atom contact*, Nature **394**, 154 (1998).

[9] H. van den Brom and J. van Ruitenbeek, *Quantum Suppression of Shot Noise in Atom-Size Metallic Contacts*, Physical Review Letters **82**, 1526 (1999).

[10] H. Birk, M. J. de Jong, and C. Schonenberger, *Shot-Noise Suppression in the Single-Electron Tunneling Regime*, Phys. Rev. Lett. **75**, 1610 (1995).

[11] M. Reznikov, M. Heiblum, H. Shtrikman, and D. Mahalu, *Temporal Correlation of Electrons: Suppression of Shot Noise in a Ballistic Quantum Point Contact*, Phys. Rev. Lett. **75**, 3340 (1995).

[12] A. Kumar, L. Saminadayar, D. C. Glattli, Y. Jin, and B. Etienne, *Experimental Test of the Quantum Shot Noise Reduction Theory*, Phys. Rev. Lett. **76**, 2778 (1996).

[13] R. de Picciotto, M. Reznikov, M. Heiblum, V. Umansky, G. Bunin, and D. Mahalu, *Direct observation of a fractional charge*, Nature **389**, 162 (1997).

[14] L. Saminadayar, D. C. Glattli, Y. Jin, and B. Etienne, *Observation of the $e/3$ Fractionally Charged Laughlin Quasiparticle*, Phys. Rev. Lett. **79**, 2526 (1997).

[15] X. Jehl, M. Sanquer, R. Calemczuk, and D. Mailly, *Detection of doubled shot noise in short normal-metal/ superconductor junctions*, Nature **405**, 50 (2000).

[16] P. Roche, J. Ségala, D. C. Glattli, J. T. Nicholls, M. Pepper, A. C. Graham, K. J. Thomas, M. Y. Simmons, and D. A. Ritchie, *Fano Factor Reduction on the 0.7 Conductance Structure of a Ballistic One-Dimensional Wire*, Phys. Rev. Lett. **93**, 116602 (2004).

[17] D. Djukic and J. M. van Ruitenbeek, *Shot noise measurements on a single molecule*, Nano Letters **6**, 789 (2006).

[18] O. Tal, M. Krieger, B. Leerink, and J. M. van Ruitenbeek, *Electron-Vibration Interaction in Single-Molecule Junctions: From Contact to Tunneling Regimes*, Phys. Rev. Lett. **100**, 196804 (2008).

[19] P. Dutta and P. M. Horn, *Low-frequency fluctuations in solids: $\frac{1}{f}$ noise*, Rev. Mod. Phys. **53**, 497 (1981).

[20] F. Hooge, *$1/f$ noise is no surface effect*, Physics Letters A **29**, 139 (1969).

2

MEASUREMENT TECHNIQUE : NOISE

In mesoscopic physics, the conductance measurement has clearly dominated the past two decades of its experimental and theoretical arena. The conductance measures the effective average transmission of electron near the Fermi surface. This measurement only focuses on the averaged properties of the system and clearly misses its phase and temporal behavior. The fluctuation in current is a fundamental quantity which in past few years attracted the attention of experimentalists and theoreticians. The fluctuations in current measures the charge statistics. The second order moment of the statistics is known as shot noise which measures the deviation from the mean number of the electron transmitted through the device under study. Measurement of this deviation gives detailed information about the nature of the charge of the particle and the characteristic of mesoscopic device. Measurement of shot noise is technically challenging. The design of the measurement setup is always a compromise between the different scientific requirements like low temperature, low noise, external noise filtering, broadband frequency domain measurements etc. Here I present briefly the different noise measurement techniques.

2.1 LOW FREQUENCY MEASUREMENT TECHNIQUE

A low frequency measurement set up is used to determine the electron counting statistics. It generally consists of sets of amplifiers and filters and either an analogue integrator or spectrum analyzer for measuring power spectrum. Analogue integrators were common in the past to measure the noise power, but with the advancement of the technology, they were replaced by FFT spectrum analyzers. They are fast and have better sensitivity. The biasing circuit is preferably battery operated to avoid spurious and 50Hz and its harmonics originating from power lines. The preamplifier amplifies the noise signal of the device above the noise floor of the spectrum analyzer but adds a technical constraint. The preamplifier generates voltage noise and current noise which add quadratically to the noise signal of the device. Hence, the noise measurement system should be calibrated with respect to the background noise and it should be subtracted from the measured noise power spectrum of the device. A typical low frequency noise setup is shown in the figure(2.1)[1]. Usually current noise is of more interest because of its closer physical institution to the current fluctuations. The current noise in the mesoscopic systems we will be considering is as of the order of a few pA$\sqrt{\mathrm{Hz}}$ to fA/$\sqrt{\mathrm{Hz}}$. Current noise is deduced from the voltage noise as

$\langle \Delta I_D^2 \rangle = \frac{\langle \Delta V_D^2 \rangle}{R_D^2}$, where R_D^2 is the resistance of the device.

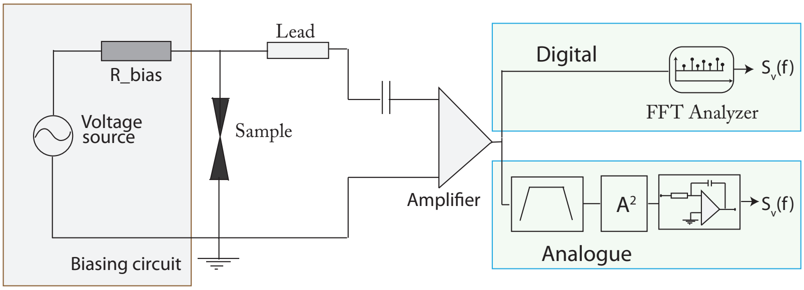

FIGURE 2.1: A typical low frequency noise measurement set up: Analogue and Digital.

2.1.1 SINGLE CHANNEL NOISE MEASUREMENT TECHNIQUE

A single channel noise measurement set up consists of a preamplifier coupled to the sample and a next stage amplifier which post amplifies the signal above the noise floor of the spectrum analyzer and background noise of the coupling environment. Such measurement setup is shown in figure (2.2 a). The main constraint of this design is the input noise of the preamplifier. This should ideally be at least an order of magnitude smaller than the noise signal of the sample. This is also the reason why for low impedance samples, voltage noise measurement is preferred over the current noise measurement as the thermal noise of the feedback resistor of transimpedance of current amplifiers limits the sensitivity of current noise measurements. The input noise of the second amplifier must be smaller than the effective noise seen at the input of the second amplifier due to the input noise of the preamplifier considering second amplifier completely noiseless. In this case noise due to second amplifier can be ignored and effective noise seen at the spectrum analyzer could be given by:

$$\langle V^2\rangle = \langle \Delta V_D{}^2\rangle + \langle R_D + R_L\rangle^2 \langle \Delta I_A{}^2\rangle + \langle \Delta V_A{}^2\rangle \tag{2.1}$$

Here $\langle \Delta V_D{}^2\rangle$ is the voltage noise of the sample, $\langle \Delta I_A{}^2\rangle, \langle \Delta V_A{}^2\rangle$ are the current noise and voltage noise at the input of the preamplifier and R_D, R_L are sample resistance and lead resistance. Since R_L is very small in comparison toR_D, one can neglect the thermal noise of the leads. To determine $\langle \Delta V_D{}^2\rangle$ accurately, $\langle \Delta I_A{}^2\rangle, \langle \Delta V_A{}^2\rangle$ should be measured separately and subtracted from total noise$\langle V^2\rangle$ measured by the spectrum analyzer. Hence the sensitivity of the single channel noise measurement technique is limited by the input noise of the preamplifier. It suffers from $1/f$ noise which dominates at the lowest frequency. The effective noise resistance of the preamplifier is given as $R_{eq} = R_{eq_0}\left(1 + f_c/f\right)$ where f_c is the corner frequency of the $1/f$ noise. This limits the single channel noise measurement for the low frequency noise measurement. Especially, for the measurements below 100Hz, this technique is of no avail.

2.1.2 TWO CHANNEL CROSS CORRELATION TECHNIQUE

Generally, voltage noise of samples is in order of a few nV/$\sqrt{\text{Hz}}$ and designing a preamplifier with input voltage noise of nV/$\sqrt{\text{Hz}}$ is a technical feat. Moreover the $1/f$ noise makes the matter more difficult. One way to circumvent this issue is to employ a two channels cross correlation technique. A typical example for such setup is shown in figure (2.2b)[2]. Each channel measures the device noise and the input noise of the preamplifier (neglecting other sources of noise) *i.e.* $\langle V_{oi}{}^2\rangle = \langle \Delta V_D{}^2\rangle + \langle R_D + R_L\rangle^2 \langle \Delta I_i{}^2\rangle + \langle \Delta V_i{}^2\rangle(1 + f_c/f); i = A1, A2$. The uncorrelated noise of the amplifier of each channel averages out due to phase randomization while the correlated noise from the sample in both channels has same phase hence dominates over the non-correlated signal. Neglecting theR_L, the cross-spectral density is given by the cross conjugate product of the voltage noise measured by two channels. Here $*$ is cross conjugate product.

$$\langle V_{oA1} * V_{oA2}\rangle = \langle \Delta V_D{}^2\rangle + \langle R_D\rangle^2(\langle \Delta I_{A1}{}^2\rangle + \langle \Delta I_{A2}{}^2\rangle) \tag{2.2}$$

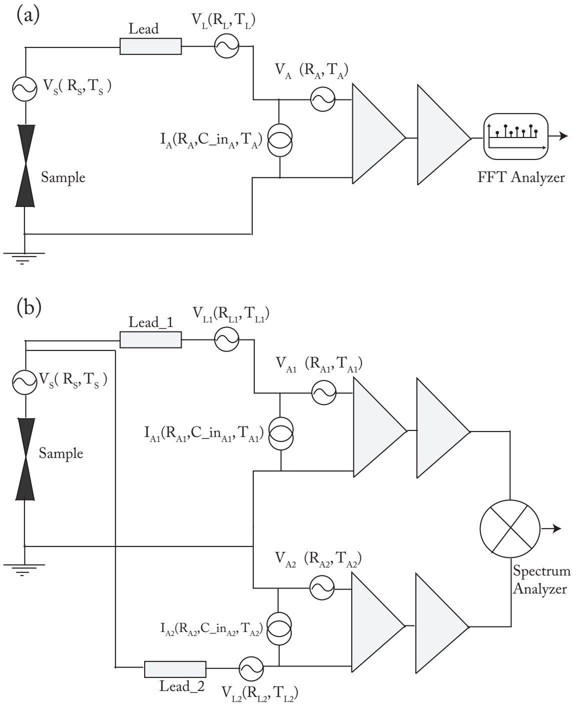

FIGURE 2.2: Low frequency noise setup. a) A Single channel noise measurement setup with a set of preamplifier and amplifier. b) A two channel noise measurement setup showing cross correaltion technique to measure the noise of the device below the noise floor of the preamplifier.

Over long measurement times, the uncorrelated noise reduces well below the other noise sources. The remaining noise is mainly due to amplifier's noise. The effective efficiency of cross correlation measurements is measured by a parameter called coherence. The coherence $R(f)$ is measure of the correlation between the two channels.It can be defined as :

$$|R(f)|^2 = \frac{S_{v12}^2(f)}{S_{v1}(f) * S_{v2}(f)}; \tag{2.3}$$

Where $S_{v1}(f)$, $S_{v2}(f)$ are the noise measured by channel 1 and 2 and $S_{v12}(f)$ is cross spectrum noise. The coherence value of the cross spectrum noise measurement lies between 1 and 0. Lower value indicates the less correlation between the two channel signal and value of 1 indicates the 100% correlated signal measured by both channel. Longer the integration time, higher the coherence in the measurement. Considering the $|R(f)| \sim 1$ being the ideal case for the cross spectrum analysis, N the number of averages, should satisfy the following condition[3]:

$$N \geq |\frac{1}{R(f)|^2} \tag{2.4}$$

The longer the averaging of data points, the lower will be the residual noise. The standard deviation of the residual noise can be defined as $\sigma_{V_{rcor}} = \langle {V_{rcor}}^2 \rangle / \sqrt{2N}$ where $\langle {V_{rcor}}^2 \rangle$ is residual correlated noise in cross spectrum measurement[4]. The sensitivity obtained by this method on $140k\Omega$ sample by Glattli *et al.*[5] is $S_v = 7.7 \times 10^{-20} \mathrm{V}^2/\mathrm{Hz}$ after 100s of averaging at 1kHz.

Limitation due to residual correlations between two channels :

The limitation to the cross spectrum analysis technique as seen by equation (2.2) is set by the residual correlation due to current noise of the preamplifier. Due to the ac coupling of the preamplifiers, its input voltage noise with the coupled becomes sample noise though the input capacitance *i.e.* C_{in} and stray capacitance *i.e.* C_{stray} of the coax connecting the sample to the preamplifiers. Considering both preamplifiers having the same noise behavior then residual correlation voltage noise could be written as[6][1]:

$$\langle {V_{rcor}}^2 \rangle = 2\langle {\Delta i_n}^2 \rangle {R_D}^2 + 2\langle {V_D}^2 \rangle \omega^2 {R_D}^2 \left(C_D + C_{stray} + C_{in}\right) C_{in} \tag{2.5}$$

If the current noise is small, the first term in equation (2.5) can be neglected, while the second term increases with frequency and becomes dominant with higher device impedance. This limits the use of this technique for high impedance at higher frequency. Generally, for higher impedances a current noise measurement scheme is employed where residual correlations are seen at the lower frequency end in contrast to the voltage noise measurement scheme. As per a rule of thumb for sample impedance ≥ 100kΩ a current noise measurement scheme is preferred and for sample impedance < 100kΩ a voltage noise measurement scheme with two channel cross correlation analysis is preferred. The exact cross over between the two measurement schemes is parameter dependent[2].

---

[1] Detail study has been done by Sampietro *et al.*[6].

[2] For our case, R_D, the sample impedance is in the $10k\Omega$ regime, hence we keep focus mainly on the voltage noise measurement technique in rest of the thesis.

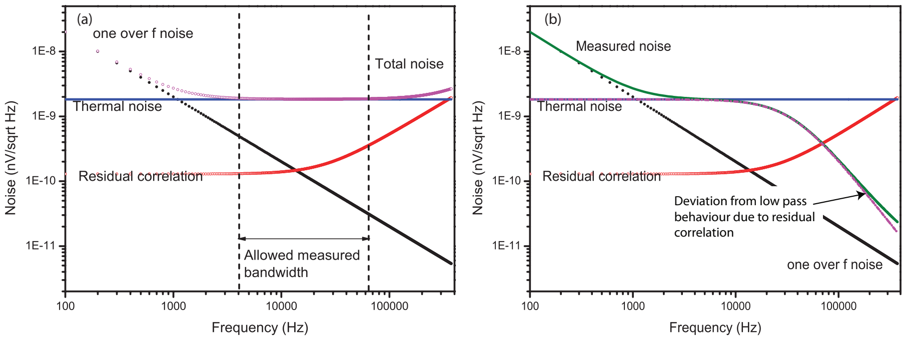

FIGURE 2.3: Residual correlation effect due to the current noise and voltage noise of the preamplifier: Using equation (2.5), residual correlated noise is calculated. Here $\langle \Delta i_n \rangle = 10\text{fA}/\sqrt{\text{Hz}}$, $\langle V_D \rangle = 2\text{nV}/\sqrt{\text{Hz}}$, $C_{in} = 50\text{pF}$, $C_{stray} = 300\text{pF}$, $R_D = 12.9\text{k}\Omega$ and $T = 4.7\text{K}$. a) Reduction in the bandwidth of noise spectrum due to residual correlation. (b)Residual correlation effect for the more realistic situation of a cryogenic set up, where the sample is situated far from preamplifier giving rise to the low pass behavior due to the stray capacitance of coaxes. A clear deviation from the low pass behavior is seen at 100kHz.

2.2 HIGH FREQUENCY MEASUREMENT TECHNIQUE

HIGH frequency measurement in MHz regime is useful for systems where $1/f$ noise limits the sensitivity of the low frequency noise measurement technique. In 2 dimensional electron gas systems and single-molecule systems, the corner frequency of the $1/f$ noise runs to a few hundred of kHz. The noise of the mesoscopic device is studied at sub cryogenic temperatures to avoid electron dephasing the high temperature phononic bath. The coaxes running from Kelvin sample bath temperature chamber to the room temperature low noise preamplifier have generally a capacitance of 100pF/m which gives an effective bandwidth of a few 10kHz. This can be easily seen from the figure (2.3b). The high sample impedance (12.9kΩ) combined with the cable capacitance (350pF) gives the low pass behavior with a cut off frequency of 35kHz which can be far below the $1/f$ noise corner frequency of a system like single molecule junction under high bias condition. To circumvent this technical issue, the stray capacitance needs to be reduced because the impedance of the sample is imposed by the experiment. This can be achieved by moving the low noise preamplifier very close to the sample. This puts a design constraint on the amplifier, which should be suited for the cryogenic environment. The Si based FET device have best noise performance but it suffers from the carrier freeze out at 77K. GaAs based FET suffers less from the carrier freeze out but their mobility decreases exponentially at the cryogenic temperature. Higher doping of the GaAs will not increase the mobility performance as the excess dopant atoms will act as sources of scattering and charge traps leading to high $1/f$ noise. One option is to mount them on the heat regulated finger but this will increase the heat load on the He bath. Alternative to this problem is to use the high electron mobility transistor (HEMT). These are hetrojunction (GaAs-InAs) transistor. HEMT is suited best for the cryogenic amplifier due to its best noise and

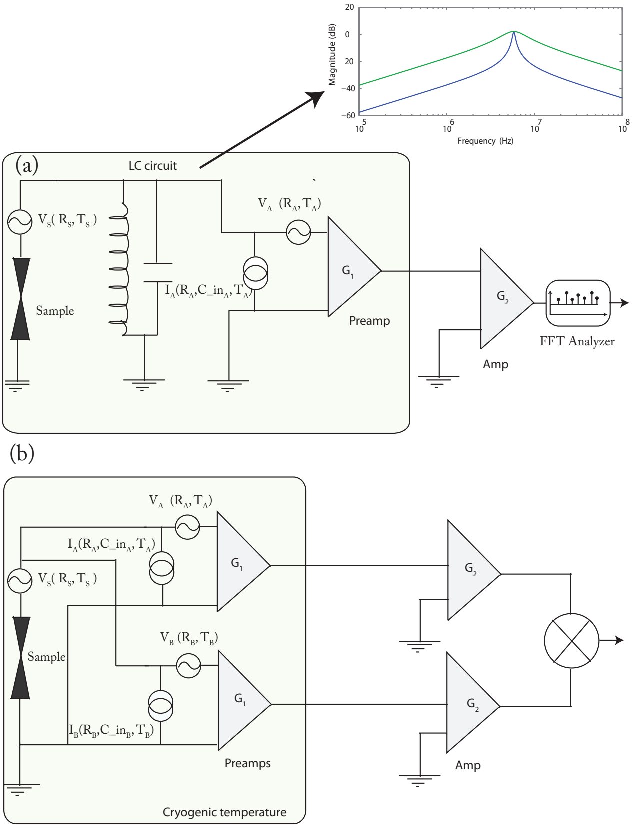

FIGURE 2.4: High frequency noise setup: a) A Single channel noise measurement setup with a chain of a low temperature preamplifier and a post-amplifier. A tank circuit is added to increase the central frequency of measurement band. Inset shows the typical measurement band of such system. Here parameter used for simulating this transfer functions are $R = 12.9\text{k}\Omega$, $C = 222\text{pF}$ and $L = 132.8\mu\text{H}$. This parameter gives sharp resonance peak at $f_0 = 5.8\text{MHz}$(Blue line). On reducing the C and L one could worsen the Q of tank circuit enabling the broadband measurement using tank circuit. The green line is obtained for $C = 22.2\text{pF}$, $L = 1328\mu\text{H}$ and $R = 12.9\text{k}\Omega$. b) A two channel noise measurement setup showing the cross correlation technique to measure the noise of the device below the noise floor of the preamplifier.

mobility performance[7]. The cryogenic amplifier are susceptible to the temperature drift and hence all the passive and specially active components needed to be thermalized properly. The proper thermalization ensures the stable operating point of the transistors. The HEMT amplifier are also preferred over Ge based FET due to its lower heat load. In order to reduce the heat load on the He bath, Adrian T. Lee *et al*[8] proposed the two stage amplifier. The cryogenic stage acts is cascode stage which acts as the impedance transformer while main gain comes from the room temperature part. The main advantage of the cascode stage is to reduces the Miller capacitance and hence it increases operational bandwidth. The main disadvantage of the two stage amplifier is high output impedance of the cryogenic amplifier. This give rise to reflection of the signal at the high frequency and hence giving rise to high frequency oscillation due to interference of reflected signals. Another alternative of the above design is to use the common-source gain stage with follower stage. This gives the better impedance matching at the cost of the bulkier design at the cryogenic end and higher heat load to He bath.

The design of rest of the high frequency noise set up is in analogous to the low frequency set up, apart from adding a cryogenic amplifier at the sample stage. Depending upon the sensitivity required by a single channel measurement or a two channels cross correlation method can be employed. A typical noise measurement setup is shown in figure (2.4) Achieving a broad spectrum, above few MHz can be achieved by just coupling the cryogenic amplifier very close to the sample. Even a few cm of wires coupling the sample to the preamplifier have a capacitance of a few pF. This limits the bandwidth of the noise measurement for high impedance samples to a low pass corner frequency of a few MHz. Adding a tank circuit (LCR) at the input of the amplifier increases the measurement frequency band to several of MHz. This technique can be employed with both two channel and single channel noise measurements. Noise is measured within the 3dB bandwidth around resonance peak. The sensitivity obtained by this technique is $1.1 \times 10^{-24}\mathrm{A}^2/\mathrm{Hz}$ [9] . It could be further improved to $6.7 \times 10^{-27}\mathrm{A}^2/\mathrm{Hz}$ by using the lockin technique[10].

2.3 VERY HIGH FREQUENCY NOISE MEASUREMENTS

VERY high frequency noise measurements are relevant for understanding the electron - phonon statistics in a quantum conductor. Detecting fluctuations of the order of a single electron detection is challenging. Even the cold amplifier having equivalent noise temperature of 40K with 50Ω input impedance will gives the amplifier input noise of $k_B T/50 \sim 10^{-23}\mathrm{A}^2/\mathrm{Hz}$. This brings the system design to the quantum limit. One of such design is shown in figure (2.5 a) which is based on M. Reznikov *et al.*[10]. In the frequency regime of GHz, all electronics component sizes are of the order of the wavelength of electromagnetic field.

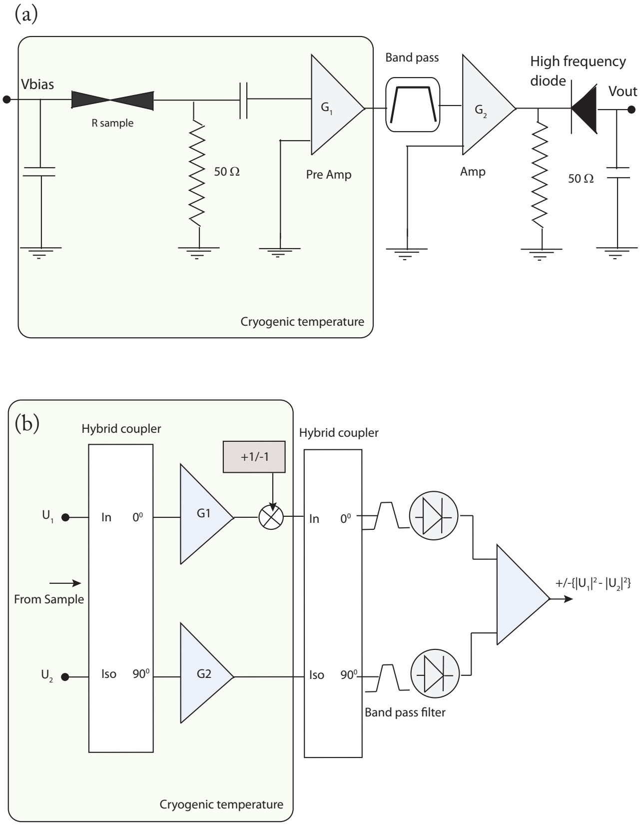

FIGURE 2.5: Very high frequency noise setup: a) A Single channel very high frequency noise measurement setup with a cryogenic low noise preamplifier and post-amplifier followed by a high frequency diode and capacitor load. b) A principle scheme showing the modulated double balanced amplifier set up.

Hence, all electronic circuit could be modeled as wave guides. A slight mismatch in the impedance leads to the reflection which further leads to instability of the electronics due to interference of reflected signals. In order to minimize such mismatch, all lines are 50Ω terminated. The high impedance sample is coupled to the 50Ω terminated input of a high frequency low noise cryogenic amplifier using a quarter wave impedance transformer. The very high frequency amplifier has a higher input noise temperature than the sample noise temperature which leads to measurements with very long integration times. Like in low and high frequency measurement techniques, the sensitivity of the noise measurement can be improved by using a lock in technique or cross-correlation technique. M. Reznikov *et.al.*[10] successfully used the lockin technique for noise measurement on quantum point contacts (QPC). The bias circuit is modulated with a low frequency signal and the amplified noise is synchronously measured with modulation signal. This improves the signal to noise ratio by the factor of $\sqrt{\Delta\tau \times \Delta\nu}$ where τ is integration time of the lock in amplifier and ν is measurement bandwidth. The sensitivity obtained in their experiment was $6.2 \times 10^{-27} \mathrm{A}^2/\mathrm{Hz}$. The sensitivity could be further improved by using a modulated balanced amplifier. Such technique was used by F.D. Parmentier *et al.*[11]. The key element in their setup is a 90° hybrid coupler. The sample is coupled to a cryogenic amplifier through a quadrature hybrid coupler.The coupler is 4 port device with two inputs in which the signal is equally splits in amplitude but 90° out of phase. Hence while measuring the difference across the output of coupler, amplifier noise is nullified. The sensitivity is further improved by modulating the biasing signal. The sensitivity obtained by F.D. Parmentier *et al.*[11] is an order improvement *i.e.*$2 \times 10^{-28} \mathrm{A}^2/\mathrm{Hz}$.

2.4 ON CHIP NOISE DETECTION

ON chip detection of noise is another approach in noise measurement techniques. All noise measurements mentioned above suffer from bandwidth problems, high frequency resonances and long integration times. If we follow the technological chronology of noise measurement setup: First amplifiers were used to increase the noise signal from the sample above the intrinsic noise of the spectrum analyzer or integrator, but this limits the measurement to the low frequency regime. Then amplifiers were put very close to the sample to reduce the stray capacitances and noise measurement in the MHz regime became possible. If we look here, all technological feats were done such that one could amplify the signal above the noise floor of the spectrum analyzer. If one could design a very low noise spectrum analyzer and coupled it directly to the sample this could solve above all technological problems. This is the basic motivation for the on chip detection. The idea of on chip detection was first suggested in D.E.Prober *et al.*[12] where the authors reported about the coupling of a quantum device directly to a quantum dot (QD) or a superconducting-insulator-superconductor(SIS) junction which acts as detector of the high frequency signal by converting it into a DC signal. This measurement provides a very large bandwidth, typically allowing to do frequency resolved measurements in GHz-THz regime. The current fluctuations in the quantum device induce fluctuations in capacitive environment coupling to SIS junction.This leads to photon assisted tunneling (PAT) of the quasi particle across the insulating barrier between the two superconductor[13]. The measures of this PAT gives the direct value of the noise in quantum device. In similar system, a quantum dot coupled to quantum device like quantum point contact can acts like on chip noise detector. The QPC current fluctuations induce the photo-ionization which drives the quantum dot out of the Coulomb blockade. This allows the sequential tunneling of the electron in the excited state. Hence the transient current through the quantum dot gives the information about noise in the quantum point contact[14]. The main advantages of on chip detection are fast and ultra high charge sensitivity *i.e.* $1.2 \times 10^{-5} \mathrm{e}/\sqrt{\mathrm{Hz}}$ as stated by R.J. Schoelkopf *et al.*[12].

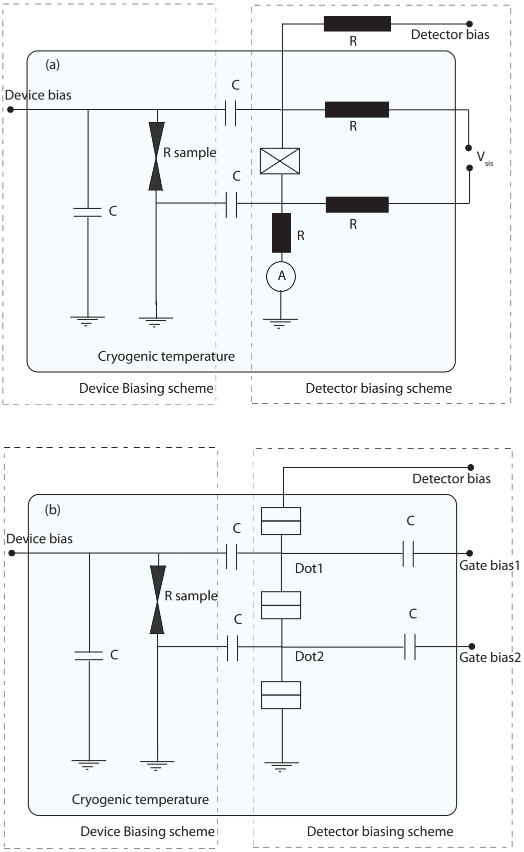

FIGURE 2.6: On chip noise detection noise setup: (a)A scheme showing electrical circuitry for the on chip noise detection using SIS junction capacitively coupled to quantum device. (b) On chip noise detection scheme using double quantum dot coupled to quantum point contact (Rsample).

Above both techniques are hampered by the low current levels. An improvement to above on chip noise detection schemes can be done by using double quantum dot capacitively coupled to the quantum point contact. This was first time proposed by Onac *et al.* [15]. The such measurement scheme for DQD coupled to quantum device is shown in figure (2.6). The current fluctuations in the quantum device induce fluctuations in the energy states of the DQD. This leads to the inelastic electron tunneling events. During inelastic tunneling events electrons exchange energy with the environment *i.e.* by absorption or emission of a photon. This inelastic tunneling current carries a measure of the fluctuations due to single tunneling of the electron with a photon. The modulation of the inter-dot barrier amplifies the inelastic current signal. The double dot system can be tuned to measure either emission or absorption spectra by tuning the energy difference between the dot in the bias window. The main advantage of this technique is wide detection window. The lower bound depends upon the inter-dot width of the resonant tunneling peak which is in the GHz regime and the upper end is given by the level spacing within the same dot which is in the THz regime. Both can be easily engineered to change the bandwidth. This concept was first realized by Gustavsson *et al.*[16] enabling them to do real time electron counting statistics. In another similar approach, Küng *et al.* used the above technique to do the cross correlation measurement[17]. This techniques enable them to measure the shot noise in μV regime. This techniques allows them to measure the third moment of full counting statistics on the QPC[18].

In this thesis we will use the low frequency noise measurement using the cross spectrum technique for noise measurement on the atomic contact. This is discussed in the chapter Shot noise measurement circuit . We also worked on the development of the high frequency noise measurement based on the Two channel cross correlation technique . This is discussed in the chapter The cryogenic amplifiers. Here we discussed the complete design of the noise measurement setup suited for the mechanical break junction. Criticality of both measurement scheme lies on the sensitiveness of our atomic and molecular junction on electro mechanical noise. The high frequency noise measurement setup is ongoing work and still needed to be tested on the atomic contacts.

REFERENCES

[1] L. K. J. Vandamme, in *Advanced Experimental Methods for Noise Research in Nanoscale Electronic Devices, Proceedings of the NATO Advanced Research Workshop, Nato Science Series II* (2003), vol. 151, pp. 1–370, URL `http://rd.springer.com/book/10.1007/1-4020-2170-4/page/1`.

[2] F. Crupi, G. Giusi, and C. Pace, in *Instrumentation and Measurement technology conference IMTC 2007* (Warsaw, 2007), pp. 1–4.

[3] J. Briaire and L. K. J. Vandamme, *Uncertainty in Gaussian noise generalized for cross-correlation spectra*, Journal of Applied Physics **84**, 4370 (1998).

[4] G. Ferrari and M. Sampietro, in *Advance Experimental methods for noise research in nanoscale electronics devices* (2003), 978-1-4020-2170-1, URL `http://rd.springer.com/book/10.1007/1-4020-2170-4/page/1`.

[5] D. C. Glattli, P. Jacques, A. Kumar, P. Pari, L. Saminadayar, and I. Introduction, *A noise detection scheme with 10 mK noise temperature resolution for semiconductor single electron tunneling devices*, Journal of Applied Physics **81** (1997).

[6] M. Sampietro, L. Fasoli, and G. Ferrari, *Spectrum analyzer with noise reduction by cross-correlation technique on two channels*, Review of Scientific Instruments **70**, 2520 (1999).

[7] A. T. Lee, *Broadband cryogenic preamplifiers incorporating GaAs MESFETs for use with low temperature particle detectors*, Review of Scientific Instruments **60**, 3315 (1989).

[8] A. T. Lee, *A low-power-dissipation MESFETs in parallel broadband cryogenic preamplifier utilizing GaAs*, Review of Scientific Instruments **64**, 2373 (1993).

[9] F. Wu, L. Roschier, T. Tsuneta, M. Paalanen, T. Wang, and P. Hakonen, *Setup for shot noise measurements in carbon nanotubes*, AIP Conference Proceedings **850**, 1482 (2006).

[10] M. Reznikov, M. Heiblum, H. Shtrikman, and D. Mahalu, *Temporal Correlation of Electrons: Suppression of Shot Noise in a Ballistic Quantum Point Contact*, Phys. Rev. Lett. **75**, 3340 (1995).

[11] F. D. Parmentier, A. Mahe, A. Denis, J.-M. Berroir, D. C. Glattli, B. Placais, and G. Feve, *A high sensitivity ultralow temperature RF conductance and noise measurement setup*, Review of Scientific Instruments **82**, 013904 (pages 8) (2011).

[12] R. Schoelkopf, P. Wahlgren, A. Kozhevnikov, P. Delsing, and D. Prober, *The radio-frequency single-electron transistor (RF-SET): A fast and ultrasensitive electrometer*, Science (New York, N.Y.) **280**, 1238 (1998).

[13] R. Deblock, E. Onac, L. Gurevich, and L. P. Kouwenhoven, *Detection of Quantum Noise from an Electrically Driven Two-Level System*, Science **301**, 203 (2003).

[14] E. Onac, F. Balestro, L. H. W. van Beveren, U. Hartmann, Y. V. Nazarov, and L. P. Kouwenhoven, *Using a Quantum Dot as a High-Frequency Shot Noise Detector*, Phys. Rev. Lett. **96**, 176601 (2006).

[15] R. Aguado and L. P. Kouwenhoven, *Double Quantum Dots as Detectors of High-Frequency Quantum Noise in Mesoscopic Conductors*, Phys. Rev. Lett. **84**, 1986 (2000).

[16] S. Gustavsson, M. Studer, R. Leturcq, T. Ihn, K. Ensslin, D. Driscoll, and A. Gossard, *Frequency-Selective Single-Photon Detection Using a Double Quantum Dot*, Physical Review Letters **99**, 2 (2007).

[17] B. Küng, O. Pfäffli, S. Gustavsson, T. Ihn, K. Ensslin, M. Reinwald, and W. Wegscheider, *Time-resolved charge detection with cross-correlation techniques*, Phys. Rev. B **79**, 035314 (2009).

[18] S. Gustavsson, R. Leturcq, B. Simovič, R. Schleser, T. Ihn, P. Studerus, K. Ensslin, D. C. Driscoll, and A. C. Gossard, *Counting Statistics of Single Electron Transport in a Quantum Dot*, Phys. Rev. Lett. **96**, 076605 (2006).

3

EXPERIMENTAL SETUP: DESIGN AND TECHNIQUES

The smallest nanoscale systems such as atomic chains and single molecule bridges show rich physical properties. They form test-beds for probing concepts in quantum transport. Among the experimental techniques scanning tunneling microscope and mechanically controllable break junctions have been extensively used to study such systems. The mechanically controllable break junction technique used here is based on thinning down to single atom a macroscopic wire having a weak link at the center by mechanical force. Once a single-atom contact is formed the physical properties of the system are dominated by quantum mechanics. The coupling of this atom with the bulk metal can be controlled at the sub-Ånsgstrom level, giving an opportunity to tune the quantum properties of the system. This simple set up forms the platform for our studies of the quantum properties of one-dimensional quantum system such as atomic chains and single-molecule junctions. In this chapter we are introducing the basic terminology, concepts and experimental techniques which we have used in further chapters.

3.1 THE MECHANICALLY CONTROLLABLE BREAK JUNCTION TECHNIQUE

THE mechanically controllable break junction (MCBJ) technique for the study of atomic-size junctions was developed by Muller *et.al.* [1] in Leiden, based upon an earlier design that Moreland and Ekin *et.al.* [2] used for the study of the tunnel current through vacuum between Nb electrodes. The design is very simple and basically consists of a metal wire with a weak link in the center. It is placed on top of a bendable substrate. The wire is stretched at its weakest link by bending the substrate using a mechanical screw mechanism. A schematic of such a design is shown in figure (3.1). Once the wire is broken, the distance between the two ends of the freshly cleaved lead can be further controlled mechanically. The vertical displacement of the mechanical drive δz produces a lateral displacement δd at the weak link of the wire that is much smaller due to the small stretching of the substrate surface with the bending. The ratio of the lateral displacement with respect to the vertical displacement gives the attenuation factor of the MCBJ set up, which is also called the reduction ratio[3]. This factor r is given as:

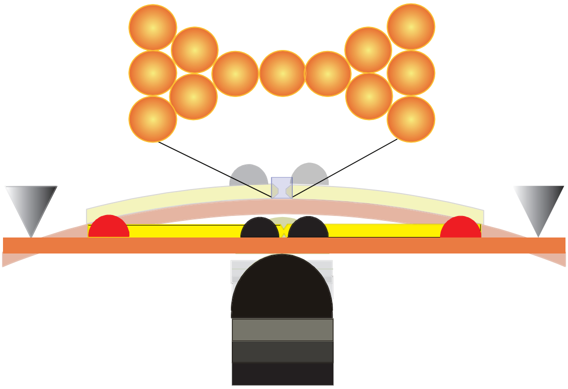

FIGURE 3.1: Schematic of the mechanically controllable break junction technique: A sample wire is fixed on top of a bendable substrate using epoxy glue (black droplets). An atomic-scale contact is formed using fine control by a piezo-electric drive (black cylindrical rod) in a three-point bending configuration.

$$r = \frac{\delta d}{\delta z} = \frac{6tu}{L^2}, \tag{3.1}$$

where t is the thickness of the substrate, u is the length of the wire between the anchoring points, and L is the length of the sample between the counter supports.

For the sake of reference let us calculate the reduction ratio for a typical MCBJ sample. The typical numbers for the parameters in (3.1) are $t = 1$mm, $u = 0.1$mm and $L = 20$mm, which gives $r \approx 1 \times 10^{-3}$. The significance of this number can be understood considering the example of a mechanically feasible displacement $\delta z = 0.1 \mu$m for which δd is about 0.1Å. This is about $1/25^{th}$ of the atomic diameter of a Au atom. Hence, the spatial resolution of the MCBJ control is much smaller than the inter-atomic distance. This spatial resolution can be further improved using a piezoelectric element to push the bendable substrate. A spatial resolution well below $1pm$ can be obtained in this way. [1]

Two types of break junctions

The MCBJ can be classified into two different types, that are illustrated in figure (3.2) :

Notched wire break junctions : This type of break junction is quite commonly used for metals other than Au. It uses a wire having a notch carved in the center. Usually the notch in the wire is made by means of a surgical knife. At the notch the diameter of the wire is reduced to 25%–50% of its original diameter. The wire is fixed upon a kapton covered phosphorous bronze substrate using epoxy adhesive. A top layer of kapton tape acts as the insulator between the sample wire and the phosphorous bronze substrate. The two epoxy anchoring points around the notch should be very close to the notch in order to have better stability and higher spatial resolution. The sample is left curing for a day and then is mounted an the three point bending configuration of the mechanical drive system. The junction is broken first using a mechanical screw, but once the sample is broken the piezo element is used to fine tune the distance between the two freshly cleaved surfaces[1].

Lithographic break junction : This type of break junction is made by electron beam lithographic processes and is almost exclusively used for Au metal electrodes. The sample wire is formed by thermally evaporating a high purity metal film directly on a polished bendable substrate, that is planarized by spincoating of a polymer layer, often polyimide. The notch in the junction is formed using electron beam lithography, and a freely suspended bridge is formed by a step of isotropic ion etching, which attacks the polyimide under the metal film. The lithographic junction is first broken and controlled by means of a mechanical gear and an electromotor drive[5].

---

[1] For measurement of the electrode displacement one needs to calibrate each sample individually [4].

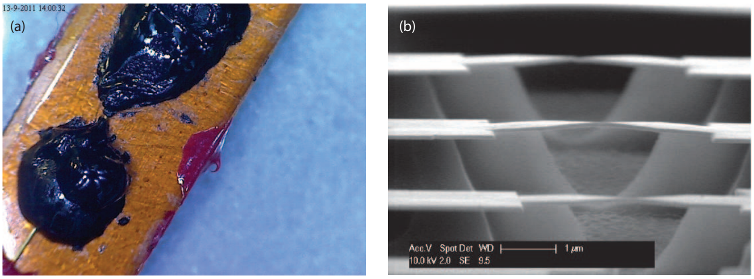

FIGURE 3.2: Left: Photograph of a notched wire break junction. Right: SEM image of lithographically fabricated break junctions; in this case three are formed on the same substrate (courtesy C.A. Martin [6]).

Each of the above two MCBJ methods has its own advantages and disadvantages. The lithographic junctions have a better stability and their distance resolution is at least three orders of magnitude better than the notched wire break junction. The much smaller reduction ratio gives a stability of the order of 10^{-5}Å$/min$. This permits characterizing the atomic system for longer periods of time without drift in the contact. The stability for the notched wire MCBJ is $1-2$ orders of magnitude smaller than the above mentioned value but is still quite sufficient for longer duration junction characterization. Below we will show that this stability allows us to measure the noise on Au atomic chains over $2-3$ hours without any discernible drift in the contact. The most important disadvantage of the lithographic junctions is the fact that statistical measurements are much more time consuming. Since for lithographic break junctions the reduction ratio is too small for a piezo-electric element to have much effect, an electromotor is used for making and breaking of the contact. This process is quite slow in comparison to notched wire break junctions, where a series of rapid voltage ramps on the piezo permits collecting a histogram of 1000 breaking traces in a matter of minutes.

The main disadvantage of above two techniques is that the actual topography of the contact is not observed during the junction characterization. Some contacts show quite stable configurations and some can form very long atomic chains, while the same contact after reforming could snap. It is not very practical to work with the single crystals in the MCBJ. A SEM image of various contacts which we have used for the work in this thesis is shown in figure (3.3). Even the same sample at different stages of the making and breaking processes forms microscopic structures giving completely different properties. Generally, Au atomic contacts show much more stable contacts in comparison to ferromagnetic atomic contacts. The difference is related to the structures seen from the SEM images. Au has a much

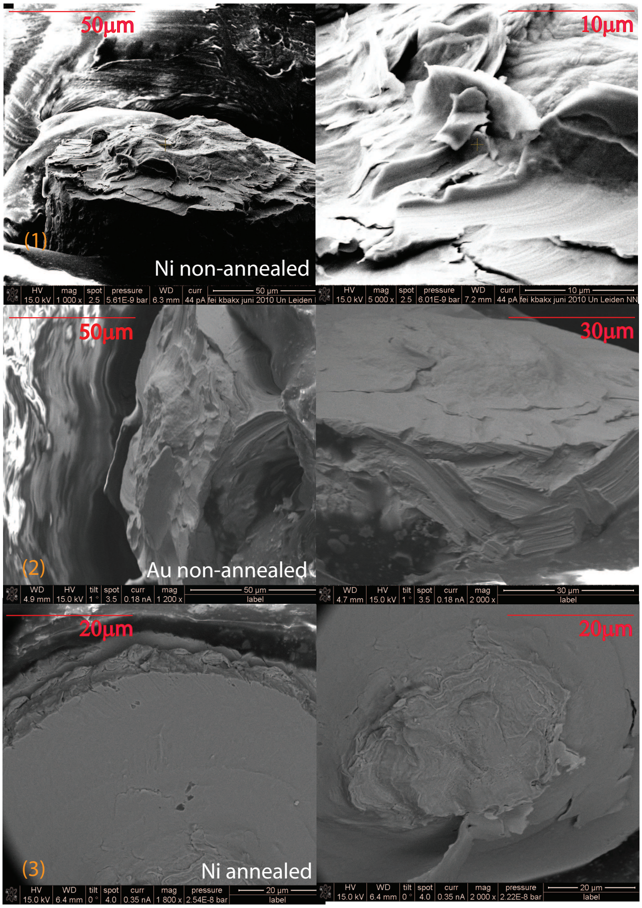

FIGURE 3.3: SEM images of different MCBJ: Scanning tunneling microscope images of the the broken surface for six different MCBJ samples. There is a drastic difference between the surface topography of Ni and Au wires. Generally, non-annealed Ni wires show a strong drift in the contact conductance. The annealing of the wire gives increased stability of the contact[2]. The SEM image of annealed Ni contacts shows less flakes in the contact region, but note that the configuration which is involved in the atomic contact formation cannot be identified in the SEM image. This is a clear disadvantage of MCBJ over STM measurements.

smoother notch area while Ni has lots of flakes in the notch area. Annealing of the Ni sample wires improves the stability of the contact by removing the granularity near the contact. Note that in these SEM images the real atomic configuration of the contact point is missing, which determines the actual geometry determining the different physical properties of the contact. Scanning tunneling microscope has the advantage over MCBJ that it allows scanning the topography of the surface and precisely controlling and manipulating the atomic structure. Nevertheless, due to the extreme stability and to the possibility of producing atomically clean contacts gives MCBJ an edge over STM and makes it suitable for our research work. In our studies we have used the notch wire break junction technique. A photograph of one of our samples is shown in figure (3.2).

3.2 MCBJ INSERT

MCBJ experiments were done in cryogenic vacuum at helium temperatures. The MCBJ sample was mounted in a custom-made home-designed dipstick. The top of the dipstick, called the head, contains a vacuum coupling for the pumping line and several electrical feedthroughs. The bottom of the dipstick, called the sample chamber, hosts the sample. All electrical wires at the connections inside the head of the dipstick were soldered using flux and lead free soldering tin. The vacuum couplings were mainly sealed by O-rings except from those feedthroughs which needed to be baked out, which were Swagelok type. A schematic layout of the lower part of the dipstick is shown in figure (3.4). The head and bottom of the dipstick are connected by a long hollow tube of 48mm in diameter and 1.2m long, which holds several hollow tubes inside it. These small tubes are used for the wiring and are anchored to the interior wall of the dipstick, using silver welding for better thermal coupling. A Cu-Ni alloy was used for the wiring inside the dipstick for optimized electrical conduction combined with poor thermal conduction. All the wires running from the top of the dipstick are coupled to a Cu cold plate which is in contact with the He bath through a cold finger. Cu wires were used from this cold plate for connections to the sample. This differential wiring scheme helps us to keep the sample decoupled from the room temperature heat bath.

Along the center of the tube a 1.1m long mechanical axis runs from the head to the sample chamber. This axis is made of a hollow stainless steel tube in order to reduce the heat load on the He bath and the sample. On the top of the dipstick this mechanical axis is connected to a $1:100$ gear box that is attached through a Rikagou magnetic feedthrough [8]. This gear box gives us sub-micron resolution for the z-axis movement of the mechanical rod. At the lower end of this axis a fork-blade structure is mounted to allow decoupling the axis from the sample chamber. The extension of the axis at the cryogenic side is connected to a differential screw. A piezo electric element is mounted with epoxy adhesive to the bottom of the differential screw. The advantage of this design is that the mechanical axis can be used for breaking of the sample at cryogenic temperatures. Once the sample is

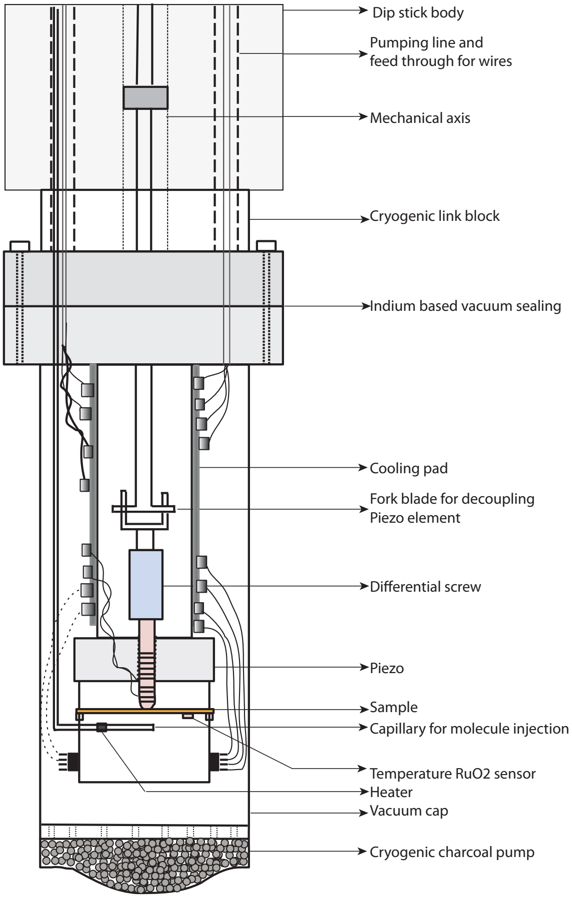

FIGURE 3.4: Schematic of the dipstick used for MCBJ experiments. The different parts of the dipstick and sample chamber are shown and labeled. The head of the dipstick is connected to the sample chamber through a long hollow tube which contains several smaller tubes for wiring and for the introduction of gas molecules in the sample chamber.

broken the axis is decoupled from the lower end using the fork and blade configuration. With the axis decoupled the piezo element can be used for fine tuning the inter-electrode distance. In this way the atomic contact is maximally decoupled from mechanical vibrations coming from the top of the dipstick. A stainless steel capillary tube of 6mm in diameter runs from the head of the dipstick to the sample chamber, and ends in a detachable nozzle. This tube we use for introducing the lighter molecules to the atomic contact. The capillary tube is fitted with a vacuum-sealed heater wire running inside the tube. The nozzle has an orifice facing the sample wire. A heater wire is mounted on the nozzle to heat it when introducing the gas while the sample is at cryogenic temperatures. The whole capillary and nozzle are thermally isolated from the He bath. On the top of the dipstick the capillary is connected to a needle valve through a Swagelok connection. The advantage of this design is that the whole capillary can be baked out without damaging the wire connections and other vacuum sealing. In order to measure the temperature of the capillary tube during bake out process, several Pt-10K resistive thermometers are placed along the tube. The nozzle is fitted with a Pt-100K resistor. A 10K $Ru0_2$ resistor is used for measuring the temperature of the sample. A four-probe wire connection is preferred for the $Ru0_2$ thermometer for accurate temperature measurement of the sample. The other resistance thermometers are fitted with a 2-wire measurement scheme. The sample holder is clamped to the dipstick through a screw mechanism and vacuum sealed by an indium seal. The cryogenic cap of the dipstick is fitted with a compartment filled with Norit activated carbon which acts as a cryogenic pump.

The dipstick is pumped using a two-stage pump system. For rough pumping a rotary pump is used and, once the base pressure of the dipstick is approximately 10^{-3}mbar, it is further pumped using a turbomolecular pump. The dipstick is pumped to a pressure of 10^{-5}mbar, as measured at the top of the dipstick. Once this pressure is reached the capillary is baked out for a day. After the baking the base pressure improves to $10^{-6}-10^{-7}$mbar. Next, the dipstick is cooled down in the liquid nitrogen first and then lowered into liquid He[3]. Once the dipstick is in the liquid He the cryogenic pump overtakes the turbo pumping, hence all the valves on the top of the dipstick are closed, apart from the capillary valve. With the dipstick closed the cryogenic vacuum is expected to be well below 10^{-10}mbar, but this was not measured directly.

3.3 THE ELECTRONIC CIRCUIT

THE electronic circuits employed in our setup can be divided into three independent circuits: (a) The conductance measurement (ac and dc) setup. (b) Piezo biasing circuit. (c)The noise measurement setup. The schematic of our conductance measurement circuit is shown in figure (3.5). We have employed a two-probe measurement technique for the conduction measurement. The dc voltage biasing is provided from a National Instruments data acquisition card (DAQ-NI 6221). NI DAQ provides a digital to analog convertor with 16 bit digital accu-

---

[3] The two-step cooling is followed in order to reduce the liquid He consumption; one can also cool down the dipstick first in cold He gas and dip it gradually in the liquid He bath.

racy. The current is measured through a current/voltage converter and one of the analog-to-digital inputs of the data acquisition card. For point contact spectroscopy an ac modulation signal of 2mV amplitude and a frequency of 3.33kHz was added, as obtained from the generator in a SR830 lockin amplifier. In this lockin measurement technique a reference signal is used to modulate the dc bias signal. The lockin amplifier takes the signal from the sample, multiplies it with the reference signal, integrates it over a specified time constant, and gives a signal proportional to the harmonics of the reference (see below, equation(3.2)). The lockin amplifier can extract the phase and amplitude information of a signal in a noisy environment. The lockin measurement technique is used to detect small changes of about 1% in the signal with an accuracy better than 1%. The overall accuracy of ac conductance measurement was checked using fixed calibration resistors. The resistance measured in our setup is within 1% of the four probe measurement value. We have two switches (S1 and S2) for the coupling and decoupling of the conductance measurement with the noise measurement circuit. The S1 is used to short the sample while S2 decouples the ac signal from the sample. The dc measurement setup is used to characterize the junction by measuring the conductance breaking/making traces while the ac measurement is done to study the smaller signals like the perturbation in the current due to electron-phonon coupling.

The potential on the piezo element is controlled using the DAQ. The signal from the DAQ is amplified using a homemade high voltage amplifier. Special attention is taken to decouple the ground of the piezo element from the common ground of the dipstick. The noise measurement setup is discussed below, in the section (3.5.1)

3.4 THE CHARACTERIZATION OF ATOMIC CONTACTS

THE MCBJ technique can attain a distance resolution of sub-Ångstrom level with a stability of 10^{-5}Å/min. It being very simple the MCBJ technique is a strong tool to investigate the properties of individual atoms in the contact. Once the wire is broken to the point where only single atom is bridging between the two bulk leads the physical properties of the system are dominated by the species at the center of the contact. To investigate the properties of this atom in detail, it is needed to characterize the atomic contact first.

3.4.1 DC CONDUCTANCE CHARACTERIZATION

The most obvious way to characterize the contacts is to look into the evolution of the current while stretching the contact. It is evident that one could see an increase in the resistance while pulling and, hence, one could expect a gradual decrease in the conductance upon increase in the distance. This is correct when the wire is still

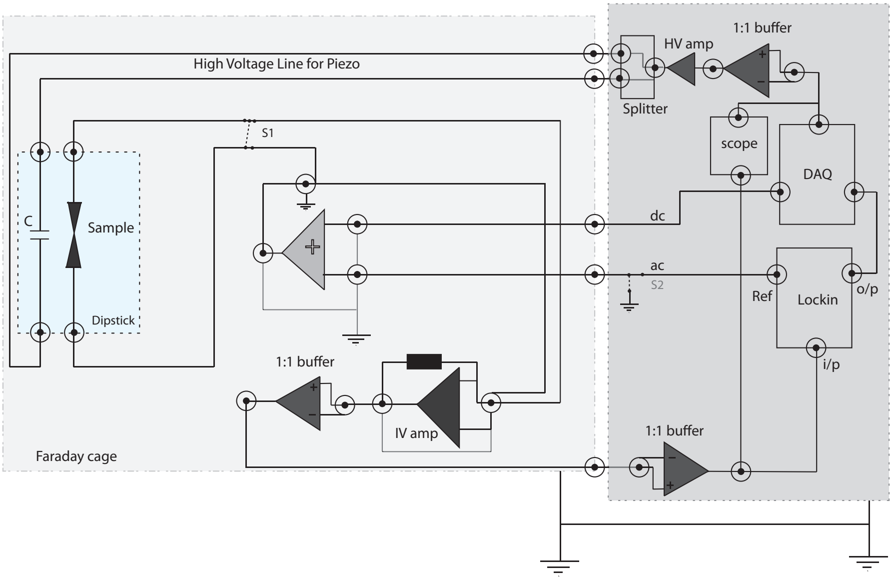

FIGURE 3.5: Schematic of the conductance circuit used in our measurement. A two-probe measurement technique is used to measure the conductance of the atomic contact. For ac measurements a lockin technique is used. The ac signal is added to t he dc signal using a home made adder. The current from the circuit is converted back to voltage using an I-V converter with variable gain. The output of the IV converter is fed into the lockin to measure the first harmonics.

in the bulk regime but when the cross section of the wire is reduced to a few atoms diameter one should expect sudden changes in the conductance due to movement of individual atoms. A few typical traces recorded on Au atomic contacts is shown in figure (3.6 a). It is remarkable to see that the conductance indeed reduces in a step fashion upon stretching of the contact. This step-wise conductance variation should not be confused with conductance quantization as in experiments on 2-dimensional electron gases [9, 10]. In our experiment the conductance follows from the step-wise variation in the atomic configuration of the contact. This is also the reason why the traces do not show regular and reproducible quantization in the conductance plateaus. Another remarkable feature to be noted here is that there is a long plateau forming just before the conductance vanishes. This long plateau can be understood in terms of the formation of perfectly well coupled regular structure upon stretching. One could ask why such structure be could formed and especially around the quantum of resistance. The presence of this structure at the quantum of resistance implies that our system has already entered into the quantum domain, where the resistance does not depend upon diffusive scattering of the electrons by the lattice structure, but only at the interface of the quantum system with the bulk structure. These structures have been studied in detail by Yanson *et al.*[11] who have shown that these structures are in fact one dimensional atomic chains. Au and Pt are among the few metals which form atomic chains. Experimentally, van den Brom *et al.*[12] have demonstrated that Au atomic chains carry a single conductance channel. Hence, in the trace shown in figure (3.6 a) is explained by the formation of a single channel Landauer conductor a few atoms long.

Returning to the traces, one can see that it is difficult to predict the evolution of the traces, which depends upon the local atomic configuration of the leads. Hence one needs statistical averaging over atomic contact configurations. Two types of statistical analysis on conductance traces have been developed: one based on the conductance scale, the other on the piezo voltage scale. The first statistical study gives the frequency of occurrence of the conductance values, which is called the conductance histogram. A conductance histogram constructed from the recordings of 8000 Au atomic contact breaking traces is shown in figure (3.6 b). The conductance histogram shows predominantly a sharp peak at $0.98G_0$ and broader peaks at higher conductances. This is a characteristic of Au atomic contacts. Regardless of the measurement technique and for all samples Au atomic contacts always show a sharp peak around $1G_0$. In the same way histograms for Pt atomic contacts show a broad peak at $1.5G_0$. Deviations of the peak from the observed value indicates the presence of foreign atoms or molecules in the contact. The second statistical study gives information of the frequency of occurrence of the breaking voltage. The breaking voltage is the piezo voltage at which the atomic contact is broken into the tunneling regime. This type of statistics gives information on the length of chain formation. Looking at figure (3.6 c) we can see the presence of multiple peaks. This shows that occurrence of lengths of the atomic structure is not smooth, but it is discrete. The first peak is attributed to the breaking of a dimer contact, and subsequent peaks represent the breaking of atomic chains with additional atoms in the contact. This length histogram is recorded for the last plateau only. The last plateau corresponds to the first peak in the conductance histogram which signifies a contact of a single atom in cross section. For Au length histograms are recorded for sections of the conductance traces between $G_{min} = 0.85G_0$ and $G_{max} = 1.05G_0$. These parameters vary for different atomic species.

For a correct determination of the chain length one needs to calibrate the reduction ratio of the contact. One of the methods proposed by Muller *et al.*[13] is based on measurement of the tunneling current as the function of the inter-electrode distance. The tunneling current decays exponentially with increasing inter-electrode distance. The logarithmic derivative of this function gives a mea-

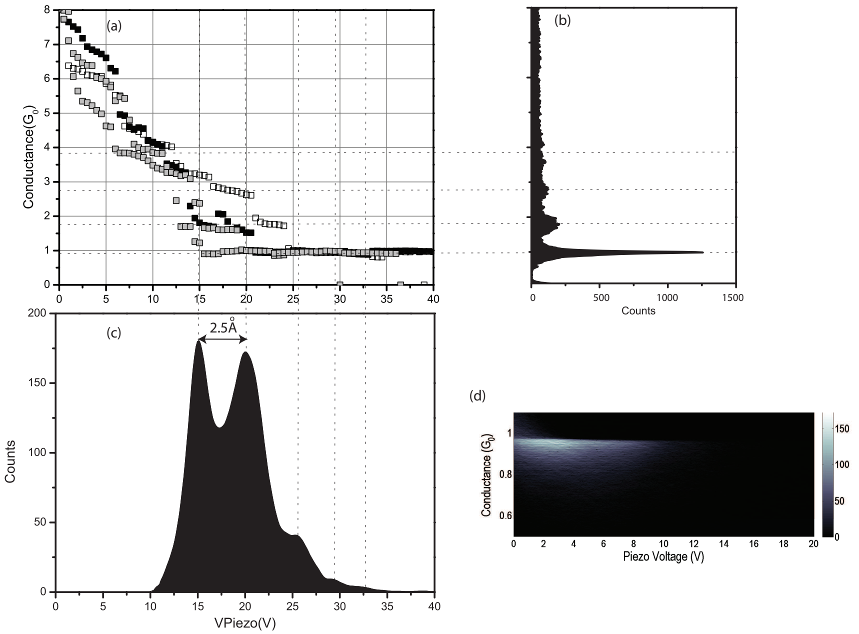

FIGURE 3.6: Characterization of atomic contacts for Au. (a) Three examples of dc conductance traces recorded for Au atomic contacts. The biasing voltage used to record the trace was 80mV. The conductance traces show the formation of a long last plateau formation upon stretching of the contact, after which the contact breaks into the tunneling regime. The traces shown here are a few selected traces showing the presence of the 4-5 atom long atomic chains. (b) A statistical representation of the frequency of occurrence of conductance values during breaking of the contacts. This conductance histogram was recorded for values between $0.1G_0 - 8G_0$. For Au atomic contacts the histogram shows a prominent peak at $0.98G_0$. (c) Histogram of the lengths of last plateaus for the breaking of atomic contacts. For Au, it shows the probability for long chain formation with peaks at regular distances suggesting an origin in the atomic spacing. The length histogram was recorded for conductance values between $1.05G_0 - 0.85G_0$. The first peak corresponds to a 2 atom contact and subsequent peaks correspond to chains having additional atoms in the contact. (d) The combination of the conductance histogram and the length histogram in the form of a 2D density plot. For construction of the plot 8000 conductance traces were taken.

sure of the reduction ratio. This procedure is not very precise due to the dependence of the tunneling current on the work function, which explicitly depends upon the atomic configuration of the leads. Another more sophisticated approach uses Gundlach oscillations, *i.e.* the oscillations in the tunneling resistance in the field emission regime. Here, we rather use a simpler approach to calibrate the reduction ratio for our samples, as proposed by Untiedt *et al.* [4]. Using their number for the inter-atomic distance between Au atoms in a chain is 2.5Å, a comparison with the distance between the peaks in the length histogram gives for the reduction ratio $r = 5.0/2.5 = 2.0V/\text{Å}$.

3.4.2 AC CONDUCTANCE MEASUREMENT

The dc conductance characterization can accurately verify the cleanliness of the atomic contacts. However, this method cannot identify the exact nature of the species in the contact. The dc measurements are done at fixed bias, but the conductance varies with bias, depending on the nature of the species in the contact and its coupling with the leads, on the presence of vibration modes and on local atomic configurations of the leads. Hence, probing this bias dependence gives valuable information, not only about the nature of the atomic species but also its coupling to the leads. The vibration mode signal is quite small, typically of the order of $1-2\%$ of the zero-bias conductance. Hence, the common method to reveal this signature is to measure the differential conductance using a lockin technique, or by numeric derivatives of the current. For lockin measurements the dc signal is modulated by a small ac signal. Lockin measurements give a much better signal-to-noise ratio through detection of the harmonics of the conductance. This can be seen from a Taylor expansion of the modulated signal $I\left(V_b^{dc} + V_m^{ac}\cos(\omega t)\right)$ up to second order.

$$\begin{aligned} I\left(V_b^{dc} + V_m^{ac}\cos(\omega t)\right) &= I(V_b) + \left|\frac{dI}{dV}\right|_{V_b} V_m \cos(\omega t) + \frac{1}{2}\left|\frac{d^2I}{d^2V}\right|_{V_b} V_m^2 \cos^2(\omega t) \\ &= I(V_b) + \left|\frac{dI}{dV}\right|_{V_b} V_m \cos(\omega t) + \frac{1}{4}\left|\frac{d^2I}{d^2V}\right|_{V_b} V_m^2 (1+\cos(2\omega t)) \end{aligned} \tag{3.2}$$

There are two broad classes of ac conductance spectroscopy: (a) Point contact spectroscopy, which refers to the studies of inelastic scattering of electrons in the ballistic regime of metallic point contacts, and (b) Inelastic electron tunneling spectroscopy, which refers to study of inelastic scattering of electrons in the tunneling regime.

Inelastic electron tunneling spectroscopy

In systems like metal-molecule-metal junctions the metal electrodes often can be regarded as separated through a tunneling gap. If the voltage applied across the molecular junction is such that $eV \geq \hbar\omega$, for an given vibration mode energy $\hbar\omega$ then there is a certain probability that the electron will interact with the vibration mode of the molecule. This interaction leads to forward scattering of the electron with a reduced energy of $E_F + eV - \hbar\omega$. This can be understood as the opening of a new inelastic channel. In the differential conductance this can be seen as an increase in the conductance at the threshold energy [14].

Point contact spectroscopy

Point contact spectroscopy (PCS) was introduced by Yanson *et al.*[15] in the early 1970's. In the ballistic regime electrons traverse a junction without any scattering. However, at higher bias there is a finite probability of electron to be scattered by vibration modes at the contact. The probability for backscattering of the electrons depends upon the ratio $(a/d)^2$ where a is the radius of the constriction and d the distance to the center of the contact. Hence the backscattering of the electrons takes place within a spherical volume of radius a. The early works of Yanson *et al.* and others[15–17] on metallic point contacts concluded that PCS can be used as a tool to identify the phonon density of states of the metals, or more precisely, the spectrum of electron-phonon scattering strength.

In case of atomic contacts a is the radius of a single atom, hence the volume of electron backscattering is small. This also implies that electrons scatter back from a single lattice distance, or within the atomic contact. Hence, point contact spectra for atomic contacts show local vibration modes rather than bulk phonons. The strength of this inelastic signal is on the order of 1% which can be easily hidden in the conductance fluctuations that result from interfering electron waves[18]. These conductance fluctuations can be understood in terms of partial reflection and transmission of electron waves at the contact. If there is single transmission channel in a contact and there is a finite probability that the electron is reflected from the contact this reflected wave could undergo multiple partial reflections. As long as the total path of the reflected electron is within the coherence length of the electron the partial waves superimpose with the transmitted partial wave. The phase accumulated along a path of length L can be written as kL where k is the momentum of the interfering electron wave, which is voltage dependent. This gives an bias-dependent interference signal in the differential conductance.

These conductance fluctuations are dependent on the transmission probability τ of the atomic contact. In the limit of $\tau \simeq 1$ the amplitude of conductance fluctuations is negligible, but for other values they may mask the vibration mode signal. This is the main limitation of PCS in atomic contacts. Since for Au the s electrons form a perfectly transmitting single conductance channel its easier to obtain the vibron signal in the differential conductance. However, this is not case for Pt atomic contacts, where more than one channel is present and some of the channels are partially transmitting, giving rise to stronger conductance fluctuations. Also for Au for some of the contacts our vibronic signal is hidden inside these conductance fluctuations. For vibronic frequency signal analysis it helps to compare the differential conductance with its symmetric component. The sym-

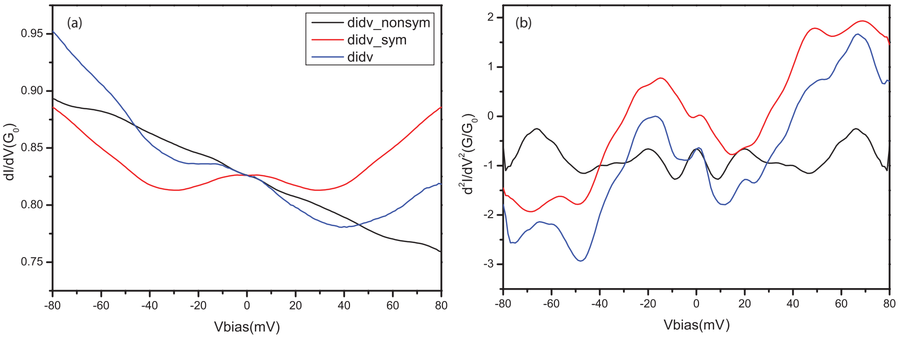

FIGURE 3.7: Characterization of Au atomic contacts by ac conductance measurements. (a) The blue curve shows the differential conductance. The symmetric component of the differential signal is computed as $G_{\mathrm{sym}}(+V) = G_{\mathrm{sym}}(-V) = [G(+V) + G(-V)]/2$ and shown as the red curve. A broad vibronic step down can be seen in the differential conductance at about ±15mV but this is completely overtaken by the asymmetric component $G_{\mathrm{nonsym}}(V) = G(V) - G_{\mathrm{sym}}(V)$ which is plotted in black color. (b) The derivatives of the corresponding differential conductance of panel a. Comparing the features in the second derivative of the current and in its symmetric component the vibronic energy is similar but shifted by asbout 3meV. This difference is incorporated in error analysis.

metric component is calculated using $G_{\mathrm{sym}}(+V) = G_{\mathrm{sym}}(-V) = [G(+V)+G(-V)]/2$. Figure (3.7) shows one of the worst examples where the vibronic signal is almost hidden in the background of conductance fluctuations. We included the shift in the vibronic signal of the differential conductance and its symmetric component in the error analysis. The symmetric component shows the presence of a vibronic step down feature in the signal, which is expected for a contact with $\tau = 0.83$. The second derivative of the current shows the fist peak (minimum) at $\nu_+ = 12$meV at positive bias while the corresponding peak at opposite bias sits at $\nu_- = 15$meV. In a well-coupled atomic chain with symmetric biasing the vibronic signal should be the same for positive and negative bias. Although a shift due to conductance fluctuations is likely, the discrepancy could also be due to asymmetric coupling of the atomic chain with the two leads. Hence, the symmetrized signal does not give the correct answer, and in order to obtain an estimate of the accuracy of the vibronic energy we use the difference between the two in our error analysis.

3.5 SHOT NOISE

SHOT noise in electrical conductors arises due to the discreteness of the electronic charge. It becomes prominent in quantum systems such as quantum dots, tunnel junctions and atomic contacts. In a quantum conductor with an eigen channel with transmission probability $\tau \sim 1$ shot noise is significantly reduced.

But if the transmission probability $\tau \neq 1$ electrons traversing the quantum system will be partially reflected and partially transmitted. The partial occupation of forward and backward traveling states gives rise to shot noise in the quantum conductor. The measurement of shot noise gives information on the number of the eigen channels taking part in the conductance[4]. Here we concentrate on low-frequency noise measurements for atomic contacts and singe molecule junctions.

3.5.1 SHOT NOISE MEASUREMENT CIRCUIT

We have employed a cross spectrum analysis technique for the noise measurements. The signal that we need to measure is of the order of 1nV/$\sqrt{\text{Hz}}$ which is comparable to the noise of the best low-noise amplifiers available. In case of Au atomic contacts $1/f$ noise is very low, and starts to dominate only below 20kHz for bias values above 25meV. This is why we can use a low-frequency noise measurement setup, up to 100kHz, for this system. For single molecule junctions $1/f$ noise is much higher and we have developed a noise measurement technique with a frequency window extending to 10MHz for this purpose, which we will describe in chapter "A high-frequency noise measurement setup for MCBJ". A schematic of our low-frequency noise measurement circuit is shown in figure (3.8). The voltage signal across the sample is measured differentially using two amplifier chains in parallel. The first stage is formed by the low-noise preamplifier LI75A of gain 100, which is further amplified by an EG&G amplifier of gain 1000. The amplified signals are fed to a SRS-785 two-channel spectrum analyzer. In differential ac mode the input voltage noise and current noise of the LI75A is 1.4nV/$\sqrt{\text{Hz}}$ and 10fA/$\sqrt{\text{Hz}}$, respectively. The input noise of the EG&G is 4nV/$\sqrt{\text{Hz}}$. In this two-channel measurement scheme we can see that the noise added by the LI75A is crucial, since it is of same order as the voltage noise signal of 1.89nV/$\sqrt{\text{Hz}}$ for a junction of 1G_0 at 5K. The current noise, which we cannot suppress by the cross spectrum (equation(2.5), is just 0.13nV/$\sqrt{\text{Hz}}$ the same junction, which is still small in-comparison to our voltage noise signal. The main constraint comes from the amplifier voltage noise and its coupling to our measurement signal through intrinsic capacitance of the coax, as illustrated in figure (2.3). The bandwidth of our noise measurement setup is 100kHz, but due to the high impedance of the sample and the high intrinsic cable capacitance (typically ~ 350pF) of the coax running down the dipstick to the sample chamber, the noise spectra show a low-pass roll-off at 35kHz for a junction of 1G_0. Due to this low-pass roll-off the noise signal level at the higher frequency end (typically around 80kHz) hits the noise level due to the residual correlations. This adds to the error in our noise measurements. Typically, the error in

---

[4] Shot noise measurement on the quantum conductors only helps to fix the transmissions for two channels, in some cases for 3 channels. See section (Shot noise analysis) for more details.

the noise measurements is on the order of 4%.

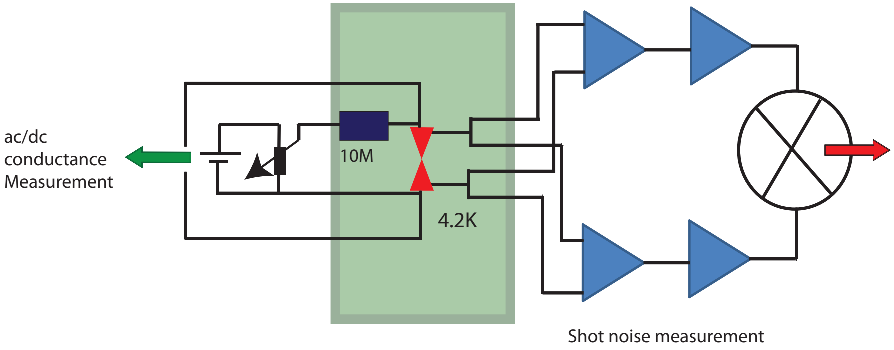

FIGURE 3.8: Schematic of the two-channel cross spectrum shot noise measurement circuit. The voltage across the sample is measured differentially using two sets of preamplifiers. The combined gain of first and second stage amplifiers is $10,000X$. The amplified signal is fed into the two-channel FFT spectrum analyzer. The cross spectrum of the two channels and the FFT of the individual channels are measured with frequency resolution of 250Hz. Averaging over 10,000 spectra takes about 2 minutes. A pseudo current-biasing scheme was used to bias the sample. Initially we have used a battery in parallel with a potentiometer to set the bias. This biasing scheme was later changed to a computer controlled voltage bias system with third order low-pass filters, with a cut off at $f_c = 3$Hz. All amplifiers are battery powered. All noise measurements were done in a shielded environment[19].

3.5.2 DESIGN RULES FOR NOISE MEASUREMENT

The noise measurement can be difficult and cumbersome. Few basic rules should be strictly followed for successful noise measurement techniques. These rules are listed below:

- ***Wiring***: Short shielded coaxes should be used for all electrical connections. Cables connected to the same hot point should be twisted to avoid the electromagnetic field pickups. Wires in the cryostat should be properly anchored and thermalized.
- ***Biasing***: Biasing of sample should be done either by battery manually or using computer. In case of using computer controlled instrument as biasing source, filtering of the spurious noise from the computer should be taken care of. Ground of the computer should be separated from the sample ground.
- ***Filtering***:All DC lines which are coupled directly to the sample especially for high frequency measurement noise should be filtered. The cryostat and

all low noise sensitive equipment like amplifiers should be placed inside a Farady cage to shield the measurement from stray electro-magnetic fields like 50Hz. Usually, transformer steel is considered as the best element for a Faraday cage. All noisy equipment like spectrum analyzers and monitors should be kept outside the Faraday cage. All the components in the Faraday cage should be battery operated.

* ***Ground***: Star ground connection is preferred and the star point should be in the cryostat. Dirty ground should be separated from the clean ground. If samples are biased using the computer then the common signal from the computer should be separated using isolation amplifiers.

* ***Cleanness***: All the wires should be labeled and properly tied up. High power lines, pumps and power transformers should be placed at a distance from Faraday cage. Non connected cables should be dismounted from the connectors. Back ground noise should be measured and characterized properly such that the origin of unwanted signals appearing on the measurement spectra can be identified.

* ***Measurement***: All measurements should be done in a noiseless environment. Usually in the night, the measurements are better when surrounding equipment is turned off. The cryostat should be held by acoustic dampers and all low frequency vibration coupling to the sample should be avoided.

Above all, one should be patient with the noise measurement, especially while measuring noise on atomic contacts which requires a quite noiseless environment. It requires long integration times and it is better to make use of automation but regular manual input is needed for checking the coupling of the external environment with the measurement. All the control parameters like the gain of amplifier and the temperature of the sample should be measured regularly to keep tab on its change.

3.5.3 SHOT NOISE ANALYSIS

For the analysis of the shot noise we measured the ac conductance of the atomic contact, and the temperature of the sample using a 10kΩ RuO_2 resistor. This helps us to determine the expected thermal noise of the sample. The noise was measured at zero bias, for obtaining the thermal noise, at a series of bias voltages in steps of typically 5mV. At the end of the shot noise measurement series, thermal noise and ac conductance of the contact is measured again. The ac conductance and thermal noise measurements at the beginning and the end of the shot noise measurement act as checks on the stability of the contact during the noise measurement. We only considered data for which the change in the thermal noise and zero bias ac conductance during the whole noise measurement process was within 2%. We will show one of the noise measurement sequences for Au contacts below to illustrate the analysis technique.

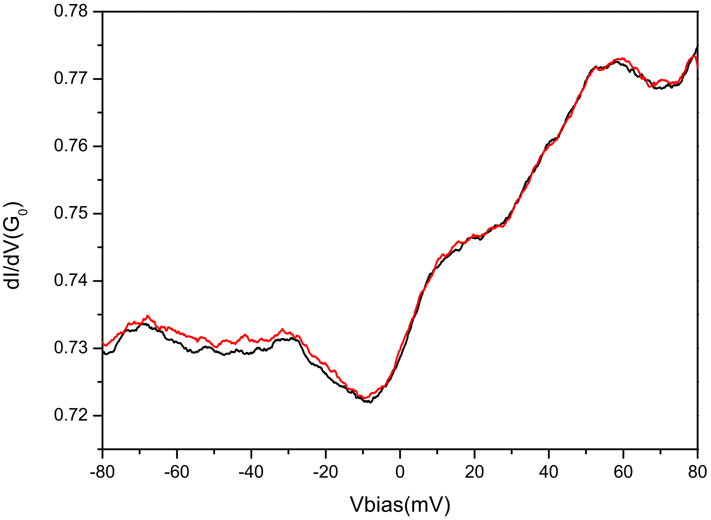

FIGURE 3.9: Differential conductance of the Au atomic used in the example shot noise measurement. The conductance of the Au atomic contact was measured at the beginning (black) and at the end (red) of the noise measurement sequence. The two are exactly same apart from the small deviation at the negative bias. The zero bias conductance agrees within the accuracy at in both differential conductance measurements.

A Au atomic contact is formed in the cryogenic environment using breaking by the piezo element. Once the stability of the contact was checked, the ac conductance of the Au atomic contact was measured using the lockin measurement technique. An ac sinusoidal signal of amplitude 2mV and frequency 2.777kHz was used to modulate the dc signal. Figure (3.9) shows the ac conductance measured at the beginning and at the end of the Au measurement run. The zero bias conductance $G(V) = 0.725G_0$ for both measurements and the shape of the curve has not changed. This shows that the contact was stable during the noise measurement. In the negative bias regime a small deviation between the two measurements can be seen. This could be due to a very small change in distance between the two electrodes. The voltage at which this change is observed is irrelevant for the noise that is measured at much lower bias voltage. The asymmetric differential conductance feature is attributed to conductance fluctuations by interfering electron paths in the contact.

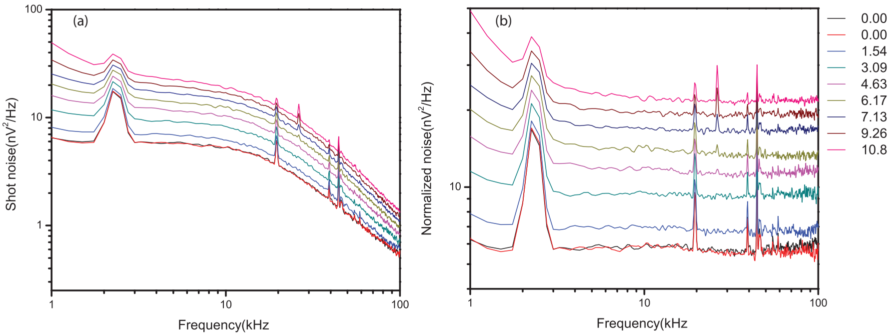

FIGURE 3.10: Noise spectra for a Au atomic contact. (a) Raw noise data measured on a Au atomic contact of conductance $0.725G_0$. The spectra were measured at different bias voltages in steps of approximately 1.5mv. The spike at about 2.5kHz corresponds to the lockin signal; other higher frequency spikes around $20, 26, 39$, and 45kHz correspond to stray signals picked up from the oscilloscope and from the Wheatstone bridge for thermometer measurement. (b)The spectra are corrected for the low-pass behavior by normalizing to the thermal noise and correcting for the mean thermal noise value. The spectra show the some $1/f$ noise at lower frequency, but are nicely flat above 10kHz. The labels in the index show the biasing voltage(mV) used for the noise spectra. The color indexes in both panels are the same.

Noise spectra measured for this contact are shown in figure (3.10). The thermal noise measured on the contact corresponds to a temperature of 6.21K which agrees within the experimental accuracy with the thermometer reading of 6.3K obtained from the RuO_2 resistor. The thermal noise shows a roll-off with a corner frequency of 25kHz. This roll-off agrees within the accuracy with that expected for a stray capacitance of 350pF and conductance of $0.725G_0$. We present spectra in in the range $1-100$kHz because below 1kHz the contribution of $1/f$ noise becomes prominent. A range of the noise spectrum far from the $1/f$ noise corner frequency is selected for further noise analysis. For this particular case the $1/f$ noise corner frequency is below 1kHz and the range between $20-80$kHz was selected for the analysis. We have seen that The spikes seen in the spectra do not reflect intrinsic properties of the atomic contact and they were removed manually. The corrected and spikes-removed spectra are shown in figure (3.11). For each bias setting the mean noise value over the selected frequency range, and its standard deviation normalized to the number of frequency bins, was calculated as shown in figure (3.11 a). This stan-

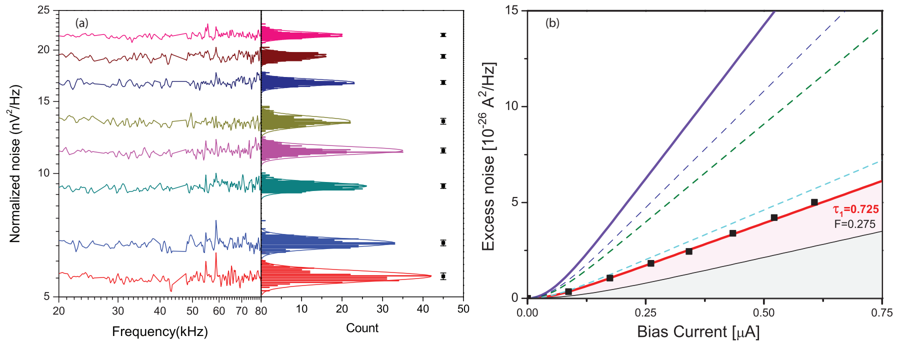

FIGURE 3.11: Shot noise analysis for a Au atomic contact. (a) Normalized spectra for the Au atomic contact data in figure (3.10) , limited to the range 20 – 80kHz, with the spikes removed. The histogram for these spectra gives the mean values of the noise and standard deviations. (b) The mean current noise values with their accuracies are plotted w.r.t. the corresponding biasing parameter. The violet curve shows the full shot noise behavior, $S_I = 2eI$, while the red curve shows a fit to the Lesovik-Levitov expression (1.28). The corresponding Fano factor is 0.275, which agrees with a transmission $\tau = 0.725$ expected for a single conductance channel and a conductance of 0.725G$_0$. The light blue dashed curve is the Lesovik-Levitov (1.28) noise for a hypothetic two-channel conductor with $\tau_1 = 0.7$ and $\tau_2 = 0.025$, which lies well above the experimental data points. The Fano factor for this case is $F = 0.323$. This shows the sensitivity of shot noise for the channel composition in the atomic contact. The green dashed line is the Lesovik-Levitov noise(1.28) for $\tau_1 = 0.362$ and $\tau_2 = 0.363$ giving a Fano factor of $F = 0.637$. The more the transmission value moves towards $\tau = 0.5$, the higher the noise. The blue dashed curve is the Lesovik-Levitov noise(1.28) for three equal channels giving a Fano factor of $F = 0.758$; the higher the number of channels the larger the noise. The red curve is, in fact, the minimum level of noise for a conductor of G= 0.725G$_0$. The pink shaded region is inaccessible for spin degenerate electrons. The black curve shows the minimum noise level for the case that spin splitting of the channels is allowed ($\tau_\uparrow = 1$ and $\tau_\downarrow = 0.45$). The black shaded region is inaccessible for any kind of Landauer conductor.

dard deviation gives a measure of the accuracy of the mean value. The mean current noise value is calculated from the voltage noise $S_I(V) = S_V(V) \cdot G^2$. The mean current noise power is plotted *w.r.t.* the corresponding current bias as shown in figure (3.11 b). The experimental data points are fit to the Lesovik-Levitov expression(equation(1.28)) with a single transmission channel value of $\tau = 0.725$, which corresponds to Fano factor of $(1 - \tau) = 0.275$. The Fano factor agrees with the conductance of 0.725G$_0$. The data clearly confirm that Au atomic contacts form single channel Landauer conductors. This is consistent with previous noise measurements on Au atomic contacts by van den Brom *et al.* [12] and to calculations of the number of channels in Au atomic contacts by Scheer *et al.*[20] This measurement also serves as a calibration for our noise setup.

In this analysis, we need to fit the transmission probability of the channel iteratively which is cumbersome. Figure(3.12) shows the analysis based on equa-

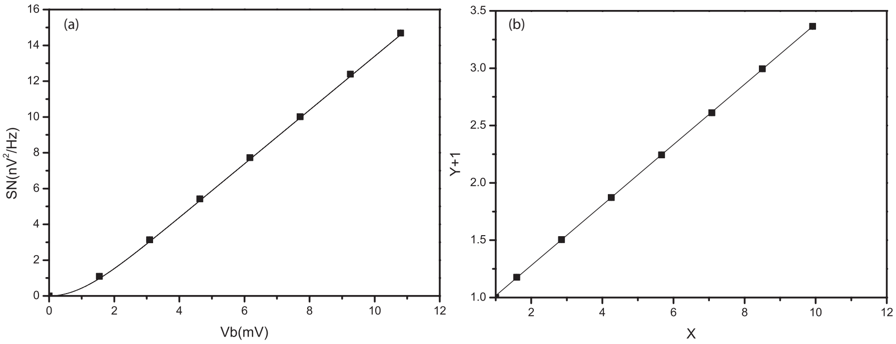

FIGURE 3.12: Reduced axis shot noise analysis. The experimental data points are plotted in the reduce axis format (right panel) and the slope of the linear fit of the experimental data points gives a Fano factor of 0.271 ± 0.02. The error here is standard deviation of the fit of the slope. The Fano factor obtained equals the expected value for a single channel Landauer conductor, $F = 1 - G$, to within the experimental error of 1% in the conductance measurement. Using this Fano factor, the noise values in the standard plot (left panel) are shown to be well-described by the Lesovik-Levitov expression(equation(1.28)).

tion (1.29). The experimental noise values are plotted using the reduced axis plot, where $Y = \frac{S(V)}{S(0)} - 1$ and $X = \left[\frac{eV}{2k_BT}\coth\left(\frac{eV}{2k_BT}\right)\right]$. The slope of this plot immediately gives the Fano factor, $F = 0.271 \pm 0.02$, which is close to value of 0.275 obtained by above technique[5]. The Fano factor calculated from the reduced axis plot is used to produce the curve from the Lesovik-Levitov expression (equation(1.28)) which correctly describes the experimental data points. Note that we are plotting the voltage noise instead of the current noise. We follow this analysis in remainder of this thesis.

In the figure (3.11 b) we show a curve for the full shot noise, $S_I = 2eI$ (violet curve). This is the maximum noise one could see in in a Landauer conductor, and it corresponds to a Fano factor of 1. Any observation of noise above this curve, *i.e.* $F > 1$, implies the presence of positive correlations in the electron transport in the contact, which is super-Poissonian noise. Any noise below this curve, *i.e.* $F < 1$, is sub-Poissonian noise. The noise we found for our contact is at the minimum noise level for a spin degenerate Landauer conductor. The pink region below this curve is inaccessible for a spin degenerate conductor. Data points in this region would indicate the presence of the spin split channels in the conductor. The black curve is the minimum noise for the case when spin degeneracy of the transmission

---

[5] The two values agree within the experimental accuracy limit when we consider the error of 1% in the conductance.

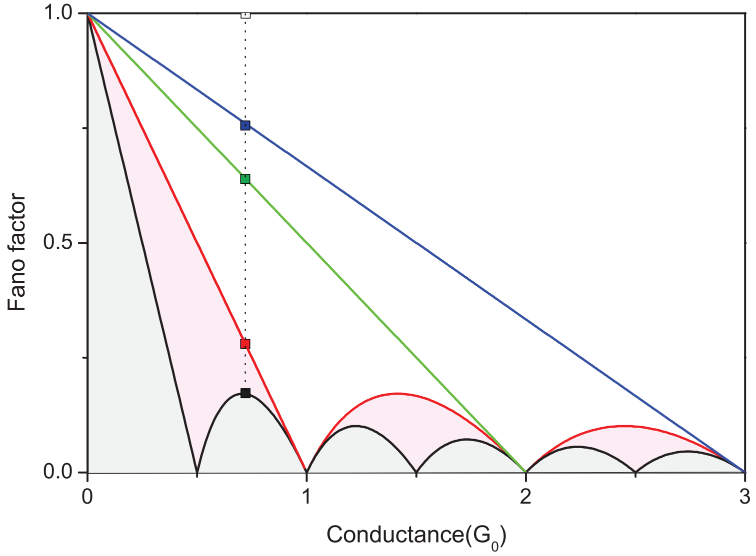

FIGURE 3.13: Fano plot for Landauer conductor. This figure is the generalized form of figure (3.11 b). The color code is kept the same. The black curve is the minimum noise level for a spin-split Landauer conductor as a function of the total conductance. The light-grey region is inaccessible to any kind of Landauer conductor. The red curve is the minimum noise for a spin-degenerate Landauer conductor. Data points in the light pink region signify the presence of the spin splitting. The green and blue lines show the maximum level of noise for two and three channels, respectively. For the reference the Fano factors discussed in figure (3.11 b) are represented as dots here. The black dot gives the point on the minimum Fano curve once spin degeneracy is lifted, ($F = 0.17$), the red dot is for the experimental Fano factor, *i.e.* $F = 0.275$, the green dot is for the presence of two equally open channels, $F = 0.638$ and the blue dot is for three equally open channels, $F = 0.758$. The white dot gives the full shot noise with the Poissonian value and $F = 1$. This plot helps in determining the number of channels in a Landauer conductor. Any solution above the green line requires more than 2 channels and cannot be uniquely determined.

channels is lifted. The light grey region is inaccessible for any kind of Landauer conductor.

This concept can be generalized to all conductance values. Figure (3.13) shows this generalized concept. Here, the Fano factor in different limiting cases is plotted with respect to the conductance value. The black curve is the minimum Fano factor for a conductor with spin-split channels. The grey shaded region is inaccessible for any kind of conductor. The red curve is the minimum noise level for a spin-degenerate conductor. The green line is the maximum noise for a two-channel Landauer conductor (four spin channels). Any conductor having a Fano factor lying above this green line signifies the presence of at least three channels taking part in the conduction. The blue line is the maximum noise for three channels taking part in the conduction (six spin channels). The presence of any data point between the red curve and the green line implies the presence of at least two channels in the conductor and presence of a data point between the green and the blue line shows the presence of at least three channels taking part in the conduction.

These are the solutions for a Landauer conductor imposed by the relations $F = \sum_{i=1}^{N} \tau_i (1 - \tau_i) / \sum_{i=1}^{N} \tau_i$, $G = \sum_{i=1}^{N} \tau_i$ and $\tau_i \in [0, 1]$. Any data points above the red curve does not have a unique solution. When assuming the numbers of channels are limited to 2 or 3, information that may be derived from calculations, more restricted solutions may be obtained. Hence, in this thesis we focus on our finding at low Fano factors.

REFERENCES

[1] R. J.M.Krans and C.J.Muller and I.K. Yanson, Th.C.M. Govaert and J. Ruitenbeek, *One atom point contacts*, Physical Review B **48**, 14721 (1993).

[2] J. Moreland and J. W. Ekin and L. F. Goodrich and T. E. Capobianco and A. F. Clark, *Break-junction tunneling measurements of the high-T c superconductor*, Physical review Rapid Communications **35**, 8856 (1987).

[3] A. I. Yanson, Ph.D. thesis, Universitiet Leiden (2001).

[4] C. Untiedt, a. Yanson, R. Grande, G. Rubio-Bollinger, N. Agraït, S. Vieira, and J. van Ruitenbeek, *Calibration of the length of a chain of single gold atoms*, Physical Review B **66**, 1 (2002).

[5] J. M. van Ruitenbeek, A. Alvarez, I. Pineyro, C. Grahmann, P. Joyez, M. H. Devoret, D. Esteve, and C. Urbina, *Adjustable nanofabricated atomic size contacts*, Review of Scientific Instruments **67**, 108 (1996).

[6] C. A. Martin, D. Ding, H. S. J. van der Zant, and J. M. van Ruitenbeek, *Lithographic mechanical break junctions for single-molecule measurements in vacuum: possibilities and limitations*, New Journal of Physics **10**, 065008 (2008).

[7] I. K. Yanson, O. I. Shklyarevskii, J. M. van Ruitenbeek, and S. Speller, *Aluminum nanowires: Influence of work hardening on conductance histograms*, Phys. Rev. B **77**, 033411 (2008).

[8] H. Walter, Tech. Rep., Rigaku Vacuum Products USA (2002).

[9] D. A. Wharam, T. J. Thornton, R. Newbury, M. Pepper, H. Ahmed, J. E. F. Frost, D. G. Hasko, D. C. Peacock, D. A. Ritchie, and G. A. C. Jones, *One-dimensional transport and the quantisation of the ballistic resistance*, Journal of Physics C: Solid State Physics **21**, L209 (1988).

[10] B. J. van Wees, L. P. Kouwenhoven, H. van Houten, C. W. J. Beenakker, J. E. Mooij, C. T. Foxon, and J. J. Harris, *Quantized conductance of magnetoelectric subbands in ballistic point contacts*, Physical Review Letters **38**, 3625 (1988).

[11] A. I. Yanson, G. R. Bollinger, H. E. van den Brom, N. Agrait, and J. M. van Ruitenbeek, *Formation and manipulation of a metallic wire of single gold atoms*, Nature **395**, 783 (1998).

[12] H. van den Brom and J. van Ruitenbeek, *Quantum Suppression of Shot Noise in Atom-Size Metallic Contacts*, Physical Review Letters **82**, 1526 (1999).

[13] C. Muller, J. van Ruitenbeek, and L. de Jongh, *Experimental observation of the transition from weak link to tunnel junction*, Physica C: Superconductivity **191**, 485 (1992).

[14] J. Lambe and R. C. Jaklevic, *Molecular Vibration Spectra by Inelastic Electron Tunneling*, Phys. Rev. **165**, 821 (1968).

[15] I. K. Yanson, *Non Linear effects in electric-conductivity of point junctions and electron-phonon interaction in normal metals,* Sov. Phys. JETP **39,**, 1974 (1974).

[16] S. R. I. Kulik I. O., Moskalets M V and Y. I. K, *Spectroscopy of Electron-Phonon Interaction in Point Contacts with a Barrier Layer,* JETP Lett. **50**, 1989 (49).

[17] A. G. M. Jansen, F. M. Mueller, and P. Wyder, *Normal Metallic Point Contacts*, Science **199**, 1037 (1978).

[18] B. Ludoph and J. M. v. Ruitenbeek, *Conductance fluctuations as a tool for investigating the quantum modes in atomic-size metallic contacts*, Phys. Rev. B **61**, 2273 (2000).

[19] Helko Elbert van den Brom, Doctoral thesis, Leiden university, Leiden (2000).

[20] Elke Scheer and N Agräit and J C Cuevas and A Levy Yeyati and B Ludoph and Martin-Rodero Alvaro and G R Bollinger and J van Ruitenbeek and U Cristian, *The signature of chemical valence in the electrical conduction through a single-atom contact*, Nature **394**, 154 (1998).

4

DETECTION OF VIBRATION MODE SCATTERING IN ELECTRONIC SHOT NOISE

Manohar KUMAR, Remi AVRILLER, Alfredo Levy YEYATI, Jan van RUITENBEEK

Generally, current shot noise is measured at low bias currents, and it reflects the transmission probability of the electrons. Here we present the first measurement at bias currents above the phonon energy of the system, i.c. a chain of Au atoms. The onset of phonon emission processes is signaled by an abrupt jump in differential conductance. One should expect a sign of this change to be visible in shot noise. Indeed, a distinct signature in the current shot noise signal is observed due to inelastic scattering as a linear deviation from the Levitov- Lesovik classical shot noise. In accordance to recent theoretical predictions the sign of the inelastic signal, i.e., the signal due to vibration excitations depends on the transmission probability, becoming negative below a certain transmission value. We argue that the negative contribution to noise arises from coherent two-electron processes mediated by electron-phonon scattering and the Pauli exclusion principle.

Parts of this chapter have been published in Physical Review Letters **108**, 146602 (2012).

4.1 INELASTIC NOISE SPECTROSCOPY

THE inelastic interaction of electrons with vibrons leads to abrupt changes in the conductance. This effect has been studied extensively[1–6]. This technique is widely used in transport spectroscopies, *i.e.* point contact spectroscopy (PCS) and inelastic electron tunneling spectroscopy (IETS). Transport spectroscopy has been used to identify the nature of the species in the point contact[7–12]. Shot noise, as the second cumulant of the current, is another fundamental quantity of quantum transport. Together with conductance spectroscopy noise spectroscopy can help to characterize in detail atomic and molecular junctions. It can provide valuable insights in the fundamental nature of the processes taking place in quantum transport. An elusive property in molecular electronics is the lattice temperature of the molecule in the contact, for which shot noise may provide quantitative information. Shot noise S for a single channel conductor is proportional to $\tau(1-\tau)$, where τ is the transmission probability of the channel. This noise should also show the signature of the inelastic electron-phonon interactions. Recently Refs. [13–15] have predicted the presence of an inelastic shot noise signature of electron-phonon interaction in their studies on a simple model of a molecular junction having single resonant level, symmetrically couple to both leads, and for weakly interacting conduction electrons with a single phonon mode. In case of a small decay rate of the vibration modes into phonon modes of the leads a non-equilibrium vibron occupation is expected[14, 16–19]. The fluctuations in the non-equilibrium vibronically excited state affects the dynamics of the traversing electrons. Hence the measurement of this non-equilibrium vibronic population in noise measurement could reveal the lattice temperature of the quantum device. Au atomic chains, forming a simple test bed for the inelastic scattering in conductance, have been used here as a first test system for inelastic scattering effects in noise spectroscopy. We have looked into, both, equilibrated and non-equilibrated vibronic interactions on the conduction electrons in Au atomic chains.

4.2 AU ATOMIC CONTACT FORMATION

GOLD atomic chains were formed at liquid helium temperatures using mechanically controllable break junctions (MCBJ). This technique permits freshly exposing clean Au metal electrodes, which are then pressed gently together such as to form a cold weld of atomic size. This contact can be repeatedly made and broken such that the contact changes its cross section atom-by-atom. In the last stages of breaking Au contacts the atoms have been found to spontaneously arrange into a linear strand of up to 8 atoms in length. At the start of the experiments the sample chamber is pumped to $\sim 10^{-5}$mbar before cooling down in liquid helium. The chamber is fitted with active charcoal for cryogenic pumping such that the pressure in the chamber drops below measurable values when reaching the base temperature, which is between 5 and 8K. Once cold and under vacuum the Au sample wire is first broken by mechanical bending of the substrate. By relaxing the bending the broken wire ends can be rejoined and the contact can be adjusted with sub-atomic precision by means of a piezo-electric actuator[20].

4.2.1 DC CHARACTERIZATION

A first step in characterizing the quality of the junction is taken by recording conductance histograms. Contacts are repeatedly made and broken, controlled by the piezo voltage that regulates the substrate bending of the mechanically controllable break junction device. While gently breaking the Au atomic contacts the conductance of the junction decreases in steps due to the atom-by-atom reduction in contact size. The points of the digitized traces of conductance are collected into a histogram and the counts are plotted as a function of the conductance. Conductance histograms such as shown in figure(4.1 a) are obtained by combining typically 2000 conductance breaking traces. The first peak at 1G$_0$ represents the average conductance of a contact of a single Au atom in cross section, which has a lot of weight because of the long atomic chains being formed. This can be seen from the traces shown in the inset of figure(4.1 a) having long plateaus at 1G$_0$. On these plateaus the conductance is changing very little while the contact is being stretched. This is explained by the formation of the long atomic chains and, upon further stretching the contact, the chains finally break to form clean vacuum tunnel junctions, shown by the diminishing counts at lower conductance in the conductance histogram.

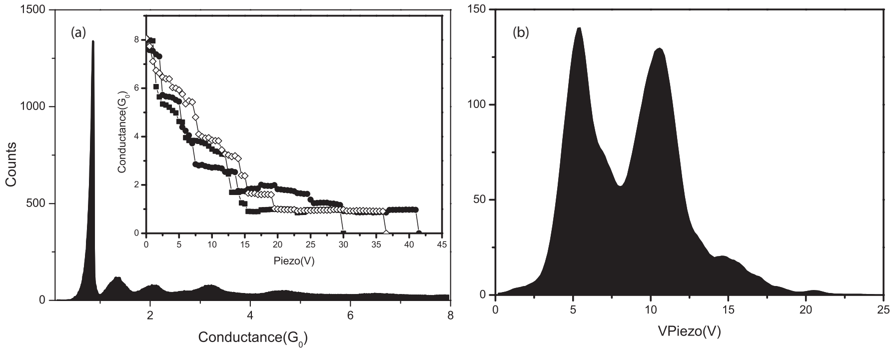

FIGURE 4.1: The dc characterization of Au atomic contacts: (a) A conductance histogram recorded for 2000 conductance traces. Typical conductance traces are shown in the inset. (b) A length histogram recorded for the same conductance traces. The two prominent peaks show the presence of 2 and 3 atom long atomic chains forming predominantly. The inter-peak distance gives the calibration factor of 1.96V/Å

In the conductance breaking traces a last conductance plateau near $1G_0$ signals the formation of a junction of only a single atom in cross section. The value of the length of this plateau for several hundreds of breaking cycles is collected into a length histogram, see figure(4.1 b). The histogram is obtained by combining 2000 traces and recording the length of the conductance plateaux with conductances between 0.8 and $1.1G_0$, i.e. in the range of the first conductance peak in figure(4.1). The length axis is given in units of the voltage on the piezo element, where the proportionality constant is 1.96 V/Å. The histogram is consistent with the earlier work of Untiedt *et al.* [21]. This length histogram shows several peaks with a separation consistent with the inter-atomic distance in a chain of Au atoms. The first four peaks can be interpreted as the lengths corresponding to chains of 2, 3, 4 and 5 atoms. Still longer chains have diminished counts and hence are not always visible in the length histogram.

4.2.2 AC CHARACTERIZATION

The ac characterization of Au atomic contacts has been done using lockin measurements. A small amplitude modulation sine signal of 2mV amplitude and 2.3kHz frequency is used for these lockin measurements. The electrical circuit used for the lockin measurement is shown in figure (3.5). Point contact spectroscopy signals for a perfectly transmitting conductor are expected to show a step down feature in the conductance at the vibration mode energy. This is a known concept and has been briefly described in section (3.4.2). In a ballistic conductor, due to electron-phonon interaction, electrons lose energy by emitting a phonon of energy $\hbar\omega_{k_F}$, and in the process are get scattered backwards. This backscattering of the traversing electrons is seen as a decrease in the conductance at the finite voltage $V_{ph} = \hbar\omega_{k_F}$ [22]. For perfectly transmitting atomic contacts one expects a similar phenomenon to be seen in their differential conductance measurements. Having a single *s* valence orbital and a conductance around $1G_0$ Au atomic chains show a nearly perfect transmission. The differential conductance measurement of figure (4.2) for such a contact indeed shows a step-down feature. The scattering on the vibration mode is seen typically as a drop of about 1% in the conductance [23]. The point of extremum in the second derivative of the current gives a measure of the value of this vibronic energy and its amplitudes gives the electron-vibron interaction strength. Although Au atomic chains permit many vibration modes only the longitudinal mode with the largest moment has a significant cross section for inelastic electron scattering [1, 24]. The longitudinal character of the mode of the vibronic signal can be confirmed by looking at figure (4.3). Here, we have measured the differential conductance for various stages of stretching of the contact. The second derivative of the current clearly shows a decrease in the vibronic energy and an increase in the electron-vibron interaction strength. This is in accor-

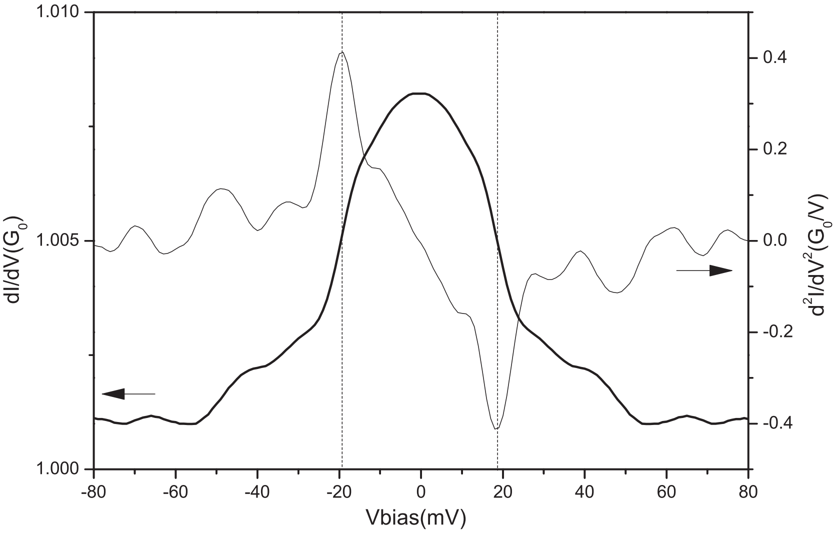

FIGURE 4.2: The ac characterization of Au atomic contacts: The differential conductance of a Au atomic contact (bold curve, left scale) shows a step-down feature at both polarities of the voltage bias. The second derivative of the current (light curve, right scale) shows a dip and a peak at at these positions, at ±19meV at positive and negative bias voltage. The positions of these extrema correspond to the vibron energy in the Au atomic contact.

dance with the longitudinal nature and is due to the softening of the interatomic bond strength upon stretching of the contact. The finite size of the chain, its mechanical coupling to the leads and the finite temperature, lead to broadening of the step feature in the contact. Upon stretching of the contact the corrugation of the potential seen by the electrons increases which leads to a much sharper change in the conductance at the vibronic energy [5].

These features are more pronounced in longer chains as compared to shorter chains. For longer chains the effective change in the vibronic energy with stretching is much larger than for shorter chains. In shorter chains the strong mechanical coupling of the chain with the leads give rise to a strong broadening of the vibration resonance due to fast decay into bulk phonons, which smears out the inelastic signature in the differential conductance. It is also possible to have more than one vibrational mode coupling to the traversing electrons [24]. In our experiment we focus on the longitudinal mode coupled to the electrons in the chain. Hence, for our experimental studies we have pulled Au atomic chains of 3 atoms or longer, and done all point contact spectroscopy and noise spectroscopy on these.

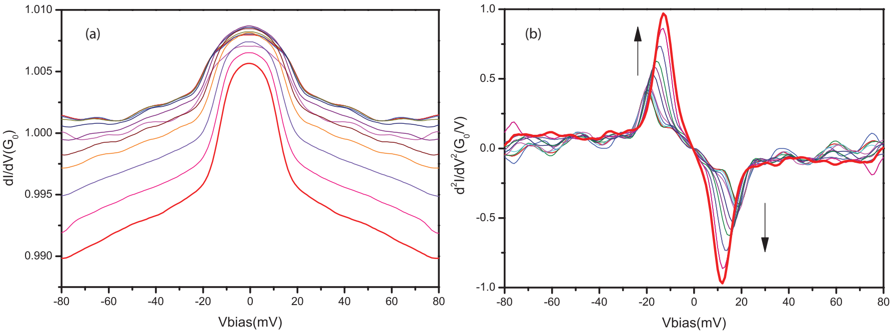

FIGURE 4.3: Stretching dependence of the inelastic electron-vibron interaction energy in Au atomic contacts: (a) Differential conductance measurement on a 4 atom long Au atomic chain at various stages of stretching, in steps of 0.2Å. The green curve shows the starting atomic contact configuration and the red curve shows the final contact, just before breaking. (b) The second derivative of the current shows the evolution of the vibronic energy upon stretching of the contact.The effective rate of change in the vibronic energy is 1.9meV/Å. the color code is the same as that for the differential conductance.

4.3 SHOT NOISE SPECTROSCOPY

THE shot noise studies on the Au atomic contacts are done using a low frequency cross-spectrum analysis technique. The detailed measurement scheme and circuit diagram is shown in figure (3.8). The noise spectra were recorded in a window from 250Hz to 100kHz. An example of such spectra is given in figure (4.4 a). At the low-frequency end of the spectrum one observes an increase in the spectrum above the white noise level due to a $1/f$-like noise contribution, the amplitude of which varies between different junction settings, which has been attributed to defect fluctuations in the leads. This part of the spectrum is ignored for the analysis, but it influences the accuracy of the determination of the white noise power. At the high-frequency end of the spectrum a roll-off is seen, with a characteristic frequency of about 30kHz that is due to the RC time constant of the stray capacitance of the leads in combination with the junction resistance. First, the thermal noise is recorded at zero bias, and after recording noise at several bias settings the zero bias noise is recorded once more (labeled as $0V_r$). The thermal noise level corresponds to a temperature of 6.3K, which agrees within the accuracy of the temperature measurement with a reading of 6.1K, as obtained from a Ruthenium Oxide 10kΩ resistance thermometer. After correction for the roll-off with a single RC time constant the spectra become white above 10kHz, figure (4.4 b). The thermal noise (at zero bias) is subtracted, which explains the negative values in the data fluctuations for the lowest currents. The data points are projected in the form of a histogram, shown at the right, and the level of white noise is obtained from the

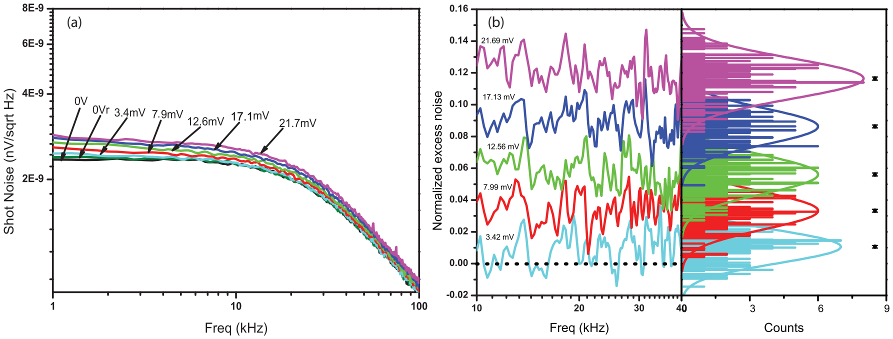

FIGURE 4.4: The raw noise data for a Au atomic contact and its analysis: (a) Noise spectra for a Au atomic chain of ~ 3 atoms in length having a conductance $G = 0.987\mathrm{G}_0$ at a temperature of $T = 7.95$ K. The roll off in the spectra is seen at 32.5kHz (b) Noise after subtracting the thermal noise and correcting for the RC roll off.

center of the histogram for each voltage bias. The points and error bars at the right indicate the position and accuracy of the noise as determined from a Gaussian fit to the histograms. The mean noise value is plotted in reduced axis format to obtain the Fano factor, as shown in figure (4.5) (for an explanation of this procedure see section 3.5.3). The Fano factor calculated from the reduced axis plot for this contact is $F = 0.135 \pm 0.004$.

We recorded noise for over 450 atomic configurations formed using 5 different Au wire MCBJ devices. For each configuration we recorded 25 bias voltage settings in steps of about 1mV. We discarded those data for which the scatter in the reduced-axis plot is larger than 3% and those for which the measured thermal noise at the end of the measurement series differs by more than 2% of the starting value. The scatter is mostly due to contributions of $1/f$ -noise interfering with the white spectrum. Changes in thermal noise may result from changes in the resistance of the contact. Figure (4.6) shows the results for the Fano factor for many such atomic chains as measured for bias voltages below 10mV, and plotted against the conductance as done for instance by Kumar *et al.* [25]. Most atomic chain junctions have a conductance slightly below $1\mathrm{G}_0$, but somewhat smaller values frequently occur because of scattering on defects in the leads [26]. All data in figure (4.6) fall close to the black solid line, which is the expected dependence for a single conductance channel, as given by equations (1.28) and (1.27). This clearly shows that Au atomic chains agree with a model of single-channel Landauer conductors.

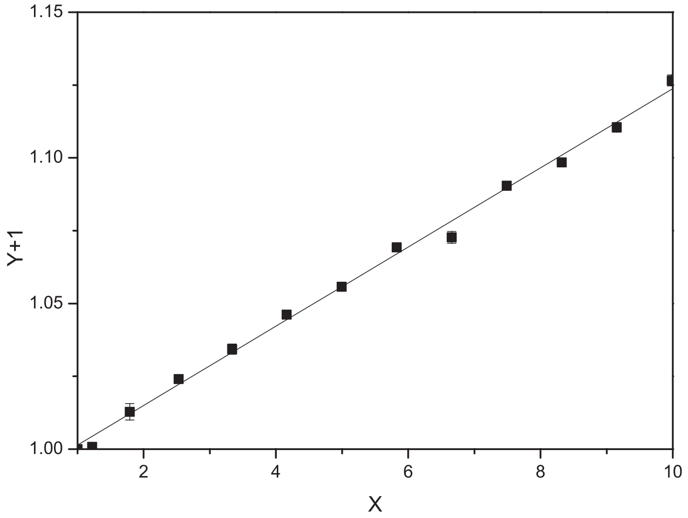

FIGURE 4.5: Determination of the Fano factor from shot noise measured on an Au atomic contact: The mean noise value as obtained from figure (4.4 b) represented in a reduced axis plot. From the slope of this reduced axis plot we obtain a Fano factor of $F = 0.135 \pm 0.004$.

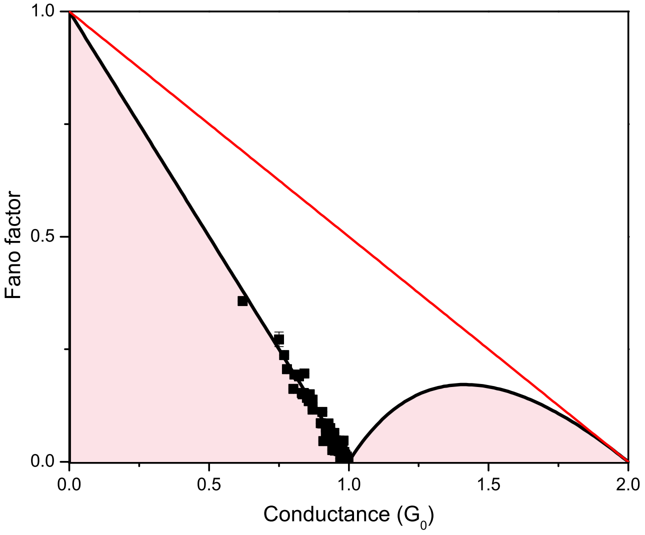

FIGURE 4.6: Fano factor plot for Au atomic contacts: Noise measurements on over 450 atomic configurations formed using 5 different Au wire MCBJ devices. Here we are showing the Fano factor obtained on all these contacts[1]. The Fano factors for all atomic contacts lie on the line $F = 1 - \tau$, *i.e.* on the theoretical limit of minimum Fano factor that is attained only for a single spin-degenerate Landauer conductor.

4.4 INELASTIC VIBRONIC SCATTERING IN NOISE

The inelastic scattering on vibron modes is seen as a drop of about 1% in the conductance measurements. For Au chains these vibration modes can attain values between about 10mV and 20mV, which varies due to the softening of the bonds with the applied strain in the atomic wire [24], as was discussed in section (4.2.2). For such systems inelastic scattering should also affect shot noise. Most noise measurements on atomic and molecular conductors have been focused on the low bias regime. Here we will look into the noise above the vibronic energy of the Au atomic chain. Figure (4.7a) shows the differential conductance and noise measurement for a Au atomic chain of 4 atoms long. The differential conductance shows the step down feature at the vibronic energy as expected. The second derivative shows a peak and dip feature at about 20mV in both negative and positive bias regime, giving the vibronic energy of the atomic chain. Figure (4.7b) shows the noise power *w.r.t.* the bias voltage upto 28mV. The small curvature at low bias voltage below 3mV is due to the crossover from thermal noise to non-equilibrium noise. Above 3mV the noise power closely follows the expected linear dependence. The red curve is a fit to equation(1.28) and gives a Fano factor $F_1 = 0.020 \pm 0.002$, which agrees with the zero bias conductance $G = 0.98\mathrm{G}_0$ for a single conductance channel, within the accuracy of 1% in G [27]. Above 20mV we observe a sudden kink in the noise signal, which matches the energy of the vibration mode seen in figure (4.7a). If we take the slope above the kink

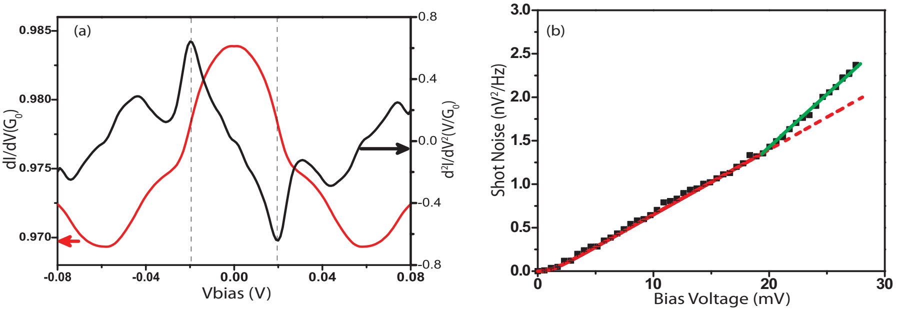

FIGURE 4.7: Inelastic scattering in conductance and noise in a Au atomic contact: The differential conductance (left axis) measurement and its derivative (right axis) on a 4 atom long Au atomic chain. The second derivative was computed numerically. The peak at 20.0 ± 0.4mV signals the onset of scattering by a vibration-mode. (b) Shot noise as a function of bias for the same atomic contact as in (a). The red curve is a fit to the equation(1.28) upto 20mV. The Fano factor $F_1 = 0.020 \pm 0.002$ agrees with the conductance of $G = 0.98\mathrm{G}_0$ in (a). The broken red curve is an extrapolation of the fit. The green line is linear fit for the data above 20mV.

to define a modified Fano factor F_2 the relative change in Fano factor is given as $\delta F/F = (F_2 - F_1)/F_1 = \pm 0.90$. We interpret this kink as evidence of an inelastic scattering contribution to shot noise. This interpretation was further tested, and the results are shown in figure (4.8).

Figure (4.8) shows data for seven different chain configurations, plotted as $Y(V)$ vs. $X(V)$. For G close to 1 G_0 (lowest curves) we find a positive correction above the kink. Note the curve with $G = 1.00 G_0$, which shows zero noise ($F = 0$) until a kink appears when reaching the vibration mode energy. Remarkably, for $G < 0.95 G_0$ the correction above the kink has the opposite sign. The observed dependence is linear in $X(V)$, above and below the kinks, within the experimental accuracy. In some cases we observe a second kink at still higher bias voltages (not shown here), but for the moment we limit attention to the first kink only.

Figure (4.9) shows the position of the steps in the differential conductance against the observed position of the kink in the reduced-axis plot. The kink position in the shot noise is obtained by extrapolating the linear deviation in shot noise due to inelastic scattering and the fit to the equation(1.28). The intersection of these two extrapolated lines gives the position of kink in the shot noise. The derivative of the symmetrized differential conductance curve gives the vibron energy of the Au atomic contact. The difference between the position of the vibron energy in the differential conductance and its symmetric part is incorporated in the error analysis of the vibron energy.[2] The uncertainty and the scatter in the mode energy are due to the difficulty of removing the contributions by conductance fluctuations from the differential conductance. Despite the large uncertainties, a clear trend is observed and the data lie close to the line 1:1. This observation provides strong support for the interpretation of the kink in the noise data as being due to inelastic scattering on vibration modes of the system.

The relative change in the Fano factor for a set of about 120 measurements is shown in figure (4.10), plotted as a function of the transmission probability τ. For τ close to 1 exclusively positive values for $\delta F/F$ are found, while for $\tau < 0.95$ only negative values occur, confirming the trend observed in figure (4.8).

While the effect of inelastic scattering on vibration modes in atomic-size systems has been extensively analyzed theoretically [4, 23, 28, 29] the generalization of these studies to noise properties has only recently started [13–15]. Most of these studies are based on a minimal model corresponding to a single resonant molecular level E_d coupled to the left and right leads by tunneling rates, Γ_L and Γ_R, interacting with a localized vibration mode with frequency ω_0 and a coupling parameter λ. This model, schematically depicted in the inset of figure (4.10), is adequate

---

[2] Asymmetric coupling in the atomic chain with the leads could also give rise to asymmetry in the differential conductance.

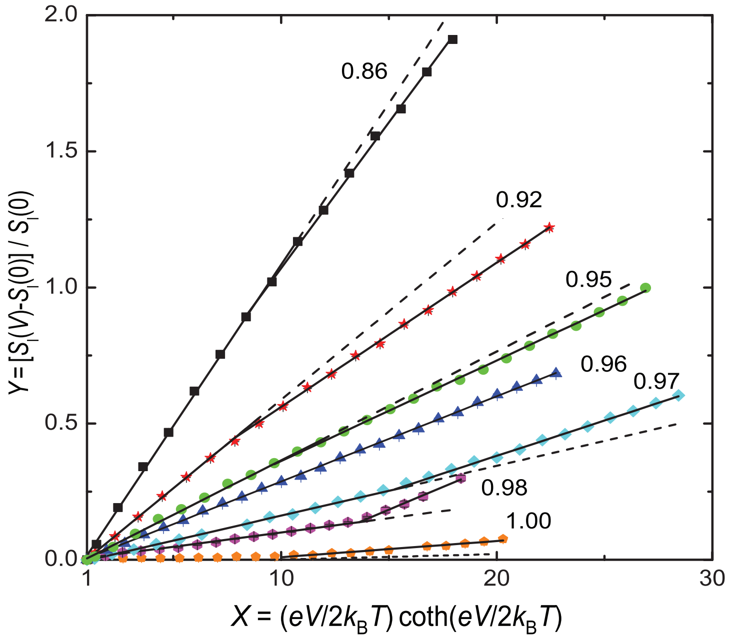

FIGURE 4.8: Kink in shot noise for a range of transmission values of Au atomic chain: In this reduced axis plot the data below the vibron energy are described by a linear dependence (fitted with a solid line up to the kink, and extrapolated by a dashed line). The slope of this line gives the Fano factor. The transmission probability obtained from the conductance is shown as a label to each curve. Above the phonon energy a new linear dependence is observed. The kink is towards higher slope when the transmission probability τ is close to 1. For τ below 0.94 we observe a reduced slope.

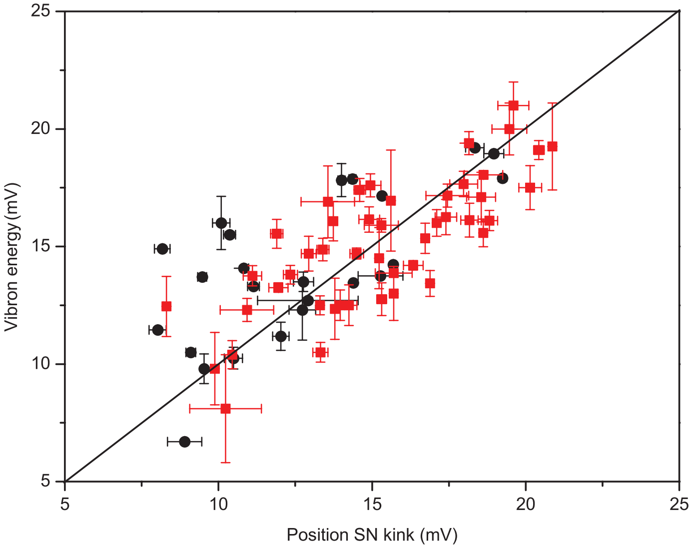

FIGURE 4.9: Correlation between the position of the kink in shot noise and the vibron energy measured using second derivatives of the current: The phonon energy as observed in the differential conductance plotted as a function of the position of kink in the shot noise. The line shows the expected 1:1 relation. Red and black points are for positive and negative kinks, respectively.

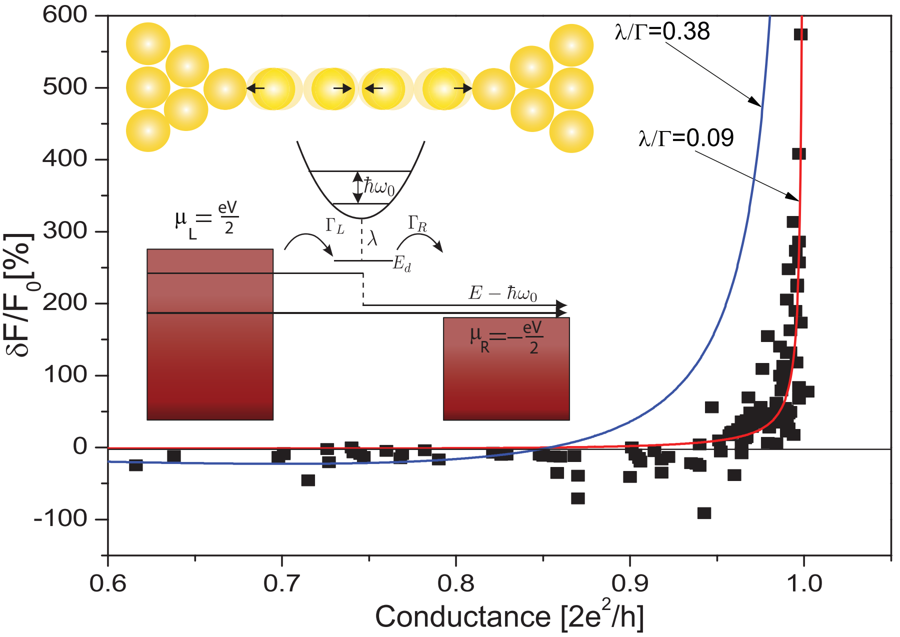

FIGURE 4.10: Distribution of the observed change in the Fano factor at the kink, plotted as a function of the conductance. The points are obtained for different realizations of Au atomic chains. For conductance (*i.e.* transmission $\sim \tau$) close to 1 we find exclusively positive values for $\delta F/F$. Below a cross over regime near $G = 0.95G_0$ only negative values are observed. The curves are obtained from the theory of [13–15], for fixed values of the inelastic scattering strength λ. Inset: The top part illustrates the atomic chain configuration and the vibration mode involved in the scattering. The lower part sketches an example of a two-electron process giving rise to reduction of the Fano factor: two electrons injected from the left lead at different energies tend to compete for the same outgoing state after the emission of a phonon (see section (A.2.2) for further explanation)

for representing a nanosize junction in the regime $\Gamma_{L,R} \gg \omega_0$.

The effect of the phonon mode in the electronic noise properties has been analyzed up to second-order in λ, which is reasonable when the step in the conductance due to inelastic scattering is at most a few percent, see figure (4.7). When the energy dependence of the transmission can be neglected, $\tau(E) \simeq \tau(0)$, the analysis simplifies, and for the zero temperature and positive voltages, the inelastic correction to the noise becomes [13].

$$\delta S_I \simeq \frac{e^2}{h}\left(\frac{\lambda}{\Gamma}\right)^2 \tau^2 \left\{2(1-\tau)(1-2\tau)eV + (8\tau^2 - 8\tau + 1)(eV - \hbar\omega_0)\theta(eV - \hbar\omega_0)\right\} \quad (4.1)$$

where the transmission probability at the Fermi energy is given by $\tau = 4\Gamma_L\Gamma_R/(E_d^2+\Gamma^2)$ with $\Gamma = \Gamma_L + \Gamma_R$. This expression clearly predicts a crossover from a positive to a negative correction in the noise as the transmission is reduced from the unitary limit. A positive correction due to inelastic scattering giving additional shot noise, such as observed for τ close to 1, is quite intuitive. However, a negative correction such as observed for lower transmission values cannot be understood in simple terms. Eq.(4.1) indicates that the crossover from positive to negative correction is predicted at $\tau_\pm = 1/2 \pm 1/2\sqrt{2}$. The higher crossover point, relevant for the present data set, is $\tau_+ \simeq 0.854$. The microscopic processes contributing to inelastic noise in Eq.(4.1) can be classified into one-electron and two-electron processes, i.e. $\delta S^{(in)} = \delta S_{1e}^{(in)} + \delta S_{2e}^{(in)}$ (see section(A.2.2)). While $\delta S_{1e}^{(in)}$ scales as τ^2 and is thus always positive, the two electron contribution $\delta S_{2e}^{(in)}$ scales as $\{-8\tau^3(1-\tau)\}$ and thus it is always negative[13]. This behavior can be qualitatively understood as arising from the Pauli principle as illustrated by the diagram in the inset of figure (4.10). In this diagram two electrons are injected from the left lead with energies E and $E - \hbar\omega_0$ within the interval $(-V/2, +V/2)$. If the higher energy electron emits a phonon it would tend to occupy the same outgoing state as the other electron. This process would thus be blocked at perfect transmission. Additionally, this process tends to reduce the noise by narrowing the energy distribution of the outgoing electrons. The solid curves in figure (4.10) show the calculated dependence of $\delta F/F$ as a function of τ for two fixed choices of electron-vibron scattering strength λ. The variation of the data can be largely attributed to variations in λ for different chain configurations. There appears to be a trend of λ growing when τ decreases below 1. The crossover in the data to negative values for δF appears at higher τ than expected. The fluctuations in the background of the differential conductance indicate that our assumption of an energy independent transmission may need to be relaxed. Such energy dependence modifies the theory for inelastic scattering but may also affect the linearity of the Fano plots directly, i.e. the usual elastic component of the noise. We have used the measured differential conductance curves to estimate the size of this energy dependence, and have calculated the bias dependence of the noise numerically. Figure (4.11) shows fits to representative data sets (see also sections (A.3.1) and (A.3.2)). It demonstrates that the curves can be correctly described with reasonable values for the parameters, and that the corrections due to the energy dependence of τ to the elastic noise are modest in these cases (see Appendix (A.2.2)).

We also looked into the symmetry of the position of kink in noise and the relative change in the Fano factor due to inelastic scattering *w.r.t.* bias voltage polarity. Figure (4.12) shows a noise measurement for both bias polarities on a Au atomic contact and a Au-O-Au molecular junction. The elastic Fano factors F_1 for positive

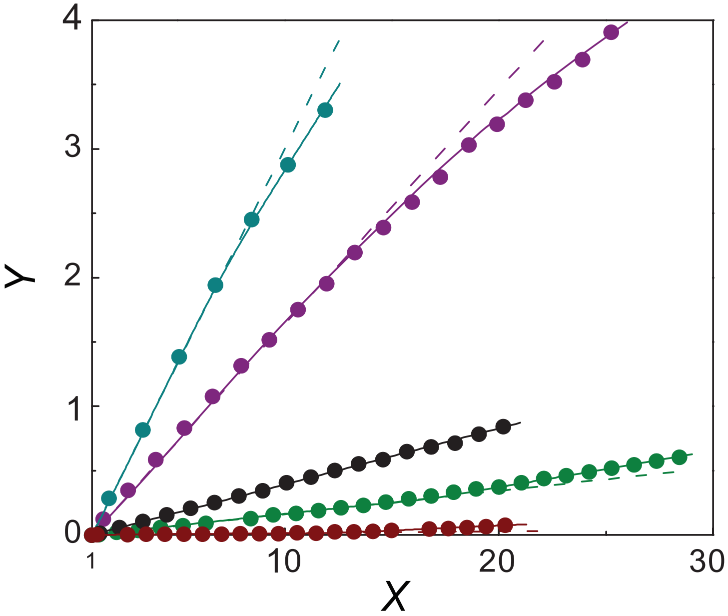

FIGURE 4.11: Theoretical fit of the shot noise data taking energy dependence into consideration: The fits of the theory include the energy dependence of the transmission as estimated from the dI/dV signals (full curve). The broken lines show the linear extrapolation of the zero-bias curve. The values for the zero-bias transmission τ and the inelastic scattering strength are (from top to bottom): $\tau = 0.669$, $\lambda = 0.35\Gamma$; $\tau = 0.818$, $\lambda = 0.20\Gamma$; $\tau = 0.956$, λ undetermined; $\tau = 0.981$, $\lambda = 0.11\Gamma$; $\tau = 0.998$, $\lambda = 0.08\Gamma$.

and negative biases are equal within the experimental error. However, the deviation in noise due to inelastic scattering is different for the positive and negative bias regimes. Also, the kink positions at positive and negative biases for both contacts are different[3]. This may be attributed to an asymmetry in the coupling factor for the atomic chain with the left lead and right lead, $\Gamma_L \neq \Gamma_R$. It is interesting to note that in case of the Au-O-Au chain the inelastic correction in noise is positive for τ as low as 0.91. For Au atomic contacts a negative correction in noise is seen for $\tau < 0.95$. We do not have enough data to identify the cross over regime for Au-O-Au, but our limited data suggests that the cross over may shift somewhat for

---

[3] The kink in noise for Au-O-Au is seen at $v_+ = 12.7$mV and $v_- = 11.76$mV. This is quite a low energy, which is to be associated with the Au-O-Au atomic chain structure. The derivative of the differential conductance of this particular contact shows extrema at 59meV and 9meV. The high energy mode is related to the presence of a light element in the chain. An example of the differential conductance and its derivative for Au-O-Au is shown in figure (**??**). The inelastic scattering in noise shown in (b) is related to a vibronic mode involving Au atoms, not just oxygen.

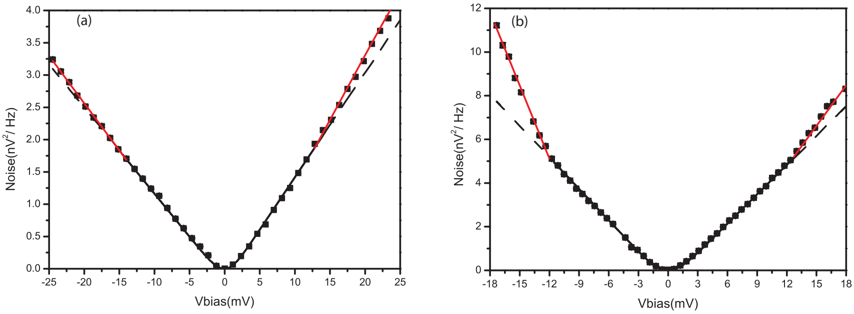

FIGURE 4.12: Inelastic noise for both bias polarities: The noise is measured in both bias polarity regime. (a) Au atomic chain with a conductance of $G = 0.94G_0$. The Fano factor was calculated using the reduced axis plot, giving Fano factors for positive bias of $F_1 = 0.044$ and $F_2 = 0.057$, and for negative bias $F_1 = 0.040$ and $F_2 = 0.043$. (b) Noise measured on a Au-O-Au atomic chain with a conductance of $G = 0.911G_0$. The Fano factors for positive bias are $F_1 = 0.091$ and $F_2 = 0.138$ and for negative bias $F_1 = 0.098$ and $F_2 = 0.25$.

various realizations of atomic chains. The few high bias measurements obtained for the Au-O-Au system are consistent with our observation of a kink in the noise at the vibron energy (see figure (4.9)). The relative change in Fano factor at positive bias and at negative biases are different in the two examples shown and this could be due to asymmetric coupling of the atomic chains to the leads contact [30]. The differential conductance curve for the Au-O-Au chain shows signatures of at least two vibrons due to gold and oxygen in the chain. It would be worthwhile to investigate the coupling of both vibronic signals to the traversing electrons using noise spectroscopy, but this must await the completion of a set-up for higher bias noise measurements.

4.5 NON-EQUILIBRIUM VIBRONIC SIGNATURES IN NOISE

THE inelastic interaction of the electrons with local vibron (vibrons localized within the chain) depends on the electron tunneling rate Γ, the vibronic energy $\hbar\omega_0$, the electron-vibron coupling strength λ, and the vibron relaxation rate η. Depending upon the interplay between these parameters different atomic contacts show different strengths of inelastic signatures in shot noise. As an example, the dependence on λ/Γ is illustrated in figure (4.10). The inelastic signals can be broadly classified in two groups: those for equilibrated vibrons with $\eta \gg \lambda^2\omega_0/\Gamma$ and those for non-equilibrated vibrons with $\eta \ll \lambda^2\omega_0/\Gamma$. The experimental results and the analysis shown above have been assumed to be in the equilibrated vibron limit. The traversing electron dissipates energy into a localized vibron mode

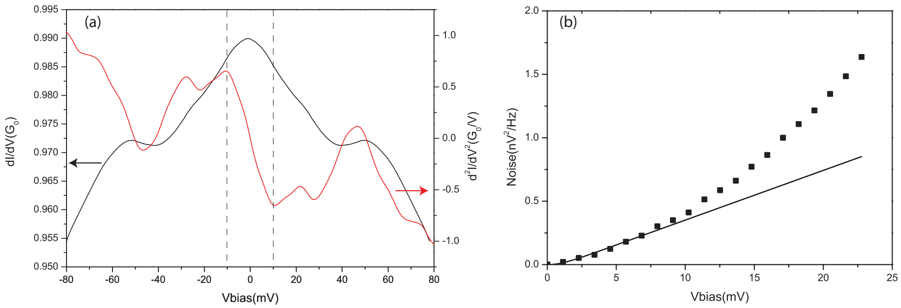

FIGURE 4.13: The non-equilibrium vibronic interaction in noise: (a) The ac conductance characterization of the atomic contact showing the differential conductance (black curve) and its derivative (red curve). The dashed line shows the position of the vibron energy *i.e.* ±10meV. (b) The inelastic shot noise spectroscopy of the Au atomic contact. The black solid line is the fit of equation(1.28). The experimental data points shows the non linear deviation above $V \geq 9.10$meV.

but due to the strong relaxation rate the localized vibron mode decays into bulk phonon modes before a new scattering event takes place. Hence, even at $V > \hbar\omega_0$, the local vibron mode is in equilibrium. In this case the interaction of the traversing electrons with the vibron states in equilibrium gives a correction to the noise (either positive or negative correction) that is linear in the voltage, as seen in figures (4.7 and 4.9).

Now let us consider the non-equilibrated case. When the relaxation rate of the local vibrational mode is low the electron-vibron interaction creates a non-equilibrium vibron population in the local vibrational states. Atomic chains are coupled well to the leads and hence local vibrational mode decays into bulk phonon modes. We tried to decouple an atomic chain by stretching the contact. Careful stretching of the contact either results in the pulling of a new atom into the contact or in stretching of the atomic bonds. With the MCBJ set up one can stretch the atomic contact with sub-Ångstrom precision using a piezo element. We formed a fresh atomic contact and performed high bias noise spectroscopy on the contact. Once the contact was showing a regular linear deviation in the noise above the vibron energy, the contact was stretched carefully to reduce its vibrational energy to 10meV, see figure (4.3). Once the differential conductance shows a clear vibron feature new inelastic noise spectroscopy on the contact was done. Figure (4.13) shows one example of the results. The differential conductance and its numerical derivative show a virbron energy at ±10meV for positive and negative bias. The shot noise measurement on the contact shows a non linear deviation above $V \sim 9$ meV. This observation is in contrast with the measurements shown in figure (4.7).

A non-linear deviation in the noise above the vibronic energy has been pre-

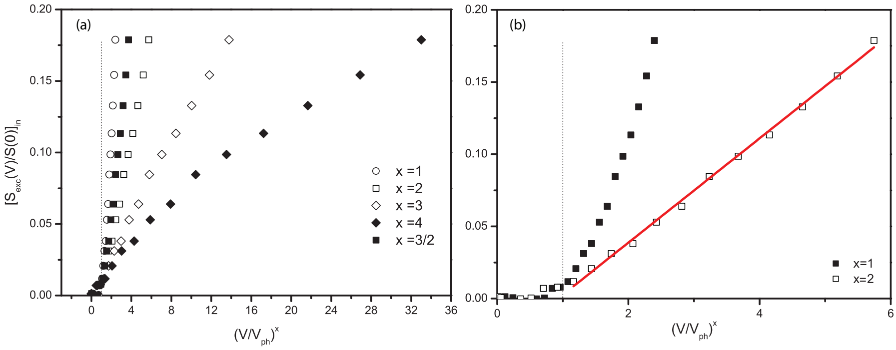

FIGURE 4.14: Evidence for non-equilibrium inelastic correction in noise: The normalized inelastic noise is plotted *w.r.t.* powers of the normalized bias voltage*i.e.*$(V/V_{ph})^x$, for $x = 1$, $x = 2$, $x = 3$, $x = 3/2$ and $x = 4$. The non-equilibrium noise shows a quadratic behavior above the vibron energy. The red line is a linear fit for the quadratic dependence.

dicted by several groups [14, 16–19]. The expected leading power varies between $V^{3/2}$[16], V^2 [14], V^3 [18], and V^4[17, 19], independent of the details of the system. We define the normalized inelastic excess noise as:

$$S_{in}(V) = (S_V(V) - S_e(V))/S(0) \tag{4.2}$$

where $S_e(V)$ is the low-bias fit to Lesovik-Levitov equation(1.28) and $S(0)$ is the thermal noise. In figure (4.14) we have plotted the inelastic noise $S_{in}(V)$ *w.r.t.* powers of normalized bias voltage *i.e.*$\left(V/V_{ph}\right)^x$ where x is the power indicated in the plot. The inelastic shot noise plot shows a good linear dependence for $x = 2$. All data sets that show non-equilibrium vibronic corrections in the noise shows powers $x = 2.0 \pm 0.1$. The experimental evidence clearly shows the feedback of the vibron fluctuations on the charge statistics of the traversing electrons. The noise increases quadratically due to this effect, which appears to agree with the predictions by Haupt and Novotny and coworkers [14]. However, the information on the actual relaxation rate of the vibron is only very indirect and it is too early to make a full comparison of the theory with the experiment.

In some of the experiments only weak non-linearities are seen above the vibron energy and sometimes slight non-linearities are seen at higher bias too. The second kink in the noise is perhaps related to the higher order of the vibron scattering process.

4.6 CONCLUSION

The inelastic interaction of the traversing electrons with the localized vibrons shows up as a jump in the differential conductance measurements. This jump in the differential conductance can be positive or negative, depending on the interplay between the opening of an inelastic channel and the availability of the final states in the lead. This gives rise the a cross over between positive and negative inelastic corrections in the conductance at $\tau = 0.5$. A related effect was predicted for noise. The noise is expected to show two cross over regimes, at $\tau_1 = 0.15$ and $\tau_2 = 0.85$, for a model system having a single conductance channel. For $0 \geq \tau \leq 0.15$ the noise should show a positive inelastic contribution, for $0.15 \geq \tau \leq 0.85$ it should show a negative inelastic contribution, and for $0.85 \geq \tau \leq 1$ again a positive inelastic contribution to the noise. Here we have investigated the cross over regime at $\tau = 0.85$. The inelastic correction to the noise is seen as a positive or a negative linear deviation from the classical Lesovik-Levitov expression, depending on the transmission probability (τ). We have proposed that the negative correction to the noise can be interpreted as a two-electron effect. The cross-over in the sign of the noise correction is seen at a slightly higher value than expected, namely at 0.95. The parameters in the model used in the theory of inelastic correction in noise are the tunneling rate Γ, the vibronic energy $\hbar\omega_0$, the electron-vibron coupling strength λ, and relaxation rate η. The cross over point does not depend on these parameters, but a shift can be found when we relax the assumption that τ is energy independent.

Due to the fast relaxation rate of vibrons in Au atomic chains the local vibron occupation is in equilibrium with the bulk phonons. This results in the linear dependence of the inelastic noise *w.r.t.* to bias voltage. In some cases where we stretched the atomic chain we have observed non-linear deviations in the noise above the vibron energy. This inelastic correction in noise shows a quadratic dependence upon normalized bias voltage (V/V_{ph}). This non-linear dependence in noise of atomic chain is quite critical to the state of stretching of chains. These effects should be more clearly pronounced in noise spectroscopy on Pt-D_2-Pt or Au-O-Au systems, where the vibrons of the molecular species are more decoupled from the bulk phonons. The non-linear dependence of the noise is due to non-equilibrium vibron fluctuations in the atomic chain. The non-equilibrium vibron produces a back action in the charge counting statistics, which could give valuable information about the phonon statistics in the molecular electronics. This can be further exploited for the determination of the lattice temperature in molecular junctions under applied bias.

REFERENCES

[1] N. Agräit, C. Untiedt, G. Rubio-Bollinger, and S. Vieira, *Onset of Energy Dissipation in Ballistic Atomic Wires*, Phys. Rev. Lett. **88**, 216803 (2002).

[2] M. J. Montgomery and T. N. Todorov, *Electron phonon interaction in atomic-scale conductors : Einstein oscillators versus full phonon modes*, Journal of Physics: Condensed Matter **15**, 8781 (2003).

[3] J. K. Viljas, J. C. Cuevas, F. Pauly, and M. Häfner, *Electron-vibration interaction in transport through atomic gold wires*, Phys. Rev. B **72**, 245415 (2005).

[4] L. de la Vega, a. Martín-Rodero, N. Agraït, and a. Yeyati, *Universal features of electron-phonon interactions in atomic wires*, Physical Review B **73**, 1 (2006).

[5] T. Frederiksen, M. Paulsson, M. Brandbyge, and A.-P. Jauho, *Inelastic transport theory from first principles: Methodology and application to nanoscale devices*, Phys. Rev. B **75**, 205413 (2007).

[6] S. Monturet and N. Lorente, *Inelastic effects in electron transport studied with wave packet propagation*, Phys. Rev. B **78**, 035445 (2008).

[7] T. Frederiksen, M. Paulsson, and M. Brandbyge, *Inelastic fingerprints of hydrogen contamination in atomic gold wire systems*, Journal of Physics: Conference Series **61**, 312 (2007).

[8] O. Tal, M. Krieger, B. Leerink, and J. M. van Ruitenbeek, *Electron-Vibration Interaction in Single-Molecule Junctions: From Contact to Tunneling Regimes*, Phys. Rev. Lett. **100**, 196804 (2008).

[9] M. Kiguchi, O. Tal, S. Wohlthat, F. Pauly, M. Krieger, D. Djukic, J. C. Cuevas, and J. M. van Ruitenbeek, *Highly Conductive Molecular Junctions Based on Direct Binding of Benzene to Platinum Electrodes*, Phys. Rev. Lett. **101**, 046801 (2008).

[10] O. Tal, M. Kiguchi, W. Thijssen, D. Djukic, C. Untiedt, R. Smit, and J. van Ruitenbeek, *Molecular signature of highly conductive metal-molecule-metal junctions*, Physical Review B **80**, 0854271 (2009).

[11] M. Taniguchi, M. Tsutsui, K. Yokota, and T. Kawai, *Inelastic electron tunneling spectroscopy of single-molecule junctions using a mechanically controllable break junction*, Nanotechnology **20**, 434008 (2009).

[12] M. Tsutsui, M. Taniguchi, and T. Kawai, *Single-molecule identification via electric current noise*, Nature communications **1**, 138 (2010).

[13] R. Avriller and A. L. Yeyati, *Electron-phonon interaction and full counting statistics in molecular junctions*, Physical Review B **80**, 0413091 (2009).

[14] F. Haupt, T. c. v. Novotný, and W. Belzig, *Phonon-Assisted Current Noise in Molecular Junctions*, Phys. Rev. Lett. **103**, 136601 (2009).

[15] T. L. Schmidt and A. Komnik, *Charge transfer statistics of a molecular quantum dot with a vibrational degree of freedom*, Physical Review B **80**, 0413071 (2009).

[16] Y. Chen, *Searching for entangled electron spin states with shot noise detection*, PhD thesis (2005).

[17] O. Jouravlev, Ph.D. thesis, Delft university of technology (2005).

[18] D. F. Urban, R. Avriller, and A. Levy Yeyati, *Nonlinear effects of phonon fluctuations on transport through nanoscale junctions*, Phys. Rev. B **82**, 121414 (2010).

[19] T. Novotný, F. Haupt, and W. Belzig, *Nonequilibrium phonon backaction on the current noise in atomic-sized junctions*, Phys. Rev. B **84**, 113107 (2011).

[20] A. I. Yanson, G. R. Bollinger, H. E. van den Brom, N. Agrait, and J. M. van Ruitenbeek, *Formation and manipulation of a metallic wire of single gold atoms*, Nature **395**, 783 (1998).

[21] C. Untiedt, a. Yanson, R. Grande, G. Rubio-Bollinger, N. Agraït, S. Vieira, and J. van Ruitenbeek, *Calibration of the length of a chain of single gold atoms*, Physical Review B **66**, 1 (2002).

[22] I. K. Yanson, *Non Linear effects in electric-conductivity of point junctions and electron-phonon interaction in normal metals*, Sov. Phys. JETP **39,**, 1974 (1974).

[23] T. Frederiksen, M. Brandbyge, N. Lorente, and A.-P. Jauho, *Inelastic Scattering and Local Heating in Atomic Gold Wires*, Phys. Rev. Lett. **93**, 256601 (2004).

[24] N. Agräit, C. Untiedt, G. Rubio-Bollinger, and S. Vieira, *Electron transport and phonons in atomic wires*, Chemical Physics **281**, 231 (2002).

[25] A. Kumar, L. Saminadayar, D. Glattli, Y. Jin, and B. Etienne, *Experimental test of the quantum shot noise reduction theory.*, Physical review letters **76**, 2778 (1996).

[26] B. Ludoph, M. H. Devoret, D. Esteve, C. Urbina, and J. M. van Ruitenbeek, *Evidence for Saturation of Channel Transmission from Conductance Fluctuations in Atomic-Size Point Contacts*, Phys. Rev. Lett. **82**, 1530 (1999).

[27] H. van den Brom and J. van Ruitenbeek, *Quantum Suppression of Shot Noise in Atom-Size Metallic Contacts*, Physical Review Letters **82**, 1526 (1999).

[28] M. Paulsson, T. Frederiksen, H. Ueba, N. Lorente, and M. Brandbyge, *Unified Description of Inelastic Propensity Rules for Electron Transport through Nanoscale Junctions*, Phys. Rev. Lett. **100**, 226604 (2008).

[29] C. Untiedt, G. Rubio Bollinger, S. Vieira, and N. Agräit, *Quantum interference in atomic-sized point contacts*, Phys. Rev. B **62**, 9962 (2000).

[30] F. D. Novaes, A. J. R. da Silva, E. Z. da Silva, and A. Fazzio, *Oxygen Clamps in Gold Nanowires*, Phys. Rev. Lett. **96**, 016104 (2006).

5

ANOMALOUS SUPPRESSION OF SHOT NOISE IN AU ATOMIC CHAINS

Manohar KUMAR, Yaroslav BLANTER, Jan van RUITENBEEK

Au atomic chains have recently been studied by Manohar Kumar et al.[1] in order to reveal the electron-phonon inelastic contribution in shot noise. In that work it was shown that inelastic scattering leads to a linear deviation of shot noise from the classical Lesovik-Levitov expression for bias eV above the vibron frequency. This deviation at the vibron frequency shows a cross over in sign from a positive deviation above a transmission of $0.95G_0$ *to a negative deviation below this value. All atomic junctions with a transmission below* $0.95G_0$ *show a suppression in noise above the vibron frequency. The size of this suppression in terms of the relative change in Fano factor depends upon the details of the contact, such as the stress in the atomic chain, but such linear deviations never exceed 100%. However, for a fraction as large as* 60% *of Au atomic contacts having an exceptionally low conductance, below* $0.8G_0$*,*

Parts of this chapter will be submitted as a publication in Phys. Rev. B.

we observe a very strong noise suppression, which is accompanied by oscillations in the noise as a function of bias voltage. This kind of strong suppression and the oscillations are unexpected and are not explained by the existing theory. Here we consider these contacts and explore possible explanations.

5.1 ANOMLALOUS NOISE SUPPRESSION IN AU CHAINS

As we have seen in chapter 4(a) suppression in the noise due to inelastic scattering is seen for all contacts having a conductance below $0.95G_0$, and this suppression is attributed to a two-electron processes taking place in the contacts[1]. In this chapter we are going to look into the noise properties of contacts with exceptionally low conductance, below $0.8G_0$, in more detail. Au being an s metal it generally forms stable single-atom contacts with conductance close to $1G_0$. However, due to the presence of local defects in the leads close to the atomic contact scattering and interference of partial electron waves occasionally gives rise to a conductance of significantly lower value. The formation of a contact having a conductance below $0.8\mathrm{G}_0$ is quite rare. This can be easily seen from the conductance histogram shown in figure (4.1 a). The counts below $0.8\mathrm{G}_0$ are quite small in comparison to counts between 0.9 and 1.1 G_0.

All atomic contacts are formed using the mechanical controllable break junction (MCBJ) technique in a cryogenic vacuum environment and they are characterized by recording conductance histograms and length histograms. For details of the experimental procedure we refer to chapter 3. First, an atomic contact is formed by pulling the junction from a high conductance value to a value near $1\mathrm{G}_0$ by ramping the piezo voltage at 1V/s. Next, it is further pulled gently by ramping the piezo voltage at 0.1V/s until the conductance drops below $0.8\mathrm{G}_0$. Often the contact breaks before such low values are reached, in which case we restart the process. Once a conductance of a required value is formed we characterize the contact by measuring its stability as a function of time, and by looking for possible two-level fluctuations in the contact. Usually, contacts at lower conductance are due to the presence of several metastable states in the leads. This kind of instability has also been reported for Nb lithographic junctions [2]. One can often stabilize the contacts by gently stretching such that the contact sinks more deeply into one of the metastable states. Once a stable contact has been formed the junction is further characterized by recording its differential conductance, for which a modulation sine signal of frequency 3.33kHz and amplitude of 2mV is used. Due to the presence of local defects in the leads very close to the atomic contact large amplitude conductance fluctuations may be present. These conductance fluctuations have an asymmetric component *w.r.t.* bias voltage and they add up onto the symmetric inelastic feature in the differential conductance. Hence in our experiments we mainly consider the symmetric component of the differential conductance. Here the symmetric conductance is calculated as[1] $G_S(V) = [G(V_+) + G(V_-)]/2$. Af-

---

[1] The symmetrization removes only the asymmetric component due to conductance fluctuations, but there can also be a symmetric component. In order to estimate it, while looking for the vibron signal in the numerical derivatives of the differential conductance we always compare the signature in

ter the characterization of the atomic contact we first measure its thermal noise at 0V and the shot noise in steps of approx. 1mV. The thermal noise is measured at the beginning and at the end of noise measurement. At the end of each noise measurement sequence the junctions are characterized again by recording the differential conductance. When changes in the contact configuration take place during the measurement sequence this will show up in a change in thermal noise or in the differential conductance. All the data considered below have been selected to have changes in the differential conductance or the thermal noise at the beginning and at the end of the measurement that remain within 2% of the full signal.

Shot noise is white in nature but due to the high impedance of the sample in combination with the stray capacitance of the coaxial cables running from room temperature down to the 4K chamber produces a roll off at about 30kHz. Typical noise spectra for a Au atomic contact of $0.67G_0$ are shown in figure (5.1) The shot noise spectra are corrected for the roll off by dividing by the thermal noise measured on the same contact. The spurious spikes in the noise spectra were removed. The spectral range between 5kHz - 40kHz is selected for evaluation of the noise level and its mean value is plotted *w.r.t* corresponding bias voltages, as shown for the Au atomic contact of conductance $0.69G_0$ in figure (5.2a). Here the red curve gives the fit up to 7mV to the Lesovik-Levitov expression for a single eigen channel of transmission 0.69. The experimental data points below 7meV are clearly well described by the fit. The Fano factor is calculated using the reduced noise plot and found to be 0.312 and 0.306 for positive and negative bias, respectively. The small difference in the Fano factor between positive and negative bias regime is attributed to a non-linearity in the conductance as a result of conductance fluctuations in the contact. Strikingly, the experimental data deviates from the fit above 7meV and it shows a strong suppression in noise, superimposed with some kind of oscillation *w.r.t.* bias voltage. The noise suppression is seen in both positive and negative bias regimes.

This strong suppression in noise has been observed in a number of different atomic contacts. Figure (5.2b) shows the noise for a different contact of conductance 0.71 for bias voltages from 0V to 31.79mV, and then measured again with same voltage steps back to 0mV. The Fano factor below 6meV is found to be 0.306 and 0.305, respectively, for up and down sweeps of bias, which is within the experimental error. This measurement clearly shows the reproducibility of the noise within the experimental error, apart from a few points. This clearly shows that the strong suppression in noise is not a random phenomenon but is connected to some physical process in the contact.

---

derivative of the symmetric component of differential conductance with the original differential conductance.

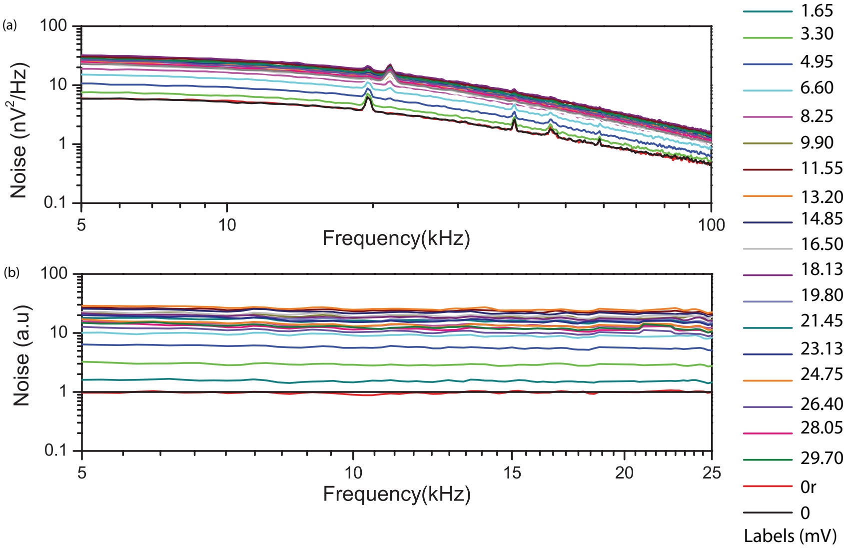

FIGURE 5.1: Noise spectra for a 5-atom long Au chain with a conductance of $0.67G_0$: (a) Raw noise spectra measured on the atomic contact. The roll off at 24kHz is due to the transfer function of the noise measurement setup. Spikes in the spectra are external spurious signals coupling into our measurement. The thermal noise at the end and at the beginning of the measurement series lay on top of each other. (b) Spectra normalized by the thermal noise, with the spurious noise peaks removed. The mean value of the noise at each current level is calculated from these normalized spectra. On the right hand side the color code indicates the voltage bias values in mV on the sample.

On further analysis of the strong suppression in noise we studied the noise evolution while stretching the contact. An atomic chain was formed at $0.98G_0$ and pulled subsequently with steps of 0.1Å through control of the piezo voltage. After stretching the contact by 2.6Å the conductance trace shows a long stable plateau as shown in figure (5.3). The differential conductance at the red point shows a nice step-down feature as shown in figure (5.4). The numerical derivative of the differential conductance clearly identifies the vibron energy as a dip in the positive bias regime and a peak in the negative regime, with a vibron energy of 15meV. Its noise properties were studied to above the vibron energy. The classical Lesovik-Levitov expression explains the data below 15meV shown as the red curve in figure (5.4-1a). The noise deviates linearly from this curve above the threshold of 16meV. The linear increase in the noise above the vibron energy is consistent with our previous observations reported in chapter 4. When the contact is further pulled by 5.2Å the contact jumps to a conductance value of $0.65G_0$. The sudden step in the conductance trace results from the presence of the local defect in the leads close to the atomic chain. The chain is then further stretched by 0.6Å and the conductance trace starts showing a new plateau level. At this point with a conductance of 0.697G$_0$ the junction is again characterized by recording the differential conductance and noise properties, as well as for two subsequent stages of stretching of the contact. The red data points in the trace shown in figure (5.3) are the configurations for which the noise was measured, shown in figure (5.4). Panel (5.4-b) shows the evolution of the differential conductance, panel (c) its derivative and panel (a) the noise, for the four stages of stretching of the Au atomic chain. The vibron energy for the stretched states of the contact is not as well defined. We tentatively take the first peak as indicating the energy of the vibron. This energy is lower than for the relaxed state, which is in accordance with the longitudinal character of the vibron, for which weakening of the linear bond in the atomic chain upon its stretching leads to a lowering of the vibron energy [3].

The noise at higher bias deviates strongly from the 'classical' Lesovik - Levitov expression shown by the red curve in figure (5.4(a)) and it is found to be strongly suppressed for the stretched configurations of the atomic chain. In addition there appears to be an oscillation in the noise, but its periodic nature is not clear from

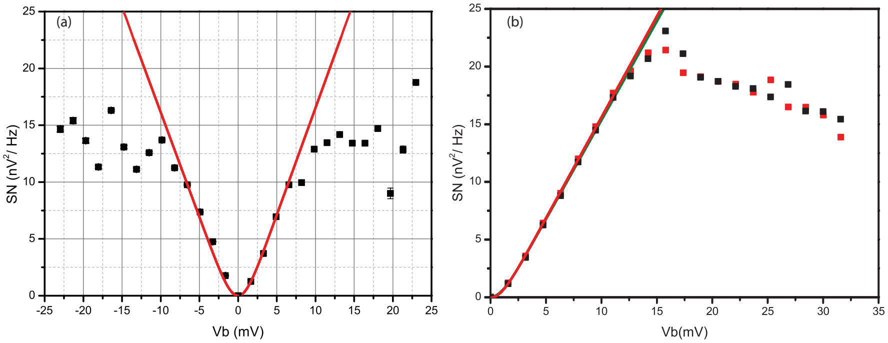

FIGURE 5.2: Mean noise value plotted *w.r.t.* bias voltage for Au atomic chains having a low transmission. (a) Au chain with a conductance of 0.67G$_0$. The red curve shows the fit up to 7mV to the Lesovik-Levitov expression for a single channel with $\tau = 0.69$. The shot noise is strongly suppressed above 7meV at, both, positive and negative bias. The Fano factor for the positive bias side is 0.312 and for negative bias regime is 0.306. The difference in these Fano factors may be due to an asymmetry in transmission as a result of conductance fluctuations, but is comparable to the experimental error. (b) Noise measurements for a Au chain with a conductance of 0.710G$_0$ for increasing bias voltage from 0V to 31.79mV (black dots) and for decreasing bias back from 31.79mV to 0V (red dots) in steps of approx. 1mV. The red and green curves are Lesovik-Levitov expression fits for the increasing bias and decreasing bias measurements, respectively.

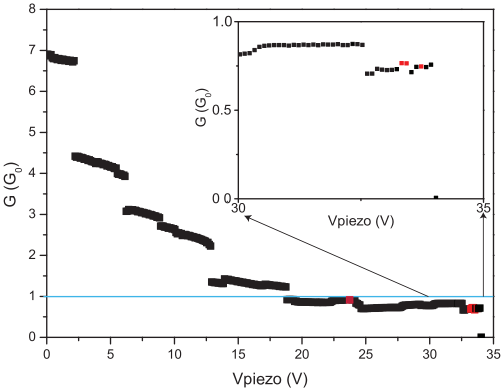

FIGURE 5.3: Conductance trace leading to a 5-atom long Au atomic chain. The atomic contact was streched in steps of 0.1Å. The red data points are the contact configurations for which junctions the differential conductance spectrum and shot noise is measured, shown in figure (5.4). The blue line marks the level $1G_0$ and shows the appearance of configurations with lower conductances for this particular atomic chain.

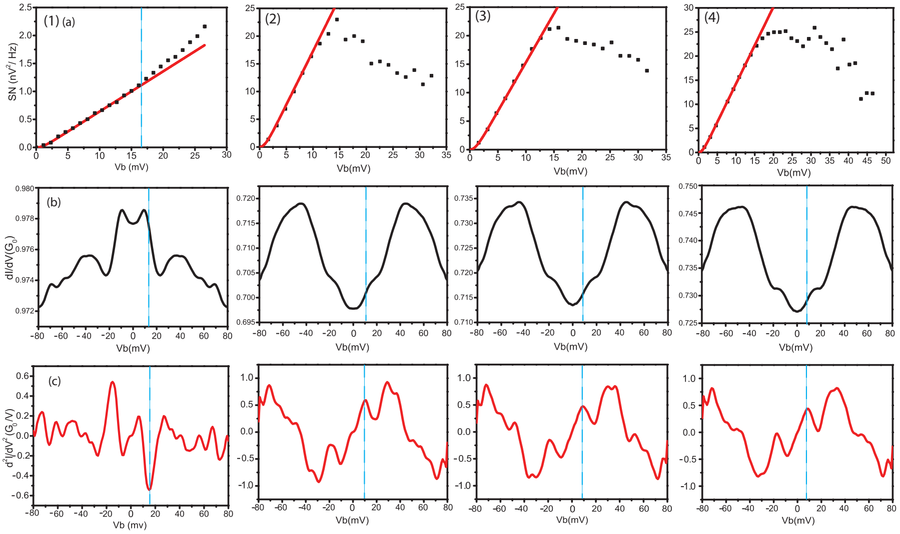

FIGURE 5.4: Evolution of the noise for several stages of stretching (1 – 4) of a long Au atomic chain for the trace shown in figure (5.3) at the points marked in red. (a) The mean noise value plotted *w.r.t.* bias voltage. The red curve is the Lesovik-Levitov expression fit in the low-bias regime for a single channel with $\tau = G/G_0$. In (1a) the contact with a conductance of $0.98G_0$ shows the expected linear increase in noise above the vibron energy in agreement with the results discussed in chapter 4. For (2 – 4) the shot noise is found to be strongly suppressed above the threshold energy. Panels (b) and (c) show the corresponding symmetric component of the differential conductance and its numerical derivative, respectively. The blue dotted line indicates the energy of the lowest feature in the conductance spectrum.

the experimental data.

5.2 DISUSSION OF THE RESULTS

FROM the two-electron/one-phonon processes discussed in chapter 4 we would expect a negative deviation from the Lesovik-Levitov noise above the phonon frequency for atomic chains with a conductance as low as $0.7G_0$, and this should be linear. However, here we observe something much more dramatic, with a suppression in noise that is so strong that it does not just lead to a lower slope but even to a decrease in the total level of the noise. What could be the reason for such a strong suppression? We will first consider a model of weak shuttling, and discuss a possible connection with the discussion on non-conservative forces in section (5.2.2) below.

Usually in quantum transport noise is suppressed if there is some kind of process that leads to a regular flow of the electrons. Since the experiment suggests that its onset is related to a vibron frequency of the atomic chain, this has led us to consider the possibility of a phonon-induced shuttling of electrons in the atomic chain, in analogy to the mechanisms proposed in Refs. [4, 5]. Considering, e.g., a 3-atom chain the central atom in the atomic chain could act as a shuttle and the electrons would experience enhanced hopping rates when the central atom is close to the lead. The hopping rates are very high in our case, which does not make the applicability of the model immediately obvious. However, if we simply consider the numbers they are very suggestive: The rate of electron transfer is $\nu_\mathrm{e} = I/e = GV/e$, while the vibron frequency is $\nu_\mathrm{v} = eV/h$. With the voltage bias at threshold we find that the ratio $\nu_\mathrm{e}/\nu_\mathrm{v} = 2\tau$, with τ the transmission probability. This ratio is remarkably close to 1 for $\tau \sim 0.7$, which is very suggestive of a strong coupling between ionic vibrations and electron flow.

A schematic illustration of this kind of quantum transport in the atomic contact is shown in figure (5.5). The quantum shuttling processes in a single electron transistor are quite rich and have seen intensive theoretical and experimental in-

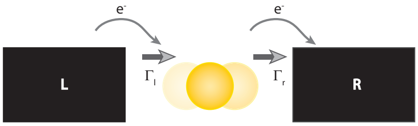

FIGURE 5.5: Simple pictorial representation of quantum shuttling in a two terminal device: In the limit of weak electron tunneling during the shuttle of the central atom only two events are possible, either an electron hops onto the central atom from the left lead with tunnel rate Γ_l when it is close to the left lead, or it hops off with tunnel rate Γ_r when it is close to the right lead.

vestigations [5–14]. Recently, in an experiment reported by Alexei Marchenkov *et al.* [2] they give evidence for the formation of a dimer in Nb lithographic junctions, and their shuttling between the leads. Interestingly, they have studied the transmission probability of the contact by measuring the sub gap structure of the Nb atomic contacts. They found that the transmission probabilities of the channels remain the same except for one, which reduces from 0.81 to 0.57. This can be understood if we assume that when the dimer is approaching one of the leads the transmission probability of the channel increases due to the large overlap of atomic orbitals, and when the dimer is away from the lead the transmission probability decreases. In their case the mechanical instability was very slow, in the order of tens of seconds, which can be easily followed in the time trace of the conductance. Because of the large difference in time scales noise measurements on this kind of system will give either Poissonian or super-Poissonian noise.

The actual noise behavior of the quantum shuttle system considered here will depend upon correlations of the charge fluctuations with the shuttle cycle. This correlation depends upon a number of parameters, such as the voltage bias, the tunneling probability, the oscillation amplitude *etc.* In the pure shuttling regime the actual number of electrons transferred is limited by Coulomb blockade. This would fix the electron flow rate and would give a strong noise suppression [15]. We will now consider the possibility that a similar effect is relevant to our experimental observation and we will analyze the model below in more detail.

5.2.1 TIME DEPENDENT TRANSMISSION

A time dependent transmission could be a reason for the strong suppression in noise in the atomic contacts. Let us have a look into this in more detail. Here we will consider two simple models of electron phonon interaction in molecular junctions based on a 1-D tight binding model [16–18]. The models use the fact that the vibrons are much slower than electrons, and thus for electrons the interaction can be modeled as a slow (adiabatic) time-dependent potential [18–20]. The goal of these models is to explain the experimental observations in which the junctions have a low average transmission around 0.7, which is approximately voltage independent. In contrast, the noise power is strongly voltage dependent and acquires a negative correction when the bias voltage crosses the vibron energy. For much higher voltages, the noise should approximately stabilize and become voltage independent.

A model with one dynamic bond

First, we investigate the situation when the dynamics in the molecular bridge is determined by just one dynamic bond between two atoms as shown in figure (5.6). We model the chain as a 1D tight-binding system with lattice period a, interrupted by a single dynamic bond for which the properties differ from all other bonds. All overlap integrals in the chain equal t_0, with the exception of one, connecting the site at $x = 0$ with that at $x = a$, which is equal to t. We assume for simplicity that both t and t_0 are real. For reference, we first solve the ideal tight-binding model

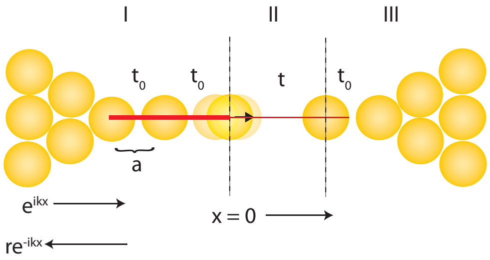

FIGURE 5.6: Tight binding model with one dynamic bond. The 1D lattice has a period a, while the atom at $x = 0$ in the middle of the chain is rigidly attached to the left lead but is free to move with respect to the right lead. The motion of the atom at $x = 0$ leads to a modulation of the transmission of the electrons from the left lead to right lead. The overlap integrals in the chain are all equal to t_0, apart from the dynamic bond which has an overlap integral of t.

for an infinite 1D chain, taking all overlap integrals equal to t_0. For any site the Schrödinger equation looks like

$$E\psi(x) = t_0\,[\psi(x-a)+\psi(x+a)] \tag{5.1}$$

Assuming that the wave function is a running wave with wave vector k such that $\psi(x) \propto \exp(ikx)$, we obtain a sinusoidal band,

$$E = 2t_0\cos(ka) \tag{5.2}$$

Now we solve the problem with the dynamic bond as a scattering problem. We assume that the wave function at all sites $x \leq 0$ is a superposition of incident and reflected waves, $\psi(x) = \exp(ikx) + b\exp(-ikx)$, and for all sites with $x \geq a$ it is a transmitted wave, $\psi(x) = w\exp(ikx)$. Then the Schrödinger equation for the two contact sites is

$$\begin{aligned} E(1+b) &= t_0(e^{-ika} + b\,e^{ika}) + tw \qquad \text{at x = 0} \\ Ew &= wt_0e^{ika} + (1+b)t \qquad \text{at x = a} \end{aligned} \tag{5.3}$$

Substituting $E = 2t_0\cos(ka)$ the solution for w can be written as,

$$w = \frac{2itt_0\sin\,ka}{t^2 - t_0^2\,e^{-2ika}} \tag{5.4}$$

Hence, the transmission probability $T = |w|^2$ becomes,

$$T = \frac{4t_0^2 t^2 \sin^2 ka}{t^4 + t_0^4 - 2t^2 t_0^2 \cos 2ka} \tag{5.5}$$

Taking $t = t_0$, $T = 1$ which serves as sanity check. As a function of energy T has maximum at $T_{\max} = 4t_0^2 t^2/(t^2 + t_0^2)^2$ at E = 0 *i.e.* $ka = \pi/2$ and decreases with energy, vanishing at $E = 2t_0$. In the rest of this section we will consider only $T_{\max}$ at $E = 0$ for further calculation.

Let us now introduce the vibration in the contact atom at $x = 0$ through a time dependence in its overlap integral $t \to t + \delta t$, with $\delta t \propto \cos(\omega\tau)$, where τ is the time. We assume that in all the cases $\delta t \ll t$. This leads to a time dependence of the transmission probability which we write as $T = T_0 + \delta T_1 + \delta T_2$, where T_0 is given by equation (5.5), $\delta T_1 \propto \cos(\omega\tau)$, and $\delta T_2 \propto \cos^2(\omega\tau)$. We will disregard higher order corrections. After time averaging T_1 is removed and thus in lowest order approximation (neglecting also T_2) the conductance is not affected and remains $G = TG_0$. However, in this approximation shot noise, which is proportional to $T(1-T)$, does show a negative correction, which we find by substituting $T = T_0 + \delta T_1$:

$$S/2eI = T_0(1 - T_0) + (1 - 2T_0)\delta T_1 - (\delta T_1)^2 \tag{5.6}$$

In this equation the second term averages out, but the last term has a finite value since $\langle \cos^2(\omega\tau)\rangle = \frac{1}{2}$. The correction δT_1 can be written as $(\partial T/\partial t)\delta t$. This allows us to express the correction to the transmission probability in terms of the modulation of the overlap integral t,

$$\delta T_1 = 2T_0 \frac{(t_0^2 - t^2)}{(t_0^2 + t^2)} (\delta t/t) \tag{5.7}$$

In our experiment $T_0 \sim 1$, so that $\delta T_1 \sim \delta t/t_0$. From first principle calculations (A. Levy Yeyati, private communications) we obtain an estimate $\delta t/t \sim 7 \times 10^{-3}\, \delta a/a$, where δa is the elongation in the bond length. Considering $\delta a/a \sim 0.1$ as a reasonable estimate gives as an estimate for the relative correction of noise in equation (5.6) $\delta S/S < 10^{-6}$. While it is interesting to observe that such a correction would appear in the noise without any associated correction in the conductance, the size of the effect is quite small in comparison to experimental accuracy, and it does not offer an explanation for the large effects observed.

Apart from this we assumed that second order correction should be neglected, which does not match with the fact that the effect in noise is of second order. The second order correction in δt can be written as,

$$\delta T_2 = \frac{1}{2}\frac{\partial^2 T}{\partial t^2}(\delta t)^2 = \frac{1}{2}\frac{8t_0^2}{(t^2 + t_0^2)^4}(3t^4 - 8t^2 t_0^2 + t_0^4)(\delta t)^2 \tag{5.8}$$

The second order correction T_2 vanishes at $t = 0.13t_0$, at a transmission value of $T = 0.066$, which is much lower than the transmission values in the experiment. This does not improve the correspondence with the experimental observation, as the second order correction gives a correction in the conductance as well as the noise and eventually may give a positive correction in noise. Hence, this model fails to capture the basic observations of our experiment. Let us next look into a slightly more elaborate model when we have single atom suspended by two dynamic bonds, and take image charge interaction into account.

Two suspended bonds with image charge interaction

Lets us now consider case of an atom suspended between two leads with two dynamic bonds. Figure (5.7) shows a 1D tight binding approach for this model. Here the central atom at $x = a$ is suspended between the fixed atoms at $x = 0$ and $x = 2a$. The overlap integrals of these two suspended bond are t and taken to be equal, and for of all other bonds the overlap integral is t_0. The assumption of equal overlap integrals to left and right of the central atom can be viewed as corresponding to a transverse vibrational mode or a breathing mode of the atomic chain. It is easy to generalize the model to the situation when these overlap integrals are unequal.

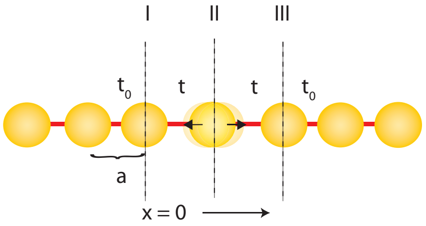

FIGURE 5.7: One-dimensional tight binding model for an atom suspended with two dynamic bonds between two fixed atoms. The atom (at $x = a$) in the middle of the chain is suspended between the atoms at $x = 0$ and at $x = a$. The lattice period of the atomic chain here is a. The motion of the atom at $x = a$ gives a time dependent transmission for electrons between the left and right leads. The overlap integrals in the chain are all given by t_0, apart from those for the bonds between the central atom to the right and left atom, which are taken to be equal, with a value t.

Furthermore, we introduce the interaction of electrons on the central atom with image charges in the leads here. In this simplified model the image charge potential can be written as

$$U_0 = \alpha\, e^2/a \tag{5.9}$$

where the Madelung constant α covers screening effects, which for our case is $\alpha \sim 1$.

We now formulate a tight-binding equation for the three central atoms. In our calculation we assume again that the wave function in the left bank $x \leq 0$ is a superposition of incident and reflected waves $\psi(x) = e^{ikx} + b\ e^{-ikx}$, and in the right bank $x \geq 2a$ we have only a transmitted wave $\psi(x) = w\ e^{ik(x-2a)}$. Let us call the wave function at atom-section II $\psi_{II(x)}$, then Scrödinger equation for all these three atomic section I,II,III could be written as:

$$\begin{aligned} E(1+b) &= t_0(e^{-ika} + be^{ika}) + t\psi_{II}; \qquad x = 0; \\ (E+U_0)\psi_{II} &= t(1+b+w); \qquad x = a; \\ E\ w &= t_0\ w\ e^{ika} + t\psi_{II}; \qquad x = 2a. \end{aligned} \tag{5.10}$$

This set of equations can be solved for w, giving,

$$w = -2ie^{ika}\sin(ka)\frac{t^2}{E+U_0}\left(t_0e^{-ika} - \frac{2t^2}{E+U_0}\right)^{-1} \tag{5.11}$$

Let us first verify this result for $U = 0$, in which case we obtain for the transmission probability T,

$$T = \frac{\sin^2 ka}{|t_0^2 t^{-2}\cos(ka)\ e^{-ika} - 1|^2}. \tag{5.12}$$

At the band edge $E = \pm 2t_0$ the transmission probability vanishes, while at the center of the band the transmission is perfect ($T = 1$), irrespective of t/t_0. This result is consistent with the expectation for resonant tunneling for a symmetric double-barrier system. For all other cases T is a function of t/t_0.

In the previous section we already seen that $\delta t/t_0$ is very small from which we expect that the effect on the noise correction will be insignificant, also in this case of two dynamic bonds. Now let us introduce the effect of the image potential in our model. For the case $ka = \pi/2$, $E = 0$, the solution of the expressions (5.10) for w is straightforward,

$$w = -\frac{2}{2 + i(t_0U_0)/t^2} \tag{5.13}$$

This gives as solution for the transmission probability

$$T = \frac{1}{1 + \frac{U_0^2 t_0^2}{4t^4}} \tag{5.14}$$

Here both t and U_0 are time dependent, but the time dependence of t is quite weak giving insignificant correction in noise, as we have seen. Hence, we will consider t to be time independent and for simplicity we set $t = t_0$. For this choice the transmission probability T is given as

$$T = \frac{1}{1 + \frac{U_0^2}{4t_0^2}} \tag{5.15}$$

In contrast to t the relative change in U_0 due to the modulation of the barrier is much stronger, $\delta U_0/U_0 \sim \delta a/a \sim 10^{-1}$. This may result in an effect that is large enough, as it produces a relative correction to the noise of,

$$\frac{\delta S}{S_0} = -T_0(1-T_0){\frac{\delta U_0}{U_0}}^2 \tag{5.16}$$

where T_0 is given by equation (5.15) for the case of $\delta U \sim 0$.

Now, just as before, we need to consider the second order correction. The second order correction to the conductance will be given by,

$$\delta T_2 = 2T_0(1-T_0)(1-4T_0)\delta a^2/a^2 \tag{5.17}$$

And the total second order correction to noise is

$$\delta S_2 = 2T_0(1-T_0)(1-7T_0+9T_0^2)\delta a^2/a^2 \tag{5.18}$$

Equation (5.18) shows a cross over in sign at $T = 0.589$ and the correction in noise is positive at $T = 0.7$. Clearly this does not match the experimental observations. The size of the correction in the noise can be large in this model, although the parameters needed to describe the observed effect appear to be at the limit of acceptable values. Although the sign is not correct, this may depend on the choices we have made to parametrize the problem. In order for the correction to the conductance to be small, as in the experiment, the parameters may be such that $\partial^2 T/\partial U_0^2$ is small.

The effect due to image charges could be more drastic if $\delta a/a$ would be larger. Such large amplitude oscillations have been proposed to arise from "Non conservative forces" as components of current induced force. We will briefly discuss these in the next section.

5.2.2 NON-CONSERVATIVE FORCES

The flow of electrons couples with the atomic lattice of a nanoscale conductor under non-equilibrium. The steady flow of electrons at high current densities in the presence of an electron-ion interaction leads to momentum and energy transfer from electrons to ions and hence to Joule heating. But it also leads to a force on the ions, which is called the current induced force. The combined effect of current induced forces and Joule heating is responsible for the breakdown of the electrical components by elecromigration.

Smit *et al.* [21] have studied the high-bias stability of Au and Pt atomic chains. Part of their observations was captured well by a model of current heating and thermally induced fracture. However, they found that for a fraction of the longer chains breaking occurs at lower bias voltages, which was not explained by the Joule heating. Recently, during writing of this report we[2] observed a similar pattern in our experiments for Au. Atomic chains of length below 8Å show breaking voltages above 1V (which was the limiting value in these experiments), while some of the chains longer than 8Å show breaking voltages around 200mV – 300mV. The breaking of atomic chains at such low bias voltage is surprising.

Todorov and coworkers have recently proposed a new mechanism for current induced forces, which are explicitly shown to be non-conservative [22–24]. Its non-conservative nature comes from the ability of the force to do work on a closed path. In model systems they connect this effect with the emission of directional phonons [25]. Right moving electrons can emit right moving phonons and scatter into left moving electron states. The reverse process would be suppressed due to unavailability of the states. It is possible that this leads to a self-sustained directional emission of phonons. The appearance of such self sustained directional phonon emission relies on the presence two orthogonal phonon modes lying very close to each other in energy. Coupling these two low-lying phonon modes two new angular modes (clockwise and anticlockwise) are generated. Torodov *et al.* have shown that electron scattering lifts the degeneracy of the angular momenta and pumps energy into one of the two and damps the other. This gives rise to self-sustained stimulated emission of directional angular momentum carrying phonons. This process will lead to an exponential growth of the phonon population without equilibration, finally leading to failure of the device.

Since these kind of processes are possible at lower bias voltages they are candidates for explaining the anomalous experimental observations in the work by Smit *et al.* [21], although this interpretations is still speculative and remains to be tested. Returning to the experimental data shown in figure(5.4-1) for the evolution of the noise while stretching of the contact, we observe another anomaly for longer chains. For the initial length of the chain (1a) the same atomic contact shows normal behavior with a well-defined vibron feature in the second derivative of the current. But once the contact jumps to a lower conductance of $< 0.7G_0$ the vibron features in the differential conductance curves are no longer well-defined and the conductance shows even a step-up feature, which is unexpected in this range of conductance, as shown by Tal *et al.*[26]. at the same time the noise measurement shows an anomalously strong suppression. Could we associate this with a non-conservative current-induced force? Possibly it may lead to anomalously large amplitudes for atomic vibrations, which is an ingredient needed in the models that we have described above. Experiments are under way that search for a

---

[2] This experiment was done in collaboration with Carlos Sabter of the Universidad de Alicante, Spain, during an extended visit in our lab.

connection between the anomalous breaking voltages of long Au atomic chains, the anomalously strong suppression in noise, and the shapes of the differential conductance curves. Until new results come available the physical models for our observation remain speculative.

5.3 STRONG NOISE SUPPRESSION IN SHORT ATOMIC CHAINS

THE strong noise suppression reported above was seen in approximately 60% of all contacts with conductance values around $0.7G_0$. Apart from these we found a few contacts (approx 1%) with conductance values of $(0.93 \pm 0.01)G_0$, which were just 3 atoms long, that show a strong suppression in the noise.[3] Figure (5.8) shows the differential conductance curve and its numerical derivative for such a contact in two stages of stretching. The differential conductance has a prominent zero-bias anomaly which masks a possible inelastic vibron feature. The first dips and peaks in the second derivative of the current are too low in energy to be attributable to longitudinal vibrons in Au atomic chains. Testing for stability with traces of conductance vs. time, and differential conductance curves taken before and after the noise measurement, did not reveal any changes in conductance. Hence, it is unlikely that the atomic configuration of the contact changed during the noise measurement. Noise measurements on these contact reveal a strong suppression above an energy that corresponds to the first extremum in the second derivatives

---

[3] This work was done in collaboration with Kiran Kumar

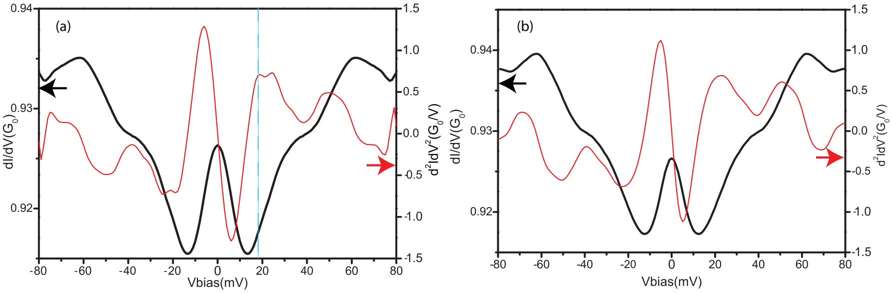

FIGURE 5.8: Differential conductance and its numerical derivative for a 3 atom long Au atomic chain showing anomalous noise, as presented in figure (5.9). The black curves show the differential conductance and red curves show the numerical derivatives, with the arrows indicating the corresponding axes for the plots. (a) gives the data for the initial contact, and (b) shows data for the same contact after stretching by 0.2Å . The differential conductance curves show a dominant zero-bias anomaly and the derivatives have prominent peaks due to this anomaly. A clear vibron signal is absent, but it possibly lies at 19meV in curve (a) (shown by the dashed line).

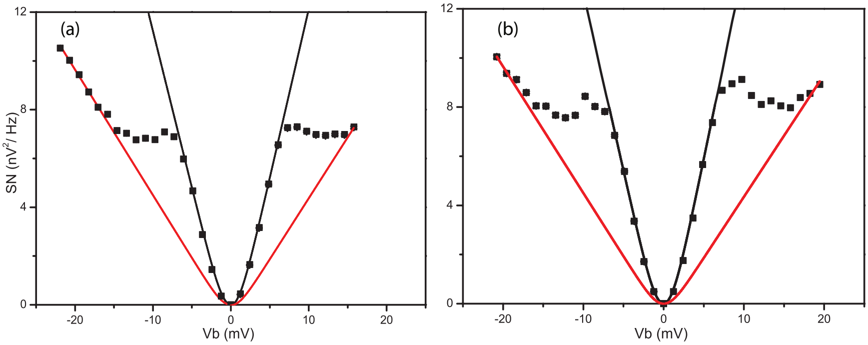

FIGURE 5.9: Mean noise values plotted *w.r.t.* bias voltage for a 3 atom long Au atomic chain showing anomalous noise. The black and red curves are Lesovik-Levitov fits for two channels, for low bias voltages and for high bias voltages, respectively. The shot noise is observed to be strongly suppressed above 8meV both at positive and negative bias. The noise starts showing linear behavior *w.r.t.* bias voltage again above 15meV, approximately. The initial state of the contact is shown in (a), while (b) shows the noise measured after stretching the contact by 0.2Å. The corresponding differential conductance curves are shown in figure (5.8).

of the current, shown in figure (5.9). The noise is observed to deviate strongly from the Lesovik-Levitov extrapolation for a few mV above their corresponding extremum energy and then starts increasing linearly *w.r.t.* bias voltage again. This behavior differs from the previous cases where we have seen the strong suppression in noise. An important observation is the fact that the Lesovik-Levitov fit on these contacts reveals the presence of two channels in the transport. In the example shown here the two channels have transmission probabilities of $\tau_1 = 0.78 \pm 0.02$ and $\tau_2 = 0.14 \pm 0.04$ for figure (5.9-a) and $\tau_1 = 0.75 \pm 0.02$ and $\tau_2 = 0.15 \pm 0.01$ for figure (5.9-b). The Fano factor increases from 0.29 to 0.35 on stretching the contact.

The second stage at higher bias voltages where the noise is increasing again *w.r.t.* applied bias voltage can be fitted with the Lesovik-Levitov expression. On fitting it suggests that a change has taken place in the transmission probabilities of the channel, which are now described by $\tau_1 = 0.91 \pm 0.01$ and $\tau_2 = 0.01 \pm 0.01$. The fits are shown in figure (5.9) by the red curves. The high-bias fit shows the regular behavior for gold atomic chains, with a single channel that is nearly completely open. In this state the anomalous noise suppression appears to be absent and the junction behaves normal. Note that the observed suppression in noise occurs for the main channel having a transmission probability very close to close to the conductance value for which we have seen the strong suppression in the noise in the single channel case. However, since also the second transmission channel changes, it is more likely that the changes in transmission should be attributed to voltage dependent changes in localized scattering centers in the leads very close to atomic contact.

5.4 CONCLUSION

Our recent studies of shot noise for Au atomic chains reveal an inelastic signature, due to electron - vibron interaction. Shot noise is seen to deviate linearly from the Lesovik-Levitov expression, for bias values above the vibron energy of the atomic chain. A cross over in sign of this noise deviation is seen at $\tau \sim 0.95\mathrm{G}_0$ for the single channel Landauer conductor. The noise increases above its value given by a Fano factor of $F = 1 - G/\mathrm{G}_0$ for conductance $G > 0.95\mathrm{G}_0$, while noise decreases below the value of $F = 1 - G/\mathrm{G}_0$ for conductance $G < 0.95\mathrm{G}_0$. The noise deviation depends upon the strength of the electron-phonon interaction in the atomic chain, and on the energy of the dominant vibron mode, which in turn shift with the state of stretching of the chains. The suppression in slope in these experiments is never greater than 100% for the linear deviation in noise above the vibron energy. However, in this chapter we have presented data for atomic contacts of conductance $G \leq 0.75\mathrm{G}_0$ which show anomalously large suppressions in the noise above the vibron energy. This behavior was seen in approx. 60% of contacts with conductance in this regime.

We have investigated whether this anomalous suppression in noise can be attributed to the quantum shuttling of the atoms in the atomic chain induced due to the vibronic degree of freedom. This interpretation is suggested by the close match between the electron transfer rate and the vibration mode period. We analyzed the tight binding models for a single dynamic bond and for two dynamic bonds in 1D atomic chains. Although we find some interesting effects, both of these models fail to show corrections to the noise due to vibron induced shuttling that are large enough to serve as a viable explanation. Next, we introduced the concept of the image charge in the model with two dynamic bonds in order to capture some of the charging physics. In this case, the correction to the noise that we find is much larger, and is proportional to the square of the relative fluctuations in the atomic bond length due to vibration excitations. Although the correction in this case is significant, for a proper description the amplitude of the vibrations should be exceptionally large, and some problems concerning the sign of the noise correction and size of the correction to the conductance remain, although these may depend on refinement of the models.

An exceptionally large amplitude of the oscillations suggests a possible connection with recent developments in current-induced non-conservative forces, which are held responsible for electromigration in the nanoscale devices. The relative change in the bond length could be quite large due to this non-conservative force and this could give rise to strong noise suppression in noise along with the image charge effect in the atomic contact. Recent ongoing experiments show that chains with 5 or more atoms in length often break at the relatively low bias voltages. It has been suggested that this may be the result of the proposed non-conservative forces. The theory describes the phenomenon as being related to the uncompensated directional stimulated emission of vibrons. The vibron population exponentially increases with the bias voltage and finally the chain becomes unstable and breaks. In our noise measurements we are at lower bias voltage, well below this breaking voltage, where large but non-catastrophic amplitudes of vibrations may be found. It will be interesting to investigate whether the anomalies are found in breaking voltage and vibron features at higher bias voltages on the same atomic contacts for which the strong anomalous noise suppression is found. Currently, this experiment is ongoing.

REFERENCES

[1] M. Kumar, R. Avriller, A. L. Yeyati, and J. M. van Ruitenbeek, *Detection of vibration-mode scattering in electronic shot noise.*, Physical review letters **108**, 146602 (2012).

[2] A. Marchenkov, Z. Dai, C. Zhang, R. N. Barnett, and U. Landman, *Atomic Dimer Shuttling and Two-Level Conductance Fluctuations in Nb Nanowires*, Phys. Rev. Lett. **98**, 046802 (2007).

[3] N. Agrãit, C. Untiedt, G. Rubio-Bollinger, and S. Vieira, *Electron transport and phonons in atomic wires*, Chemical Physics **281**, 231 (2002).

[4] R. I. Shekhter, L. Y. Gorelik, M. Jonson, Y. Galperin, and V. M. Vinokur, *Handbook of theoretical and computational nanotechnology* (American Scientific Publishers, 2006), chap. 1, pp. 1–59.

[5] L. Y. Gorelik, A. Isacsson, Y. M. Galperin, R. I. Shekhter, and M. Jonson, *Coherent transfer of Cooper pairs by a movable grain.*, Nature **411**, 454 (2001).

[6] N. M. Chtchelkatchev, W. Belzig, and C. Bruder, *Charge transport through a single-electron transistor with a mechanically oscillating island*, Phys. Rev. B **70**, 193305 (2004).

[7] A. D. Armour, *Current noise of a single-electron transistor coupled to a nanomechanical resonator*, Phys. Rev. B **70**, 165315 (2004).

[8] T. Novotný, A. Donarini, C. Flindt, and A.-P. Jauho, *Shot Noise of a Quantum Shuttle*, Phys. Rev. Lett. **92**, 248302 (2004).

[9] J. Koch and F. von Oppen, *Franck-Condon Blockade and Giant Fano Factors in Transport through Single Molecules*, Phys. Rev. Lett. **94**, 206804 (2005).

[10] F. Pistolesi and R. Fazio, *Charge Shuttle as a Nanomechanical Rectifier*, Phys. Rev. Lett. **94**, 036806 (2005).

[11] C. Flindt, T. Novotný, and A. P. Jauho, *Current noise spectrum of a quantum shuttle*, Physica E: Low-dimensional Systems and Nanostructures **29**, 411 (2005).

[12] H. Hübener and T. Brandes, *Vibrational Coherences in Single Electron Tunneling through Nanoscale Oscillators*, Phys. Rev. Lett. **99**, 247206 (2007).

[13] F. Pistolesi and S. Labarthe, *Current blockade in classical single-electron nanomechanical resonator*, Phys. Rev. B **76**, 165317 (2007).

[14] M. Poot and H. S. van der Zant, *Mechanical systems in the quantum regime*, Physics Reports **511**, 273 (2012).

[15] F. Pistolesi, *Full counting statistics of a charge shuttle*, Phys. Rev. B **69**, 245409 (2004).

[16] J. C. Slater and G. F. Koster, *Simplified LCAO Method for the Periodic Potential Problem*, Phys. Rev. **94**, 1498 (1954).

[17] P.-O. Lowdin, *Band Theory, Valence Bond, and Tight-Binding Calculations*, Journal of Applied Physics **33**, 251 (1962).

[18] L. de la Vega, a. Martín-Rodero, N. Agraït, and a. Yeyati, *Universal features of electron-phonon interactions in atomic wires*, Physical Review B **73**, 1 (2006).

[19] A. Pecchia and A. D. Carlo, *Atomistic theory of transport in organic and inorganic nanostructures*, Reports on Progress in Physics **67**, 1497 (2004).

[20] J. K. Viljas, J. C. Cuevas, F. Pauly, and M. Häfner, *Electron-vibration interaction in transport through atomic gold wires*, Phys. Rev. B **72**, 245415 (2005).

[21] R. H. M. Smit, C. Untiedt, and J. M. van Ruitenbeek, *The high-bias stability of monatomic chains*, Nanotechnology **15**, S472 (2004).

[22] D. Dundas, E. J. McEniry, and T. N. Todorov, *Current-driven atomic waterwheels.*, Nature nanotechnology **4**, 99 (2009).

[23] J.-T. Lu, M. Brandbyge, and P. Hedegård, *Blowing the Fuse: Berrys Phase and Runaway Vibrations in Molecular Conductors*, Nano Letters **10**, 1657 (2010).

[24] N. Bode, S. V. Kusminskiy, R. Egger, and F. von Oppen, *Scattering Theory of Current-Induced Forces in Mesoscopic Systems*, Phys. Rev. Lett. **107**, 036804 (2011).

[25] T. N. Todorov, D. Dundas, A. T. Paxton, and A. P. Horsfield, *Nonconservative current-induced forces: A physical interpretation*, Beilstein Journal of Nanotechnology **2**, 727 (2011).

[26] O. Tal, M. Krieger, B. Leerink, and J. M. van Ruitenbeek, *Electron-Vibration Interaction in Single-Molecule Junctions: From Contact to Tunneling Regimes*, Phys. Rev. Lett. **100**, 196804 (2008).

6

A SEARCH FOR MAGNETISM IN PT ATOMIC CHAINS USING SHOT NOISE

Manohar KUMAR, Alexander SMOGUNOV, Oren TAL,
Roel H.M.SMIT, Erio TOSATTI, Jan van RUITENBEEK

Pt is known to show spontaneous formation of chains of metal atoms upon breaking a metallic contact. From model calculations these have been suggested to become spin polarized, which is related to the Stoner enhanced susceptibility of bulk Pt and the increased density of states due to the reduced dimensionality. Here, we use shot noise measurements to search for evidence on the magnetic state of Pt atomic chains. We find evidence for a non-magnetic ground state for the conductance channels of Pt atomic chains. This may imply that the magnetic splitting of the conductance channels in Pt atomic chains is too small for detection via shot noise, that our chains are not long enough for the magnetic order to fully develop. Surprisingly, we find many atomic chains that have just two conductance channels, for which one has a full transmission of $\tau \simeq 1$.

This chapter is submitted to Phys. Rev. B.

6.1 MOTIVATION: ITINERANT MAGNETISM IN PT ATOMIC CONTACTS

AT nanometer size scales one often finds unexpected behavior of matter. A particularly appealing example is the spontaneous formation of chains of metal atoms upon breaking a metallic contact [1–3]. Pt is a metal with a modestly Stoner-enhanced magnetic susceptibility, indicating proximity to a ferromagnetic state. A transition to ferromagnetism can be induced by an increase in the density of states due to Van hove band edge singularities at the Fermi level. This can bring the system beyond the Stoner limit, e.g. by reduction of dimensions, as evidenced by recent work on Pt clusters of 10 atoms [4]. This makes it likely that for purely 1D systems magnetism may also develop, i.e. for atomic chains. Regarding long-range order the Leib-Mattis theorem predicts that the ground state of the 1-D system should be non magnetic. However, local magnetic order in an atomic chain of finite length suspended between the two bulk metal leads could still develop. Moreover, a large magnetic anisotropy energy barrier makes magnetic state as ground state of 1-D system feasible [5]. For these reasons, the ferromagnetic order predicted from model calculations for atomic chains [6–10] was not fully unexpected. Remarkable features for Pt atomic chains are the fact that the Stoner instability is expected close to the equilibrium lattice spacing, and that it becomes more pronounced with increase in chain length [7]. The obvious question is how to obtain experimental evidence for this induced local moment magnetism in the Pt monatomic chains. For Pt atom contacts an advantage is the fact that the leads are paramagnetic and that any evolution of magnetism can be safely attributed to the point contact. Here, we exploit shot noise, the intrinsic noise due to the discrete character of the electronic charge, for revealing information on the magnetic state of Pt atomic chains. We find evidence for a non-magnetic ground state of the conductance channels for Pt atomic chains in our experiments.

6.2 FORMATION OF PT ATOMIC CHAINS

FORMATION of platinum atomic junctions was done at liquid helium temperatures using mechanically controllable break junctions (MCBJ) [11, 12]. The electronic circuit for the measurement is shown schematically in figure (3.5). The sample chamber was pumped to $\sim 10^{-5}$mbar before cooling down in liquid helium. The chamber was fitted with active charcoal for cryogenic pumping such that the pressure in the chamber drops below measurable values at liquid He temperature. Once cold and under vacuum the Pt sample wire was first broken by mechanical bending of the substrate. By relaxing the bending the broken wire ends can be rejoined and the size of the contact can be adjusted with sub-atomic preci-

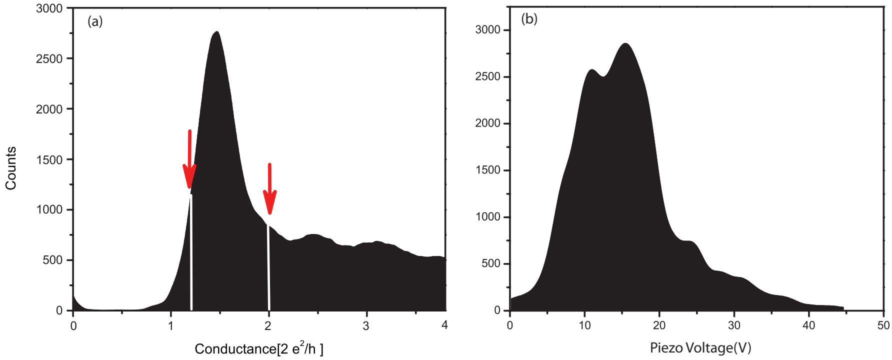

FIGURE 6.1: DC characterization of Pt atomic contacts: (a) Conductance histogram for a clean Pt contact at liquid helium temperatures. Histogram made from 1000 conductance traces. The peak at $1.5G_0$ shows the typical conductance of the clean Pt atomic contact. (b) Corresponding length histogram recorded for a Pt break junction, by recording the lengths of the conductance traces between the boundaries shown by the red arrows in (a).

sion by means of a piezo-electric actuator.

6.2.1 DC CHARACTERIZATION

Before starting shot noise measurements the Pt contact was first characterized by recording a conductance histogram, figure (6.1 a). The conductance histogram for a clean Pt contact at liquid helium temperatures is recorded by combining one thousand conductance breaking traces. Contacts are repeatedly made and broken, controlled by the piezo voltage that regulates the substrate bending of the mechanically controllable break junction device, at a fixed bias voltage setting of 80mV. The points of the digitized traces of conductance are collected into a histogram and the counts are plotted as a function of the conductance. The first peak at $\sim 1.5\cdot(2e^2/h)$ represents the average conductance of a contact of a single Pt atom in cross section. Below this peak the count drops to very low numbers, indicating that the contact finally breaks to a clean vacuum tunnel junction. Note that we use units[1] of $2e^2/h$ here for reasons of comparing to earlier work, but that the conductance units per spin, e^2/h, are used throughout the text in this chapter. The arrows indicate the boundaries used for recording length histograms as in figure (6.1 b). Figure (6.1 b) shows a length histogram obtained for a clean Pt junction at low temperatures. This is used to verify chain formation and for calibrating the displacement. The histogram in figure (6.1 b) is obtained by combining 4500 traces and recording the length of the conductance plateaux with conductances between

---

[1] $1G_0 = 2e^2/h$

1.2 and 2 times $(2e^2/h)$, *i.e.* in the range of the first conductance peak between the red arrows in figure (6.1 a). The length axis is given in units of the voltage on the piezo element, where the proportionality constant is 2.5 V/Å. The histogram is consistent with the earlier work of Untiedt *et al.*[1]. The first three peaks can be interpreted as the lengths corresponding to chains of 2, 3, and 4 atoms.

6.2.2 AC CHARACTERIZATION

Differential conductance spectra were measured by means of a small modulation voltage (2mV and 2.3kHz) and a lock-in amplifier. Typical differential conductance traces measured on Pt atomic contacts of several lengths are shown in figure (6.2). The differential conductance traces have predominantly zero bias anomalies in the form of a Kondo-like dip, a Kondo-like peak or split peak features. The zero bias anomalies seen here for Pt atomic contacts are similar to what has been seen for ferromagnetic atomic contacts (see figures (7.4, 7.5)). In a few cases clear step features have been seen that could be attributed to the inelastic electron-phonon interaction, similar to the inelastic features seen in case of Au atomic contacts, see section 4.2.2.

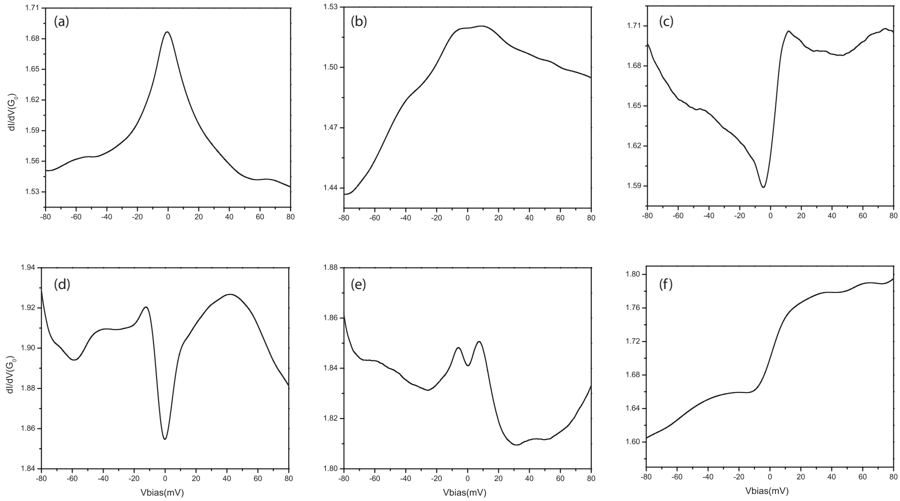

FIGURE 6.2: Differential conductance spectra for Pt atomic contacts: The variation in the differential conductance spectra is quite rich. It shows zero bias peaks, dips, or Fano-like resonances, and step features that may be due to inelastic interaction

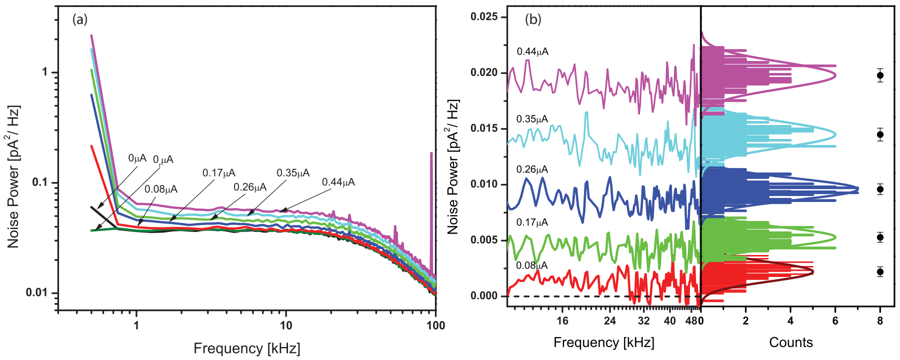

FIGURE 6.3: An example of the noise power data analysis. (a) Noise power spectra for a Pt atomic chain of ~ 3 atoms in length having a conductance $G = 1.52 \cdot (2e^2/h)$ and a Fano factor F=0.192. The peaks are due to spurious signals that could not be fully shielded. (b) Same data after subtracting the thermal noise and correcting for the roll-off. The spurious signals are effectively removed by the subtraction procedure.

6.3 SHOT NOISE SPECTROSCOPY

SHOT noise was measured by using two sets of low-noise amplifiers, with a total amplification factor of 10^5, and by taking the cross spectrum of the two channels in a frequency range between 250Hz and 100kHz. After averaging of 10^4 spectra the uncorrelated noise of the preamplifiers is strongly suppressed. During the shot noise measurements the conductance circuit was disconnected in order to eliminate external noise sources. An example of noise spectra for a series of current settings is given in figure (6.3), which illustrates how the noise power is obtained from the data. The spectra are flat in the middle but at the low-frequency end one observes an increase above the white noise level due to a $1/f$-like noise contribution. The amplitude of this feature varies between different junction settings, and it has been attributed to defect fluctuations in the leads [13]. This part of the spectrum is ignored for the analysis, but it influences the accuracy of the determination of the white noise power. At the high-frequency end of the spectrum a roll-off is seen, with a characteristic frequency of about 50kHz that is due to the RC time constant of the stray capacitance of the leads in combination with the junction resistance. Finally, a slight upturn in the spectra at the highest frequencies is due to residual correlations in the noise of the two amplifiers. The analysis presented below eliminates the roll-off, but is sensitive to the residual correlations and the $1/f$ noise, which limit the accuracy in determination of the Fano factor.

After the initial characterization of the junction an atomic chain was made by pulling, starting from a large contact until the conductance dropped to a value near $1.8 \cdot (2e^2/h)$. Measurements of conductance and noise were taken at several points of subsequent stretching starting from here. The corresponding piezo voltages were recorded in order to identify the length in terms of the mean number of atoms forming the chain. The zero-bias differential conductance, dI/dV, was recorded, which is needed in combination with the noise for the analysis of the conductance channels. The accuracy of the ac conductance measurement is better than 1%, as verified by tests on standard resistors. First, the thermal noise is recorded at zero bias, and after taking noise spectra at several bias settings the zero bias noise is recorded once more (labeled as $0_r \mu$A) in order to verify that the junction has remained stable. The thermal noise level corresponds to a temperature of 6.3 K, which agrees within the accuracy of the temperature measurement with a reading of 6.1 K, as obtained from a ruthenium oxide 10k resistance thermometer. For several junction settings conductance measurements were repeated after the shot noise bias sequence in order to detect possible changes in the conductance. Typical changes observed were smaller than 2%. Figure (6.3 b) shows that the spectra become white above 10kHz after correction for the roll-off with a single RC time constant. The thermal noise (at zero bias) is subtracted, which explains the negative values in the data fluctuations for the lowest currents. The data points are projected in the form of a histogram, shown at the right, and the level of white noise is obtained from the position of the center of the histogram for each voltage bias. The bullets and error bars at the right indicate the position and accuracy of the noise power as determined from a Gaussian fit to the histograms.

6.4 SHOT NOISE IN A SPIN DEGENERATE CONDUCTOR

THE theory for shot noise is discussed in detail in section (1.3) and the measurement techniques are presented in chapter 2. For a nanoscale conductor with N spin non-degenerate conductance channels, each characterized by a transmission probability τ_n, the current noise power at an applied bias voltage V is given by,[2]

$$S_I = 2eV \coth\left(\frac{eV}{2k_\mathrm{B}T}\right) \frac{e^2}{h} \sum_{n=1}^{N} \tau_n (1-\tau_n) + 4k_\mathrm{B}T \frac{e^2}{h} \sum_{n=1}^{N} \tau_n^2 . \tag{6.1}$$

where k_B is Boltzmann's constant, and T is the temperature of the nanoscale conductor. In equilibrium (at $V = 0$) equation (6.1) reduces to the Johnson-Nyquist thermal noise, $4k_\mathrm{B}TG$, describing the current fluctuations that are driven only by the thermal motion of electrons. $G = (e^2/h)\sum \tau_n$ is the conductance. Again, in

---

[2] Anticipating spin splitting of the conductance channels we treat conductance channels for each spin direction separately. Equation (6.1) is similar to equation (1.23), except that the spin degeneracy of the channels is lifted.

the expression for G we take the conductance quantum as e^2/h and sum over spin states. In the low-temperature limit, $k_\mathrm{B}T \ll eV$, equation (6.1) reduces to $S_I = 2e\bar{I}F$, where the Fano factor F measures the quantum suppression of Schottky's classical result,

$$F = \frac{\sum_n \tau_n(1-\tau_n)}{\sum_n \tau_n}. \tag{6.2}$$

From this analysis it is apparent that one may obtain information on the transmission probabilities of the conductance channels by measurement of the noise power, and in favorable cases it is even possible to determine the number of conductance channels [14]. The Fano factor reduces to zero when all conductance channels are either fully blocked ($\tau_n = 0$), or fully open ($\tau_n = 1$). For a nanowire with a given conductance $G = (e^2/h)\sum \tau_n$ the noise has a lower bound that is obtained by taking all open channels to have perfect transmission, except for one that takes the remaining fraction of the conductance. This minimum will sensitively depend on whether the spin channels are restricted to be degenerate. Let us take as an example the case $G = 1.5 \times 2e^2/h$: the minimum Fano factor for the spin degenerate case would be $F = 0.166$, for a channel composition of $\tau_1 = 1$ and $\tau_2 = 0.5$. In case of spin split channels the conductance is written in terms of the transmission probabilities for the spin channels as $3 \times e^2/h$ and the minimum Fano factor is now obtained for all three spin channels completely open, giving $F = 0$. It is this property that we exploit when investigating the magnetic state of Pt atomic chains. This has been elaborated in figure(3.13).

Since shot noise and thermal noise are of comparable magnitude in these experiments it is useful to represent the data such that the expected dependence on the applied bias in equation (6.1) is apparent. The voltage dependence in equation (6.1) can be lumped into a single variable X that we take to be $X = x\coth(x)$, with $x = eV/2k_\mathrm{B}T$. We define the reduced excess noise Y as $Y = (S_I(V) - S_I(0))/S_I(0)$, where $S_I(V)$ is the noise at finite bias, and $S_I(0)$ is the thermal noise, at zero bias. The reduced excess noise is now expected to depend linearly on the control parameter X, $Y = (X-1)F$, from which the Fano factor F can be easily obtained (please see section (3.5.3) for details). Figure (6.4) shows a series of measurements on a Pt atomic chain with a conductance of $G = 1.425 \pm 0.01(2e^2/h)$ at a short length of 2 atoms in the chain, for 26 settings of the bias voltage in the range from 0mV to 16.6mV (0 to 1.83μA). The slope of the plot gives a Fano factor $F = 0.269 \pm 0.009$. The accuracy for each of the points is 3%, as obtained by a fit to the power spectrum after correction for the roll-off as in figure (6.3). The measurement required about 50 minutes, illustrating the long-term stability of the atomic chains. It shows a very nice agreement with the expected dependence, and the scatter around the linear slope is within the data point accuracy.

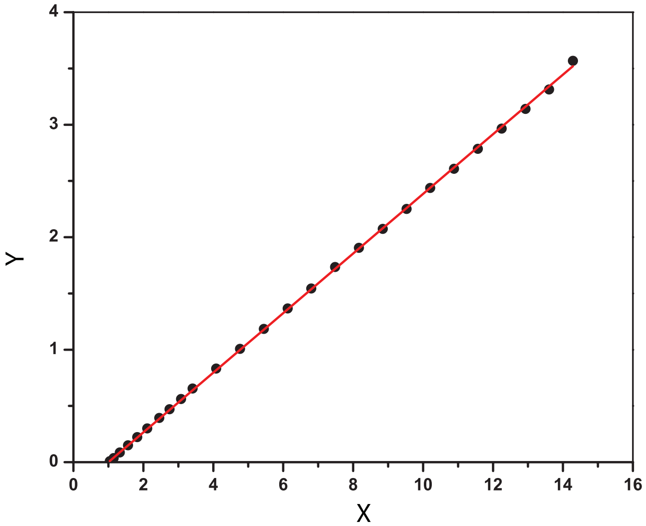

FIGURE 6.4: Reduced excess noise $Y = (S_I(V) - S_I(0))/S_I(0)$ for a Pt atomic chain. The excess noise is given as a function of $X = x\coth(x) = (eV/2k_BT)\coth(eV/2k_BT)$, for a chain having a conductance of $G = 1.425 \pm 0.01(2e^2/h)$ at a length of about 2 atoms in the chain. The slope of the linear fit (solid red line) gives a Fano factor $F = 0.269 \pm 0.009$.

We have recorded similar plots for over 500 configurations of Pt atomic chains of various length, for which we took 7 bias voltage points between 0 and 0.44μA. When the scatter in the plot of the reduced excess noise was larger than 3%, or the thermal noise at start and end of the measurement differed by more than 2%, we rejected the data. The scatter is mostly due to a large $1/f$ component in the noise spectrum and the contribution of the residual amplifier noise correlations to the spectra. After this selection 119 configurations remain. Figure (6.5) shows the Fano factors determined from these 119 sets of shot noise measurements.

The red curve shows the minimum noise curve when spin degeneracy is imposed. Relaxing spin degeneracy results in a minimum noise curve shown by the black curve. The blue broken lines show the *maximum* noise that can be obtained with $N = 4$ or $N = 6$ (spin) channels. This maximum is obtained by taking all channels to have the same transmission probability $\tau = Gh/Ne^2$, leading to $F = 1 - \tau$. The measured data points form a diffuse cloud in (G,F)-space, with its centre of mass near $G = 1.5 \times (2e^2/h)$ and a spread in this conductance in agreement with the position and width of the first peak in the conductance histogram. A large fraction of the points lie above the line labeled $N = 4$, which represents the maximum

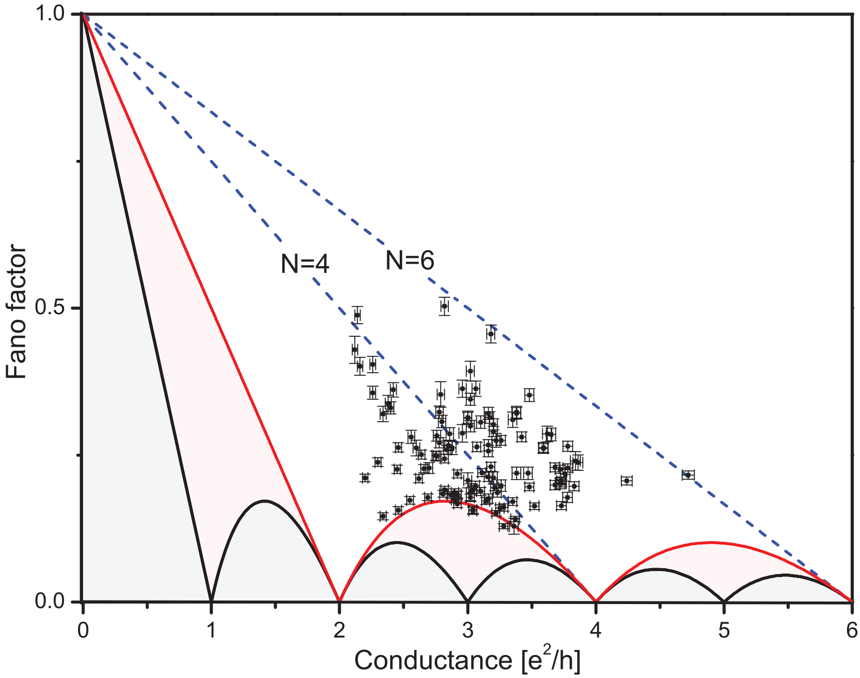

FIGURE 6.5: Fano factor vs. conductance for 119 different Pt atomic chain configurations. The bold red curve shows the minimum noise curve that applies when spin degeneracy is imposed. Relaxing the requirement of spin degeneracy results in a minimum noise curve shown by the thin black curve. The inset illustrates the principle of the break junction experiment.

Fano factor when only four channels are available. This shows that these Pt atomic chains have at least five conductance channels, in agreement with calculations [8, 15, 16]. The points below the blue broken line $N = 4$ can be explained by four channels, but for the majority of points the only conclusion we can draw is that *at least* four channels are involved. The most striking observation, and the central result is that all Fano factors for the Pt chain configurations fall on, or well above, the curve describing the minimum noise for *spin-degenerate* channels. More than 15% of the measured points are even found to coincide within the error bars with the minimum Fano curve for spin-degenerate channels, and none of the points are found significantly below it. For spin-split conductance channels the limiting curve is represented by the black curve in figure (6.5) [17, 18]. This suggests that any possible spin splitting of the conductance channels in the Pt atomic chains formed in the experiment is small, which does not appear to agree with the results

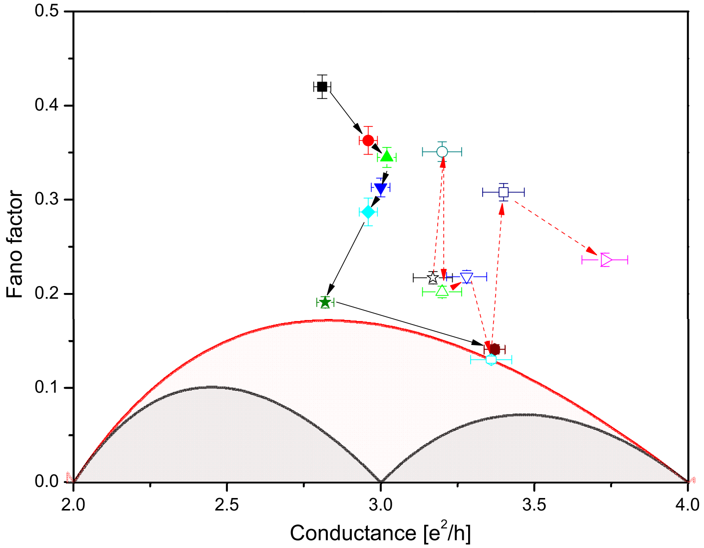

FIGURE 6.6: Fano factor evolution with stretching sequence of the Pt atomic contact. Two examples are shown of the evolution of conductance *G* and Fano factor *F* when a Pt atomic chain is stepwise elongated. The stretching sequence has a length of 3.0V on the piezo (~ 12Å, solid arrows and filled symbols) and 3.52V (~ 14Å, dashed arrows and open symbols), corresponding to 5 or 6 atoms final length, respectively. These two examples are chosen to illustrate that there does not appear to be a systematic evolution towards the minimum noise curve for longer chains, although points at the boundary curve are more frequently found for longer chains.

from DFT calculations [6, 8–10, 16]. The most complete calculations [8], fully relativistic Density Functional Theory for realistic chain sizes, show that a magnetic moment above 0.4μB per atom already appears for a chain only three atoms in length, at equilibrium interatomic distance. Most points in figure (6.5) are measured for Pt chains of 3 to 4 atoms in length, occasionally 5 or 6 atoms. We do not find any systematic evolution of the Fano factor with stretching of the chain. While increasing the length of the chain in steps the Fano factor may be seen to jump towards the minimum noise curve, but then it jumps away from the curve to higher values at next steps in increasing the chain length (see figure (6.6)). A second remarkable observation is the fact that there is a group of 18 points that coincide with the curve describing the minimum noise power for spin degenerate channels. All calculations predict that at least six spin channels are involved, [8, 15, 16, 19], but the transmission probability for each of these channels may be sensitive to the particular arrangements of the atoms at the leads. Pauly *et al.* have presented tight binding model calculations for Pt atomic chains at many stages of stretching of the contact [20]. Their results, that do not include spin polarization, show that frequently the system is found in a configuration with one spin-degenerate channel nearly fully open, while there is only one additional spin-degenerate channel that has significant contribution to the conductance. These configurations may correspond to the ones at the red boundary in figure (6.5).

6.5 THEORY AND DISCUSSION

We wish to evaluate the impact of spontaneous spin polarization of long chain Pt break junctions on their electron transmission, and from that on their shot noise. Spin polarized DFT, including spin orbit interaction,[8, 9], (with the possible addition of self-interaction corrections for d orbitals) constitutes in principle a valid approach to this problem. To be sure, DFT is a mean field theory, ignoring all possible many body Kondo screening effects – generally non negligible at magnetic atomic and molecular contacts.[21]. However in long chains whose overall spin is expected to be large, $S \gg 1/2$, magnetic anisotropy will only allow for two low energy states $\pm S$. In that case, it will be impossible for conduction electrons to cause spin flip, and no Kondo screening and no zero bias anomalies should occur, in agreement with experiment – except possibly for $S = 1/2$, a situation which may be realized in very short contacts.

Moreover, because the calculated energy barrier between states S and $-S$ of the chain is very large[9], we anticipate a blocking temperature safely above 4 K, so that thermal fluctuation effects should also be negligible during the typical short electron traversal time across the contact.

High symmetry Pt chain contact spin polarized DFT calculations showed a large number of channels and a conductance generally above $2G_0$, to be compared with an experimental break junction histogram peak around $1.5G_0$. Spontaneous polarization emerges from 3-atom chains upwards, increasing with chain length and with chain stretching. Somewhat disappointingly however, the predicted dependence of transmission and of ballistic conductance upon the onset of magnetism was only modest. The reason for the relative insensitivity of transmission upon magnetism is that the main electronic state driving magnetism, $|m_j| = 5/2$, has a narrow-band d character, with a small group velocity at the Fermi level, and low or negligible electron transmission. On the other hand, wide-band states with a large group velocity that dominate electron transmission, and thus both conductance and shot noise, possess more s-band admixture and are only modestly spin polarized. As we will see, that insensitivity carries over to shot noise.

Ideally, we would need to calculate transmission, conductance and noise applying the same DFT accuracy of [8] to realistic geometries such as those identified in Ref. [20]. Even without that, we can anticipate that the main effect of reduced symmetry in long chain contacts will again be, as in the tight binding modeling of Pauly *et al.*, to effectively block most channels except four surviving ones. In that case, a qualitative understanding of their spin polarization dependence can be obtained even without explicitly calculating transmissions, by simply studying the conduction channels of the infinite ideal chain. Its simple electronic structure in the end is better suited for qualitative understanding than a specific, cumbersome calculation for long chain contact transmission and noise. The main questions are: what is the level of spin polarization of those chain bands that will lead to surviving channels, and what effect would that magnetism have on noise? Another question is whether the presence of Pt chain magnetism could be endangered by self-interaction errors, that are uncorrected in straight DFT. To clarify first this last point, we conducted DFT calculations, for the infinite ideal Pt chain at its equilibrium spacing of 2.35Å , in three different flavors, namely LSDA, LSDA+U and LSDA+U+J, as implemented in the PWSCF code of Quantum Espresso[22].

As shown in figure (6.7), mitigation of self-interaction errors does lead to a change of magnetism. Addition of a small Hubbard U=1eV for d states is enough to quench magnetism at equilibrium spacing as in (b). However, upon successive addition of a moderate exchange parameter ($J = 0.5$ eV is a standard value for Pt) the chain reverts back to strong magnetism as shown in (c). This leads us to conclude that the uncertainty connected with self-interactions in DFT, an aspect only rarely addressed so far in this context [23], makes the presence and magnitude of spin polarization hard to predict in a Pt chain contact at zero mechanical strain. Nonetheless, we find that a frank spin polarization is recovered even in the worst case for even moderately stretched chains. A substantial level of strain is generally expected in chains formed by break junctions [20], that should therefore be magnetic. Conductance channels in a long chain nanocontact can be identified by infinite chain bands that cross the Fermi level. For increasing k-vector, there are in all cases six channels: $(1\pm) m_j = \pm 1/2(d_z^2 + s)$; $(2\pm)$ $m_j = \pm 3/2(d_{xz}, d_{yz})$; $(3\pm) m_j = \pm 1/2(s + d_z^2)$. In addition, depending on spontaneous magnetization, additional d channels $(4\pm)$ $m_j = \pm 3/2$, and (5-) $m_j = -5/2$ may also be open at Fermi. The latter band is poorly dispersive (has a small group velocity) and is largely spin split across Fermi by magnetism, and can be considered the main "actor" band responsible for spontaneous spin polarization. Other bands are "spectators" whose spin splitting is small or irrelevant, while their group velocities at Fermi are larger. Even without a detailed calculation, the circumstances of conduction in Pt chain contacts are now apparent. The fully spin polarized actor channel(s) is easily blocked because of its large mass, and only some of the poorly po-

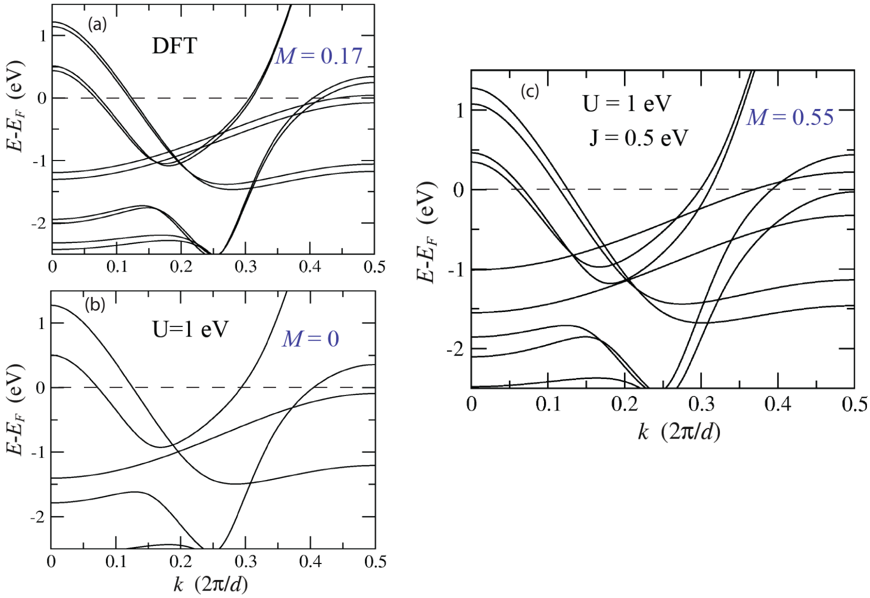

FIGURE 6.7: Electronic structure of an infinite Pt chain at T=0 and at the equilibrium spacing of 2.35Å, calculated by DFT in different approximations, namely: (a) LSDA, yielding a spin moment of $0.17\mu_B$ and an orbital moment of $0.22\mu_B$ per atom; (see [8] for computational details). (b) LSDA + U with $U = 1$ eV, yielding a nonmagnetic ground state. (c) LSDA+U+J, with $U = 1$ eV and $J = 0.5$ eV, yielding a spin moment of $0.55\mu_B$ per atom. Self-interaction corrections influence magnetism, by either removing it as in (b), or enhancing it as in (c). Magnetism is recovered in all cases under stretching. Bands crossing the Fermi level identify conductance channels in a long chain nanocontact: For increasing k-vector, all cases have six channels: (1±)$m_j = \pm 1/2(d_z^2 + s)$; (2±) $m_j = \pm 3/2(d_{xz}, d_{yz})$; (3±)$m_j = \pm 1/2(s + d_z^2)$. Depending on magnetization, additional d channels (4±) $m_j = \pm 3/2$, and (5-) $m_j = -5/2$ also cross Fermi.

larized, less massive ones conduct. The small spectator channel spin splittings are expected to have a negligible effect on transmission. As a result, conductance is poorly spin sensitive, and so is shot noise.

Experimental conductance and Fano factors are reasonably compatible with $\tau_{4\pm} = \tau_5 \sim 0$, and with e.g., $\tau_{1\pm} \sim 0.25$, $\tau_{2\pm} \sim 0.25$, $\tau_{3\pm} \sim 1$, or even better with $\tau_{1\pm} \sim 0.5$, $\tau_{2\pm} \sim 0$, $\tau_{3\pm} \sim 1$, restricting conductance in this case to the two channels that contain some s admixture. The latter hypothesis is particularly attractive, both because the large kinetic energy of s electrons naturally suggests a larger transmission despite low symmetry, and because in that two band case the shot noise will fall neatly on the two channel boundary, as noted for 18 experimental points.

6.6 CONCLUSION

It has been argued [24] that the zero bias anomalies observed in the differential conductance for Pt atomic chains provide evidence for local magnetic order. Indeed, the differential conductance often shows a pronounced structure near $V = 0$ (see figure (6.2)). However, this structure is very irregular and may have any sign or structure, which hampers a straight-forward interpretation. The shot noise measurement provides no direct evidence for magnetic order in the conductance channels for Pt atomic chains. Theoretical arguments however suggest that conductance and noise should involve only weakly polarized channels, where presence or absence of magnetism will make very little difference. A simple model where only two channels that contain s and d state admixture carry all the current is compatible with the data and the DFT calculations. Theoretically, it is found that safe predictions cannot be made about unstrained Pt chain magnetism without a proper correction, not yet available, of self-interaction errors in DFT. Yet, the strained Pt chains which are likely to dominate break junction histograms should theoretically be magnetic, and also possess a large orbital moment besides the spin moment. If any magnetic order is present for a consistent interpretation we would have to assume such moments would be formed by states that do not participate in the conductance.

In conclusion, we find strong evidence for an absence of strong magnetic order in the conductance channels for Pt atomic chains. The fact that this observation disagrees with many DFT-based computations suggests that effects beyond the present models, such as electron-electron correlations, may need to be considered. Some other tool will need to be devised to check whether this state of affairs is realized or not.

REFERENCES

[1] C. Untiedt, a. Yanson, R. Grande, G. Rubio-Bollinger, N. Agraït, S. Vieira, and J. van Ruitenbeek, *Calibration of the length of a chain of single gold atoms*, Physical Review B **66**, 1 (2002).

[2] A. I. Yanson, G. R. Bollinger, H. E. van den Brom, N. Agrait, and J. M. van Ruitenbeek, *Formation and manipulation of a metallic wire of single gold atoms*, Nature **395**, 783 (1998).

[3] K. T. Hideaki Ohnishi, Yukihito Kondo, *Quantized conductance through individual rows of suspended gold atoms*, Nature Physics **395**, 780 (1998).

[4] X. Liu, M. Bauer, H. Bertagnolli, E. Roduner, J. van Slageren, and F. Phillipp, *Structure and Magnetization of Small Monodisperse Platinum Clusters*, Phys. Rev. Lett. **97**, 253401 (2006).

[5] J. Dorantes-Dávila and G. M. Pastor, *Magnetic Anisotropy of One-Dimensional Nanostructures of Transition Metals*, Phys. Rev. Lett. **81**, 208 (1998).

[6] A. Delin and E. Tosatti, *Magnetic phenomena in 5d transition metal nanowires*, Phys. Rev. B **68**, 144434 (2003).

[7] J. Fernández-Rossier, D. Jacob, C. Untiedt, and J. J. Palacios, *Transport in magnetically ordered Pt nanocontacts*, Phys. Rev. B **72**, 224418 (2005).

[8] A. Smogunov, A. Dal Corso, and E. Tosatti, *Magnetic phenomena, spin-orbit effects, and Landauer conductance in Pt nanowire contacts: Density-functional theory calculations*, Phys. Rev. B **78**, 014423 (2008).

[9] A. Smogunov, A. D. Corso, A. Delin, R. Weht, and E. Tosatti, *Colossal magnetic anisotropy of monatomic free and deposited platinum nanowires*, Nature Nanotechnology **3**, 22 (2008).

[10] A. Thiess, Y. Mokrousov, S. Heinze, and S. Blügel, *Magnetically Hindered Chain Formation in Transition-Metal Break Junctions*, Phys. Rev. Lett. **103**, 217201 (2009).

[11] D. Djukic and J. M. van Ruitenbeek, *Shot noise measurements on a single molecule*, Nano Letters **6**, 789 (2006).

[12] N. Agraït, *Quantum properties of atomic-sized conductors*, Physics Reports **377**, 81 (2003).

[13] D. C. Ralph and R. A. Buhrman, *Observations of Kondo scattering without magnetic impurities: A point contact study of two-level tunneling systems in metals*, Phys. Rev. Lett. **69**, 2118 (1992).

[14] H. van den Brom and J. van Ruitenbeek, *Quantum Suppression of Shot Noise in Atom-Size Metallic Contacts*, Physical Review Letters **82**, 1526 (1999).

[15] S. K. Nielsen, M. Brandbyge, K. Hansen, K. Stokbro, J. M. van Ruitenbeek, and F. Besenbacher, *Current-Voltage Curves of Atomic-Sized Transition Metal Contacts: An Explanation of Why Au is Ohmic and Pt is Not*, Phys. Rev. Lett. **89**, 066804 (2002).

[16] J. Fernández-Rossier, D. Jacob, C. Untiedt, and J. J. Palacios, *Transport in magnetically ordered Pt nanocontacts*, Phys. Rev. B **72**, 224418 (2005).

[17] P. Roche, J. Ségala, D. C. Glattli, J. T. Nicholls, M. Pepper, A. C. Graham, K. J. Thomas, M. Y. Simmons, and D. A. Ritchie, *Fano Factor Reduction on the 0.7 Conductance Structure of a Ballistic One-Dimensional Wire*, Phys. Rev. Lett. **93**, 116602 (2004).

[18] L. DiCarlo, Y. Zhang, D. McClure, D. Reilly, C. Marcus, L. Pfeiffer, and K. West, *Shot-Noise Signatures of 0.7 Structure and Spin in a Quantum Point Contact*, Physical Review Letters **97**, 1 (2006).

[19] L. de la Vega, A. Martín-Rodero, A. L. Yeyati, and A. Saúl, *Different wavelength oscillations in the conductance of* 5d *metal atomic chains*, Phys. Rev. B **70**, 113107 (2004).

[20] F. Pauly, M. Dreher, J. Viljas, M. Häfner, J. Cuevas, and P. Nielaba, *Theoretical analysis of the conductance histograms and structural properties of Ag, Pt, and Ni nanocontacts*, Physical Review B **74**, 1 (2006).

[21] P. Lucignano, R. Mazzarello, A. Smogunov, M. Fabrizio, and E. Tosatti, *Kondo conductance in an atomic nanocontact from first principles*, Nature Materials **8**, 563 (2009).

[22] URL `http://www.pwscf.org`.

[23] M. Wierzbowska, A. Delin, and E. Tosatti, *Effect of electron correlations in Pd, Ni, and Co monowires*, Phys. Rev. B **72**, 035439 (2005).

[24] M. R. Calvo, Fernández-Rossier, Joaquín, Palacios, J. José, D. Jacob, Natelson, Douglas, and C. Untiedt, *The Kondo effect in ferromagnetic atomic contacts.*, Nature **458**, 1150 (2009).

7

KONDO EFFECTS IN FERROMAGNETIC ATOMIC CONTACTS

Manohar KUMAR, Zheng BARDMANN, Kiran KUMAR,
Jan van RUITENBEEK

The differential conductance measurements on Pt atomic contacts show dominant zero bias anomalies similar to what is seen for Kondo systems. The Kondo effect is a many-body electron scattering problem that is usually found for magnetic impurities in a non-magnetic host metal. The recent experiments by Calvo et al. [1] unexpectedly show similar zero bias anomalies in ferromagnetic atomic contacts. They attributed these anomalies to the presence of localized magnetic moments in the atoms in the contact interacting with the continuum states in the bulk leads. Here we have used noise measurements to investigate the origin of the zero bias anomalies in the ferromagnetic atomic contacts and critically evaluate a possible connection to Kondo scattering. For this purpose we have studied the evolution of the conductance and noise while mechanically tuning the Kondo-like anomaly.

7.1 ZERO BIAS ANOMALIES AND THE KONDO EFFECT IN PCS

THE Kondo effect in ferromagnetic atomic contacts has been a topic of recent interest. Most of the previous studies were concerned with, either, quantum dots having an odd number of electrons [2–7], with magnetic ad-atoms on non-magnetic host metal surfaces [8–10], with metal complex ligand/single molecule devices [11], or with carbon nanotubes [12]. In all of the above cases the studies involved localized magnetic moments interacting with a non-magnetic electron bath. Very recently Calvo *et.al.* [1] presented the first discussion of Kondo effects in ferromagnetic atomic contacts formed in break junctions. They observed Kondo-like zero bias anomalies in ferromagnetic atomic contacts for Fe, Ni, and Co.

The zero bias anomalies in the differential conductance have been associated with Kondo scattering, but other effects lead to similar signals. Notably, scattering of the electrons in the point contact with slow two-level fluctuators (s-TLF's) present close to the point contact [13, 14] is often hard to discriminate from signals due to Kondo scattering.[1] Experimentally, s-TLF's are found in metallic glasses and have been observed in disordered metallic contacts by Ralph and Burman [17], Akimenko and Gudimenko [18], and by Keijsers *et al.* [19]. A critical observation in the latter work was that both the theories by Kozub and Kulik [14] and by Vladar and Zawadowski [13] fail to explain the observed zero bias anomalies for contact resistances above ~ 400Ω. Experiments have clearly shown zero bias anomalies in non-magnetic atomic contacts [20–22] so that a non-magnetic origin and a role of TLF's can not be ruled out. The evidence for a possible Kondo origin of the zero bias anomalies comes from fitting of the differential conductance measured on the ferromagnetic atomic contacts using equation (B.6) [1], see below. However, the similarity of the fits with those observed in established Kondo systems having magnetic impurities in a non magnetic environment [8]are very suggestive. A brief summary of the physics of Kondo effects and zero bias anomalies is given in Appendix B.

In ferromagnetic atomic contacts, both, the local magnetic moment and the itinerant electron bath are formed by atoms of the same species. The proposed scenario in this case is that low coordination of the central atoms in the atomic contact leads to the formation of localized moments that are weakly coupled to the delocalized electrons in the leads. According to ref. [23] enhanced s-d hybridization, anti-ferromagnetic coupling J^{AF}_{s-d} with s-p itinerant electrons, and reduced d-d ferromagnetic coupling with neighboring atoms in the leads could give rise to

---

[1] Another physical phenomenon which could also give a zero bias dip in differential conductance spectra is (dynamical) Coulomb blockade [15, 16]. This effect could only explain dips in the differential conductance, making this interpretation less applicable.

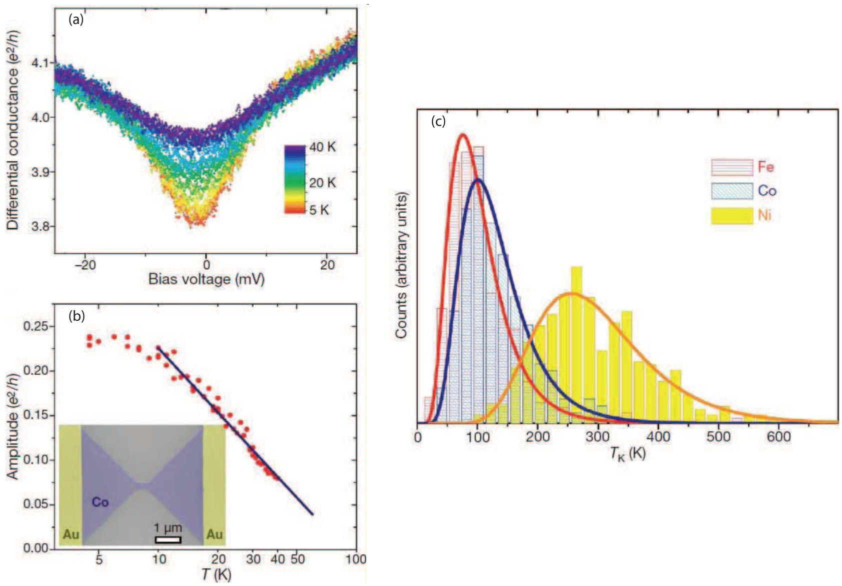

FIGURE 7.1: Kondo effect in the ferromagnetic atomic contacts: (a) Evolution of the Kondo resonance with the temperature in Co-Co atomic contacts. (b) Logarithmic decrease in the Kondo resonance amplitude with the increase in the temperature. The inset shows the point contact device in a false-color SEM image. (c) The Kondo temperature obtained from its to the differential conductance on ferromagnetic atomic contacts for Fe, Ni and Co. Taken from Calvo *et al.* [1].

the formation of a Kondo system. Figure (7.1) shows the central result of Calvo *et al.* Figure (7.1 a-b) shows the evolution with temperature of the zero bias anomaly observed in a Co atomic contact. The logarithmic dependence of the resonance amplitude with temperature agrees with the behavior expected for a Kondo effect, although the range of temperatures is limited. From a Lorentzian fit of the differential conductance values for the Kondo temperatures of the atomic contacts were obtained and the results are shown in figure (7.1 c). The logarithmic dependence of the resonance amplitude on the temperature shown by Calvo *et al.* is also compatible with an interpretation in terms of s-TLFs in the contact. In order to further test the nature of the zero bias anomaly we have measured shot noise for ferromagnetic atomic contacts. In case of s-TLFs in the atomic contact one would expect Lorentzian noise spectra, as illustrated in figure (1.7) [18], with large (super-Poissonian) noise power.[2] In contrast, the spectra we have observed are white and

---

[2] This has been studied in detail by van den Brom *et al.* [24].

the noise power stays below the Schottky value (is sub-Poissonian). Although this would provide support for the Kondo interpretation by Calvo *et al.* further experiments will be needed for a more definitive assignment.[3] This chapter is divided in two parts: (a) We present several aspects of the zero bias anomalies, such as mechanical tunning of the zero bias anomalies and inelastic scattering effects in the ferromagnetic contacts. (b) Noise measurements on ferromagnetic atomic contacts. These shot noise measurements were originally done to search for spin polarized channels taking part in the conduction. We have studied ferromagnetic contacts for Ni and Fe using the MCBJ setup.

7.2 NI AND FE ATOMIC CONTACT FORMATION IN MCBJ

Ni or Fe atomic contacts were formed from metallic wires of purity 99.998%, by breaking under cryogenic vacuum. The contact formation process in the break junction can be viewed as the formation of narrower and narrower necks in the contact while stretching, and finally the formation of atomic contacts at the last stages just before breaking. Stretching with sub-angstrom precision of the contact is feasible using a piezo element. Conductance traces were recorded during the process of contact formation. Typical traces observed for Ni and Fe atomic contacts are shown in figure (7.2). Conductance traces for Ni atomic contacts show conductance plateaus around $1.3-1.2G_0$ and $1.6-1.5G_0$ while conductance traces for Fe typically show a last plateau around $2G_0$. Both Ni and Fe fail to form atomic chains. The histograms for the traces of the Ni and Fe atomic contacts confirm the above observations. Typical conductance histograms for Ni and Fe are shown in figure (7.3). The conductance histogram for Ni shows two dominant peaks, one around $1.3G_0$ and another around $1.6G_0$ and the conductance counts drop to a low background around $0.7G_0$. In contrast, Fe atomic contacts show a single dominant peak at $2.1G_0$. The counts drop to very small numbers around $1.1G_0$ and then increase again at lower conductance toward the tunneling regime.

Our experimental observations provide no evidence for peaks at half-integer quanta in the conductance histograms. We do find occasionally traces showing conductance steps near $0.5G_0$, but this averages out on the statistics of all the conductance traces. This demonstrates that these plateaus have no particular significance. In previous experiments half integer quantization peaks were reported for ferromagnetic contacts [25–27]. These observations were interpreted in terms of spin polarization of the electronic current in the contact. However, most of these experiments were either done under ambient atmosphere [26], where contamination of the atomic contact is expected, or the reported histograms are based upon very limited statistics and selection of curves for inclusion in the histograms

---

[3] In our experimental setup we are limited to measurements at a fixed temperature of ~ 6K.

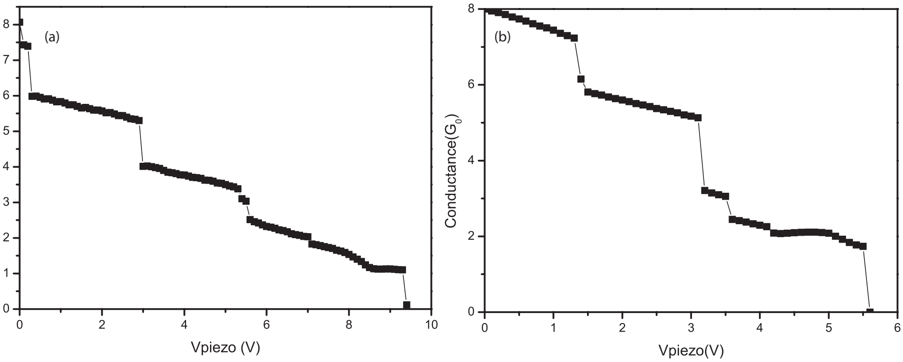

FIGURE 7.2: Typical traces for Ni and Fe ferromagnetic atomic contacts: (a) A conductance trace for a Ni atomic contact showing a last conductance plateau at $1.25G_0$ followed by a break into the tunneling regime upon further stretching. (b) A conductance trace for an Fe atomic contact showing a last plateau at $2.1G_0$, with the conductance monotonically decreasing after further pulling, eventually leading to breaking into the tunneling regime.

[25, 26]. It has been already reported that the contamination of CO in Pt atomic contacts gives rise to peaks resembling fractional quantization [28]. Our observations on the statistical properties of Fe and Ni atomic contacts is in line with previous observations by Calvo *et al.* [29] and by Häfner *et al.*[30]. Fe and Ni are transition metals with electronic configurations [Ar]$3d^6 4s^2$ and [Ar]$3d^8 4s^2$, respectively. The partially filled d bands contribute to the conductance along with the

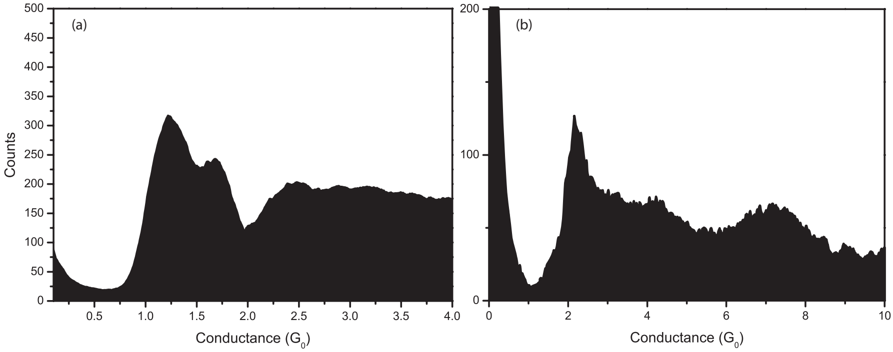

FIGURE 7.3: Typical conductance histograms for ferromagnetic atomic contacts of Ni and Fe: (a) A conductance histogram for Ni atomic contacts showing a peak around $1.3G_0$ and a second peak around $1.6G_0$. (b) A conductance histogram of Fe atomic contacts showing a peak at $2.1G_0$.

hybridized s-p orbitals give rise to a high transmission. The combination of all these orbitals simply produces a total conductance above 1G_0 with several partially transmitting d channels.

7.3 POINT CONTACT SPECTROSCOPY FOR NI AND FE CONTACTS

POINT contact spectroscopy (PCS) for different samples of Ni and Fe was studied. Figures (7.4) and (7.5) show typical differential conductance curves for Ni and Fe atomic contacts. Both Fe and Ni atomic contacts predominantly show zero bias anomalies. Apart from zero-bias peaks and dips, asymmetrical structures were also seen. These zero bias anomalies were absent in our PCS measurements on Au atomic contacts. The origin of these zero bias anomalies have been proposed to be related to localized spin moments in the partially filled d orbitals in the ferromagnetic atomic contacts, leading to Kondo scattering [1].

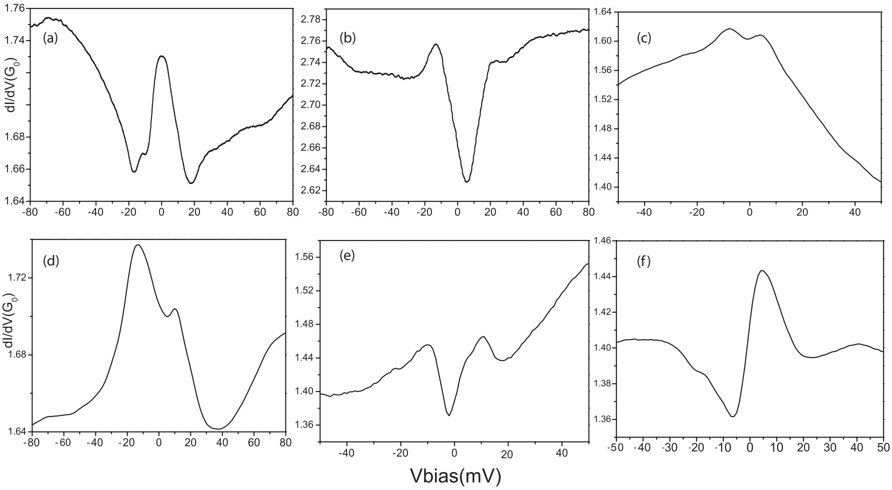

FIGURE 7.4: Typical differential conductance curves for Ni atomic contacts: We observe Kondo-like peaks, dips, split peaks, and Fano-like resonances. All zero bias anomaly features are frequently seen in atomic contacts, with no particular preference.

Figure (7.6) shows Lorentzian fits for differential conductance curves measured on Ni and Fe contacts, using equation (B.6). The fits agree with the observations by Calvo *et al.* suggesting a Kondo signal in our atomic contacts. The associated Kondo temperatures were obtained by fitting hundreds of differential conductance

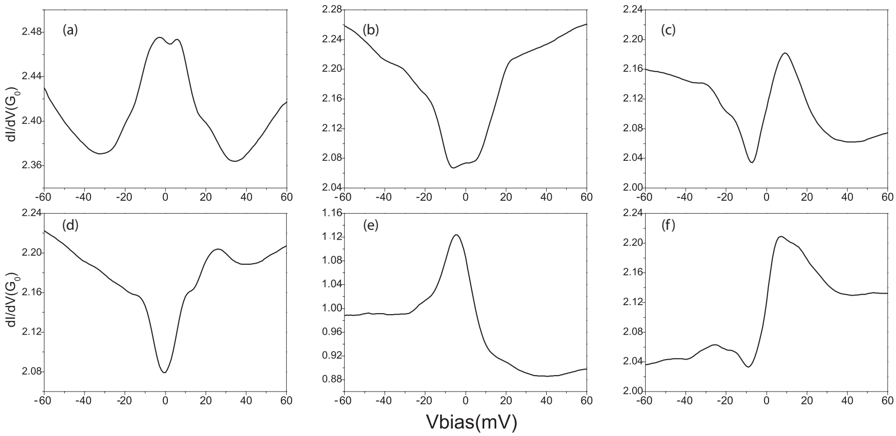

FIGURE 7.5: Typical differential conductance curves for Fe atomic contacts: We observe Kondo-like peaks, dips, split peaks, and Fano-like resonances. All zero bias anomaly features are frequently seen in atomic contacts, with no particular preference.

traces for both Ni and Fe atomic contacts. The average Kondo temperatures obtained in our experiments for Ni and Fe are 230 and 100 K, which is in very close agreement with the values obtained by Calvo *et al.*

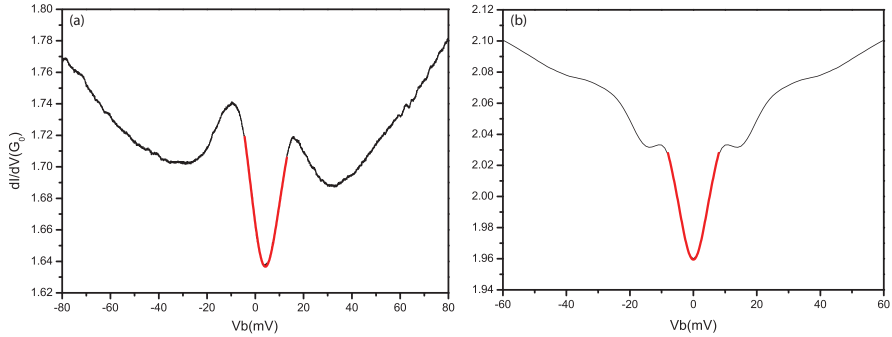

FIGURE 7.6: Lorentzian fits: (a) Lorentzian fit (red) to the differential conductance obtained for a Ni atomic contact. The Kondo temperature obtained from the fit is 118K. (b) The Lorentzian fit (red) to the differential conductance curve obtained for a Fe atomic contact, giving a Kondo temperature of 100K. Equation (B.6) was used for the fitting.

7.3.1 MECHANICAL TUNING OF ZERO BIAS ANOMALIES

Looking at Haldane equation (B.4) the Kondo temperature depends exponentially on the electronic coupling strength. In mechanical controllable break junctions the coupling strength between the presumed localized orbitals on the central atom and the leads can be tunned with sub-Angstrom precision using a piezo element. Hence, for ferromagnetic atomic contacts it should be possible to tune the Kondo temperature by tunning the coupling between the central atom and the leads. For this purpose we started by forming stable atomic contacts and then measuring the differential conductance for various stages of stretching of the junction. This process of stretching and differential conductance measurement is repeated until the junction is broken. Figure (7.7) shows an example for the evolution of the differential conductance upon stretching of a Ni contact. The Ni atomic contact was formed at about $1.5G_0$ and shows a step-like feature in the differential conductance at $\sim$ 10mV. In this case a Lorentzian fit to the curve does not converge. The contact was stretched in steps of 0.05Å and after two steps the Lorentzian fit converges for the new curve and for further stretching of the contact. Kondo temperatures are calculated from the full width at half maximum of the Lorentzian fits to the zero bias anomalies. The Kondo temperature as obtained from the fit and

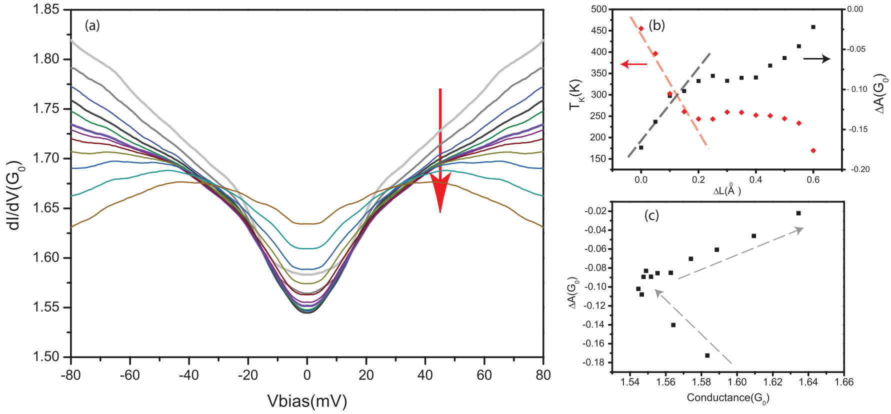

FIGURE 7.7: Evolution of the zero bias anomaly with stretching of a Ni atomic contact: (a) Evolution of the shape of the differential conductance. The Ni atomic contact was stretched in steps of 0.05Å from a conductance of $1.58G_0$ shown in light grey color. The contact is stretched by a total length of 0.6Å and the dip resonance structure is seen to evolve to a double-peak structure. (b) Kondo temperatures are calculated from the full width at half maximum of the Lorentzian fits to the zero bias anomalies of the curves. The Kondo temperatures determined in this way and the amplitudes of the anomalies decrease with stretching of the contact. (c) Evolution of the zero bias conductance with stretching of the contact.

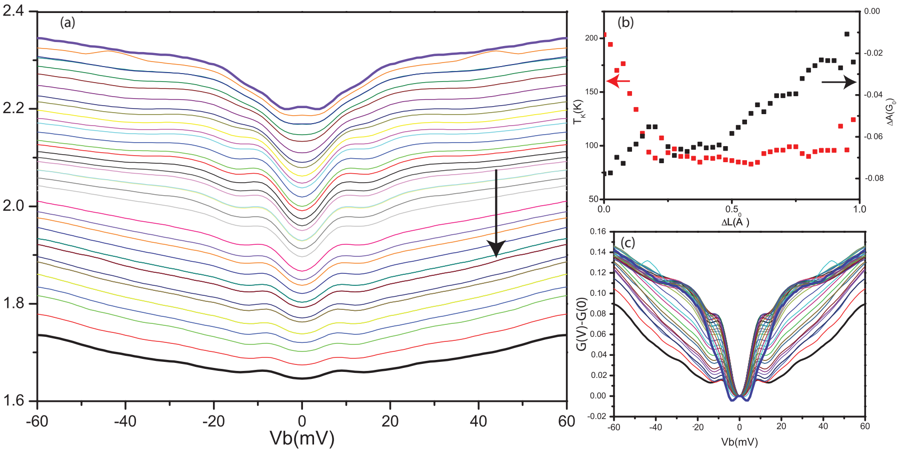

FIGURE 7.8: Evolution of the zero bias anomaly with stretching for an Fe atomic contact: (a) Evolution of the shape of the differential conductance. The Fe atomic contact was stretched in steps of 0.025Å from a conductance of $2.20G_0$ shown in violet color. The contact is stretched by a total length of 0.75Å and a single-dip resonance structure is seen to evolve from an initial double dip structure, similar to Bork *et al.* [31]. (b) Kondo temperatures as obtained from the full width at half maximum of the Lorentzian fits to the zero bias anomalies of the differential conductance curves in (a). The Kondo temperatures obtained in this way and the resonance amplitudes decrease with stretching of the contact, with a saturation after stretching the contact by 0.25Å. (c) The same differential conductance curves shown in (a) now vertically offset by the zero bias conductance, which helps visualization of the evolution of the shape of the curves.

the resonance amplitude both show a monotonous decrease upon stretching of the contact, with a saturation in the region between 0.2Å – 0.4Å . In this range of stretching the conductance G passes through a minimum at $1.54G_0$. This could signal the transition to a new atomic configuration at the contact-lead interface, which may reduce the effective coupling of the central atom in the contact with the leads.

Similar effects are seen in Fe atomic contacts with stretching. Figure (7.8) shows an example of the evolution of the zero-bias anomaly on stretching of the Fe contact in steps of 0.025Å. The Kondo temperature as obtained from the first decreases upon stretching first and then it fluctuates around 80 K-90 K upon further stretching. At this point resonance amplitude keeps decreasing after some saturation. Looking at figure (7.8 c) we see that the initial double dip feature evolves into the dip resonance feature. The merging of the split dip could be related to the observed saturation in the Kondo temperature. We will come back to double resonance structure and its merging into to a single resonance structure in the next

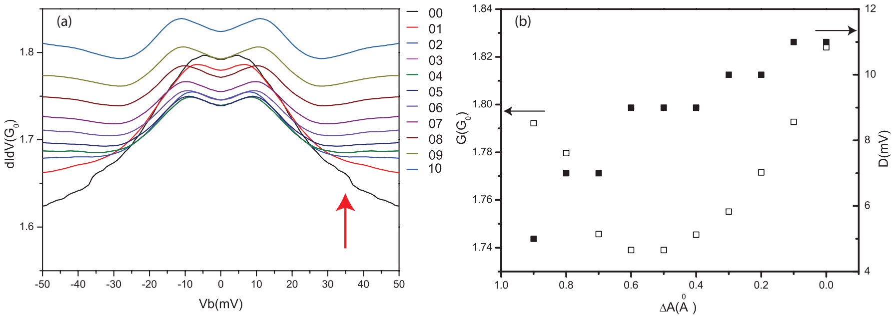

FIGURE 7.9: Splitting of the zero bias peak for a Ni atomic contact upon pushing the electrodes together: (a) Evolution of the resonance into a double peak structure by reducing the electrode distance in steps of 0.1Å from an initial conductance of 1.795G_0, shown in black. (b) Variation of the zero-bias conductance G (open squares) and the separation between the peaks D (filled squares) for the curves shown in (a).

section where we discuss it in terms of possible double Kondo system.

Our observation of a monotonically decreasing Kondo temperature and Kondo resonance amplitude upon stretching of the contact is reminiscent of the observations made by Parks *et al.* [32]. They measured the Kondo temperature for a C_{60}-based single molecule device, which shows a spin-1/2 Kondo resonance. Parks *et al.* used a Au mechanically controllable break junction to control the electrode coupling with C_{60}. They observed changes in the Kondo temperature and amplitude with tuning of the inter electrode spacing, with an effective decrease in the Kondo temperature by 20% over the electrode displacement of 1Å, which is comparable to our observations for the ferromagnetic contacts. In some of cases we have seen negligible changes in the Kondo temperature with the stretching of the contact.

7.3.2 SPLITTING OF THE ZERO BIAS PEAK

A splitting of the zero bias resonance structure is observed for many contacts upon pushing the ferromagnetic atomic contact, the reverse process of that shown in figure (7.8). This is reminiscent of the splitting of a Kondo resonance that can be achieved by the application of a magnetic field [33], which favors the spin triplet state S=1. Figure (7.9) shows an example of this behavior, where splitting of the zero bias peak was seen upon pushing a Ni atomic contact closer together. The distance between the two peaks increases with decreasing electrode distance. Figure (7.10) shows for an Fe atomic contact the merging of the double peak upon stretching of the contact by 0.075Å, a process that was also seen in figure (7.8)

If the resonance is indeed to be attributed to a Kondo resonance, how could we understand the observed splitting? A Kondo peak is expected to split by $2|g|\mu_B B$ in presence of an external magnetic field. A splitting of the Kondo resonance has been predicted in case of ferromagnetic leads coupling to a quantum dot or a molecule having a localized unpaired spin. In this case the zero bias splitting of the Kondo resonance can be understood by considering the large exchange field between the ferromagnetic leads and the central magnetic atom, which can be as large as $50T$ [32]. In an experiment with a better defined local moment Parks *et al.* [34] show zero field splitting of the Kondo resonance for a single molecule junction containing a Co ion, $Au-Co(tpy-SH)_2$, where tpy-SH is 4'-mercapto-2,2':6',2"-terpyridine. In an experiment by Bork *et al.* [31] a splitting of the Kondo resonance is reported in absence of magnetic fields or ferromagnetic leads. In this experiment they measured the Kondo resonance for a tunnel junction between a magnetic atom (Co) on the tip of an STM and a magnetic ad-atom (Co) on the surface of a clean Au sample. They observed an increased splitting of the zero-bias peak in the differential conductance when the magnetic atom on the tip approaches the magnetic ad-atom on the Au surface. By fitting of the Kondo resonance using equation (B.6) they showed that the Kondo resonance is a convoluted peak of two resonance peaks. They associated these two peaks with resonances due to the interaction between the two magnetic impurities, forming a double Kondo system. They did not observe the splitting of the Kondo peak in absence of either of the Co atoms, on the tip or on the Au surface. In presence of only one magnetic atom they obtained the standard Kondo resonance structure only. In absence of both Co

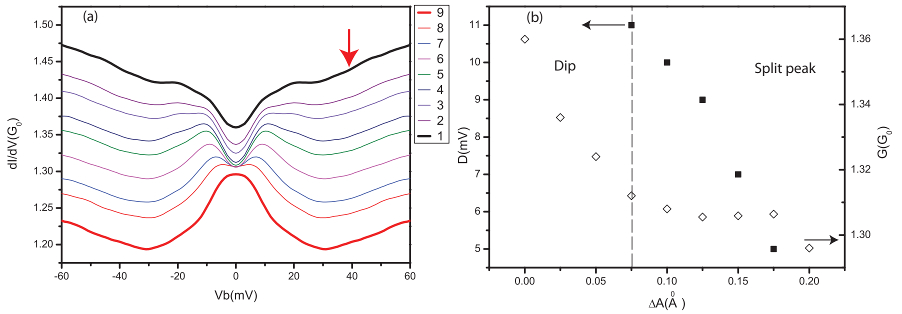

FIGURE 7.10: Splitting of resonance peak upon stretching of an Fe atomic contact: (a) Evolution of the resonance into a double peak structure upon stretching of an Fe atomic contact in steps of 0.025Å from an initial conductance of 1.360G_0, shown in black. (b) Variation of the zero-bias conductance G (open squares) and the separation between the peaks D (filled squares) for the curves shown in (a).The dashed line shows the point at which dip feature evolves into the split resonance structure.

atoms the Kondo resonance was completely absent, showing no significant features in the differential conductance while moving the tip from the tunneling to the contact regime. This shows that the splitting of the zero bias peak is clearly associated with the interaction between the magnetic Co atom on the tip and the Co ad-atom on the Au surface. If local moments can be formed for ferromagnetic atomic contacts in our experiments we could think of a similar mechanism with an atom at the apex of the left lead interacting with one at the right. When these two leads are in contact strong coupling between them leads to interaction between the unpaired spins of two atoms at apex, leading to splitting of the states with even and odd parity. When the atomic contact is stretched the strength of this interaction reduces and the interaction between the d-electron with the s-electrons of the leads becomes dominant and hence gives rise to a singlet Kondo resonant feature at Fermi energy. This interpretation requires further testing.

7.3.3 AN INELASTIC MANY BODY KONDO SIGNAL?

The presence of excited states interacting with a Kondo system can give rise to additional peaks on the flanks of a zero bias Kondo peak. Inelastic electron scattering on vibrons could lead to such signals, for a brief discussion see Appendix B.1.3. Recently, such vibrational side bands have been reported for STM spectroscopy on a single-molecular layer of tetracyanoquinodimethane (TCNQ) by Fernandez-Torrente *et al.* [35]. In these experiments the differential conductance clearly shows the presence of a zero bias anomaly along with side peaks at the vibrational energy. These side peaks were attributed to a phonon assisted Kondo effect taking place in the system.

We have possible observed a similar effect in our differential conductance spectra. Figure (7.11) shows one such differential conductance measured for a Ni atomic contact. The differential conductance shows the double peak structure near zero bias, that transforms into a single peak when changing the distance between the electrodes, in agreement with the observations discussed above. Apart from this central structure we observe side peaks at ±18meV, which would be an acceptable vibrionic energy in view of the known electron-phonon point contact spectrum for Ni [36]. The amplitudes of side peaks and the energy decrease upon stretching of the contact. The decrease in energy of the satellite peaks would suggest a coupling to a longitudinal vibrational mode in the atomic contact. On stretching of the contact to 0.6Å the side peaks merge with the main peak, which may be due to weakening of the electron-vibron coupling strength. In the tunneling regime of conductance figure (7.12) shows another typical feature seen for ferromagnetic atomic contacts. Such stretching sequence was measured for Ni atomic contact only, as Fe atomic contacts become unstable at conductance ($G < 0.4\mathrm{G}_0$). Still, Fe also shows similar features but we were not able to measure its differential conduc-

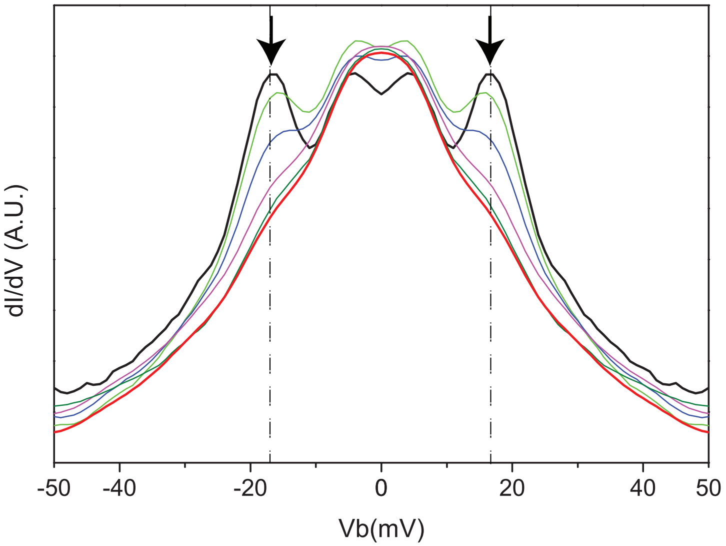

FIGURE 7.11: Possible vibrationally induced side bands at a zero bias anomaly for a Ni atomic contact. Side peaks at ±18 meV are seen along with a Kondo-like peak at zero bias. The contact was stretched in steps of 0.1Å. The black curve is taken for the starting configuration and red curve is taken last. The side peaks are seen to merge with the main zero bias anomaly upon stretching of the contact. The curves has been normalized by the zero bias conductance of the contact for better pictorial representation.

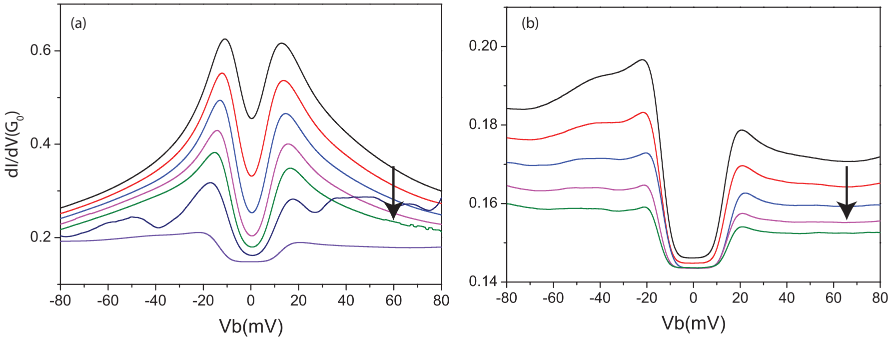

FIGURE 7.12: Stretching sequence for a Ni atomic at very low conductance. The contact was stretched in steps of 0.1Å. and the arrow shows the direction of the stretching sequence. The sequence shown in (a) is continues in (b), with the scale adjusted.

tance in a sequential stretching series. In figure (7.12) the resonance evolves into a marked step up in conductance with stretching of the contact. The position of the step is constant but its width increases with stretching of the contact. This step structure in the curves differs clearly from the features seen at higher conductance $G > 1\mathrm{G}_0$. The sign of the signal agrees with that expected for transmission values below 0.5 and resembles the signals for inelastic scattering.

7.4 SHOT NOISE FOR FERROMAGNETIC CONTACTS

SHOT noise measures the fluctuations in the current due to the discreteness of the electronic charge. Different correlation effects give rise to different levels of noise. Pauli interactions in atomic contacts can lead to sub-Poissonian noise [37], while super-Poissonian noise may be seen due to positive electron-electron interactions, such as observed for short normal metal-superconductor junctions [38]. Ferromagnetic atomic contacts shows rich many-body phenomena due to electron-spin interactions and inelastic spin and vibron scattering. Noise studies on these systems could reveal the nature of the spin interaction taking place in the atomic contacts and could give a direct measurement of the effective charge (e^*) taking part in the conduction. Here we present studies of shot noise for Ni and Fe atomic contacts.

Stable atomic contacts are formed by, either, pulling the atomic contact starting from a bulk contact of $\mathrm{G}>20\mathrm{G}_0$, or by jumping into contact from the tunneling regime. Once a stable contact is formed with G below $2\mathrm{G}_0$ the contact is gradually stretched to find a stable configuration. The stability and drift of contact are tested for a minute before we start its characterization. The differential conductance of the contact is recorded using a lockin technique with a reference sine signal of amplitude 2mV and frequency 3.33kHz. After the junction's stability test and conductance characterization shot noise on the contact is measured at increasing bias voltages, typically in steps of 1mV. An example of such noise measurement series for a Ni atomic contact of conductance $G = 1.60\mathrm{G}_0$ is shown in figures (7.13 and 7.14). The Ni atomic contact was formed from a bulk atomic contact by stretching the contact in steps of 1Å until the conductance dropped below $2.0\mathrm{G}_0$. Usually, for Ni atomic contacts the more stable contacts are found around $1.6-1.5\mathrm{G}_0$ and $1.2-1.3\mathrm{G}_0$. Once a desired contact of $1.6\mathrm{G}_0$ was obtained the stability of the contact was verified and the differential conductance was recorded. The differential conductance shows a prominent zero bias anomaly, for which a Lorentzian fit gives a Kondo temperature $T_K = 73.2\mathrm{K}$ and $\Delta G = 0.02\mathrm{G}_0$. The impedance of the noise circuit was characterized by measuring the thermal noise at the bath temperature and then the shot noise was measured for bias steps of 0.70mV. The raw noise measured on the Ni atomic contact is shown in figure (7.14 a). The spectra show a roll

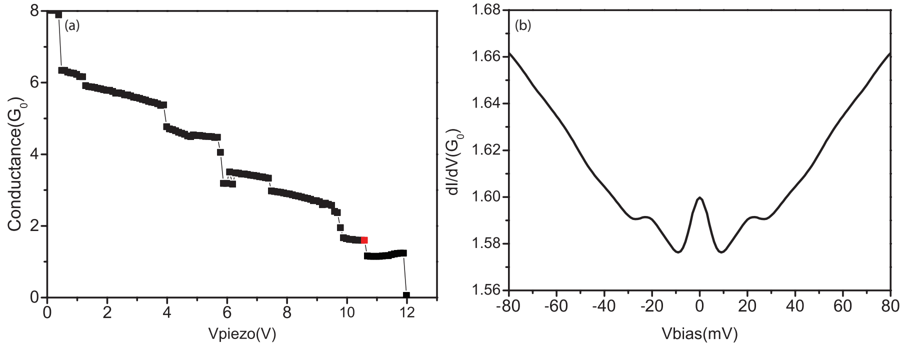

FIGURE 7.13: Characterization of a Ni atomic contact for the noise measurements shown in figure (7.14) : (a) A Ni atomic contact was formed by breaking the contact from a bulk contact to $1.60G_0$. The red data point shows the point at which noise was measured. (b) The differential conductance measurement at the same point. The contact shows a prominent zero bias anomaly which would correspond to a Kondo temperature of 73.16K.

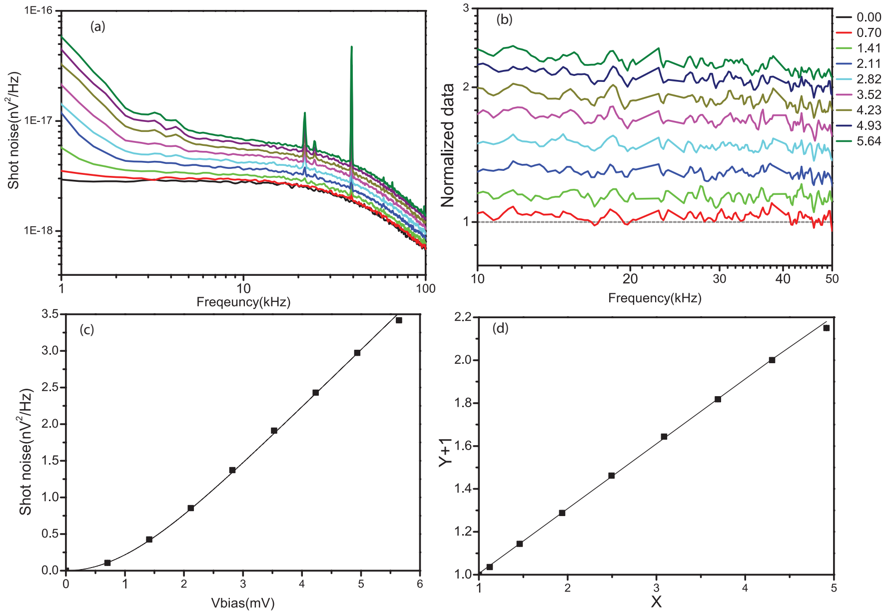

FIGURE 7.14: Shot noise measurement sequence for the Ni atomic contact shown in figure (7.14): (a) Raw noise data measured for the contact having a conductance of $G = 1.60G_0$. The noise was measured for increasing bias voltage in steps of 0.7mV up to 5.64mV. (b) Noise spectra normalized using the thermal noise in the range between 10 and 50kHz that is selected for further analysis. (c) Excess noise calculated from the normalized spectra and plotted w.r.t the bias voltage. The filled squares are the experimental data and the black curve shows the fit to the Lesovik-Levitov noise expression (1.28). The experimental data points are clearly well described by the fit. (d) Reduced axis plot for the same data as in (c). Here $Y = S_{\text{exc}}(V)/S_{\text{th}}(0)$ and $X = \left[\frac{eV}{2k_BT}\coth\frac{eV}{2k_BT} - 1\right]$. The slope of the plot gives the Fano factor, for which we find $F = 0.30 \pm 0.01$.

off at 55kHz and spurious noise peaks at 21.75, 24.5 and 39.25 kHz. The roll of the noise was corrected by normalizing the noise spectra by the thermal noise of the contact, and the spurious peaks were removed manually. Figure (7.14 b) shows the normalized spectra between 10kHz-50kHz. A first important observation is that, even though the differential conductance shows a prominent zero bias anomaly, its noise spectrum is completely white. For s-TLF system with a characteristic rate in the experimental frequency window we would see a Lorentzian noise spectrum. Such Lorentzian noise spectra were indeed seen for s-TLF in Au point contacts having a zero bias anomaly in the differential conductance. For the Ni measurement this implies that the s-TLF model can only be applicable if the fluctuation rate is high enough.

The mean value of the excess noise is plotted *w.r.t.* to bias voltage in figure (7.14 c). The Lesovik-Levitov noise expression (equation (1.28)) clearly fits the experimental data point very well. The reduced axis plot in figure (7.14 d) gives a Fano factor of 0.30 ± 0.01. The Fano factor shows the presence of at least three channels, as can be judged from the position of red data point in figure (7.15). It is important to note that the reduced axis plot does not show any deviation from a linear behavior within the experimental accuracy, and the Lesovik-Levitov provides a very good description, despite the fact that the differential conductance shows a voltage dependence in the bias window used for the noise measurements. The amplitude of the zero bias anomaly is small enough that a corresponding voltage dependence in the transmission of one of the conductance channels, would give a curvature in the Fano plot that stays within the experimental accuracy. Perhaps such a small curvature can just be noticed, but also for contacts showing larger amplitude zero bias anomalies the Fano plot is linear within the experimental accuracy.

Shot noise measurements for 120 Ni atomic contacts were done, formed from 5 different sample wires. Similar measurements were done on 55 Fe atomic contacts, formed from 3 different sample wires. Figure (7.15) shows a plot of the Fano factors vs the conductance for all ferromagnetic atomic contacts. This Fano factor plot for Ni and Fe atomic contacts allows to make the following observations:

- We find sub-Poissonian noise for all ferromagnetic atomic contacts, consistent with regular Landauer conductors with finite numbers of conductance channels. In case of s-TLF's with a characteristic frequency higher than our frequency window the noise power would be expected to lie well above the Schottky value of $F = 1$.

- Except for two points at low conductance all ferromagnetic contacts have more than a single conductance channel (two spin channels). The two exceptional points for Ni having a conductance $G < 1\mathrm{G}_0$ have a Fano factor below the red curve, which implies that the conductance channels in this

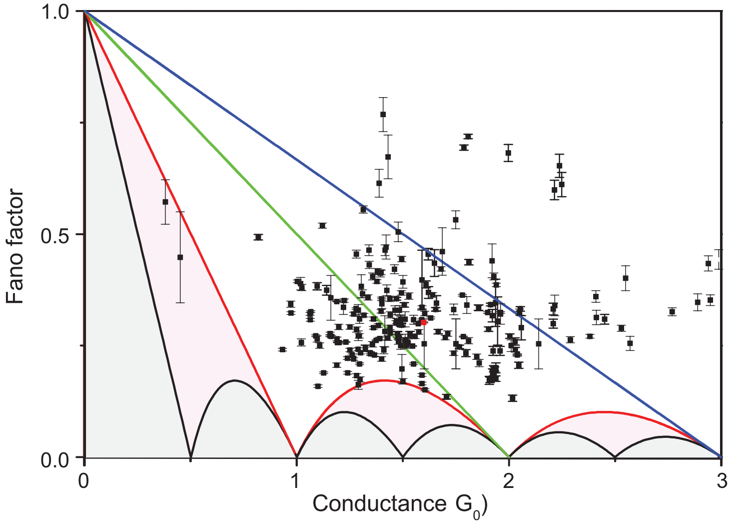

FIGURE 7.15: Fano factors measured for ferromagnetic atomic contacts of Ni and Fe (black squares). The red square shows the measurement for the contact discussed in figure(7.13 and 7.14). The red curve denotes the minimum noise for a spin-degenerate Landauer conductor. The black curve shows the minimum noise accessible to a spin split Landauer conductor. The region below the black curve shaded in light grey color is not accessible. The light pink region is the region that is only accessible if the transmissions for the spin channels differs strongly.

case are strongly spin polarized. Unfortunately, the error for the two points is also exceptionally large, which does not permit a strong conclusion. Measurements for Ni and Fe below $1G_0$ were limited due to dominant presence of $1/f$ noise.

* For the large cloud of points above the red curve we cannot draw any conclusions regarding spin polarization. Strongly spin polarized channels would only show up if they happen to be all nearly fully open/closed, which would make them show up in the pink region in figure (7.15).

* As for the Pt experiments in chapter 6 we find points on the red minimum noise curve. In this case the number of such special points is smaller, just 4% of all points coincide with the curve within their error margins. These points are consistent with a description by two degenerate (non-magnetic or weakly magnetic) conduction channels, with one completely open channel and the other partially open. They can also match more channels that are strongly spin split. In the latter case one should have expected to see also

some points below the red boundary.

The lack of completely spin polarized channels agrees with the absence of half integer quantization of the conductance in the conductance histograms. The computations by Häfner *et al.* [30] indeed predict the presence of many channels in the ferromagnetic contacts due to d orbital contributions in the conductance, with 11 channels (3 spin-up and 6 spin-down) for Ni atomic contacts, and 19 channels (8 spin-up and 11 spin-down) for Fe atomic contacts. Fe has a more partially filled *d* band leading to a larger number of channels taking part in the transport. The experimental points at or close to the red boundary for Ni atomic contacts suggest that some atomic configurations can be formed for which the numbers of active channels are much smaller. The two contacts having conductance below $1G_0$ shows the presence of a single channel, or two spin channels. It is a remarkable fact that the cloud of data points appears to be limited again by the red boundary, although not as clearly as for Pt (chapter 6). In the case of Pt atomic contacts we have observed as many as 15% of the measured points to coincide with the

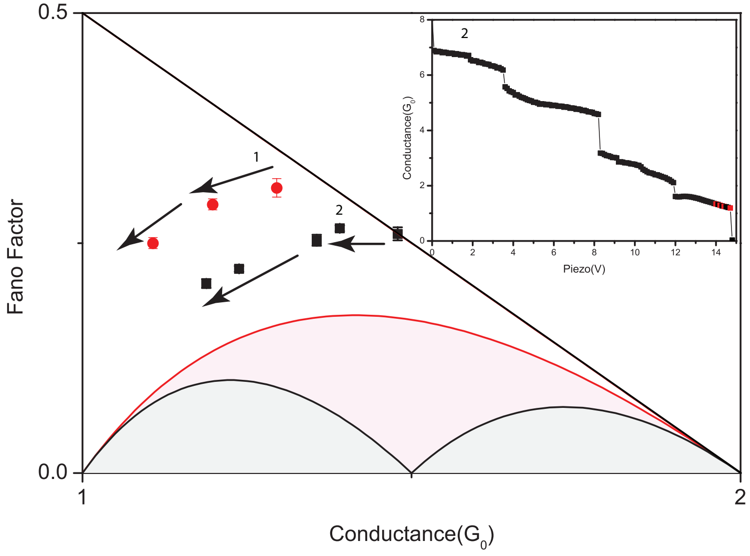

FIGURE 7.16: Evolution of the Fano factor for a Ni atomic contact with stretching: The red dots and black squares show stretching sequences of noise measured for two different Ni atomic contacts. The arrow shows the direction of stretching. The conductance trace for sequence 2 is shown in the inset. The red points mark the contact configurations for which noise was measured. Both sequences were taken by stretching in steps of 1Å.

boundary. In the calculations by Häfner *et al.* the majority spin channels for Fe are dominated by s-d hybridized orbitals, while in Ni mainly the 4s orbital contributes to the majority channel. The contribution of the d orbitals in conduction channels decreases upon stretching. Hence in case of Ni where we find the presence of only a few channels these configurations are likely strongly stressed. Indeed for those contacts for which we have been able to follow the noise with stretching we find that the noise decreases, as shown by two examples in figure (7.16).

7.4.1 NOISE AND THE SHAPE OF THE ZERO BIAS ANOMALY

We looked into the relation between the Fano factor and the different zero bias features seen in ferromagnetic atomic contacts. The zero bias features were divided into groups: Kondo-like peaks, Kondo-like dips, split peaks and split dips, and broad structures which we consider as vibron signal and hence called it no anomaly. Figure (7.17) shows the Fano factors measured on Ni and Fe atomic contacts after this classification.

Ni atomic contacts showing a dip resonance have higher noise, on average, compared to contacts showing a zero bias peak anomaly, but for Fe this difference is less clear. The Ni contacts with no anomaly clearly show low noise. Note that of the contacts having a Fano factor on the red minimum noise curve for spin degenerate channels in figure (7.17a) all show no Kondo-like anomaly. This suggests a connection between channel composition and zero-bias resonance. For these special points it is likely that only a few channels remain with dominantly s character. This supports a view where the zero bias anomaly is associated with the more localized d orbitals.

We have also looked into the relation between the Fano factor and the Kondo

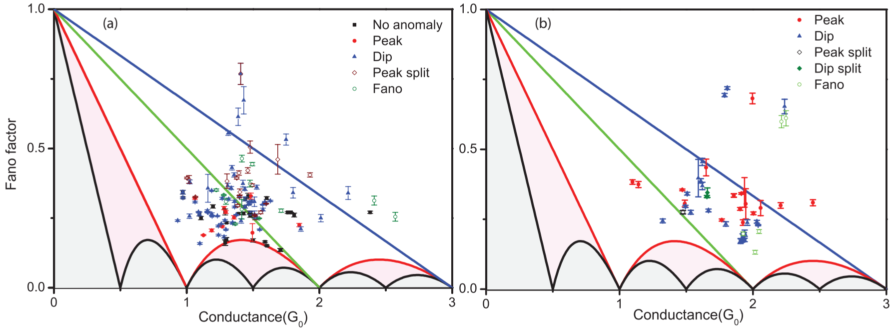

FIGURE 7.17: Shot noise for different Kondo-like anomalies for (a) Ni atomic contacts, and (b) Fe atomic contacts. The labels show the different kinds of Kondo-like anomalies for the contacts.

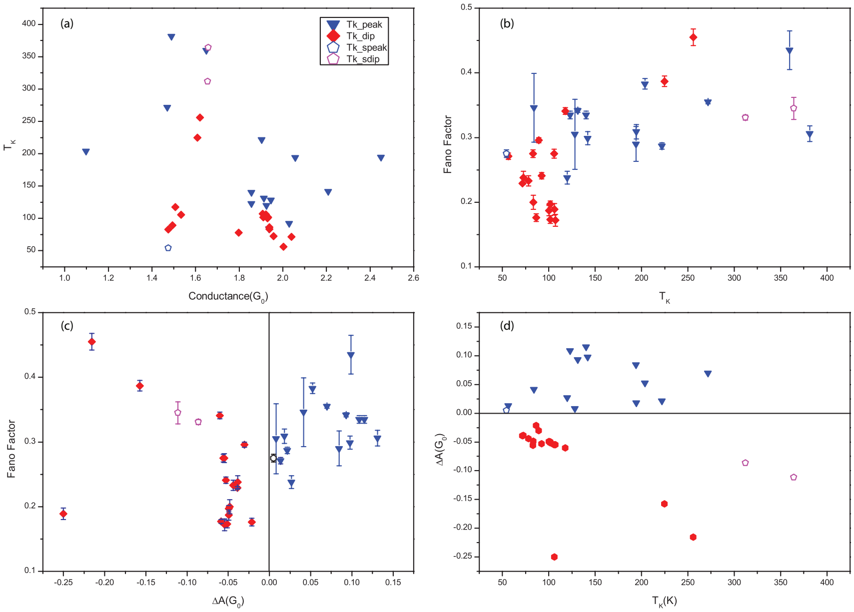

FIGURE 7.18: Relation of the Fano factor with properties of the zero bias anomaly for Fe atomic contacts: (a) Kondo temperature and conductance, (b) Fano factor and Kondo temperature, (c) Fano factor and resonance amplitude, and (d) resonance amplitude and Kondo temperature.

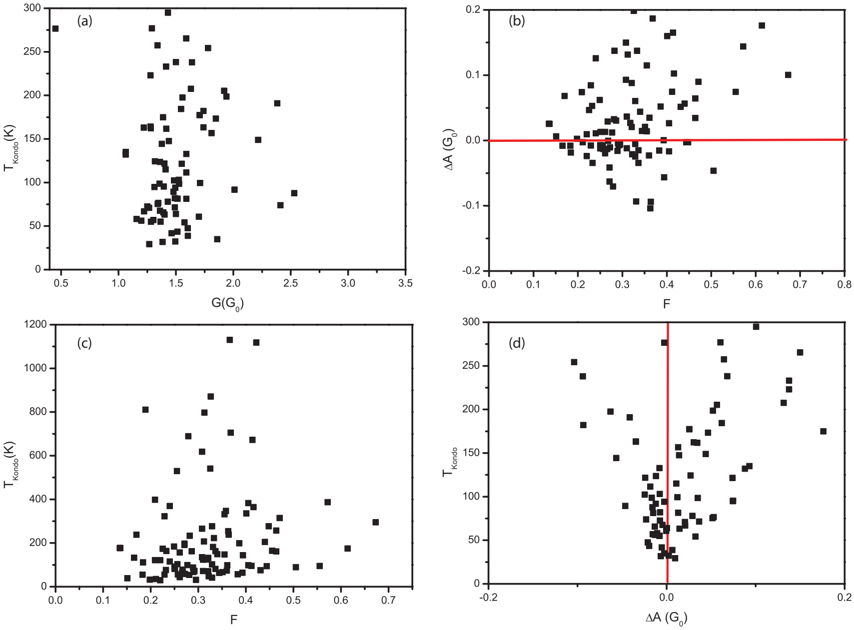

FIGURE 7.19: Relation of the Fano factor with properties of the zero bias anomaly for Ni atomic contacts: (a) Kondo temperature and conductance of the atomic contacts, (b) resonance amplitude and Fano factor, (d) Kondo temperature and Fano factor, (d) Kondo temperature and resonance amplitude.

temperature and resonance amplitude determined from the zero bias anomaly in Ni and Fe atomic contacts. In the results for Fe shown in figure (7.18) we find no specific preference for a Kondo temperature in terms of the contact conductance. A higher Fano factor correlates with higher Kondo temperatures and higher Kondo resonance amplitude, but it does not depend on the shape of the Kondo features seen in Fe atomic contact. For this reason, for the Ni data shown in figure (7.19) we do not separate out the various types of anomalies. Again, for Ni we find that the Fano factor is larger for higher Kondo temperature and Kondo resonance amplitude, with some scatter in the data. A higher Fano factor for larger amplitude and width of the zero bias anomaly agrees with our observation that the points with no anomaly have a lower Fano factor. Most of our observations appear to be consistent with regular elastic Landauer transmission channels. A larger Fano is found for those contacts that have a larger number of channels contributing to transport. The channels for which the transmission probabilities will will be most sensitive to the details of the atomic arrangements are those having a large d-electron character. The d-electron orbitals are also expected to have most of the spin polarization. Thus, the connection between Fano factor and the weight of the zero bias anomaly supports a view where the zero bias anomaly originates from spin scattering. Whether this is true Kondo scattering, as suggested by Calvo *et al.* [1] cannot be definitely concluded from our data. Inelastic scattering of local spin order may form an alternative interpretation.

7.5 CONCLUSION

We have made a systematic study of conductance spectra and shot noise for Fe and Ni ferromagnetic atomic contacts. We find no evidence for fractional quantization from the conductance histograms, which is consistent with previous experiments. The differential conductance shows pronounced zero bias anomalies. The origin of these zero bias anomalies was discussed in terms of their possible origin due to spin scattering and the Kondo effect. The data support a view that local magnetic moments due localized d orbitals in the contact are involved in the explanation for the zero bias anomalies. On the other hand, the shot noise measurements are consistent with a standard Lesovik-Levitov description, indicating that single-particle elastic transmission processes are by far dominating the electron transport. We find no clear examples for strongly spin polarized conductance channels, except for two points with rather poor accuracy. This lack of evidence is probably due to the large number of conductance channels that are involved in transport when a local magnetic moment is well developed. Similar to our observations for Pt (chapter 6) we find several examples of contacts having the Fano factors coinciding with the boundary for spin degenerate channels. This can be interpreted as being due to contacts that have just two spin degenerate channels with one channel having perfect transmission. The reduction to just two channels, which will have a large degree of s character, implies that most of the d orbitals for such contacts do not participate in transport. Since the latter are also dominantly responsible for magnetism, such contacts appear to be non-magnetic. This interpretation also fits with the observation that noise measurements for Ni as well as for Pt atomic contacts in a stretching sequence show a monotonous decrease in noise.

For a Kondo system Sela *et al.* [39] have predicted a V^3 voltage dependence of noise and an effective charge of 5/3. We have not been able to conclusively demonstrate deviations from a linear voltage dependence. Further studies focusing on more idealized model Kondo systems may be suitable for achieving progress in understanding. This may be done using an STM system, where one could think of studying the noise and conductance spectroscopy on local magnetic adatoms and on Pt and ferromagnetic islands with corresponding metallic tips. This may also help to uncover the local atomic configuration of the contacts that favor the minimum Fano factor with two spin degenerate channels with one channel completely transmitting.

REFERENCES

[1] M. R. Calvo, Fernández-Rossier, Joaquín, Palacios, J. José, D. Jacob, Natelson, Douglas, and C. Untiedt, *The Kondo effect in ferromagnetic atomic contacts.*, Nature **458**, 1150 (2009).

[2] D. G. Gordon, H. Shtrikman, D. A.-M. D. Mahalu, U. Meirav, and M. A. Kastner, *Kondo effect in a single electron transistor*, Nature **391**, 156 (1998).

[3] L. P. K. Sara M. Cronenwett, Tjerk H. Oosterkamp, *A Tunable Kondo Effect in Quantum Dots*, Science **281**, 540 (1998).

[4] S. Sasaki, S. D. Franceschi, J. M. Elzerman, W. G. van der Wiel, M. Eto, S. Tarucha, and L. P. Kouwenhoven, *Kondo effect in an integer spin quantum dot*, Nature **405**, 764 (2000).

[5] van der Wiel, W. G., Franceschi, S. De, Fujisawa, T., Elzerman, J. M., S. Tarucha, and L. P. Kouwenhoven, *The Kondo Effect in the Unitary Limit*, Science **289**, 2105 (2000).

[6] Y. Ji, M. Heiblum, D. Sprinzak, D. Mahalu, and H. Shtrikman, *Phase Evolution in a Kondo Correlated System*, Science **290**, 779 (2000).

[7] H. Jeong, A. M. Chang, and M. R. Melloch, *The Kondo Effect in an Artificial Quantum Dot Molecule*, Science **293**, 2221 (2001).

[8] V. Madhavan, W. Chen, T. Jamneala, M. F. Crommie, and N. S. Wingreen, *Tunneling into a Single Magnetic Atom: Spectroscopic Evidence of the Kondo Resonance*, Science **280**, 567 (1998).

[9] J. Li, W.-D. Schneider, R. Berndt, and B. Delley, *Kondo Scattering Observed at a Single Magnetic Impurity*, Physical Review Letters **80**, 2893 (1998).

[10] H. C. Manoharan, C. P. Lutz, and D. M. Eigle, *Quantum mirages formed by coherent projection of electronic structure*, Nature **403**, 512 (2000).

[11] W. Liang, M. P. Shores, M. Bockrath, J. R. Long, and H. Park, *Kondo resonance in a single-molecule transistor*, Nature **417**, 725 (2002).

[12] J. Nygård, D. H. Cobden, and P. E. Lindelof, *Kondo physics in carbon nanotubes.*, Nature **408**, 342 (2000).

[13] K. Vladár and A. Zawadowski, *Theory of the interaction between electrons and the two-level system in amorphous metals. I. Noncommutative model Hamiltonian and scaling of first order*, Phys. Rev. B **28**, 1564 (1983).

[14] V. I. Kozub and I. O. Kulik, *Microcontact spectroscopy of population of two level systems*, Sov. Phys. JETP **64**, 1332 (1986).

[15] A. Kamenev and Y. Gefen, *Zero-bias anomaly in finite-size systems*, Phys. Rev. B **54**, 5428 (1996).

[16] L. Bitton, D. B. Gutman, R. Berkovits, and A. Frydman, *Coexistence of Coulomb Blockade and Zero Bias Anomaly in a Strongly Coupled Nanodot*, Phys. Rev. Lett. **106**, 016803 (2011).

[17] D. C. Ralph and R. A. Buhrman, *Observations of Kondo scattering without magnetic impurities: A point contact study of two-level tunneling systems in metals*, Phys. Rev. Lett. **69**, 2118 (1992).

[18] A. Akimenko and V. Gudimenko, *Effect of tunneling two-level systems on the spectrum and electrical noise in metallic point contacts*, Solid State Communications **87**, 925 (1993).

[19] R. J. P. Keijsers, O. I. Shklyarevskii, and H. van Kempen, *Two-level-system-related zero-bias anomaly in point-contact spectra*, Phys. Rev. B **51**, 5628 (1995).

[20] A. van Oudenaarden, M. H. Devoret, E. H. Visscher, Y. V. Nazarov, and J. E. Mooij, *Conductance Fluctuations in a Metallic Wire Interrupted by a Tunnel Junction*, Phys. Rev. Lett. **78**, 3539 (1997).

[21] C. Untiedt, G. Rubio Bollinger, S. Vieira, and N. Agräit, *Quantum interference in atomic-sized point contacts*, Phys. Rev. B **62**, 9962 (2000).

[22] P. Petit, A. Anthore, M. L. D. Rocca, and P. Lafarge, *Conductance fluctuations in metallic nanogaps made by electromigration*, Journal of Applied Physics **109**, 014307 (pages 4) (2011).

[23] P. Lucignano, R. Mazzarello, A. Smogunov, M. Fabrizio, and E. Tosatti, *Kondo conductance in an atomic nanocontact from first principles*, Nature Materials **8**, 563 (2009).

[24] Helko Elbert van den Brom, Doctoral thesis, Leiden university, Leiden (2000).

[25] F. Komori and K. Nakatsuji, *Quantized Conductance through Atomic-sized Iron Contacts at 4.2 K*, Journal of the Physical Society of Japan **68**, 3786 (1999).

[26] V. Rodrigues, J. Bettini, P. C. Silva, and D. Ugarte, *Evidence for Spontaneous Spin-Polarized Transport in Magnetic Nanowires*, Phys. Rev. Lett. **91**, 096801 (2003).

[27] H. D. Chopra, M. R. Sullivan, J. N. Armstrong, and S. Z. Hua, *The quantum spin-valve in cobalt atomic point contacts*, Nature Materials **4**, 832 (2005).

[28] C. Untiedt, D. M. T. Dekker, D. Djukic, and J. M. van Ruitenbeek, *Absence of magnetically induced fractional quantization in atomic contacts*, Phys. Rev. B **69**, 081401 (2004).

[29] M. R. Calvo, M. J. Caturla, D. Jacob, C. Untiedt, and J. J. Palacios, *Mechanical, Electrical, and Magnetic Properties of Ni Nanocontacts*, IEEE Transactions on Nanotechnology (2009) **7**, 165 (2008).

[30] M. Häfner, J. Viljas, D. Frustaglia, F. Pauly, M. Dreher, P. Nielaba, and J. Cuevas, *Theoretical study of the conductance of ferromagnetic atomic-sized contacts*, Physical Review B **77**, 1 (2008).

[31] J. Bork, Y. hui Zhang, L. Diekhöner, L. Borda, P. Simon, J. Kroha, P. Wahl, and K. Kern, *A tunable two-impurity Kondo system in an atomic point contact*, Nature Physics **7**, 901 (2011).

[32] J. Parks, a. Champagne, G. Hutchison, S. Flores-Torres, H. Abruña, and D. Ralph, *Tuning the Kondo Effect with a Mechanically Controllable Break Junction*, Physical Review Letters **99**, 1 (2007).

[33] T. A. Costi, *Kondo Effect in a Magnetic Field and the Magnetoresistivity of Kondo Alloys*, Phys. Rev. Lett. **85**, 1504 (2000).

[34] J. J. Parks, a. R. Champagne, T. a. Costi, W. W. Shum, a. N. Pasupathy, E. Neuscamman, S. Flores-Torres, P. S. Cornaglia, a. a. Aligia, C. a. Balseiro, et al., *Mechanical control of spin states in spin-1 molecules and the underscreened Kondo effect.*, Science (New York, N.Y.) **328**, 1370 (2010), ISSN 1095-9203.

[35] I. Fernández-Torrente, K. Franke, and J. Pascual, *Vibrational Kondo Effect in Pure Organic Charge-Transfer Assemblies*, Physical Review Letters **101**, 2172032 (2008).

[36] A. Khotkevich and I. K. Yanson, *Atlas of Point Contact Spectra of Electron-Phonon Interactions In Metals* (Springer, 1995).

[37] H. van den Brom and J. van Ruitenbeek, *Quantum Suppression of Shot Noise in Atom-Size Metallic Contacts*, Physical Review Letters **82**, 1526 (1999).

[38] X. Jehl, M. Sanquer, R. Calemczuk, and D. Mailly, *Detection of doubled shot noise in short normal-metal/ superconductor junctions*, Nature **405**, 50 (2000).

[39] E. Sela, Y. Oreg, F. von Oppen, and J. Koch, *Fractional Shot Noise in the Kondo Regime*, Phys. Rev. Lett. **97**, 086601 (2006).

8

A HIGH-FREQUENCY NOISE MEASUREMENT SETUP FOR MCBJ

**Manohar KUMAR, Mohammed SAGHIR, Stefan STAHL,
Bert CRAMA, Ruud VAN EGMOND, Jan VAN RUITENBEEK**

We report on the realization of a fast and sensitive broadband high frequency (300kHz – 10MHz) noise measurement setup for the study of fluctuations in the non-equilibrium electric current in mechanically controllable break junctions at cryogenic temperatures. The setup relies on a combination of a cryogenic amplifier plus a room-temperature amplifier stage with a custom built FPGA cross correlator. We have incorporated a two-channel noise detection scheme allowing us to measure the cross spectrum, giving a noise power sensitivity an order of magnitude below the amplifier noise floor. We describe the principle of the set up, its implementation and its calibration. This system is ideal for high-bias noise measurements for the investigation of electron scattering on non-equilibrium vibrons in metal-molecule-metal junctions.

8.1 MOTIVATION AND CONCEPT

THE shot noise measurements on Au atomic contacts above the vibron energy show a linear deviation from the Lesovik-Levitov behavior [1]. The fact that the observed deviation is linear is believed to be due to a strong coupling of the vibrons to the phonon bath in the metallic leads. For weak vibron-phonon relaxation the life time of the vibron becomes long enough for the electrons to see a highly non-equilibrium occupation of vibrons, which would lead to non-linear deviations from the Lesovik-Levitov behaviour. Only in a few cases we have observed a quadratic deviation from the classical Lesovik-Levitov expression (section 4.5), but the degree of vibron coupling to the phonon bath cannot be easily controlled for this system. In the Au atomic chains the vibrons typically decay faster that the average electron-vibron scattering time.

Ideal candidates for the investigation of non-equilibrium vibrons would be the simple molecular junction systems Pt-D_2-Pt[2], or Au-O_2-Au[3]. The vibron energies for these molecular systems lie well above the Debye energy of the metal atoms in the leads, which is important for a small relaxation rate. The lowest vibron energy of the D_2 molecule in Pt-D_2-Pt junction is 38 ± 5meV and for O_2 in Au-O_2-Au it is 49 ± 6mV. For observation of the non-equilibrium noise properties we need to measure at bias voltages eV well above these energies. However, in these molecular contacts the noise spectra show stronger $1/f$ noise as compared to pure Au atomic contacts, and the $1/f$ noise grows even stronger at higher bias. Shot noise is proportional to the bias voltage while $1/f$ noise is proportional to the square of the bias voltage. This leads to a dominance of $1/f$ noise over the shot noise at high bias for the noise measurements in the frequency window that we have used for the experiments described in chapters 4–7 [4, 5]. An example of a spectrum for Au-O_2-Au dominated by $1/f$ noise is shown in figure (1.8b). The linear extrapolation of the $1/f$ noise crosses the white shot noise level at a frequency that we will call the corner frequency of $1/f$ noise. For bias values up to 50mV the $1/f$ corner frequency for Au-O_2-Au is in the order of 400kHz - 500kHz. The measurement bandwidth for the set up described in the previous chapters is limited by the high intrinsic capacitance of the coax running from the sample at cryogenic temperatures to the amplifier at room temperature (RT). This gives a roll off of 30kHz - 40kHz for a sample conductance of $1G_0$. In order to be able to measure the spectrum above the $1/f$ noise corner frequency we need to increase the frequency range of our measurement set up. For the measurements of inelastic scattering above the vibron energies in the molecular systems mentioned above we need to expand the frequency range into the MHz regime.

In order to measure the noise at higher bias one needs to increase the cut off frequency. One of way of increasing the high end frequency cut off is to reduce the effective impedance of the measurement circuit seen at the input of the noise amplifier. This can be done by using an impedance transformer or an LC tank circuit, but this narrows the bandwidth. Since we have seen many times that it is of great value to be able to verify the white character of the noise, we prefer to maintain a broad band noise measurement. Another solution would be to use a potential divider [6]. Although this helps to maintain a wide band and will shift the cutoff frequency, it also reduces the effective signal feeding into the amplifier. In stead of modifying the effective impedance of the sample we decided to reduce the effective capacitance of the cables running from the sample to the first stage amplifier. This is done by installing the first stage amplifiers as close as possible to the sample so that the wires can be kept short. For this purpose we use low noise cryogenic amplifiers, as has been demonstrated in refs. [7, 8]. The amplifier close to sample reduces the input capacitance of the circuit, while the output impedance of the cryogenic amplifier is matched to the 75Ω transmission line and the input impedance of the RT amplifier. This technique allow us to measure into the MHz regime, up to $f_h \sim 5$MHz. The addition of a $1:2$ potential divider at the input of the first amplifier could increase the measurement bandwidth to 10MHz.

The implementation of the high frequency measurement setup for mechanically controllable break junctions imposes a few design constraints. It requires three parallel engineering routes to custom develop the complete high frequency measurement setup. These three routes shown in figure (8.1) are: (a) The dipstick (b) The two channel spectrum analyzer (c) The low temperature amplifier, which will be described each in a separate section below.

8.2 THE MCBJ DIPSTICK

THE design of the dipstick was based upon an earlier design for a MCBJ dipstick. The new design is made with the purpose of fighting the parasitic capacitance of the wires coupling the sample to the input of the amplifier. This requires placing two cryogenic amplifiers within a few mm distance (~ 5mm) from the sample, that should operate at the bath temperature of 4.2K. The working temperature of the amplifier affects its gain and noise performance drastically so it requires good thermalization of the all the wires going to and out from the cryogenic amplifier. Hence, in the design special attention is paid to cooling and temperature stabilization of the cryogenic amplifiers. In the new design the cryo block at sample end is made as local ground, but we keep the piezo electric control circuit ground separated from sensitive ground. We have used a low-voltage type piezo element with positive bias polarity. The ceramic insulated piezo actuator has dimensions $3 \times 3 \times 9$mm with nominal working displacement of 6.5μm ±20% for the full voltage range (0 – 100V) at room temperature.

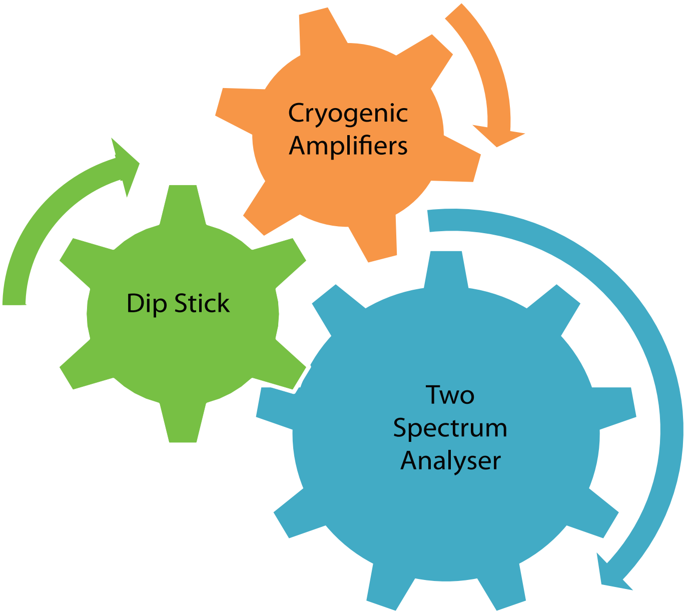

FIGURE 8.1: Churn of technology: Three distinct developments needed for a high frequency noise measurement setup compatible with the MCBJ technique - (a) The dipstick (b) The cryogenic amplifier (c) The two channel spectrum analyzer.

8.2.1 DIPSTICK DESIGN

An image of the bottom part of the dipstick is shown in figure (8.2). We will discuss each of the main design principles in the following paragraphs. In some cases we needed to find compromises in design and working principle. Further improvements in the design will be discussed at the end of this chapter. A detailed schematic of the cryo head and of the RT head of the dipstick are shown in figures (8.3) and (8.4).

Modular design

We paid special attention to make our design modular. The main modular components of our dipstick are: (i) Head (ii) Slot for the cryogenic amplifiers (iii) Cryogenic cap (iv) Wiring capsules. These four parts are coupled together and can be changed without affecting the other parts, within some design constraints. This provides a geat advantage when changes in the cryo-electronics, cryo-head or the wiring scheme are required for future new developments.

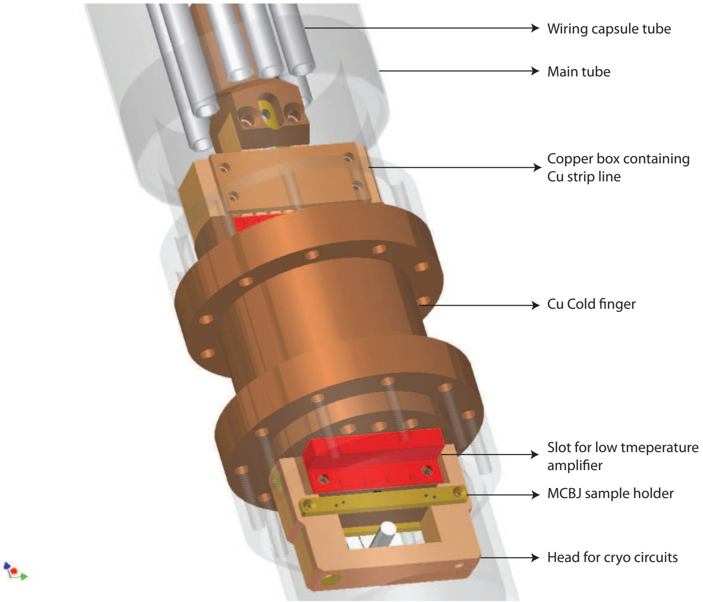

FIGURE 8.2: A 3-D view of the bottom part of the MCBJ dipstick: In the new design the dipstick has a heavy Cu block serving as a block for thermalization of the cryo-electronics. Vacuum sealing is done with Indium. The copper block connects the main tube to the sample space and the cap, and is in direct contact with the helium bath. When opening the cap the only exposed area is the input of the low temperature amplifiers and the sample. All the rest of the wiring is fixed within the copper box coupled to the top of the Cu amplifier housing.

Wiring of the dipstick

In the new design the wires running down the central tube are held by capsules, which are formed by semi-cylindrical tubes (a tube cut in half along its length). These can be inserted into the fine hollow tubes, that are coupled to the main tube of the dipstick using silver welding for good thermal and mechanical anchoring. The wires are glued onto the inside of these semi-cylindrical tubes by GE varnish with copper wool added. This has the advantage that it helps anchoring the wires thermally and mechanically to the inner wall of the rod efficiently, while the wires can be easily removed from the wiring capsule for maintainance and modifications. The wiring of the dipstick at the top and bottom of dipstick can be done independently from each other. The wiring module at the dipstick head is removable and hence is accessible for soldering.

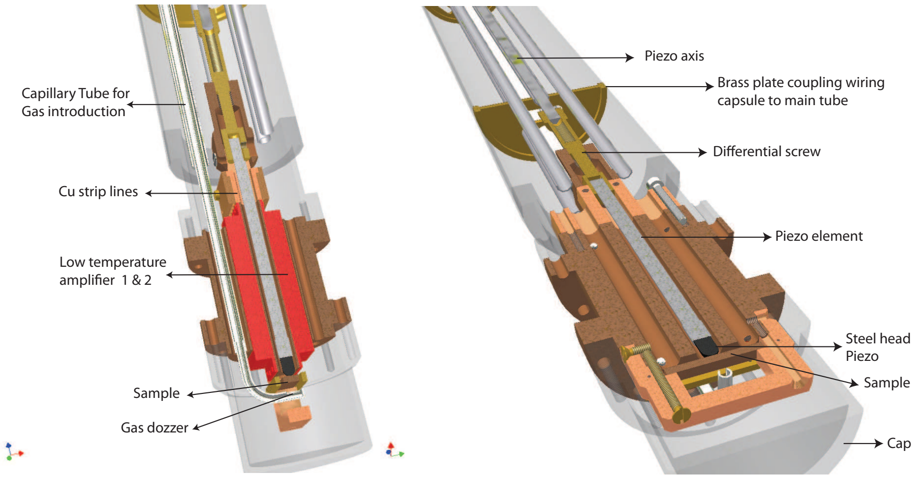

FIGURE 8.3: Cross section view of the dipstick showing the details of its cryogenic part. The large copper mass serves for thermalization and housing of the cryogenic amplifiers. The cryogenic amplifiers shown schematically in red are fixed with screws in the slots in the Cu housing. Copper wool is added between the gold plated low temperature amplifier base and the copper bock for better thermalization. The capillary tube for admitting of gases is isolated from the Cu block using a Teflon ring. The capillary tube has an extension at the cryo end with a gas dozer nozzle facing the sample. The sample sits in the slot at the end of the piezo element. Only the head of the piezo element sticks out of the central tube in the cold Cu block. All removable parts at the cryogenic vacuum end are held by brass screws. The cryogenic cap is tightened on the cryogenic Cu block using stainless steel screws and an indium seal.

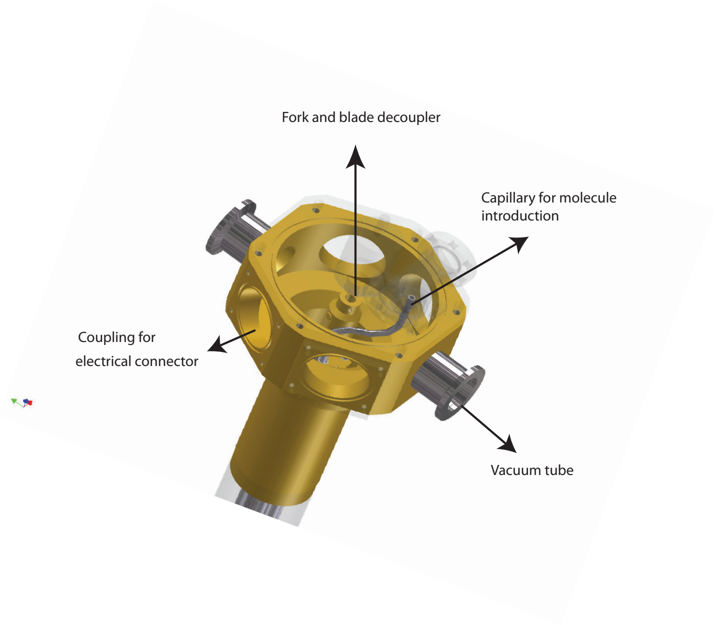

FIGURE 8.4: 3D view of the head of the dipstick. In the new design a fork-blade coupling between the external rotation drive and the screw axis is put at the top of the screw axis. Two vacuum feed throughs are welded on the head of the dipstick, while electrical feed throughs are O-ring sealed. The second stage RT amplifiers are placed inside the head of the dipstick (not shown here).

Efficient thermalization

We have taken care of proper thermalization of all wires coming from the RT head to the cryo head in two stages. All the wires coming from the RT head are manganin (Cu(86%) Mn(12%) Ni(2%)) wires, which provide a good compromise between a high electrical conductance and a low thermal conductance. These manganin wires are thermally coupled to the inner wall of the dipstick through the fixation described above, where they are cooled against the He liquid and gas temperatures inside the cryogenic vessel. All wires are soldered onto electrically isolated Cu strips on the cold finger where they are cooled efficiently by the liquid He bath. This reduces the heating of the sample and amplifier from RT phonons and also reduces the heat load on He bath, giving a longer measurement time. All the measurement wires coupling the respective strip lines to the amplifier or to the MCBJ sample are Cu wires. The screw rod is coupled to the copper block for thermalization such that it should not heat the sample during making and breaking of the contact. We have placed the copper block directly in contact with the He bath, which provides efficient thermalization of the sample and the amplifiers and gives a faster cooling time of about 2hrs to reach the base temperature of 4.2K. This is quite an improvement over the earlier designs, which give cooling times of about 6hrs to a base temperature of 5.7K.

Mechanical stability

We paid special attention to attain better mechanical stability, since the process of conductance and noise spectroscopy usually takes more than an hour and in future measurement runs stretching over more than 2hours of measurement time on a single contact setting are anticipated. Instabilities in the atomic contacts can be grouped into two classes, one inherent to the properties of the sample, *i.e.* due to the microscopic structure and atomic arrangement very close to the atomic contact, and the other due to electro-mechanical instabilities *i.e.* due to the coupling of external electro-mechanical disturbances to the atomic contact. Instabilities inherent to the sample can often be improved by annealing the sample in the cryogenic vacuum at high currents. External mechanical instabilities can be due to electrical noise on the piezo voltage, and vibrations coupling mechanically or acoustically into the setup and to the sample. Electrical noise in the piezo driver is efficiently reduced using a 3$^{\text{rd}}$ order passive low pass filter with a cutoff frequency of 10Hz. The piezo wires are separated from the sensitive measurement wires by mounting them in separate wire tubes. At the cryo head the piezo wires are coupled to separate strip lines shielded from the measurement wires though grounded strip lines. The whole construction is inside the copper block which provides further electrical shielding. The piezo element itself is inside this copper shielding and at the sample side only the hemispherical steel head sticks out, which couples the piezo element mechanically to the sample. This design helps in reducing the fluctuations in the high-voltage piezo drive coupling to the signal wires.

For mechanical stabilization we have decoupled the screw axis to the piezo element using a fork blade configuration, which is positioned at the top of the insert in our design. During the measurement the sample is suspended in a cryogenic vacuum. Further reduction of mechanical and acoustic disturbance is achieved in the usual way by placing the experiment inside an acoustically shielded box suspended on pneumatic vibration dampers. For sensitive measurements the turbo pump can be decoupled from the dipstick.

Efficient pumping

The main tube of the dipstick has a lot of empty space which we have tried to maximally use for pumping. We have further reduced the size of the cryogenic sample space to reduce the effective volume needed to be pumped. A container with active coal is mounted in the cryo cap for added cryogenic pumping. The reduction of the sample space helps in reducing the cool down time and increasing the measurement time.

Electromagnetic shielding

Electromagnetic shielding has been improved by using grounded strip lines as shields around the exposed naked wires. At the cryo head the cold strip lines are shielded by the copper box. The high voltage wires were kept far from the sensitive signal wires. A central star grounding scheme for all signal circuits was was used with the star point at the cryo head, in order to minimize ground loops.

8.2.2 CHARACTERIZATION OF THE DIPSTICK

The measurement properties of the new dipstick were characterized by measuring Au atomic contacts. A simplified schematic of the measurement circuit (figure (3.5)) is shown in figure (8.5). A Au atomic contact is formed by stretching a Au contact starting from a bulk contact size. The dc conductance characterization of the Au atomic contact is shown by the conductance histogram in figure (8.6). The conductance histogram shows a clear peak at $0.98G_0$, and the usual structure expected for Au. The typical traces in the inset show the formation of atomic chains. The length histogram recorded on the same contact shows the usual multiple peaks. The first inter peak distance gives the reduction factor of 0.08V/Å. The stability of the contact depends on the local atomic configuration but it is also affected by external disturbances. The fluctuations in the conductance of the Au atomic contact measured in the new dipstick are found to remain within the measurement accuracy of 1% in conductance for > 2hrs of measurement time. The average drift of the contact is less than 0.01% over the period of 2.5hrs, as shown in figure (8.7).

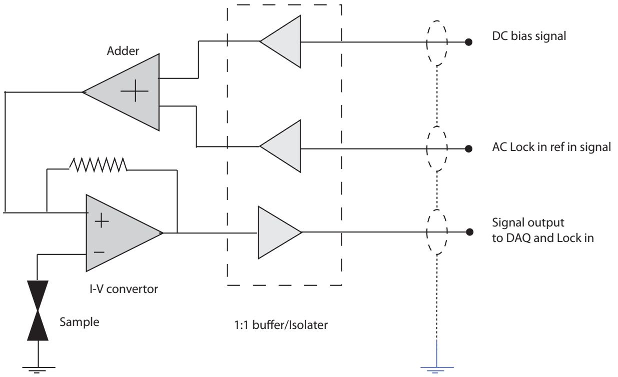

FIGURE 8.5: Circuit for conductance measurements: This is a simplified version of the circuit diagram shown in figure (3.5). The ac measurement is done using a lockin technique. The grounding of the dipstick is isolated from the ground of measurement equipment using 1 : 1 buffer amplifiers.

8.3 TWO CHANNEL SPECTRUM ANALYZER

THE high-bias noise measurements on molecular systems require extending the noise measurements into the MHz regime. We have decided to use a cross spectrum noise measurement technique, which then requires fast data acquisition and manipulation. We have adopted a National Instruments PXI-5641R data acquisition unit for the digitization of the signals. The 5641-R gives 14 bit analog to digital conversion, for single-ended AC coupled dual channels, with an analog bandwidth of 50kHz-80MHz [9]. The average input noise is $16\text{nV}/\sqrt{\text{Hz}}$ with -60dB channel-to-channel crosstalk up to 80MHz. The maximum input signal is 24dBm peak without damaging the card. A low pass filter at the input limits the band width at the lower end. In our case we have operated the unit at 10MHz band width to reduce aliasing in comparison with the 20MHz bandwidth setting. Data handling speed is accelerated by using a Virtex 5 FPGA (Field Programmable Gate Array, 94208 logic cells, 640 multipliers and 8784 block RAM) on the PXI express backplane. Due to the 32-bit PXI express bus with DMA capability data communication from the FPGA to the host computer and to FPGA from the host computer within the PXI backplane can be done above 100MB/s and 50MB/s, respectively. The combination of the PXI express bus and FPGA allows the implementation of a real time cross spectrum analyzer.

8.3.1 DATA PROCESSING

The realization of a two channel cross spectrum analyzer based on the PXI-5641R system is shown schematically in figure (8.8). The band limited noise signal is fed

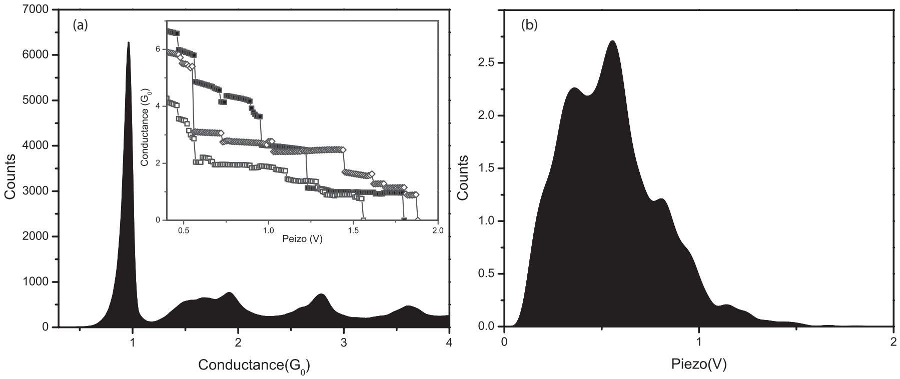

FIGURE 8.6: DC conductance characterization of the Au atomic contact in the new dipstick: A conductance histogram is recorded for Au atomic contacts. The conductance histogram shows the usual peak at 0.98G$_0$. The inset shows typical traces recorded. (b) Length histogram recorded for Au atomic contacts, which also shows the usual structure with multiple peaks. The calibration factor for the new low-voltage piezo element used in this dipstick is found to be 0.08V/Å

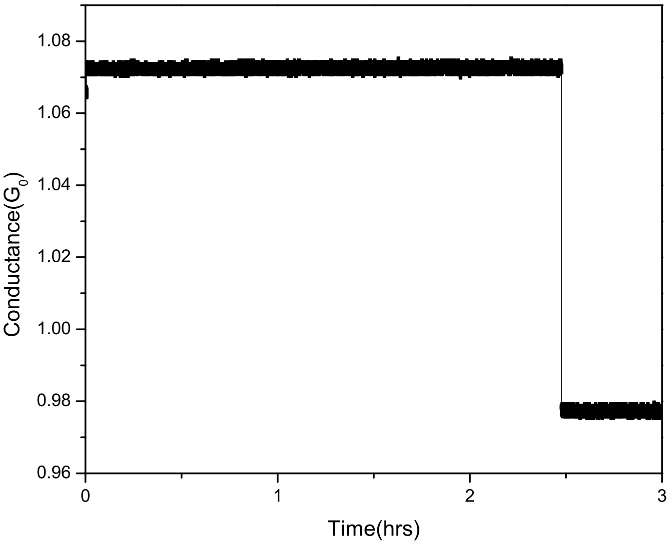

FIGURE 8.7: Stability test of a Au atomic contact in the new dipstick: An atomic contact of 1.07G$_0$ is formed and the conductance is measured as a function of time until the contact is breaks. The average drift of the contact is less than 0.01% over the period of 2.5hrs.

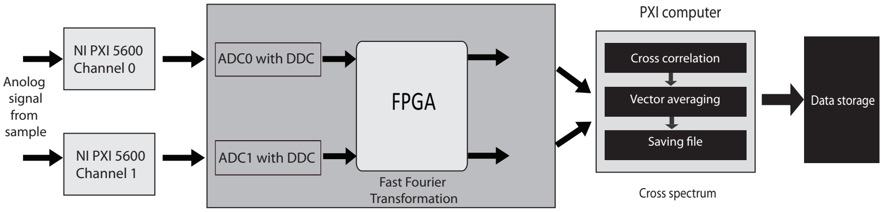

FIGURE 8.8: Data processing flow chart for the real time spectrum analyzer: The analog signals are fed into the ADC (analog-to digital conversion) channels of the 5641-R unit for digitization. The built-in FPGA unit processes a fast-Fourier transform (FFT) of the digitalized signals and the data is further processed for lower order computation (cross spectrum and vector averaging) in the host computer. The final computed data is saved on a network drive.

into the input of the data acquisition card for digitization. The sampling rate and digital down conversion (DDC) give a resolution width of ∼ 12.2kHz. The outputs of both ADC/DDC channels are fed to the FPGA simultaneously. For each acquisition time series, the FPGA takes blocks of N×1024 data points and performs a complex FFT on them[1]. Here N specifies the number of averages and 1024 is number of FFT points. The outputs of the FFT are transmitted to the host computer using direct memory access (DMA). The host computer performs the lower order computations which involves cross spectrum calculations and the running vector averaging, and it takes care of saving the data on the network drive.

8.3.2 CHARACTERIZATION OF THE TWO CHANNEL SPECTRUM ANALYZER

The operation and linearity of the spectrum analyzer was verified using a band limited (20MHz) Agilent signal source (33250A). The white noise generated by the signal source was increased in steps of $1\mathrm{mV}_{\mathrm{rms}}$ and was fed into the two input channels of the PXI-based cross spectrum analyzer. The cross spectrum of the signal with averaging over 4000 samples was calculated using the FPGA based FFT spectrum analyzer and host computer. The raw spectra are normalized by the 1mV spectrum in order to correct for the transfer function of the measurement circuit. The normalized spectra in the window of 2MHz - 6MHz are shown in figure (8.9a). The mean values calculated from the normalized spectra are plotted *w.r.t.* input noise values in figure (8.9b). The linear response of the PXI system is confirmed by the linear fit to the experimental data points.

---

[1] The FPGA program was designed by Kartsen van Zwol, NI engineer using Labview FPGA and Asynchronous wire programming

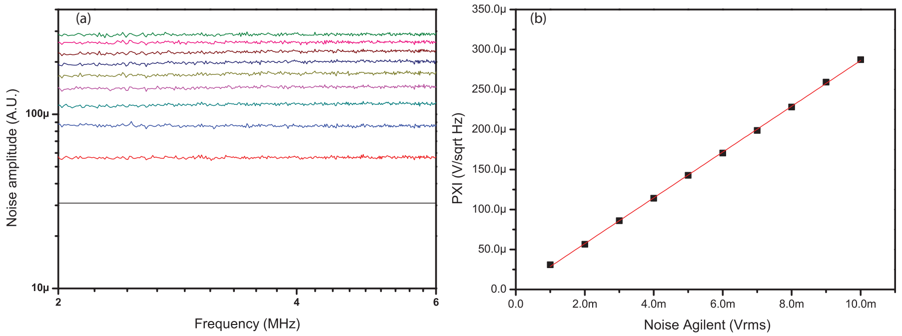

FIGURE 8.9: Test of the PXI-based cross spectrum analyzer: (a) Raw FFT spectra in the window of 2MHz-6MHz, normalized by the spectrum taken at $1mV_{rms}$ input signal. The black line shows the noise level at $1mV_{rms}$ input, used for the normalization. (b) The mean values of the normalized spectra in the window of 2MHz-6MHz are plotted *w.r.t.* to corresponding input noise values from the signal source. The straight line is a linear fit to the experimental data points.

8.4 THE CRYOGENIC AMPLIFIERS

THE cryogenic amplifiers are designed in close collaboration with Stahl Electronics. The design constraints for the amplifiers were not only given by the desired input current and voltage noise levels, but also by requirements for the effective thermalization of the all active and passive elements on the printed circuit board, and by size limitations. The main design constraints are: (1) Low current and voltage noise. (2) Low thermal load. (3) The amplifiers should fit inside a dipstick with outer diameter 50mm. (4) Long stable operation. (5) The amplifiers should operate up into the low-MHz regime.

8.4.1 AMPLIFIER DESIGN

The cryogenic amplifiers were designed inspired by the low noise amplifiers described by Adrian Tae-Jin Lee [10]. The amplifier has two stages. The first stage is a dual channel low noise cryogenic amplifier with operational frequency window of 300kHz - 30MHz. The output of this stage, with an impedance of 75Ω is coupled to the input of the second stage low noise dual channel amplifier at RT, with operational frequency window of 20kHz - 100MHz. The advantage of this design is the low heat load on He bath and the smaller size of the cryogenic amplifier. For the cryogenic stage we have used high electron mobility transistors (HEMT), and Si FET's for the RT stage amplifier [11, 12]. In our design the heat load on the He bath is 1.2mW. The main disadvantage of this design is that the noise of the RT amplifier dominates the noise performance [13]. This is also a reason why we are using the cross spectrum measurement technique.

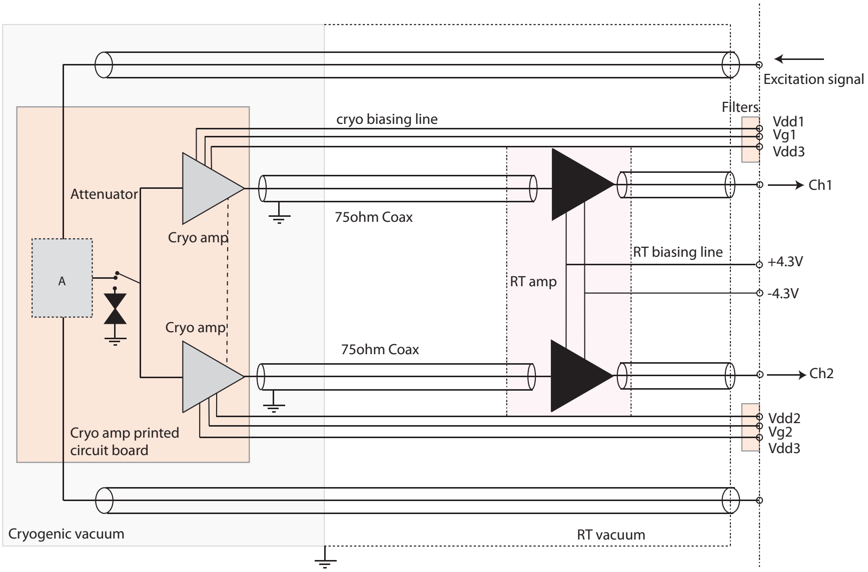

FIGURE 8.10: Schematic of the low noise amplifier: A two stage dual channel single ended low noise amplifier was realized. The power biasing lines are fitted with optional low pass filters. The excitation line is incorporated in the design for gain calibration purposes. The attenuator close to the input of the amplifier is also optional and in the current version it is omitted. The Cu cold block of the dipstick is made the ground point for the cryo circuit. The cascode stage of each channel has independent biasing parameters while the source follower of both channels have a common biasing line. This gives five independent bias voltage settings.

The design of the biasing circuitry and the conceptual design of the cryogenic amplifier is shown in figure (8.10). The cryo end of the amplifier acts as impedance transformer with a gain of 6.3X. All transistors used in the cryogenic stage are HEMT transistors because of their low noise and lower power dissipation performance at cryogenic temperatures. For Si based transistors the mobile charges would freeze out at low temperatures and would require a sophisticated heating of the amplifier and its isolation from the 4K bath. GaAs based transistors are prone to large low frequency 1/f noise. The cryogenic amplifier is based on cascode biasing to the source follower. The cascode stage eliminates the Miller effect, which is the drain to gate capacitive feedback. The Miller effect also decreases the stability of the circuit at higher frequencies, where effective feedback is positive due to the large phase shift (> 180°) between the input and the feedback signal. This feedback limits the upper cutoff frequency in the source follower circuit. The source follower is a low input impedance transimpedance amplifier. It converts the cur-

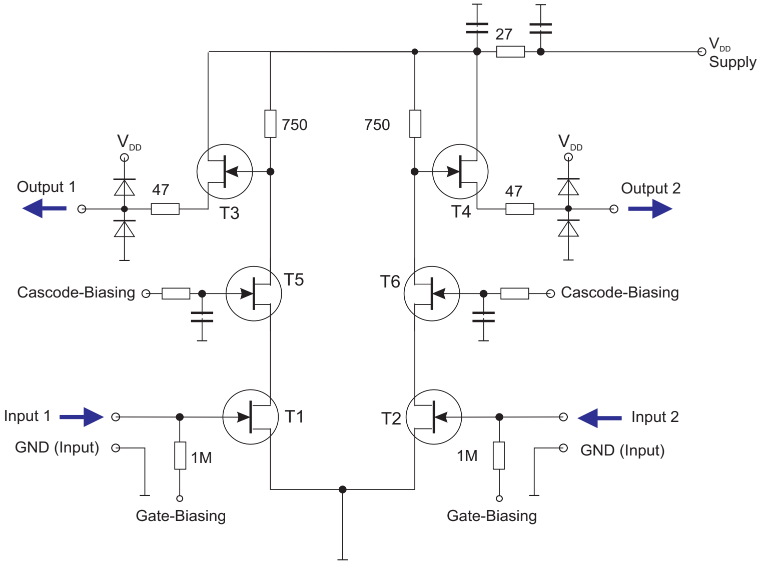

FIGURE 8.11: Schematic of the cryogenic low noise amplifier stage: The gate of the source follower is biased using a cascode stage transistor. This design gives a broadband frequency response in the low-MHz regime. The cascode biasing of the source follower is used to minimized the Miller effect. Both channels are mounted on the same printed circuit board. Apart from the source follower biasing for both channels the cascode biasing can be tunned independently.

rent fluctuations to voltage fluctuations through the source-drain resistance. The other advantage of the source follower is that the output impedance of this stage matches the cable impedance hence improves the high frequency performance.

A circuit diagram of the RT amplifier is shown in figure (8.12). The gain of the cryogenic amplifier should be high enough such that its output signal dominates the input noise of the RT amplifier (see also section 2.1.1). The effective gain of the cryogenic amplifier is approximately 5X. The input of RT amplifier is coupled to the output of the cryogenic amplifier through a transformer. The purpose of the transformer is to have better impedance matching and it reduces high frequency oscillations. The RT amplifier has a gain of 10X. The input impedance is 75Ω matching the output impedance of the cryogenic amplifier. The RT amplifier has a fixed biasing point using two voltage supplies at +4.3V and −4.3V. The RT amplifier is mounted inside the brass head at the top of the dipstick. Proper thermal anchoring is provided for stable operation of the device. The output line is protected from spurious static discharges by a buffer amplifier and diode. The output of the RT amplifier is coupled to next stage amplifier through 50Ω coax cables.

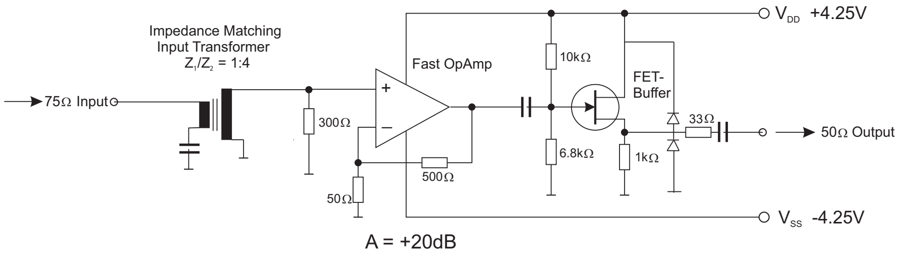

FIGURE 8.12: Circuit diagram of the RT low noise amplifier: Here only a single channel of the amplifier is shown. The output of the cryogenic amplifier is coupled to the RT stage of the low noise amplifier through an impedance transformer. The output of the high frequency Opamp is protected using a buffer amplifier and diode. The gain of the Opamp is approx. 20dB.

8.4.2 CHARACTERIZATION OF THE AMPLIFIER

The cryo and RT amplifiers were characterized independently. The voltage noise of the RT amplifier is shown in figure (8.13a). The input noise of the RT amplifier in the frequency window of 300kHz - 10MHz is approximately 2.5nV/$\sqrt{\text{Hz}}$. The noise performance degrades somewhat at the higher frequency end. At lower frequencies $1/f$ noise takes over, superimposed with several resonances. This $1/f$ noise is common for Si based transistors. Here, input current noise is not significant due to the small output impedance of the cryogenic stage amplifier. A gain-bandwidth measurement for the RT amplifier is shown in figure (8.13b). The gain for the two channels closely matches for the same ±4.3V biasing. The effective 3dB bandwidth of the RT amplifier is 400kHz - 60MHz. The spectrum is relatively flat between 300kHz - 10MHz. The total amplification in this window is 22.5dB.

The noise characterization of the cryo amplifier stage is shown in figure (8.14a). The biasing parameters used for this measurement are $V_{dd1} = 2.00$V, $V_{dd2} = 2.00$V, $V_{dd3} = 2.55$V, $V_{g1} = -0.40$V, $V_{g2} = -0.43$V. The voltage noise is determined using a shorted input of the amplifier, while the current noise is measured with a 11.5pF capacitor connected over the input and subtracting the voltage noise from the total noise. The voltage and current noise of the amplifier are found to be 0.9nV/$\sqrt{\text{Hz}}$ and 50fA/$\sqrt{\text{Hz}}$, respectively. The gain-bandwidth characteristics is shown in figure (8.14b). The characteristics of the two channels matches within 3dB between 1MHz and 28MHz. The average gain of the amplifiers in this window is 16dB. The antiresonance at 29MHz is due to an instability of the source follower due to high frequency feedback.

In our low noise amplifier design both channels for the cryogenic amplifier and RT amplifier are on same board and hence could couple capacitively, which could give rise to cross talk. A measurement of the cross talk for the RT amplifier is given

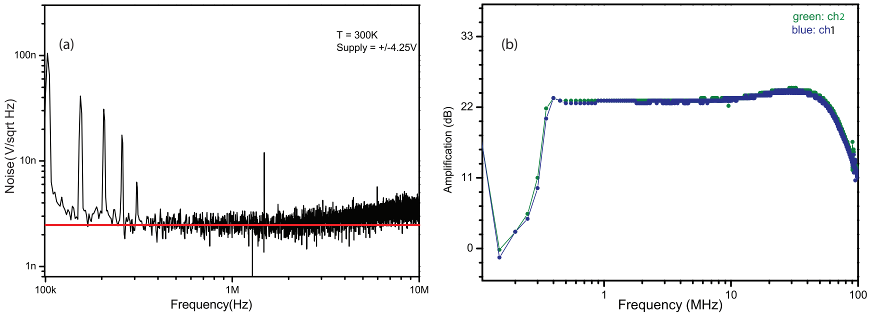

FIGURE 8.13: Gain and noise characterization of the low-noise amplifiers: (a) Noise characteristics of the RT amplifier stage. The voltage noise in the relevant frequency window is approx. 2.5nV/$\sqrt{\text{Hz}}$. (b) The effective gain of the RT amplifier is 22.5dB, or 13.1X, closely matched for the two channels, shown separately in blue and green.

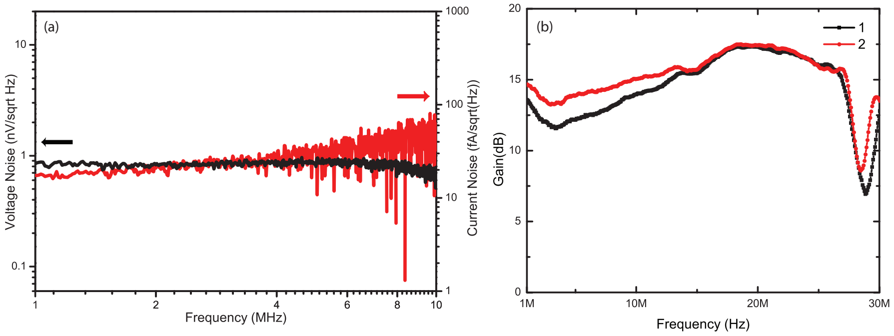

FIGURE 8.14: Gain and noise characterization of the low-noise amplifiers: (a) Voltage noise (black) and current noise (red) for the low noise cryogenic amplifier stage. The voltage noise and current noise are found to be approximately 0.9nV/$\sqrt{\text{Hz}}$ and 50fA$\sqrt{\text{Hz}}$. (b) The gain-bandwidth plot shows an effective gain of 16dB, or 6.3X.

in figure (8.15). The cross talk between the two channels for the cryo amplifier is expected to be similar. The data around 1MHz show effectively 38dB, or 1.2%, of signals parasitically coupled to each other. This could be further improved by using two separate printed circuit boards for the two channels.

The effective noise contributed by the low noise amplifier in each channel is given by

$$V_n^2 = v_n^2 + i_n^2|Z_{in}|^2 + c_n^2|iZ_{in}|^2 \tag{8.1}$$

Here v_n and i_n are the voltage and current noise at the input of the amplifier, respectively, while the c_n is the correlated noise, which could be due to cross talk or

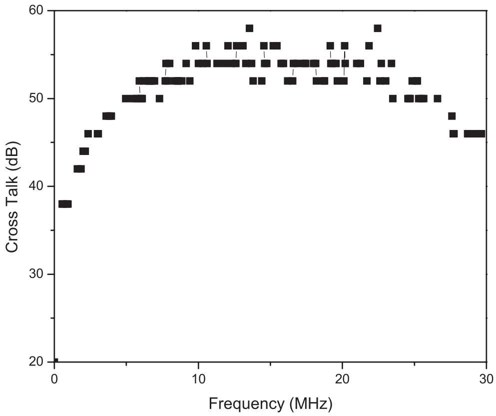

FIGURE 8.15: Cross talk for the RT stage of the low noise amplifier. The discreteness in data is due to the digital resolution setting of the spectrum analyzer.

residual correlations. The first term can be removed by using the cross spectrum measurement, while the last two terms adds up in the noise spectra, and this limits our noise measurement resolution.

8.5 FURTHER IMPROVEMENT

The current setup was designed around the implemented cryogenic amplifiers in the noise measurement circuit. Although the system is quite modular, it has its own complexity too. A few modifications could be implemented into the design of the cryo part of the dipstick. A cooling pad could be mounted on the sample side of the Cu cold block. This would give improved ease of soldering and re-soldering of the wires without dismantling the cold block from the dipstick. Although the dipstick has a quite good mechanical stability, this could be improved further by having the fork-blade decoupler at the cryo side rather than at the RT head of the dipstick. The low noise amplifier as it is now has its input noise dominated by the RT stage amplifier, which could be compensated for by increasing the transimpedance of the cryo side of the amplifier. The matching of the two channels of the cryo amplifier could be further improved. The PXI cross spectrum analyzer is working in principle, but the speed of data processing can be improved by using the FPGA for the lower order computation also.

The conceptual design of the high frequency noise measurement setup in the low MHz regime has been realized and characterized, but it needs a few further steps to be completed. Noise spectroscopy for actual atomic contacts needs to be tested. The combination of the noise measurement setup with the present conductance measurement circuit will reduce the intrinsic high frequency cutoff back to a few hundred kHz. To prevent this requires decoupling the conductance measurement circuit from the noise measurement circuit. We have tried to use a cryogenic electro-mechanical switch for this purpose, however we found that this switch introduces electrical and mechanical pulses that lead to breaking of the atomic contact during the switching. We presently aim for adding a cryogenic amplifier for the conductance measurement circuit which will decouple the wire capacitances from the sample. This will give the capability of doing the both dc and ac conductance measurements and noise measurement on the same atomic point contact.

REFERENCES

[1] M. Kumar, R. Avriller, A. L. Yeyati, and J. M. van Ruitenbeek, *Detection of vibration-mode scattering in electronic shot noise.*, Physical review letters **108**, 146602 (2012).

[2] D. Djukic, K. S. Thygesen, C. Untiedt, R. H. M. Smit, K. W. Jacobsen, and J. M. van Ruitenbeek, *Stretching dependence of the vibration modes of a single-molecule* $\mathrm{Pt}-\mathrm{H}_2-\mathrm{Pt}$ *bridge*, Phys. Rev. B **71**, 161402 (2005).

[3] W. Thijssen, D. Marjenburgh, R. Bremmer, and J. van Ruitenbeek, *Oxygen-Enhanced Atomic Chain Formation*, Physical Review Letters **96**, 0268061 (2006).

[4] Y. P. Li, D. C. Tsui, J. J. Heremans, J. A. Simmons, and G. W. Weimann, *Low frequency noise in transport through quantum point contacts*, Applied Physics Letters **57**, 774 (1990).

[5] F. Liefrink, J. I. Dijkhuis, and H. van Houten, *Low-frequency noise in quantum point contacts*, Semiconductor Science and Technology **9**, 2178 (1994).

[6] T. Delattre, C. Feuillet-Palma, L. G. Herrmann, P. Morfin, J.-M. Berroir, G. Fève, B. Plaçais, D. C. Glattli, M.-S. Choi, C. Mora, et al., *Noisy Kondo impurities*, Nature Physics **5**, 208 (2009).

[7] H. Birk, M. J. de Jong, and C. Schonenberger, *Shot-Noise Suppression in the Single-Electron Tunneling Regime*, Phys. Rev. Lett. **75**, 1610 (1995).

[8] I. T. Vink, T. Nooitgedagt, R. N. Schouten, L. M. K. Vandersypen, and W. Wegscheider, *Cryogenic amplifier for fast real-time detection of single-electron tunneling*, Applied Physics Letters **91**, 123512 (pages 3) (2007).

[9] N. Instrument, Tech. Rep., National Instrument (2009), URL `http://www.ni.com/pdf/manuals/375120b.pdf`.

[10] A. T. Lee, *Broadband cryogenic preamplifiers incorporating GaAs MESFETs for use with low temperature particle detectors*, Review of Scientific Instruments **60**, 3315 (1989).

[11] J. Bautista, Tech. Rep., Radio frequency and Microwave subsystems, NASA (1993).

[12] Z. Svindrych, Z. Janua, F. Soukup, and R. Tichy, *Operational amplifiers operating in temperature range from 300 to 4.2K*, Cryogenics **48**, 160 (2008).

[13] L. K. J. Vandamme, in *Advanced Experimental Methods for Noise Research in Nanoscale Electronic Devices, Proceedings of the NATO Advanced Research Workshop, Nato Science Series II* (2003), vol. 151, pp. 1–370, URL `http://rd.springer.com/book/10.1007/1-4020-2170-4/page/1`.

A

THEORETICAL COMPUTATION OF CURRENT AND NOISE

Remi AVRILLER, Alfredo Levy YEYATI

A.1 MODELING OF THE AU ATOMIC CHAIN

We model the Au atomic chain by using the minimal model described in detail in the supplementary material of [1]. We also adopt in the following the reduced units $\hbar = e = k_B = 1$. In such a model (see A.1), the central atomic chain is described as a single molecular level of energy ω_d which is coupled to perfect left (L) and right (R) electrodes through the $\Gamma_{L(R)}$ coupling terms. Excitation of a local phonon mode of energy ω_0 with interaction strength λ is made possible when the kinetic energy of transfered electrons given by the voltage drop $\mu_L - \mu_R = V$ exceeds the phonon energy ω_0. The total Hamiltonian of the system is then written as in [1]

$$\begin{aligned} \mathscr{H} &= \sum_{X=L,R} \mathscr{H}_X + \omega_d d^\dagger d + \omega_0 a^\dagger a + \mathscr{V}_T + \mathscr{V}_{e-ph} && \text{(A.1)} \\ \mathscr{V}_T &= \sum_{X=L,R} t_{Xd} c_X^\dagger d + \text{H.c} && \text{(A.2)} \\ \mathscr{V}_{e-ph} &= \lambda (a + a^\dagger) d^\dagger d && \text{(A.3)} \end{aligned}$$

Part of this chapter have been published as supplementary information in Physical Review Letters **108**, 146602 (2012). This appendix is supplement to the chapter(4)

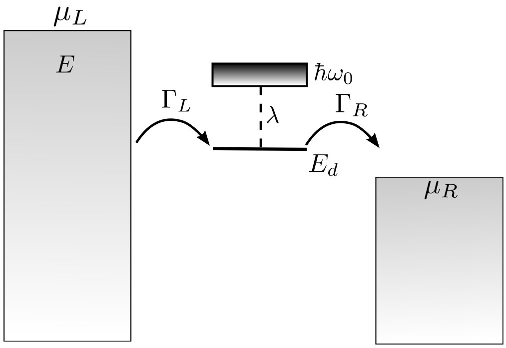

FIGURE A.1: Representation of the effective one-level model adopted for the theoretical description of the Au atomic chain: The atomic chain modeled as single quantum dot level with energy E_d. The electron traversing through the atomic chain interacts with the local vibron mode of energy ω_0 with e-ph coupling constant λ. The atomic chain is coupled to microscopic left and right lead with coupling element $\Omega_L$andΩ_R respectively.

In order to derive some analytical results for the current and noise in presence of e-ph interactions, we suppose that the coupling to the leads is symmetric ($\Gamma_L = \Gamma_R = \Gamma/2$) and that the energy dependence of the transmission factor $\tau(\omega)$ of the nano-junction can be neglected. The later assumption is equivalent to evaluate the transmission factor at Fermi energy, namely that

$$\tau \approx \frac{\Gamma^2}{\omega_d^2 + \Gamma^2} \tag{A.4}$$

This condition will have to be relaxed in part IV when trying to fit quantitatively the experimental curves at low transmission.

A.2 COMPUTING THE MEAN CURRENT AND NOISE IN THE AU ATOMIC CHAIN

We use the formalism of Avriller *et al.*[1] in order to compute the mean current and noise characteristics. It is based on a Keldysh Green functions framework which has been generalized in [2] in order to address higher order cumulants of the current operator. The correction to the current and noise upon phonon excitations are then computed at second order of the e-ph coupling strength [1, 3, 4].

In order to provide some microscopic picture of the elementary processes responsible for the correction to the noise induced by e-ph interactions, we will rewrite in a slightly different way the results derived in [1, 3, 4]. We will provide some compact expressions for the current and noise characteristics that are valid at finite temperature (for the electrons), in the limit where the energy dependence of the transmission factor $\tau(\omega)$ can be neglected.

A.2.1 MEAN CURRENT

The correction to the mean current at second order of e-ph interactions is obtained as

$$\begin{aligned} \delta I(V) &= \frac{1}{2\pi}\left(\frac{\lambda\tau}{\Gamma}\right)^2 \int d\omega \Big\{(1-2\tau)\left[2f_{L;+}(1-f_R)+f_L(1-f_{R;+})\right] \\ &+ 2\tau f_L(1-f_R) - (L)\rightarrow(R)\Big\} \end{aligned} \tag{A.5}$$

where we introduced the notation $f_{X;\pm} = f_X(\omega\pm\omega_0)$ for the Fermi distributions of the $X = L, R$ leads evaluated at energies $\omega\pm\omega_0$.

Eq.(A.6) relates the current to elementary one-electron processes during which an electron is transfered from left to right electrode either elastically or inelastically. At zero temperature, only phonon emission is allowed and one obtains for the current at positive voltages:

$$\delta I(V) \approx \frac{1}{2\pi}\left(\frac{\lambda\tau}{\Gamma}\right)^2 \Big\{2(1-\tau)V + (1-2\tau)(V-\omega_0)\theta(V-\omega_0)\Big\} \tag{A.6}$$

The first term on the rhs stands for an elastic correction that might be included into an effective transmission factor (renormalization of τ by e-ph interactions), whereas the second term is an inelastic correction that is activated when $V > \omega_0$ (the transfered electrons acquire enough kinetic energy to excite the local vibrational mode). Within our approximation, the sign of the correction to the conductance is positive (negative) for $\tau < (>) 1/2$. The crossover at $\tau = 1/2$ has been observed recently experimentally in molecular junctions made of single water molecules contacted to Pt electrode [5].

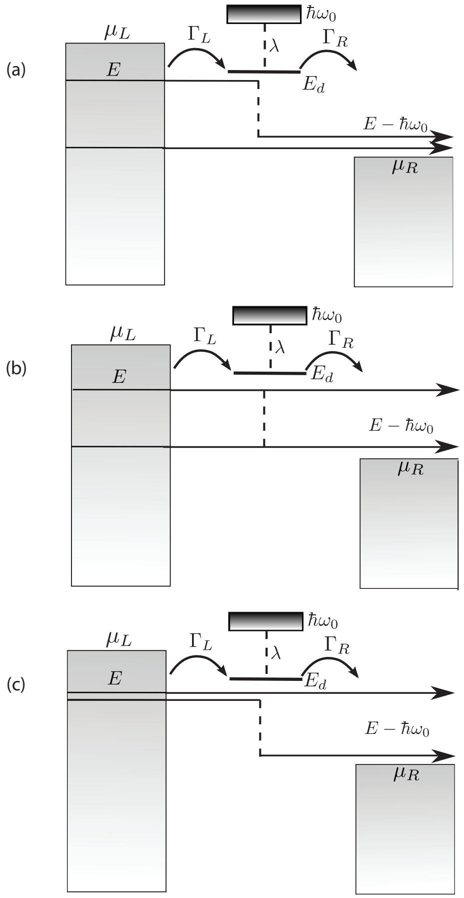

FIGURE A.2: Resonant tunneling process involving two electron and a phonon processes in a atomic chain: (a) Coherent two-electron process corresponding to the joined elastic tunneling of one electron (from left to right lead) with another inelastic tunneling event assisted by phonon emission. This process provides a contribution to the noise proportional to $f_L(1-f_R)f_{L;+}(1-f_R)$. (b) Same kind of two-electron process providing a contribution to the noise proportional to $f_{L;+}(1-f_{R;+})f_{L;+}(1-f_R)$. (c) Coherent two-electron process corresponding to an effective electron-electron interaction (exchange term). This process provides a contribution to the noise proportional to $f_L(1-f_R)f_{L;+}(1-f_{R+})$

A.2.2 NOISE

A similar although more lengthy expression can be derived for the correction to the noise induced by e-ph interactions

$$
\begin{aligned}
\delta S(V) &\approx \frac{1}{2\pi}\left(\frac{\lambda\tau}{\Gamma}\right)^2 \int d\omega \left\{(1-2\tau)A_1 - \tau A_2 + A_3 - 2\tau A_4\right\} && \text{(A.7)}\\
A_1 &= \sum_{X=L,R} \left\{f_X(1-f_{\bar{X}}) + f_{X;+}(1-f_{\bar{X};+})\right\} && \text{(A.8)}\\
&- 2\tau\left\{(f_L-f_R)^2 + (f_{L;+}-f_{R;+})^2 + (f_L-f_R)(f_{L;+}-f_{R;+})\right\} && \\
A_2 &= A_1 \sum_{X=L,R} \left\{f_{X;+} - f_X\right\} && \text{(A.9)}\\
A_3 &= \sum_{X=L,R} f_{X;+}(1-f_{\bar{X}}) && \text{(A.10)}\\
A_4 &= \sum_{X=L,R} X(f_X + f_{X;+}) \sum_{X=L,R} X f_{X;+}(1-f_{\bar{X}}) && \text{(A.11)}
\end{aligned}
$$

In the limit of zero temperature and positive voltages, we obtain a simpler expression

$$\delta S(V) \approx \frac{1}{2\pi}\left(\frac{\lambda\tau}{\Gamma}\right)^2\Big\{2(1-\tau)(1-2\tau)V+\big[1-8\tau(1-\tau)\big](V-\omega_0)\theta(V-\omega_0)\Big\} \quad \text{(A.12)}$$

The correction to the noise also exhibits a threshold behavior when the local vibrational mode is excited ($V > \omega_0$). Given the two critical values of the transmission factor $\tau_\pm = 1/2(1 \pm 1/\sqrt{2})$, the correction to the noise is positive (super-Poissonian) when the transmission factor is such that $0 < \tau < \tau_-$ and $\tau_+ < \tau < 1$. This correction to the noise becomes negative (sub-Poissonian) in the remaining regime $\tau_- < \tau < \tau_+$, which is a much less intuitive result.

In order to understand the microscopic mechanism responsible for this crossover between positive and negative correction to the noise, we kept track of the terms that dominate in the limit of zero temperature and positive voltages. In equation(A.13), we have split the correction to the noise into the sum of two contributions:

$$\delta S(V) \quad \approx \quad \delta S_{1e}(V) + \delta S_{2e}(V) \quad \text{(A.13)}$$

The first contribution $\delta S_{1e}(V)$ is first analyzed and is associated to one-electron processes written as

$$\delta S_{1e}(V) \quad = \quad \delta S_{1e}^{(el)}(V) + \delta S_{1e}^{(in)}(V) \quad \text{(A.14)}$$

$$\delta S_{1e}^{(el)}(V) \quad = \quad \frac{1}{2\pi}(1-2\tau)\delta\tau_{el}\int d\omega f_{1e}^{(el)}(\omega;V) \quad \text{(A.15)}$$

$$\delta S_{1e}^{(in)}(V) \quad = \quad \frac{1}{2\pi}\delta\tau_{in}\int d\omega f_{1e}^{(in)}(\omega;V) \quad \text{(A.16)}$$

In equation(A.15)-(A.16), the e-ph interaction modifies the elastic transmission factor $\tilde{\tau} = \tau + \delta\tau_{el}$ and opens a new inelastic channel when $V > \omega_0$, with a probability given by the inelastic transmission factor $\delta\tau_{in}$. The activation of e-ph interaction also provides an inelastic contribution to the electronic distribution functions $f_{1e}^{(el,in)}(\omega;V)$ that appear in the multi-channel version of the standard shot-noise formula [6]. The corresponding expressions for the renormalized transmission factors and electronic distribution functions are provided below

$$\delta\tau_{el} \quad = \quad 2(1-2\tau)\left(\frac{\lambda\tau}{\Gamma}\right)^2 \quad \text{(A.17)}$$

$$\delta\tau_{in} \quad = \quad \left(\frac{\lambda\tau}{\Gamma}\right)^2 \quad \text{(A.18)}$$

$$f_{1e}^{(el)}(\omega;V) \quad = \quad f_L(1-f_R) \quad \text{(A.19)}$$

$$f_{1e}^{(in)}(\omega;V) \quad = \quad f_{L;+}(1-f_R) \quad \text{(A.20)}$$

It is interesting to notice that the one electron inelastic contribution to shot-noise $\delta S_{1e}^{(in)}(V)$ is always positive. This contribution was shown to be dominant in the limit $\tau \to 1$ and to distort the counting statistics for the transfered electrons into a Poisonnian distribution upon activation of phonon emission (rare events) [1].

The second contribution to Eq.(A.13) $\delta S_{2e}(V)$ cannot be understood in terms of simple one-electron effects. It rather originates from coherent two-electron processes that provide a negative correction to the noise upon phonon excitations. Figure(A.2-(a) and (b)) show a first class of such processes, where the elastic transmission of one electron (from left to right lead) is correlated to an inelastic transmission event assisted by the emission of a phonon. The corresponding two-electron correlation finds its deep origin in Pauli exclusion principle, namely into the fact that the transmitted charges are fermions. For instance, in Fig.A.2-(a), after a first elastic transmission event has occurred, the next coming inelastic transmission event will compete for the same final scattering state. If this final state is fully occupied (which is the case in the limit of perfect transmission), the contribution of such a process will vanish as a result of Pauli blocking. At finite transmission (the final state is partially occupied), the above mentioned Pauli blocking mechanism will still reduce the current fluctuations and thus decrease the noise. Figure(A.2(c)) shows the other class of two-electron events responsible for the negative correction to the noise. It is associated to the case where two electrons are coherently transmitted (bunching of two electrons) with emission and re-absorption of a phonon, thus generating an effective electron-electron interaction.
Similarly to the previous case, we derived compact expressions for $\delta S_{2e}(V)$

$$\delta S_{2e}(V) = \delta S_{2e}^{(el)}(V) + \delta S_{2e}^{(in)}(V) \tag{A.21}$$

$$\delta S_{2e}^{(el)}(V) = \frac{1}{2\pi}\frac{\tau}{2}\delta\tau_{el}\int d\omega f_{2e}^{(el)}(\omega;V) \tag{A.22}$$

$$\delta S_{2e}^{(in)}(V) = -\frac{1}{2\pi}2\tau(1-\tau)\delta\tau_{in}\int d\omega f_{2e}^{(in)}(\omega;V) \tag{A.23}$$

In equation(A.22)-(A.23), the electronic distribution functions $f_{2e}^{(el,in)}(\omega;V)$ are modified by phonon mediated two-electron processes and are obtained as

$$f_{2e}^{(el)}(\omega;V) = \sum_{\alpha=\pm1} f_L(1-f_R) f_{L;\frac{\alpha-1}{2}}(1-f_{R;\frac{\alpha+1}{2}}) \tag{A.24}$$

$$\begin{aligned} f_{2e}^{(in)}(\omega;V) &= \sum_{\alpha=\pm1}\Big\{ f_L(1-f_R) f_{L;\frac{\alpha+1}{2}}(1-f_{R;\frac{\alpha-1}{2}}) \\ &+ f_L(1-f_R) f_{L;\alpha}(1-f_{R;\alpha})\Big\} \end{aligned} \tag{A.25}$$

Interestingly, the global contribution of two-electron inelastic processes to shot-noise $\delta S_{2e}^{(in)}(V)$ is negative and proportional to $\{-(1-\tau)\}$, as expected from the general arguments about Pauli blocking. equation(A.26) enables to perform a mapping between the diagrammatic expansion of the two-electron processes and their contribution to $\delta S_{2e}^{(in)}(V)$. Indeed, the first term in the expression of $f_{2e}^{(in)}(\omega;V)$ provides the class of two-electron processes depicted in figure(A.2(a) and (b)) whereas the second term corresponds to the class of processes depicted in figure(A.2(c)).

A.3 THEORETICAL ANALYSIS OF EXPERIMENTAL CURVES

The fitting of the experimental data at high transmission, i.e. for G close to $1G_0$, is straight forward. It becomes slightly more involved for G well below $1G_0$ because conductance fluctuations give rise to a background of asymmetric bias-dependent conductance. These conductance fluctuations are suppressed at $G = 1G_0$, as has been shown in [7]. We present now some details about the theoretical analysis of the experimental curves. Of particular interest are the samples for which $G < 0.85G_0$, *i.e.* for which the correction to the noise induced by e-ph interactions is expected to be negative. In this case, the reduced noise $Y = (S(V) - S(0))/S(0)$ versus the reduced voltage $X = (V/2T)\cot(V/2T)$ results from the interplay between conductance fluctuations induced by intrinsic disorder in the experimental setup and the inelastic signal activated when $V > \omega_0$. It is then required to deconvolute the effect of background fluctuations from the inelastic signal in the samples for this region of parameters. In the high transmission regime $G > 0.95G_0$, such an analysis is not needed, because the inelastic signal clearly dominates other the background fluctuations.

The pattern of conductance fluctuations is rich because of the contribution of several (many) scattering centers, and it cannot be described in terms of just a few parameters. In order to capture the main effects we adopt the following procedure. We need to relax the assumption of energy independence of the transmission factor and to complement the description of the nano-junction by superimposing energy dependent fluctuations to the flat density of states (DoS) of the L-lead

$$\rho_L(\omega) = \rho_0\{1+\alpha_D e^{-|\omega|/\omega_c}\cos[\frac{2\pi}{\Omega_D}\omega+\phi_D]\} \tag{A.26}$$

$$\rho_0 = 1/\pi W \tag{A.27}$$

Those fluctuations stand for the existence of intrinsic disorder in the experimental setup at the origin of conductance fluctuations. They are characterized by a typical disorder strength α_D, a mean period Ω_D, a phase ϕ_D and a cutoff ω_c (fixed so that the fluctuations decay to zero far from the Fermi energy). Within this model, the transmission factor of the junction is still given a the standard Lorentzian-shape

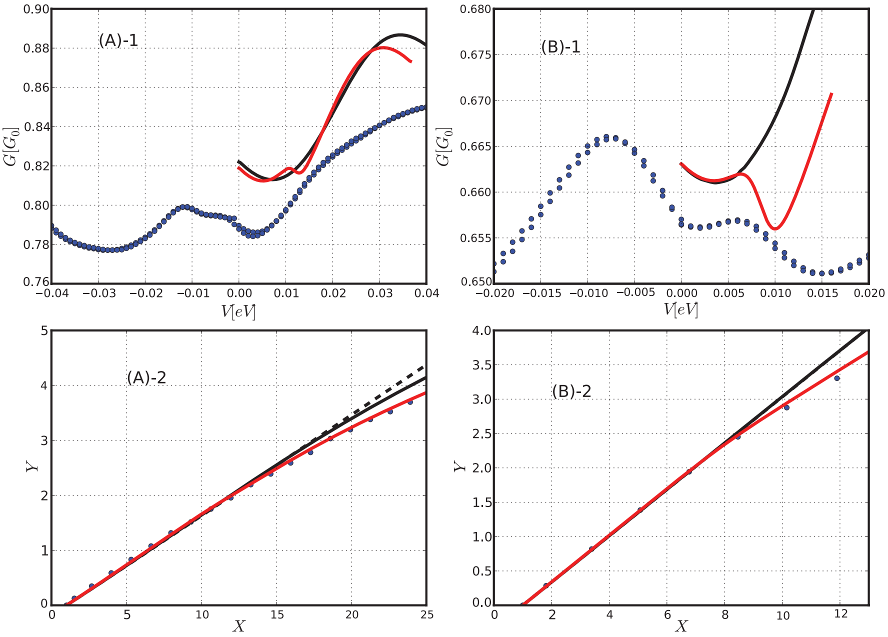

FIGURE A.3: Theoretical fitting of the experimental conductance and noise curve: Two examples A and B of conductance $G(V)$ and reduced noise $Y(X)$ measured on Au atomic chains. Common to the $G(V)$ curves $(A)-1$ and $(B)-1$: Blue points : experimental points for the conductance. Plain black curve : conductance with elastic background fluctuations only ($\lambda = 0$ and $\alpha_D \neq 0$). Plain red curve : conductance (output of the fit) with both elastic fluctuations and inelastic effects induced by e-ph interactions ($\lambda \neq 0$ and $\alpha_D \neq 0$). Common to the reduced noise curves $(A)-2$ and $(B)-2$: Blue points : experimental points for the reduced noise $Y(X)$. Dashed black curve : fitted reduced noise in the low bias regime ($V < \omega_0$), in absence of e-ph interactions and background fluctuations ($\lambda = 0$ and $\alpha_D = 0$). Plain black curve : reduced noise with elastic background fluctuations only ($\lambda = 0$ and $\alpha_D \neq 0$). Plain red curve : reduced noise (output of the fit) with both elastic fluctuations and inelastic effects induced by e-ph interactions. Parameters for the output of the fit (red curves) : Sample (A) : $\tau = 0.818; \omega_0 = 12.2$ meV; $\lambda/\Gamma = 0.20; \alpha_D = 12.7\%; \phi_D = 0.85\pi/2; \omega_D = 52.0$ meV. Sample (B) : $\tau = 0.663; \omega_0 = 8.5$ meV; $\lambda/\Gamma = 0.37; \alpha_D = 6.0\%; \phi_D = 0.98\pi/2; \omega_D = 50.0$ meV.

but with renormalized dot level position $\tilde{\omega}_d$ and coupling to the L-lead $\tilde{\Gamma}_L$

$$\tau(\omega) = \frac{4\tilde{\Gamma}_L(\omega)\Gamma_R}{[\omega - \tilde{\omega}_d(\omega)]^2 + [\tilde{\Gamma}_L(\omega) + \Gamma_R]^2} \tag{A.28}$$

$$\tilde{\Gamma}_L(\omega) = \Gamma_L \frac{\rho_L(\omega)}{\rho_0} \tag{A.29}$$

$$\tilde{\omega}_d(\omega) = \omega_d + \frac{1}{\pi}\int_{-\infty}^{+\infty} \frac{d\omega'}{\omega - \omega'} \tilde{\Gamma}_L(\omega') \tag{A.30}$$

We present on figureA.3 the results obtained for two particular samples (A) and (B), by fitting self-consistently the experimental conductance and reduced noise $Y(X)$ characteristics.

A.3.1 FITTING PROCEDURE FOR THE CONDUCTANCE CURVES

We consider the conductance curve of figure(A.3(A)-1), obtained for the sample (A) at temperature 6 K. It is characterized by a zero voltage conductance $G(V = 0) \approx 0.789G_0$. The local vibration mode energy is more difficult to recognize because it is masked by the conductance fluctuations, just as the inelastic shot noise signal. We take it to be given by the first maximum in the second derivative of current with voltage, $\omega_0 = 12.2$ meV. We will make use of the minimal model described above, for which the transmission factor is modulated by the position of the molecular level ω_d and the energy dependent DoS fluctuations in the L-electrode. For simplicity, we fix the couplings to the contacts to be symmetric $(\Gamma_L = \Gamma_R = \Gamma/2)$. We are thus left with five parameters in order to fit the experimental data, namely $\{\omega_d, \alpha_D, \Omega_D, \phi_D, \lambda\}$. Those parameters are neither free to choose nor independent and are imposed by the features of both experimental conductance and noise characteristics.

We first consider the non-interacting model $(\lambda = 0)$ and fit the behavior of the conductance close to zero voltage by modulating the energy dependence of the transmission factor. We fix the dot level position ω_d so that the transmission factor at zero energy $\tau = \tau(\omega = 0)$ is close to the experimental zero voltage value. We start by choosing an amplitude and period for the oscillations that capture the dominant behavior in the relevant voltage range, $\Omega_D = 52$ meV and $\alpha_D = 9.4\%$. The slope of the conductance curve close to zero voltage then fixes the phase ϕ_D to the value $\phi_D = 0.65\pi/2$ (see Black curve of figure(A.3-(A)-1). A similar curve is shown for the sample (B) on figure(A.3-(B)-1).

A.3.2 FITTING PROCEDURE FOR THE NOISE CURVES

We consider the noise curve of figure(A.3(A)-2) obtained for the same setting of the junction as in (A)-1. We obtain the zero energy transmission factor $\tau = 0.818$ (see the corresponding dashed black curve of figure(A.3(A)-2). When taking into account the energy dependence of the transmission factor ($\alpha_D = 9.4\%$ and $\lambda = 0$), we then obtain the plain black curve of figure(A.3-(A)-2). We notice that despite the absence of any inelastic effect $(\lambda = 0)$, the noise is decreased in the voltage region where $V > \omega_0 (X > 12.2)$ compared to the black dashed curve (energy independent transmission factor). We have made conservative estimates of the strength of the DoS fluctuations, which demonstrates clearly that there remains a large difference between the black curve and the experimental blue points of figure(A.3(A)-2), which we assign to an intrinsic inelastic effect in the noise induced by e-ph interactions.

Finally we quantify the inelastic contribution to the noise by considering the case of non-zero e-ph interaction. The renormalization of the transmission due to the e-ph interactions requires adjusting the value of the molecular level position (maintaining the other parameters fixed) in order to fit the conductance. We obtain the red curve of figure(A.3(A)-2) for a value of the e-ph coupling strength $\lambda/\Gamma = 0.2$ that describes the experimental data well.

A similar curve is shown for the measurement (B) on figure(A.3(B)-2). For this sample, the negative correction to the noise above the threshold is almost entirely due to inelastic effects in the noise induced by e-ph interactions.

A.3.3 SELF-CONSISTENCY

The procedure described above for the fitting of conductance and noise characteristics of sample (A) is repeated until self-consistency is achieved, namely all the features due to either conductance fluctuations and inelastic effects are consistent for both $G(V)s$ and $Y(X)s$. The discrepancy between the experimental zero-bias conductance and the fits is a consequence of the limited experimental accuracy (1% in $G(V)$ and $3-4\%$ in $Y(X)$). The final outputs for this fitting procedure are shown on the red curves of figure(A.3(A)-1) and figure(A.3(A)-2) for the following choices of parameters : $\tau = 0.818; \omega_0 = 12.2$ meV; $\lambda/\Gamma = 0.2; \alpha_D = 12.7\%; \phi_D = 0.85\pi/2; \omega_D = 52$ meV.

Similarly the output for the fitting procedure for the other sample (B) are shown by the red curves of figure(A.3(B)-1) and figure(A.3(B)-2) obtained with the following choices of parameters : $\tau = 0.663; \omega_0 = 8.5$ meV; $\lambda/\Gamma = 0.37; \alpha_D = 6\%; \phi_D = 0.98\pi/2; \omega_D = 50$ meV.

To conclude, the analysis of the data for high conductance, close to perfect transmission, is straight forward. For lower transmission, conductance fluctuations mask some of the intrinsic effects and a more involved analysis is required. With the analysis of the measurements (A) and (B) presented in figure(A.3), we show that it is possible to deconvolute the effects of background fluctuations induced by intrinsic disorder from the inelastic signal induced by e-ph interactions. By fitting self-consistently the experimental conductance and noise characteristics, it appears that the inelastic signal, although difficult to see in the conductance curves (masked by the background fluctuations) has a significant contribution (more than 50% for sample (A) and dominant in the case of sample (B)) to the negative correction to the noise observed above the threshold $(V > \omega_0)$.

REFERENCES

[1] R. Avriller and A. L. Yeyati, *Electron-phonon interaction and full counting statistics in molecular junctions*, Physical Review B **80**, 0413091 (2009).

[2] A. O. Gogolin and A. Komnik, *Towards full counting statistics for the Anderson impurity model*, Phys. Rev. B **73**, 195301 (2006).

[3] F. Haupt, T. c. v. Novotný, and W. Belzig, *Phonon-Assisted Current Noise in Molecular Junctions*, Phys. Rev. Lett. **103**, 136601 (2009).

[4] T. L. Schmidt and A. Komnik, *Charge transfer statistics of a molecular quantum dot with a vibrational degree of freedom*, Physical Review B **80**, 0413071 (2009).

[5] O. Tal, M. Krieger, B. Leerink, and J. M. van Ruitenbeek, *Electron-Vibration Interaction in Single-Molecule Junctions: From Contact to Tunneling Regimes*, Phys. Rev. Lett. **100**, 196804 (2008).

[6] Y. Blanter and M. Büttiker, *Shot noise in mesoscopic conductors*, Physics Reports **336**, 1 (2000).

[7] B. Ludoph, M. H. Devoret, D. Esteve, C. Urbina, and J. M. van Ruitenbeek, *Evidence for Saturation of Channel Transmission from Conductance Fluctuations in Atomic-Size Point Contacts*, Phys. Rev. Lett. **82**, 1530 (1999).

B

THE KONDO EFFECT FOR POINT CONTACTS

B.1 THE KONDO EFFECT

FOR bulk metals the electrical resistivity at room temperature is dominantly determined by electron-phonon (atomic lattice vibration) interactions. This scattering decreases with the lowering of temperature due to freezing out of phonons. At low temperatures electrons can travel with very little interaction leading to a decrease in the resistance. The resistance value of metals like gold and copper saturates at low temparatures to some value due to interaction of the electrons with lattice imperfections and grain boundaries. The value of the low temperature resistance remains constant on further reduction of the temperature and its value can only be changed by addition or removal of defects in the lattice. This can be seen from the schematic illustration shown in figure (B.1). Apart from this saturation there is a second kind of observation seen in these metals, with the resistance passing through a minimum and increasing upon futher reduction of the temperature. This effect was first seen in 1930 in Leiden by de Haas *et al.* [1]and was explained by Jun Kondo [2] in 1964. The increase in resistance is due to an increase in the effective scattering cross section of magnetic impurities. Magnetic impurities are antiferromagnetically screened by the conduction electrons by forming enveloping electron clouds around them, which leads to an increase in scatterer size. This phenomena is dominant at low temperatures, while at high temperatures electron-phonon interaction dominates which destroys the local magnetic interaction. This is illustrated in figure (B.1).

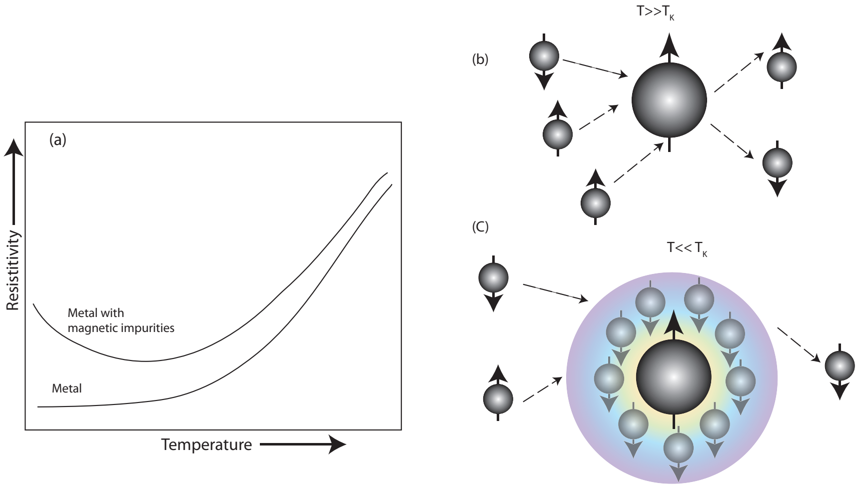

FIGURE B.1: Introduction of the Kondo effect: (a) Bulk metals containing a low concentration of magnetic impurities show an increase in the resistivity with lowering of the temperature. This is due to an increase in the effective scattering size as a result of the formation of an electron screening cloud around the magnetic impurities. (b) At high temperatures, due to a high rate of electron-phonon scattering, the magnetic impurity is not screened and hence the Kondo effect vanishes. (c) At lower temperature the conduction electrons form a screening cloud around the magnetic impurity which leads to an increase in the effective size of the scatterer, giving rise to an increase in the resistance.

B.1.1 ANDERSON SINGLE IMPURITY MODEL

The Anderson single impurity model is the simplest model to describe this many body phenomenon, where localized non-zero spin impurities are antiferromagnetically coupled to a sea of conduction electrons [3, 4][1]. In the Anderson single impurity model a magnetic impurity is viewed as a localized state with a discrete energy ϵ_d occupied by an unpaired electron, and coupled to a spin degenerate electron reservoir, as illustrated in figure (B.2) for a localized state connected between two electron reservoirs. The energy ϵ_d lies below the Fermi energy of the electron bath and U is the Coulomb charging energy for adding a second electron to the localized state. Let us consider the case that $|\epsilon_d| < U/2$. A finite s=1/2 spin moment is trapped in the energy state ϵ_d. The transfer of the electron from ϵ_d to either of the leads is classically forbidden without adding energy to the system. However, the uncertainty principle allows the transit of electrons between the leads and the localized state on the time scale $\tau \sim h/|\epsilon_d|$, where h is Planck's

---

[1] There is an excellent review on Kondo systems by Scott and Natelson[4], here we follow their approach.

constant. This can be written mathematically as:

$$H_{\text{Anderson}} = \sum_{\kappa\sigma} \epsilon_k c^{\dagger}_{\kappa\sigma} c_{\kappa\sigma} + \sum_{\sigma} \epsilon_\sigma d^{\dagger}_{\sigma} d_\sigma + U n_{d_\uparrow} n_{d_\downarrow} + \sum_{\kappa\sigma} (v_\kappa d^{\dagger}_{\sigma} c_{\kappa\sigma} + v^{*}_{\kappa} c^{\dagger}_{\kappa\sigma} d_\sigma), \quad \text{(B.1)}$$

where $c^{\dagger}_{\kappa\sigma}$ and $c_{\kappa\sigma}$ in the first term represent creation and annihilation operators for the electrons in the leads with momentum κ, spin σ and energy ϵ_k. It represents the electrons in the leads. The second term represents the electrons in the localized state ϵ_d, *i.e.* $d^{\dagger}_{\sigma}$ and d_σ create and annihilate an electron in the localized state. In the last term v is the rate of electron transfer from the localized state to the leads. A simplified pictorial representation of the Anderson single impurity model is shown in figure (B.2). For $U = 0$ and $v = 0$, the hamiltonian $H_{\text{Anderson}} = \sum_{\kappa\sigma} \epsilon_\kappa c^{\dagger}_{\kappa\sigma} c_{\kappa\sigma} + \sum_\sigma \epsilon_\sigma d^{\dagger}_{\sigma} d_\sigma$. In this case two electrons of opposite spin fill the impurity state ϵ_d as shown in figure (B.2a).

For $U \neq 0$ and $v = 0$ the Coulomb interaction leads to a cost in energy U to transfer a second electron to the discrete energy state $\epsilon_d + U$ due to the electron-electron repulsive interaction, hence ϵ_d can be only singly occupied. The situation turns out to be more complicated in the case when both $U \neq 0$ and $v \neq 0$. The coupling of the dot, *i.e.* the localized state, with the leads gives rise to a widening of the discrete energy state to a width Γ. This width depends upon the coupling strength v_κ. As stated above, through the Heisenberg uncertainty principle, electrons from the leads tunnel to ϵ_d or tunnel out of ϵ_d, which is allowed provided the transition time $\tau \backsim h/|\epsilon_d|$ is very short. This virtual process can have two transit paths as shown in figure (B.2c): In the first process an electron from the left lead tunnels to ϵ_d giving rise to a virtual double occupancy of the state, and within the time $\tau \backsim h/|\epsilon_d|$ the electron leaves the dot again. This is process 1 in figure (B.2c). In the second process the electron in the localized energy state ϵ_d transits out of the dot, leading to the formation of a virtual empty state. Then an electron from the left lead with opposite spin *w.r.t.* the initial spin state tunnels into the level ϵ_d. The spin state of the dot changes during this process, giving rise to a spin flip excitation in the dot. This is process 2 in figure (B.2c). These two virtual processes are dominant at low temperatures and give rise to a resonant feature in the conductance at zero bias. At higher temperatures, the virtual condensate state is not able to form due to dominant electron-phonon and electron-electron interactions and hence this feature is smeared out.

Using the Schrieffer-Wolff unitary transformation and considering terms up to second order in v_κ only, H_{Anderson} can be simplified to the Kondo Hamiltonian H_{Kondo} where the interaction takes the form of a net spin-spin interaction [2, 5],

$$H_{\text{Kondo}} = H_{\text{cond}} + H_{\text{int}} \quad \text{(B.2)}$$

where the first term H_{cond} defines the conduction electrons and the second term

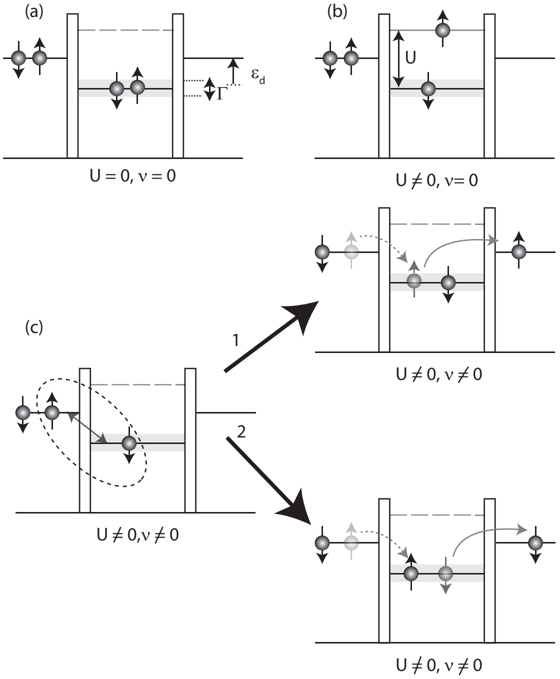

FIGURE B.2: Anderson single impurity model: (a) In the absence of Coulomb interaction ($U = 0$) and in absence of coupling between the dot and reservoir ($\nu = 0$) the dot can host a pair of electrons of opposite spins. (b) When only Coulomb interaction ($U \neq 0, \nu = 0$) is switched on, addition of a second electron on the dot costs an additional amount of energy U, which puts the electron on the next available energy state $\epsilon_d + U$. (c) When both interactions are switched on ($U \neq 0$ and $\nu \neq 0$) at low temperatures the electrons from the leads form an entangled state with the electron in the dot. Classically, the electron on the dot cannot tunnel to the leads without supplying an external amount of energy. But Heisenberg's uncertainty principle allows the electron in the dot to tunnel out of the lead provided an electron from the leads tunnels into the dot within the $\tau \backsim h/|\epsilon_d|$ where h is Planck's constant. This permits transport of an electron through the dot (either by process 1 or 2) producing an entanglement of the spins in the lead with the local spin. This leads to the Kondo resonance seen as a zero bias anomaly in the conductance.

H_{int} defines the interaction of the conduction electrons with the localized magnetic moment. This interaction is antiferromagnetic in nature [3, 5] and is given as,

$$H_{\text{int}} = J s_{\text{cond}} \cdot S \tag{B.3}$$

where S is the spin of the localized state, s_{cond} is the local spin density of the conduction electrons and J represents the spin- spin interaction. This antiferromagnetic interaction leads to the formation of a singlet state with net total spin 0. This singlet state $\frac{1}{2}(|\uparrow\Downarrow\rangle - |\downarrow\Uparrow\rangle)$ is formed between the local moment and many electrons from the conduction states of the leads. The conduction electrons collectively form a spin state $|\Uparrow\rangle$ that shields the $S = 1/2$ state of the electron in the localized state. The characteristic energy scale of the singlet state is given by the Haldane relation,

$$k_B T_K = \frac{\sqrt{\Gamma U}}{2} e^{-\pi\epsilon_d(\epsilon_d+U)/\Gamma U}, \tag{B.4}$$

where Γ is the width of the discrete energy state due to coupling to the leads. T_K is the Kondo temperature, which sets the scale below which Kondo phenomena become dominant [6]. $k_B T_K$ is the binding energy for the singlet state, illustrated in figure (B.1). We see that the Kondo temperature T_K is exponentially dependent upon Γ *i.e.* on the coupling strength of the lead to the dot. At higher temperatures transitions to higher energy states become possible and the screening of the impurity state is partially broken, leading to a decrease in the resonance at the Fermi energy. For higher temperatures a renormalization group analysis is needed to describe the conductance across the localized level, which can be approximated by [7],

$$G(T, V = 0) = \frac{G_O}{(1 + (2^{1/s} - 1)(T/T_K)^2)^s} + G_b, \tag{B.5}$$

where G_b is a background conductance due to parallel transmission paths, $s = 0.22$ for a spin-$\frac{1}{2}$ local state, and G_0 is the peak conductance of the system at $V = 0V$ with G_b subtracted. This equation defines the Lorentzian-like decay of the zero bias Kondo resonance with increasing temperature and the width of the Lorentzian at $G = G(T, 0)/2$ gives a measure of the Kondo temperature. For very low temperatures the zero bias resonance in conductance approaches a constant and it decreases approximatelu logarithmically with increase of temperature. This is a property that is generally associated as a hallmark for Kondo systems.

B.1.2 KONDO-FANO RESONANCE

The Kondo effect for a bulk metal host-impurity system results in an increase in the resistance at low temperatures due to an increase in the effective scattering size. In contrast, in reduced dimensions for transmission through a localized state the Kondo effect leads to forward scattering of the conduction electrons. This is seen as an increase in the conductance at zero bias and in the differential conductance it shows as a Lorentzian peak. However, parallel transmission of conduction electrons is often possible and this gives rise to interference between the Kondo processes and the non-Kondo processes. This produces a so-called Fano resonance, a 's'-like line shape near zero bias. This can be understood from a simple tight binding approach as shown in figure (B.4). The Fano model was originally proposed by

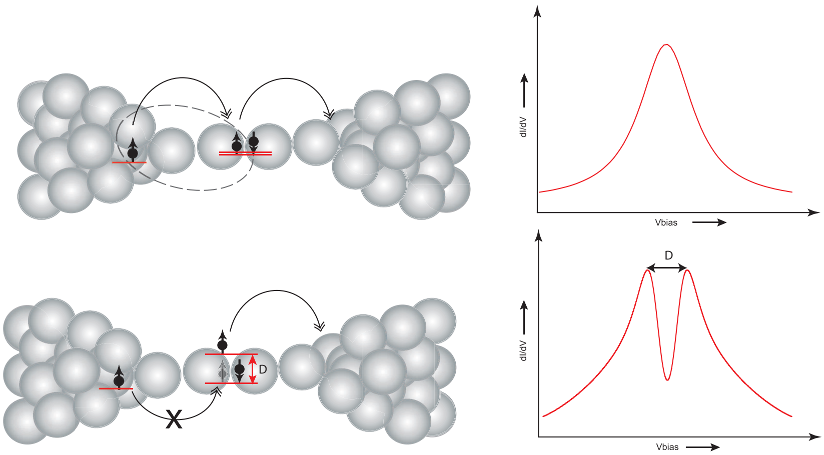

FIGURE B.3: Spin states formation for a Kondo system in a point contact due to interaction of the local spin state with the conduction electrons. The interaction leads to the formation of a spin singlet ground states of the combined electron spin-spin condensate. The spin triplet state is favored at magnetic fields above the critical field which lifts the spin degeneracy of the spin singlet states (lower panel).

U. Fano *et al.* [8] to understand the asymmetries in excitation spectra observed in He. The model describes the interaction of one discrete energy level with two or more continua of states. The coupling between the discrete energy state and the continuum give rise to different resonating features. The width and height of the resonance depends upon the coupling parameter.

The general form of the Fano lineshape in conductance can be written as [8–10],

$$G_{ac} = G_{off} + \frac{A(q+\epsilon)^2}{1+\epsilon^2}\,\frac{1}{1+q^2} \tag{B.6}$$

where A is the amplitude of the Kondo resonance, $\epsilon = \frac{eV-\epsilon_d}{k_B T}$ and ϵ_d is center of the Kondo many body resonance. A peak is found for $q \sim \infty$, a dip for $q = 0$, and a pure 's' shape for $q = -1$ and $q = 1$. Despite the complex line shape of the resonance in the conductance the height of the resonance has a universal logarithmic dependence upon the temperature.

B.1.3 PEAK SPLITTING AND SIDE PEAKS

The singlet state can be broken using a magnetic field. Application of a magnetic field lifts the degeneracy of the singlet state and splits the local moment in spin up and spin down states proportional to the applied magnetic field. This leads to

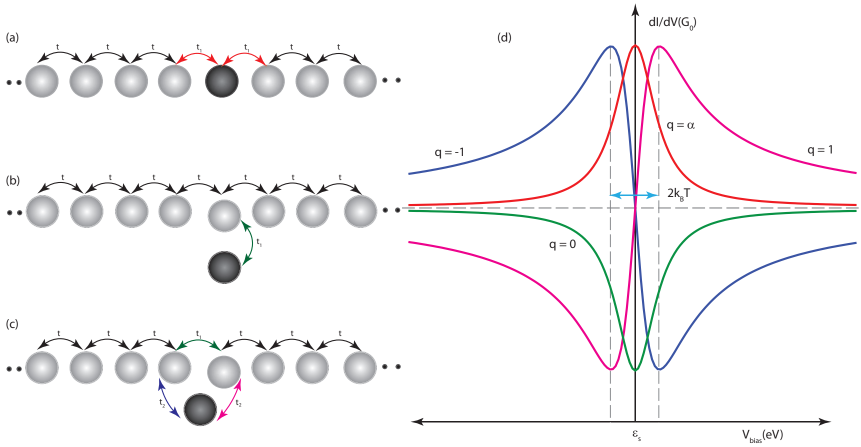

FIGURE B.4: Tight binding approach for explaining the general concept of a Kondo-Fano like resonance. (a) A semi-infinite metallic atomic chain with all atoms identical has a spin degenerate conduction band. A central atom (dark) having a localized magnetic moement is weakly coupled to two semi-infinite metallic chains, which gives rise to a resonant structure having a width that depends upon the coupling to the nearest atoms. (b) For the magnetic atom (dark) sitting on the side of the atomic chain the atom acts as an anti resonator giving rise to a dip in the conduction. (c) When the central atom (dark) is sitting in an interstitial position between two atoms of the atomic chain this gives rise to a resonant structure that depends upon the interference between the conduction path through the continuum states of the chain and the path through the resonating states of the central atom. The width and amplitude of the resonance depend upon the different coupling parameters of the central atom with its nearest atoms.

a splitting and suppression of the zero bias anomaly in the differential conductance. The expected splitting in the peak is proportional to twice the Zeeman energy for the applied field, $\Delta E_B = |g|\mu_B B$. Here, μ_B is the Bohr magneton and $|g|$ is the material dependent gyromagnetic constant [11]. Hence, one could expect peaks in the conductance at bias voltages $eV = \pm\Delta E_B$. The Kondo peak is only expected to be split for fields larger than the Kondo energy due to screening of the $s = 1/2$ magnetic impurity by the conduction electrons [12]. Experimental observations by Zumbuhl *et al.* [13] and Amasha *et al.* [14] show splitting in the zero bias resonance peak larger than twice the Zeeman energy. The splitting of the peaks decreases with increasing temperature in qualitative agreement with theory proposed by Costi *et al.*, but quantitatively the decrease in the splitting is larger than expected from the theory. This disagreement could be related to the exchange energy due to interaction between the localized spin impurity and other magnetic impurities in the leads, which was not accounted for in the calculations.

Low lying vibrational modes in combination with Kondo scattering is expected to give symmetric satellite peaks to the zero-bias peak. Inelastic electron scattering on vibration modes is a single-electron effect. For low transmission inelastic scattering opens up a new conductance channel at high bias, leading to an increase in the conductance; for high transmission it leads to backscattering above the threshold for vibration excitation. This is seen as a step-up or a step-down in the differential conductance, respectively [15]. A similar effect is possible in a system where electrons tunnel from one lead to other through a localized magnetic state. Studies on inelastic co-tunneling through localized spin states in magnetic ad-atoms, metal complex molecules, stacked molecular complexes, and carbon nanotubes can be found in Refs. [16–19]. It has been predicted that the coupling of the vibrational states with the magnetic state will give rise to resonance like structures at the vibrational energy of the system[20]. The origin of these satellite peaks in a Kondo system is illustrated in figure (B.5).

Electron transport through a localized magnetic system in the presence of inelastic scattering can be viewed as the sum of elastic and inelastic scattering through the Kondo state. The condition for inelastic scattering is that the bias window should be large enough for electrons to interact with the vibronic state. The elastic scattering gives the background conductance of the system without signature at the vibronic energy. The inelastic scattering in absence of spin interaction gives rise to a step in the differential conductance. In a Kondo system the inelastic excited state together with the localized spin states of the magnetic impurity gives the resonance structures. This can be seen in figure (B.5 d), which shows the spectral function $A(\omega)$ of the magnetic impurity state based on calculations by Korytar *et al.* The resonance peaks in the differential conductance at the vibronic energy is another signature of the Kondo physics.

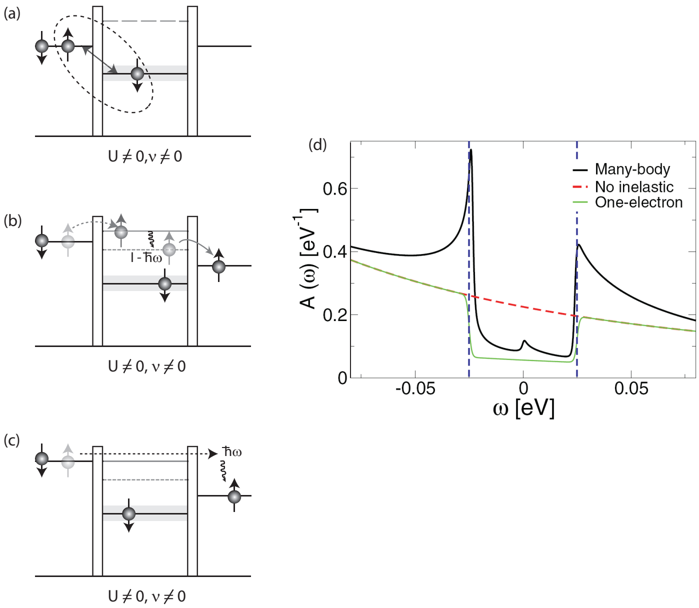

FIGURE B.5: Inelastic Kondo features: (a) A zero-bias Kondo resonance results from the coupling of a continuum electron cloud with a localized spin state. (c) The single particle inelastic electron scattering at high bias in absence of any spin interaction of the electrons with the localized spin state. (b) The many-body inelastic spin interaction due to opening of a new inelastic channel at high bias. (d) The projected density states on the localized spin state *i.e.* the spectral function A *w.r.t* bias voltage. The elastic scattering gives the background conduction without any prominent feature at the inelastic threshold (red dashed curve). In absence of any interaction with localized spin states the inelastic scattering of the electron gives a step feature at $\hbar\omega$ (green curve). The black curve shows prominent peaks at the inelastic energy ($\pm\hbar\omega$). The spectral function also shows a zero bias anomaly due to scattering through the singlet ground state (taken from [20]).

REFERENCES

[1] W. de Haas, J. de Boer, and G. van dën Berg, *The electrical resistance of gold, copper and lead at low temperatures*, Physica **1**, 1115 (1934).

[2] J. Kondo, *Resistance Minimum in Dilute Magnetic Alloys*, Progress of Theoretical Physics **32**, 37 (1964).

[3] P. W. Anderson, *Localized Magnetic States in Metals*, Phys. Rev. **124**, 41 (1961).

[4] G. D. Scott and D. Natelson, *Kondo Resonances in Molecular Devices*, ACS Nano **4**, 3560 (2010).

[5] J. R. Schrieffer and P. A. Wolff, *Relation between the Anderson and Kondo Hamiltonians*, Phys. Rev. **149**, 491 (1966).

[6] F. D. M. Haldane, *Scaling Theory of the Asymmetric Anderson Model*, Phys. Rev. Lett. **40**, 416 (1978).

[7] D. Goldhaber-Gordon, J. Göres, M. A. Kastner, H. Shtrikman, D. Mahalu, and U. Meirav, *From the Kondo Regime to the Mixed-Valence Regime in a Single-Electron Transistor*, Phys. Rev. Lett. **81**, 5225 (1998).

[8] U. Fano, *Effects of Configuration Interaction on Intensities and Phase Shifts*, Phys. Rev. **124**, 1866 (1961).

[9] R. Zitko, *Fano-Kondo effect in side-coupled double quantum dots at finite temperatures and the importance of two-stage Kondo screening*, Phys. Rev. B **81**, 115316 (2010).

[10] M. R. Calvo, D. Jacob, and C. Untiedt, *Analysis of the Kondo effect in ferromagnetic atomic-sized contacts*, Phys. Rev. B **86**, 075447 (2012).

[11] Y. Meir, N. S. Wingreen, and P. A. Lee, *Low-temperature transport through a quantum dot: The Anderson model out of equilibrium*, Phys. Rev. Lett. **70**, 2601 (1993).

[12] T. A. Costi, *Kondo Effect in a Magnetic Field and the Magnetoresistivity of Kondo Alloys*, Phys. Rev. Lett. **85**, 1504 (2000).

[13] D. M. Zumbühl, C. M. Marcus, M. P. Hanson, and A. C. Gossard, *Cotunneling Spectroscopy in Few-Electron Quantum Dots*, Phys. Rev. Lett. **93**, 256801 (2004).

[14] S. Amasha, I. J. Gelfand, M. A. Kastner, and A. Kogan, *Kondo temperature dependence of the Kondo splitting in a single-electron transistor*, Phys. Rev. B **72**, 045308 (2005).

[15] O. Tal, M. Krieger, B. Leerink, and J. M. van Ruitenbeek, *Electron-Vibration Interaction in Single-Molecule Junctions: From Contact to Tunneling Regimes*, Phys. Rev. Lett. **100**, 196804 (2008).

[16] J. Nygård, D. H. Cobden, and P. E. Lindelof, *Kondo physics in carbon nanotubes.*, Nature **408**, 342 (2000).

[17] W. Liang, M. Bockrath, and H. Park, *Shell Filling and Exchange Coupling in Metallic Single-Walled Carbon Nanotubes*, Phys. Rev. Lett. **88**, 126801 (2002).

[18] A. Kogan, G. Granger, M. A. Kastner, D. Goldhaber-Gordon, and H. Shtrikman, *Singlet–triplet transition in a single-electron transistor at zero magnetic field*, Phys. Rev. B **67**, 113309 (2003).

[19] I. Fernández-Torrente, K. Franke, and J. Pascual, *Vibrational Kondo Effect in Pure Organic Charge-Transfer Assemblies*, Physical Review Letters **101**, 2172032 (2008).

[20] R. Korytár, N. Lorente, and J.-P. Gauyacq, *Many-body effects in magnetic inelastic electron tunneling spectroscopy*, Physical Review B **85**, 1254341 (2012).

SUMMARY

Unlike bulk metals, for which the electrical resistance is due to scattering of the traversing electrons on lattice defects, lattice vibrations, grain boundaries, and impurities, electrons can travel across a quantum conductor without any scattering. For this reason transport in quantum conductors is said to be ballistic. The resistance in a quantum conductor is due to scattering of electrons at the contacts between the quantum conductor and the leads connecting it to the world outside. Atomic contacts are among the most widely studied systems of this kind, holding a special place in the field of nanoscience and nanotechnology. Unlike two-dimensional electron gas systems, the traveling electrons have a high density of states at the Fermi energy. The electrons are transmitted through discrete quantum channels and are susceptible to the local potential of the atoms in the contact. Hence, the above systems serve as a test bed to study the local interaction of electrons probing the properties of the atoms or molecules.

One of the techniques that has been widely used for probing the different physical properties of atoms or molecules is the mechanically controllable break junction technique, widely known as MCBJ. A bulk wire is thinned down to an atomic size contact by stretching. By stretching of the contact the resistance increases in discrete steps. The origin of these discrete steps is completely different from what we know from experiments in 2-dimensional electron gas systems. In our case the discrete steps are more associated with abrupt changes in the local arrangement of atoms in the contact. We are able to control the process of thinning down of the contact in the sub-Ångstrom regime. This gives us freedom to vary the coupling of the central atoms in the contact with the bulk leads. The electronic traveling states at the Fermi energy are quite sensitive to the co-ordination of the atoms; thus we have a tool to manipulate the effective electron transmission through the atomic contact just by stretching. This process creates atomically sharpened leads that are used not only for the study of the local properties of the atoms but also for the properties of foreign molecules inserted in the junction. The interaction of the electrons with these molecules shows up as distinct features in current-voltage spectroscopy. Electron-electron or electron-vibron interactions show characteristic signatures of the atomic or molecular species in the contact. While these interaction signals have now been studied in current-voltage spectroscopy by many groups, here we have studied the effect of these interactions on the current noise. The current fluctuates around its the mean value due to scattering of the electron at the contact, when the transmission probability is smaller than 1. This fluctuation is white in nature and known as shot noise. The shot noise in a conductor is proportional to the electronic charge and to mean current value. The full shot noise in a conductor in absence of any interactions is given as $S_I(A^2/Hz) = 2eI\delta(f)$, which is attained in the limit of low transmission probability, $\tau \ll 1$, for all channels. For perfect transmission ($\tau = 1$) the shot noise is fully suppressed, but in general the noise per channel is suppressed by a factor $F = (1 - \tau)$. The measure of this deviation is known as the Fano factor F. Due to electron-electron and electron-vibron scattering the shot noise value deviates from the non-interacting value, which can be seen in the case of electron-vibron scattering as a kink in the noise as a function of bias voltage. In our research we have looked into these deviations in order to study the interactions taking place in atomic or molecular conductors. This thesis can be divided into two parts: (a) Inelastic signatures in noise due to electron-vibron interactions. (b) Study of itinerant magnetism in the atomic contact: electron-electron interactions.

In the first part of this thesis we have looked into inelastic scattering effects in the noise. Previously, a cross-over in the sign of the signal in the differential conductance due to interaction of the conduction electrons with vibrons had already been seen. This interaction leads to a downward step in the differential conductance at the bias corresponding to the vibron energy for a quantum conductor having perfectly transmitting eigen channels. On the other hand, a upward step in differential conductance is found for quantum conductors with low-transmission eigen channels. The cross over was found around $\tau = 0.5\mathrm{G}_0$ for a single channel Landauer conductor. This can be understood in terms of a vibron mediated single-particle scattering effect. Since shot noise is the second cumulant of the current (the conductance is the first cumulant) it is more sensitive to subtle interactions of the conduction electrons. Our noise measurements on Au atomic chains show linear deviations at the vibronic energy of the Au atomic system. The effective change in noise is proportional to the effective change in the conductance due to the electron-vibron interaction. The cross over in the sign of the inelastic correction in noise is observed at a conductance value of $0.95\mathrm{G}_0$. This cross-over is higher than the predicted value of $0.85\mathrm{G}_0$. The positive inelastic correction in noise observed for high transmission is quite intuitive because of decrease in transmission probability due to inelastic scattering. However, the negative correction cannot be understood in a simple single-electron picture, but can be explained by processes involving two-electrons and a vibron: Two electrons, with energies E and $E - \hbar\omega_0$, are emitted from the left lead, with the higher energy electron (at energy E) emitting a vibron. The two electrons will then compete for the same outgoing states. This Pauli exclusion interaction makes the energy distribution of occupied outgoing states more uniform, and hence this lowers the noise. The observed positive inelastic correction in noise close to $\tau = 1$ is very close to the theoretical value while the negative correction deviates from the theoretical value, although this is very much model dependent. While adding conductance fluctuations in electron transport to the picture phenomenologically explains a shift in the crossover point, analytically it is not entirely satisfactory.

Similar measurements on Au-O-Au atomic chains show similar linear deviations in noise due to inelastic scattering of electrons. For Au atomic chains as well as for Au-O-Au atomic chains we have seen a second kink in the noise at higher energies. This could be a higher order vibronic processes taking place in the atomic chain.

Most of the Au contacts show a linear deviation of the measured shot noise from Leosvik-Levitov noise above the vibronic energy. A linear dependence is expected for a strong coupling of vibrons with the phonons in the leads. However, in some cases when this decoupling could be reduced the noise measurements show a non-linear deviation above the vibronic energy of the contact. This nonlinearity is due to the feedback of vibronic fluctuations on the charge statistics of the traversing electrons. The noise deviates quadratically above the vibronic energy in the experiment. However, its is too early to conclude on the relaxation rate of vibrons and make any definitive conclusion *w.r.t.* the existing theories.

A molecular system like Pt-D_2-Pt and Au-O-Au would be more appropriate to study the non-equilibrium vibron states feedback on traversing electron statistics. The disadvantage is that these systems are prone to $1/f$ noise. Typically, for Pt-D_2-Pt, the $1/f$ noise corner frequency at 34meV is 1MHz. For this reason we have developed a high-frequency low-noise cross-spectrum measurement setup, which can measure the noise in a molecular system in the MHz regime. This involves a custom-built low noise amplifier and a two-channel cross correlator. This setup is suitable to measure the inelastic noise signatures on single-mlecule systems.

For some of the Au atomic contacts we have seen an anomalously large suppression in noise at the vibronic energy. For the processes described above the suppression in noise is due to two-electron processes and is not larger than $20-30\%$. The anomalous contacts show a much higher suppression, even such that the total noise decreases at higher bias. We have investigated whether the effect can be explained by weak charge shuttling of the electrons, including the image charge in the model. We can only arrive at a sufficiently large effect for a very high amplitude periodic motion of the atom in the contact. Such anomalously large amplitudes have been suggested to arise due to non conservative current-induced forces acting on the atoms in the contact. This force may also explain earlier observations of anomalous current-induced breaking of atomic chains, hence it would be interesting to test the breaking voltages of the chains showing anomalous noise properties. Such a study is underway.

In the second part of the thesis we have looked into the role of magnetism in Pt atomic chains and ferromagnetic atomic contacts. It has been predicted that Pt atomic chains should develop a localized magnetic moment in the contact. An increased localized moment is expected due to the enhanced density of states which takes the suscepetibility beyond the Stoner limit, upon a stretching induced reduction of the atomic co-ordination. Being very close to the Stoner criterion and having high spin-orbit coupling, Pt is expected to show a transition from bulk paramagnetism to spontaneous magnetization in atomic chains. The presence of strong zero bias anomalies in differential conductance measurements for Pt atomic chains has been attributed to weakly localized magnetic moments. We have characterized the Pt atomic chains by differential conductance and noise measurements. The noise measurements shows the presence of at least 4–6 spin channels in the atomic contacts. The presence of more than one (two spin) channels is expected for transition metals, due to the participation of d orbitals in the conductance. We have observed a strong reduction in noise upon stretching of the contact and eventually a Fano factor falling on the minimum noise curve for two spin-degenerate channels (four spin channels) having one doubly occupied channel perfectly transmitting. The cloud of data points observed is clearly bound by this curve. This suggests absence of strongly spin polarized eigen channels in conductance. We propose that the conductance is dominated by weakly polarized channels, with magnetism possibly confined to channels that are poorly transmitted.

In contrast to Pt, Fe and Ni are ferromagnets in the bulk, and atomic contacts are considered to have localized moments due to the presence of partially filled d sub-orbitals. The interaction of the local magnetic moment with the continuum states gives rise to many body phenomena with the localized non-zero spin states being coupled to the sea of conduction electrons. For a spin-$\frac{1}{2}$ moment in a non-magnetic host metal this phenomenon is widely known as the Kondo effect. The signature of the Kondo effect in the differential conductance is seen as a zero bias anomaly. In experiments, the expected logarithmic dependence of the zero bias conductance*w.r.t.* bath temperature as shown by Calvo *et al.*, has led to a Kondo interpretation of the zero bias anomalies, despite the strong exchange splitting of the 'host'. We have followed the stretching dependence of the differential conductance and noise for such contacts. Applying the same analysis we find a Kondo temperature for Fe and Ni atomic contacts of 100K and 230K, respectively, in agreement with Calvo *et al.* The Kondo temperature of the contacts decreases with stretching of the contacts. Upon pushing the contacts towards the bulk limit a splitting of the Kondo resonance is observed. We tentatively attribute this to an interaction between two localized magnetic moments on two different atoms in the ferromagnetic atomic contact.

The noise measurements for the ferromagnetic contacts show sub-Poissonian noise with the presence of predominantly more than two channels (four spin channels) taking part in the conduction. We did not find any clear evidence for strongly spin polarized conductance channels below the limiting curve for spin degenerate systems, except for two contacts with ($G < 1\mathrm{G}_0$), for which we have only a low accuracy. The Fano factor measured on the ferromagnetic atomic contact scales roughly linearly with the Kondo temperature and its resonance amplitude, with some scatter. The observed connection between the Fano factor and the weight of the zero bias anomaly supports the view that the zero bias anomaly originates from spin scattering by localized magnetic moments. However, whether this is true Kondo scattering as suggested by Calvo *et al.* can not be stated conclusively from our data.

The study of shot noise on atomic contacts gives insight into electron transport properties that are missing in simple conductance measurements. Future high-bias shot noise experiments on molecular systems could reveal details of the non-equilibrium vibron occupation and its interaction with the conduction electrons. The high frequency noise measurement set up is a sure way to go head to reveal more physical phenomena in nanoscale electron transport.

SAMENVATTING

Voor bulkmetalen geldt dat de elektrische weerstand wordt veroorzaakt door de verstrooiing van elektronen aan defecten, roostertrillingen, korrelgrenzen of kunnen elektron echter onzuiverheden. Door een kwantum geleider kunnen elektronen echter reizen zonder enige verstrooiing. Om deze reden heet transport in kwantum geleiders ballistisch. Toch is de gemeten weerstand niet nul; zij wordt veroorzaakt door de verstrooiing van elektronen bij de contacten tussen de kwantum geleider en de normale geleiders die het geheel met de buitenwereld verbinden. Atomaire contacten zijn een van de meest bestudeerde systemen van dit soort en hebben een speciale plek in de vakgebieden van nanowetenschappen en nanotechnologie. Anders dan tweedimensionale elektron gas systemen, hebben de elektronen in zo'n atomair contact een hoge toestandsdichtheid bij de Fermi energie. Het transport van elektronen gaat door discrete kwantum kanalen en is vatbaar voor de lokale potentialen van de atomen in het contact. Daarom worden deze systemen gebruikt om de lokale interacties van elektronen en daarmee de eigenschappen van de atomen of moleculen te onderzoeken.

Een van de technieken die vaak gebruikt wordt om de fysieke eigenschappen van verschillende atomen of moleculen te onderzoeken is de *mechanically controlled break junction* techniek (MCBJ). Een macroscopische draad wordt ingesnoerd tot een atomair contact door de draad uit te rekken. Hierdoor wordt de weerstand in discrete stappen groter. De oorsprong van deze discrete stappen is anders dan wat wij weten van experimenten met tweedimensionale elektron gas systemen. In onze experimenten zijn deze discrete stappen geassocieerd met abrupte veranderingen in de lokale rangschikking van atomen in het contact. We kunnen het proces van uitrekking beheersen tot stappen in het sub-Ångstrombereik. Dit geeft ons de vrijheid om de koppeling van de centrale atomen in het contact met de bulk te variÃńren. Omdat we hebben gezien dat elektronische toestanden bij de Fermi energie vrij gevoelig zijn voor de coördinatie van de atomen, hebben wij een stuk gereedschap tot onze beschikking om de effectieve elektronen transmissie door het atomaire contact te manipuleren door middel van uitrekking. Dit proces creëert atomair scherpe elektroden die niet alleen voor de studie van de lokale eigenschappen van atomen, maar ook voor de studie van de eigenschappen van moleculen die in de junctie zijn geplaatst. De interactie van de elektronen met deze moleculen kan worden bepaald met behulp van stroom-spanning spectroscopie. Elektron-elektron of elektron-fonon interacties zijn karakteristiek voor de atomaire of moleculaire soort in het contact. Terwijl deze interactiesignalen door meerdere onderzoeksgroepen met stroom-spanningsspectroscopie zijn bestudeerd, hebben wij de effecten van deze interacties op de fundamentele ruis in de stroom onderzocht. De stroom fluctueert rond de gemiddelde waarde vanwege verstrooiing van het elektron bij de contacten, als de transmissiekans kleiner is dan 1. Deze fluctuatie heeft van nature een wit karakter, en staat bekend als hagelruis. De hagelruis in een geleider is evenredig met de elektrische lading en met de gemiddelde waarde van de stroom. Hagelruis in een geleider in afwezigheid van interacties, wordt gegeven door $S_I = 2eI$; deze uitdrukking geldt in de limiet van een lage transmissiekans, $\tau \ll 1$, voor alle kanalen. Voor perfecte transmissie ($\tau = 1$) is de hagelruis volledig onderdrukt. In het algemeen is de ruis per kanaal onderdrukt met een factor $F = (1-\tau)$, de Fano factor. Vanwege elektron-elektron en elektron-fonon verstrooiing wijkt de waarde van de hagelruis af van de zonder wisselwerkingen; in het geval van elektron-fonon verstrooiing kan dit worden waargenomen als een knik in de ruis-spanning grafiek. In ons onderzoek kijken wij naar deze afwijking om de interacties die plaats vinden in atomaire en moleculaire geleiders te bestuderen. Dit proefschrift bestaat uit twee delen: (a) Inelastische signaturen in de ruis als gevolg van elektron-fonon interacties. (b) De studie van magnetisme in atomaire contacten: elektron-elektron interacties.

In het eerste deel van dit proefschrift hebben we gekeken naar inelastische verstrooiingseffecten in de ruis. Eerder hebben wij al een *transitie* gezien in het teken van het signaal in de differentiële geleiding ten gevolge van de elektron-fonon interactie. Deze interactie lijdt tot een stap naar beneden in de differentiële geleiding bij de bias-spanning die correspondeert met de fonon energie van een kwantum geleider met perfecte transmissie. Daarentegen vindt men een stap omhoog in de differentiële geleiding voor kwantum geleiders met lage-transmissie. Voor een Landauer geleider met een enkel kanaal wordt de *tekenwisseling* gevonden rond $\tau = 0.5G_0$. Dit kan begrepen worden in termen van een fonon-gemedieerde enkel-deeltje verstrooiings-effect. Aangezien hagelruis de tweede cumulant van de stroom is (de geleiding is de eerste cumulant), is deze meer gevoelig voor subtiele interacties van de geleidende elektronen. Onze ruis metingen aan atomaire goud ketens laten afwijkingen zien in de fonon energie van het goud atomaire systeem. De verandering in ruis is evenredig met de verandering in de geleiding ten gevolge van de elektron-fonon interactie. De *overgang* in het teken van de inelastische correctie in de ruis wordt gezien bij een geleidingswaarde van $0.95G_0$. Deze *overgang* is hoger dan de voorspelde waarde van $0.85G_0$. De positieve inelastische correctie in de ruis gezien bij hoge transmissie is vrij eenvoudig te begrijpen. Echter, de negatieve correctie kan niet in een simpel enkel-elektron plaatje begrepen worden, maar kan uitgelegd worden als een twee-elektronen-en-een-fonon-proces.

Beschouw twee elektronen, met energieën E en $E - \hbar\omega_0$, uit het linker reservoir, waarbij het elektron met hoge energie (met energie E) een fonon genereert. De twee elektronen zullen dan concurreren om dezelfde uitgaande toestand. De wisselwerking als gevolg van het Pauliverbod zorgt ervoor dat de energie distributie van bezette uitgaande toestanden meer uniform is, en daarmee de ruis verlaagt. De positieve inelastische correctie waargenomen in de ruis dicht bij $\tau = 1$ komt goed overeen met de theoretische waarde, terwijl de negatieve correctie afwijkt van de theoretische waarde, al is dit erg afhankelijk van het model. Het toevoegen van geleidingsfluctuaties in elektron transport kan de verplaatsing in de *tekenovergang* fenomenologisch verklaren, maar is in kwantitatief opzicht niet geheel afdoende.

Vergelijkbare metingen van Au-O-Au atomaire ketens laten gelijksoortige lineaire afwijkingen in de ruis zien, als gevolg van inelastische verstrooiing van elektronen. Voor Au atomaire ketens, zowel als voor Au-O-Au atomaire ketens hebben wij een tweede kink in de ruis gezien bij hogere energiëen. Dit zou een gevolg van hogere-orde vibratie processen kunnen zijn.

De meeste Au contacten laten een lineaire afwijking zien boven de fonon energie. Een lineaire afhankelijkheid is te verwachten voor een sterke koppeling van fononen met de fononen in de elektroden. Echter, in sommige gevallen waar deze koppeling verminderd kan worden-laten de ruis metingen een niet-lineaire afwijking zien boven de fonon energie van het contact. Deze niet-lineairiteit is toe te schrijven aan een terugkoppeling van de fonon fluctuaties op de ladingstatistiek van de elektronen. De ruis wijkt kwadratisch af boven de fonon energie in het experiment. Echter, het is te vroeg om conclusies te trekken over de ontspanningssnelheid van fononen en om een definitieve conclusie te trekken over de bestaande theorieën.

Een moleculair systeem zoals Pt-D_2-Pt en Au-O-Au zou geschikter zijn om de niet-lineaire effecten die veroorzaakt worden door inelastische verstrooiing, te bestuderen. Het nadeel is dat deze systemen vaak last hebben van 1/f ruis. Doorgaans ligt de kantelfrequentie van de 1/f ruis voor Pt-D_2-Pt bij een instelspanning van 34meV is rond de 1MHz. Om deze reden hebben wij een hoogfrequentie lage-ruis kruis-spectrum meetopstelling ontwikkeld, welke de ruis in een moleculair systeem in het MHz bereik kan meten. Hiervoor gebruiken wij een op-maatgemaakte lage ruis versterker en een twee-kanaals kruiscorrelator.

Voor sommige Au atomaire contacten hebben we een abnormaal grote ruis onderdrukking bij de fonon energie gezien. Voor de processen die hierboven zijn beschreven zijn twee-elektron processen de reden voor de ruis onderdrukking (niet groter dan $20 - 30\%$). Abnormale contacten laten een veel hogere onderdrukking zien, zelfs een afnamen van de ruis bij hogere spanning. Wij hebben onderzocht of dit effect verklaard kon worden door zwakke lading *shuttling*, inclusief spiegelpotentiaal. We kunnen alleen een voldoende groot effect krijgen in ons model bij een periodieke beweging van het atoom in het contact met grote amplitude. Zulke abnormaal grote amplitudes kunnen voorkomen in recente modellen die niet-conservatieve stroom-geïnduceerde krachten in beschouwing nemen die de atomen in het contact beïnvloeden. Deze kracht kan ook eerdere waarnemingen verklaren van abnormale stroom-geïnduceerde breuken van atomaire ketens, dus zou het interessant zijn om te testen wat de breuk-spanningen zijn van de ketens die abnormale ruiseigenschappen laten zien. Een vervolg studie is aan de gang.

In het tweede deel van dit proefschrift hebben wij gekeken naar de rol van magnetisme in Pt atomaire ketens en ferromagnetische atomaire contacten. Uit modelberekeningen is voorspeld dat Pt atomaire ketens een gelokaliseerd magnetisch moment zullen ontwikkelen in het contact. Een verhoogd gelokaliseerd moment kan worden verwacht vanwege de verhoogde toestandsdichtheid, door reductie van de atomaire coördinatie bij oprekking van het contact. Omdat de susceptibiliteit van Pt erg dicht bij de Stoner limiet ligt, en Pt een hoge koppeling heeft, verwacht men dat Pt een overgang van bulk paramagnetisme naar spontaan magnetisatie in atomaire ketens zal laten zien. De aanwezigheid van sterke anomalieën in de differentiële geleiding rond het nul-spanning punt voor Pt atomaire ketens, is eerder toegeschreven aan zwakke gelokaliseerde magnetische momenten. We hebben de Pt atomaire ketens gekarakteriseerd door middel van differentiële geleiding en ruis metingen. De ruis metingen wijzen op de aanwezigheid van tenminste 4 – 6 spin kanalen in de atomaire contacten. De aanwezigheid van meer dan één (twee spin) kanalen is te verwachten voor overgangsmetalen, vanwege de deelname van d orbitalen in de geleiding. We hebben een sterke reductie in de ruis gezien bij uitrekking van het contact, en uiteindelijk een Fano factor samenvallend met de minimum ruis curve voor vier spin kanalen, waarbij een kanaal dubbel bezet is en perfect geleidt. De waargenomen wolk aan datapunten is duidelijk begrensd door deze curve. Dit suggereert de afwezigheid van sterke spin-gepolariseerde eigen kanalen in de geleiding. We stellen voor dat de geleiding wordt gedomineerd door zwak gepolariseerde kanalen, waarbij magnetisme mogelijk is beperkt tot kanalen die slecht geleiden.

In tegenstelling tot Pt, zijn Fe en Ni ferromagnetisch in de bulk, en atomaire contacten hebben gelokaliseerde momenten veroorzaakt door de aanwezigheid van gedeeltelijke gevulde d suborbitalen. De interactie van het lokale magnetische moment met de continuumtoestanden, veroorzaakt veel-deeltjes effecten met de gelokaliseerde niet-nul spin toestanden gekoppeld aan de zee van geleidingselektronen. Voor een spin-1/2 moment in een niet-magnetisch metaal staat dit fenomeen bekend als het Kondo effect. De signatuur van het Kondo effect in de differentiële geleiding wordt gezien als een anomalie bij spanning nul. In experimenten door Calvo *et al.* werd de verwachte logaritmische afhankelijkheid van de geleiding bij nul-spanning gevonden bij lage temperatuur, wat er toe leidde dat de auteurs een Kondo interpretatie van de *zero-bias* anomalieën voorstelden, ondanks de sterke *exchange opsplitsing* voor deze metalen. We hebben de uitrekkingsafhankelijkheid van de differentiële geleiding en ruis voor zulke contacten gevolgd. Gebruik makende van dezelfde analyse vonden wij een Kondo temperatuur voor Fe en Ni atomaire contacten van 100K en 230K, respectievelijk, in overeenstemming met Calvo *et al.* De Kondo temperatuur van de contacten daalt bij het oprekken van de contacten. Als de contacten naar de bulk limiet worden geduwd, zien wij een splitsing van de Kondo resonantie. Wij wijten dit voorlopig aan een interactie tussen twee gelokaliseerde magnetische momenten op twee verschillende atomen in het ferromagnetische atomaire contact.

De ruis metingen voor de ferromagnetische contacten laten een sub Poissoniaans ruisniveau zien, met de aanwezigheid van overwegend meer dan twee kanalen (vier spin kanalen) die participeren in de geleiding. We vonden geen duidelijk bewijs voor sterk ontaarde geleidingskanalen onder de limiterende curve voor spin gedegenereerde systemen, behalve voor twee contacten met ($G < 1G_0$), voor welke we slechts een lage nauwkeurigheid hebben. De Fano factor gemeten voor ferromagnetische atomaire contacten schaalt ruwweg lineair met de Kondo temperatuur en met zijn resonantie amplitude, met enige uitschieters. De waargenomen connectie tussen de Fano factor en de grootte van de anomalie ondersteunt het idee dat de anomalie afkomstig bij nul-spanning is van spin verstrooiing door gelokaliseerde magnetische momenten. Echter, of dit werkelijk Kondo verstrooiing is, zoals Calvo *et al.* voorstellen, kan niet met zekerheid gezegd worden op basis van onze data.

De studie van hagelruis op atomaire contacten geeft ons inzichten in elektron transport eigenschappen die niet verkregen kunnen worden uit simpele geleidingsmetingen. Toekomstige hoge spanning hagelruis experimenten op moleculaire systemen zouden details van de niet-evenwicht fonon bezetting en zijn interacties met de geleidingselektronen kunnen aantonen. De hoge frequentie ruismetingsopstelling is een goed opstelling om meer fysische verschijnselen in nanoschaal elektron transport aan het licht te brengen.

ACKNOWLEDGEMENTS

Over four years of work in the lab finally culminates in a book. It would be quite cheap to state that this book is the result of just my own contribution. My journey towards research started with a dream my dad and me shared. Thanks dad, for showing me the life beyond textbooks.

This thesis wouldn't be here if Prof. Jan van Ruitenbeek hadn't offered me a PhD position in his group. I am thankful to him for having faith in me, and helping me to understand the critical issues in the field of mechanical break junctions. Thanks Jan for guiding me through my PhD track.

Thanks to all theorists with whom I worked during my PhD. Remi Avriller, thanks for working on our data and correcting some of my concepts. Prof. Alfredo Levy Yeyati, thanks for working hard on publishing our results. Your promptness really pushed our article to see the light. Thanks Dr.Yaroslav Blanter for working on our anomalous noise data. Alexander Smogunov, thanks for explaining me the Kondo effect in atomic contacts. Prof. Erio Tosatti, thank you for looking into our Pt experimental data.

I wouldn't have worked in condensed-matter physics if I hadn't met Dr. Kees Harmans. Thanks Kees for giving such a stimulating course on quantum transport. Prof. Per Delsing, Prof. Pertti Hakonen and Prof. Christian Glattli, thanks for explaining me the concepts of shot-noise measurement. Sense Jan, I consider you a friend more than a Professor and that gives me comfort when you are around. Thanks for improving my oral presentation skills.

Thanks Oren and Roel, for taking up the daunting task to supervise me during the beginning of my PhD research. Your coolness and calmness kept me on track.

The biggest challenge in the high frequency noise project was to design the low noise cryogenic amplifier. Stefan, thanks for taking this challenge. Bert and Ruud you are the heart of the high frequency noise measurement project. Thanks for always helping me in a short notice.

Danielle, Ellie and Barry, you both helped me a lot. Thanks!

This thesis contain results that came out of hard work done by my students Zheng Baardman and Kiran. Thanks a lot. Satoshi Kaneko and Mohammed Saghir, the month that we worked together was wonderful. Ran, you are a great engineer and scientist.

AMC-MSM group members kept changing during my PhD period. Old members left and new ones joined. It was fun to discuss physics with coffee with all of you. Monica, thanks for pulling me to Leiden. You are a wonderful friend. Federica, thanks for annoying me by refilling the Beast while I was doing my sensitive measurements. Thanks for all the fun and help in the lab when my experiment was not working. Christian and Federica thanks for accepting to be with me on my D-Day.

Thanks Liz, Constant and Barry for helping me in writing my samenvatting.

In my life outside the lab I have a few awesome friends without whom I would be incomplete. Thanks to all of you for giving me a social blanket.

At the end, I am in deep debt to my family members especially Maa, Didiji, Bhiayaji for supporting my decision to strive for higher education. I think this journey wouldn't have come to completion without the support and love shown by Kristiina. Proty and Neo you two are the most wonderful things I have. Going for late evening walks with both of you is just wonderful. You pull me out of my own imaginary world.

CURRICULUM VITÆ

Manohar KUMAR

26-12-1979	Born in Barauni, India.

EDUCATION

1985–1994	Primary School (DAV Barauni, India)
1994–1996	Secondary School (CBSE, India)
1996–1998	Secondary High School (CBSE, India)
1999–2004	Bachelor of Technology, Electronics engineering Indian School of Mines, Dhanbad, India
2005–2006	Master of Science, Nanoscience and Nanotechnology TU Delft, The Netherlands
2006–2007	Master of Science, Nanoscience and Nanotechnology Chalmers University of Technology; Sweden *EMM masters*
2007-2012	Ph.D. research, *A study of electron scattering through noise spectroscopy* Universiteit Leiden, The Netherlands Promotor: Prof. Dr. J.M. van Ruitenbeek

LIST OF PUBLICATIONS

1. **Kumar Manohar**, Smit, R.H.M., Tal, O., van Ruitenbeek, J.M.,"Inelastic scattering effects and electronic shot noise", IEEE International Conference on Noise and Fluctuations (ICNF), 978-1-4577-0189-4, 2011.

2. **Kumar, Manohar**, Avriller, Rémi Yeyati, Alfredo Levy and van Ruitenbeek, Jan M., "Detection of Vibration-Mode Scattering in Electronic Shot Noise", Physical Review Letters,**108**, 146602, 2012.

3. **Kumar Manohar**, Smit, R.H.M., Tal, O., Smogunov, A., Tosatti, E. and van Ruitenbeek, J.M., "Surprising lack of itinerant magnetism in the conductance channels of Pt atomic chains", to be published Physical Rev. B.

4. **Kumar Manohar**, Blanter, Y. and van Ruitenbeek, J.M.,"Anomalous suppression of shot noise in Atomic contact", to be submitted to Physical Rev. B.

5. **Kumar Manohar**, Stahl, S., Crama, B., Egmond, R. and van Ruitenbeek, J.M.,"High frequency two channel cross spectrum noise measurement setup for mechanical controllable break junction", in preparation.